AD-A242 898

DTIC
NOV 1 5 1991
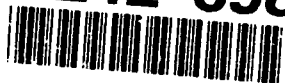C

Proceedings of

"Third SDIO/ONR Pulse Power Meeting '90"

August 2 - 3, 1990
Norfolk, Virginia

Organized by:

Dr. Vishnu K. Lakdawala
Dept of Electrical & Computer Engineering
Old Dominion University
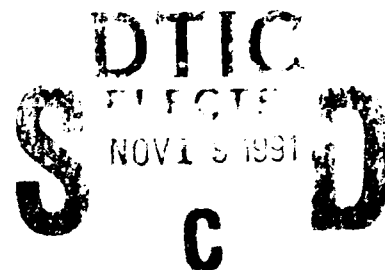Norfolk, Virginia 23529

Sponsored by:

91-12731

91 10 7 103

Proceedings of

"Third SDIO/ONR Pulse Power Meeting '90"

August 2 - 3, 1990
Norfolk, Virginia

Organized by:

Dr. Vishnu K. Lakdawala
Dept of Electrical & Computer Engineering
Old Dominion University
Norfolk, Virginia 23529

Sponsored by:

PREFACE

The "Third SDIO/ONR Pulse Power Physics meeting" was held at the Omni International Hotel in Norfolk, VA on August 2 and 3, 1990. This meeting was sponsored by the Office of Naval Research (ONR) and the Physical Electronics Research Institute (PERI) at Old Dominion University. The meeting follows the first two meetings held at the University of Rochester (Summer 1988) and in San Diego (Summer 1989). The meeting was called to report research progress and to discuss future plan for the research programs supervised by Dr. Gabriel D. Roy, the Office of Naval Research. Key scientists who are interested in pulse power physics were also invited to participate in the meeting. The objective of the meeting is to provide a forum for researchers from universities, industries and government agencies to exchange ideas and information so as to enable the research in the area of pulse power physics to proceed in a coordinated manner.

I wish to thank Gabriel Roy for giving us the opportunity to host this meeting at Norfolk. I would like to acknowledge the help of Karl Schoenbach and Martin Gundersen during the organization and planning stages of the meeting. The funding from the ONR and PERI (ODU) is greatly appreciated. Special thanks to my secretary Louise Yasaitis for help throughout and Gordhan Barevadia in preparing this proceedings. I wish to thank Art Guenther, Alan Garscadden and Gerard Mourou for accepting the invitation and present the invited talks. Finally I wish to thank all the attendees for their participation.

Vishnu K. Lakdawala

PROGRAM

Third SDIO/ONR Pulse Power Physics Meeting

Thursday   August 2, 1990

8:30 am	Welcome	Dean Cross
8:40 am	Announcement	Vishnu K. Lakdawala
8:50 am	Opening Remarks	Gabriel Roy

Session I   Semiconductor Research

Session Chairman: **Martin Gundersen**

9:00 am Paper I.A	Gerard Mourou Invited Talk	"High Power Switching in ps Domain Present and Future"
9:35 am Paper I.B	Chi Lee	"Peak Power Gain and Pulse Compression in an Inductive Energy Storage System"
10:00 am Paper I.C	Vishnu Lakdawala	"Laser Controlled Semiconductor Switch"
10:25 am Paper I.D	Brian Ditchek	"Semiconductor Metal Eutectics for Pulsed Power Switching"
10:50 am	Coffee Break	
11:15 am Paper I.E	Tangali Sudarshan	"Pulsed Surface Flashover Characteristics Along Alumina and Silicon in Vacuum"
11:40 am Paper I.F	William Donaldson	"Photoconductive Switching and Breakdown Investigated with Electro- Optic Imaging"
12:15 pm Paper I.G	Frazer Williams	"Physical Mechanisms of Surface Flashover on Silicon"
12:40 pm	Lunch	

Session II　　　Gas Discharge Research

Session Chairman: **Richard van Brunt**

2:00 pm Paper II.A	Alan Garscadden Invited Talk	"Some Plasma Physics Aspects of Pulsed Power"
3:00 pm Paper II.B	Martin Gundersen	"Research Results from the USC Pulse Power Applied Physics Program"
2:35 pm Paper II.C	Mark Kushner	"Modeling Pulse Power Plasma Switches: Hollow Cathodes and Beams"
3:25 pm Paper II.D	Glenn Gerdin	"Magnetic Control of Hollow Cathode Discharges"
3:50 pm	Coffee Break	
4:05 pm Paper II.E	Magne Kristiansen	"Insulator Damage Due to 0.3 MA Surface Discharges"
4:30 pm Paper II.F	Mark Browder	"Investigations in Modeling of Non-Linear Semiconductor Switches"
4:55 pm Paper II.G	Martin Brouillette	"Extended Duration Benchtop Hybrid Combustor"
5:20 pm Paper II.H	George Kirkman	"High Power High Rep Rate Modulators"
6:30 pm	Evening Dinner Cruise on the *American Rover*	

Friday   August 3, 1990

Session III   Panel Session

9:00 am	Panel Session	WHAT ARE THE ACCOMPLISHMENTS TO DATE?
		WHAT ARE THE GOALS FOR THE PULSE POWER RESEARCH?
	Moderator	Arthur Guenther
	Panel Members	Garscadden Mourou Gundersen Roy Kristiansen Rustan Kushner Schoenbach Lee
10:30 am	Coffee Break	
10:45 am	Panel Session	Continued
12:00 pm	Closing Remarks	Gabriel Roy
12:30 pm	Lunch	
2:00 pm	Administrative Session	
3:30 pm	ODU Lab Tour	
Evening	Reception at Karl Schoenbach's House	

HIGH POWER SWITCHING IN PICOSECOND DOMAIN, PRESENT & FUTURE

Gerard Mourou
Ultrafast Science Laboratory
University of Michigan
Ann Arbor, MI 48109-2099

PEAK POWER GAIN AND PULSE COMPRESSION IN AN INDUCTIVE ENERGY STORAGE SYSTEM

Chi H. Lee
Dept of Electrical Engineering
University of Maryland
College Park, MD 20742

Power Gain in an Inductive Energy Storage System
with a Photoconductive, Closing-and-Opening Switch

C. C. Kung, E. A. Chauchard, M. J. Rhee

L. Yan, and Chi H. Lee

Department of Electrical Engineering

University of Maryland

College Park, MD 20742

Abstract

For the first time, power gain as high as 16 has been obtained with a current charged transmission line and a photoconductive, closing-and-opening switch. The pulsed laser light source to activate the switch is specially designed. The laser pulse has a slow rise-time ($\sim$200 ns) and a fast fall-time ($\sim$10 ns). The switch used is a 5 mm GaAs cube of p-i-n diode configuration. The typical result was obtained at 500 V charging voltage producing a 2 kV output voltage pulse.

The inductive energy storage pulsed power system (IESPPS) is much more compact than the more commonly used capacitive energy storage system. This feature has stimulated the fast development of the opening switch[1-4], which is the key element in the IESPPS. In our laboratory, we have demonstrated that the photoconductive opening switch, which is the fastest among all the existing opening switches, is capable of opening the inductive energy storage circuit with an opening time on the order of nanoseconds[5,6]. Also photoconductive switches have some other advantages such as repetitive operation, controllable conduction period, and jitter-free triggering[5,6]. However, due to the limitation of the laser system and the switch fabrication technique in the past, the output voltage pulse was limited to a very low level. In this work, we successfully demonstrated that a 2 kV output voltage pulse can be achieved from the IESPPS with a 500 V source voltage.

The schematic diagram of the IESPPS used in the experiment is shown in Fig. 1. It is consisted of a photoconductive, closing-and-opening switch and a current charged transmission line (CCTL) which is the inductive energy storage device[6,7]. A 2.5 m long RG-213 coaxial cable is employed as the CCTL. The 0.1 Ω current viewing resistor is inserted in the shorted end to measure the charging current. The other end of the CCTL is connected through a semiconductor switch to a 0.1 μF capacitor C, which is initially charged to V_o. The output voltage waveform is measured at the switch end of the CCTL through a 50 Ω transmission line as shown in Fig. 1. In order for the system to function as an IESPPS, the conduction period of the switch should be long enough to build up the charging current I_0 in the CCTL, and the opening time of the switch should be faster than the round-trip time τ of the electrical pulse travelling in the CCTL, so that the produced output waveform can be nearly square. In this experiment, a specially tailored Nd:Glass laser pulse is used. The laser pulse (4 mJ pulse energy at 1.054 μm) is quite efficient in lowering the switch on-resistance[8]. Since the rise-time of the laser pulse is slow ($\sim$200 ns), the switch resistance gradually drops to a low value and the CCTL is charged up to current I_o. Due to the fast fall-time of the laser pulse ($\sim$10 ns), the switch can be opened on a

1

10 ns time scale. The switch used is a 5 mm cube GaAs of p-i-n diode configuration for which carrier recombination time is ~ 5 ns[9]; the electrode on n-type surface is connected to the positive polarity of the charging voltage. The laser pulse illuminates the switch perpendicularly to the electric field applied across the switch.

In this pulse forming experiment, the electrical energy is initially stored in the 0.1 μF capacitor; when the switch is turned on by the laser pulse, the capacitively stored energy is transferred into the CCTL. The charging current is monitored with the current viewing resistor. If we assumed that the CCTL acts as a lumped inductor and the switch is ideal, we could obtain the maximum charging current by using the equation $\frac{1}{2}LI_o^2 = \frac{1}{2}CV_o^2$. The typical results are obtained at the charging voltage of $V_o=500$ V, the corresponding charging current $I(t)$ is shown in Fig. 2(a). Notice that the current increases slowly up to 105 A which is much less than 250 A, the predicted maximum charging current. This is attributed to the slow rise of the laser pulse intensity which keeps the switch in a high on-resistance state during the early charging stage. As the laser pulse quickly terminates, the switch opens, resulting in the transfer of the stored inductive energy into the resistive load. If the opening phase of the switch were ideal (infinitive off-resistance in a short period), all of the stored energy would be transferred to the load. Because of the finite switch off-resistance, part of the energy is absorbed or reflected by the switch. The load, the 50 Ω plug-in of an oscilloscope connected through a 50 Ω coaxial cable, is in parallel with the switch, thus the resultant load resistance R_L is always less than 50 Ω. Figures 2(b) and 2(c) show the output voltage waveforms, of which the peak pulse amplitude is 2 kV. These were obtained at the charging voltage of $V_o=500$ V. By applying a charging voltage higher than 500 V, an output voltage pulse slightly higher than 2 kV was produced, but the pulse shape was very irregular.

It is shown that the CCTL produces a main pulse and a train of postpulses[10] into an

2

arbitrary resistive load R_L. The amplitudes of the pulses are given by

$$V_{out}^n = R_L Z_o I_o \frac{(Z_o - R_L)^n}{(Z_o + R_L)^{n+1}} \cdot \tag{1}$$

where n corresponding to the nth postpulse and $n=0$ represents the main pulse. In this case, only an ideal switch with infinitive off-resistance would produce just the main pulse into a matched load, $R_L = 50\ \Omega$. In actual experiment, finite switch off-resistance causes R_L to be less than Z_o, and thus the output pulse shape is a gradually diminishing staircase as shown in Fig. 3. Furthermore, the switch off-resistance is not a constant in time, thus the measured output pulse shape is not an exact staircase. As shown in Fig. 2(c), the postpulses of the staircase pattern with smooth corners are observed.

In order to characterize the switch dynamic resistance (on- and off- resistance of the switch), we have employed two methods. The first method is to use the circuit shown in Fig. 1, but with the CCTL being removed from the circuit. This circuit is a simple capacitive energy storage pulsed power system (CESPPS). In this CESPPS, the switch is connected in series with the load resistor R_L; thus, the circuit can be treated as a voltage divider. By analyzing the voltage waveform $V_{out}(t)$ across the 50 Ω matched load while the laser pulse is on and using the equation $R_{sw}(t) = 50 \times [V_o/V_{out}(t) - 1]$, the temporal variation of switch resistance was obtained. The other method is to analyze the experimentally obtained waveform from the IESPPS circuit shown in Fig. 1. Since the circuit response is very close to the basic RLC circuit, we can use the current waveform $I(t)$ obtained from the current viewing resistor and the voltage waveform $V_{out}(t)$ measured with the 50 Ω load. By using the equation

$$\frac{1}{C} \int I(t)dt + V_{out}(t) + I(t)R_{sw}(t) = V_o , \tag{2}$$

the temporal variation of the switch resistance $R_{sw}(t)$ can be easily calculated. According to the analysis, the switch (the 5 mm GaAs cube p-i-n diode) behaved differently in these two different circuits. The switch dynamic resistance behavior in these two circuits at

3

$V_o=700$ V is shown in Fig. 4. It shows that the lowest on-resistance is 6.0 Ω in the CESPPS and is 3.4 Ω in the IESPPS respectively. In the IESPPS, the switch resistance drops to a lower value during the closing phase and increases faster during the opening phase than those in the CESPPS. The lower on-resistance in the case of the IESPPS may be due to the higher thermal power dissipation while higher charging current is flowing through the switch causeing further switch on-resistance drop. When the switch is turned off, the higher induced field across the switch for the IESPPS is in favor of sweeping out the excess carriers in the switch resulting in faster opening of the switch. If this induced field does not exceed the "lock-on" field (3.6 kV/cm)[4], the switch off-resistance can increase faster to achieve better power gain.

It may be convenient to describe the capability of the pulsed power system in terms of the power gain or voltage gain. The power gain may be defined as the ratio of the output peak power of the system to the power which the source would provide directly to the same load. The voltage gain may be defined as the ratio of the output pulse voltage to the input charging voltage (V_{out}/V_o) in this case. In this experiment, the output power is $P_{out}=(V_{out}^0)^2/Z_o$ and the source power is $P_s = V_o^2/Z_o$ respectively. The highest obtained power gain is 16, which is equivalent to a voltage gain of 4. When the charging voltage is higher than 500 V, higher output peak power could be observed; however, the first postpulse of the output becomes apparent, resulting in a lower power gain. This suggests that the switch off-resistance is lowered by the induced electric field which exceeds the "lock-on" field. Hence, this phenomenon may be related to the "lock-on" effect observed in the closing switch experiments[4,11].

In conclusion, for the first time, an output voltage pulse with a power gain as high as 16 has been achieved with a current charged transmission line and a photoconductive, closing-and-opening switch. The switch is a 5 mm GaAs cube of p-i-n diode configuration controlled by a specially tailored Nd:Glass laser pulse. The system has the potential to be scaled up to a higher voltage system, but this will require a larger switch to withstand

4

higher voltage and a higher energy laser pulse to activate such a switch. The phenomenon of power gain drop with higher output voltage needs further study and investigation.

References

1. Opening Switch, edited by A. Guenther, M. Kristiansen, and T. Martin. (Plenum. New York. 1987).

2. K. H. Schoenbach. V. K. Lakdawala. R. Genuer, S. T. Ko. J. Appl. Phys. $\underline{63}$. 2460 (1988).

3. M. S. Mazzola. K. H. Schoenbach. V. K. Lakdawala. and S. T. Ko. Appl. Phys. Lett. $\underline{55}$. 2102 (1988).

4. F. J. Zutavern. G. M. Loubriel. B. B. McKenzie, W. M. O'Malley. R. A. Hamil. L. P. Schanwald. and H. P. Hjalmarson, in Digest of Technical Papers, 7th IEEE Pulsed Power Conference. edited by R. White and B. H. Bernstein (IEEE, New York. 1989). p.412.

5. E. A. Chauchard. M. J. Rhee. and Chi H. Lee, Appl. Phys. Lett. $\underline{47}$. 1293 (1985).

6. E. A. Chauchard. C. C. Kung. Chi H. Lee, and M. J. Rhee, Laser and Particle Beams. $\underline{7}$. 615. (1989).

7. M. J. Rhee. and R. F. Schneider. IEEE Trans. Nucl. Sci. $\underline{NS-30}$. 3192 (1983).

8. E. A. Chauchard. C. C. Kung, Chi H. Lee, and M. J. Rhee, Conf. Record - Abstracts. 1989 IEEE International Conf. on Plasma Sci., May 22-24. 1989, Buffalo, New York.

9. A. Rosen. P. J. Stabile. A. M. Gombar, W. M. Janton, A. Bahasadri, and P. Herezfeld. Photonics Tech. Lett. $\underline{1}$. 132 (1989).

10. M. J. Rhee, T. A. Fine, and C. C. Kung, J. Appl. Phys. $\underline{67}$, 4333 (1990).

11. G. M. Loubriel. M. W. O'Malley, F. J. Zutavern, B. B. McKenzie, W. R. Conley. H. P. Hjalmarson, IEEE Conference Record of 18th Power Modulator Symposium (IEEE. New York, 1988), p.312.
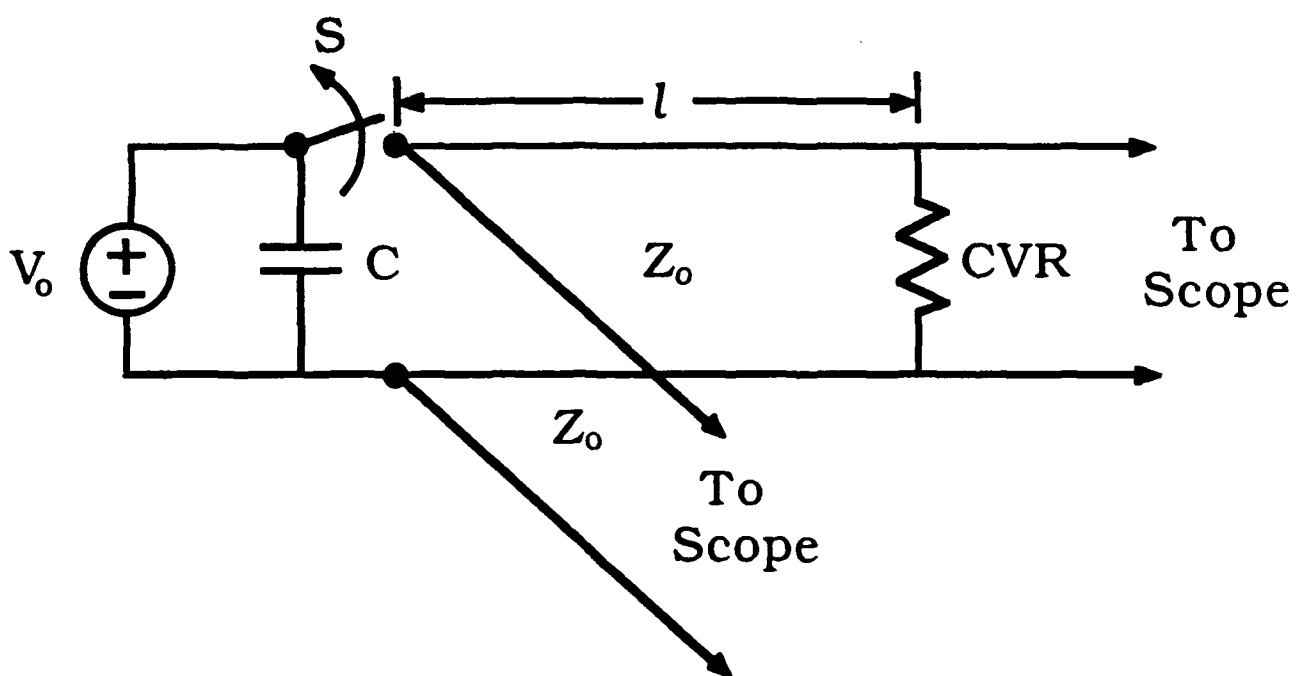
Fig. 1. Schematic representation of the experimental setup. S: switch, CVR: current viewing resistor (0.1 Ω), C: capacitor (0.1 μF).
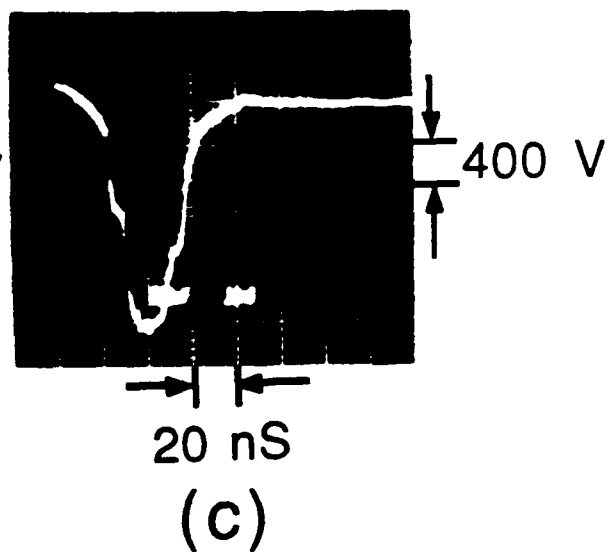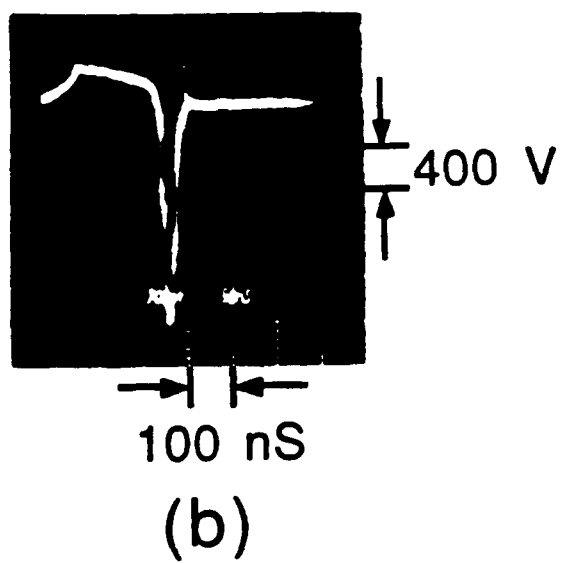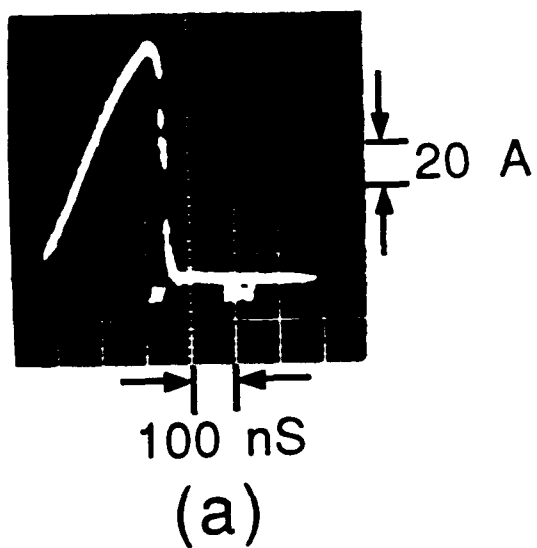
Fig. 2. Waveforms obtained with the 5 mm cube GaAs p-i-n diode switch operated at 500 V charging voltage. (a) The charging current monitored with a 0.1 Ω current viewing resistor. (b) and (c) Output voltage waveform.

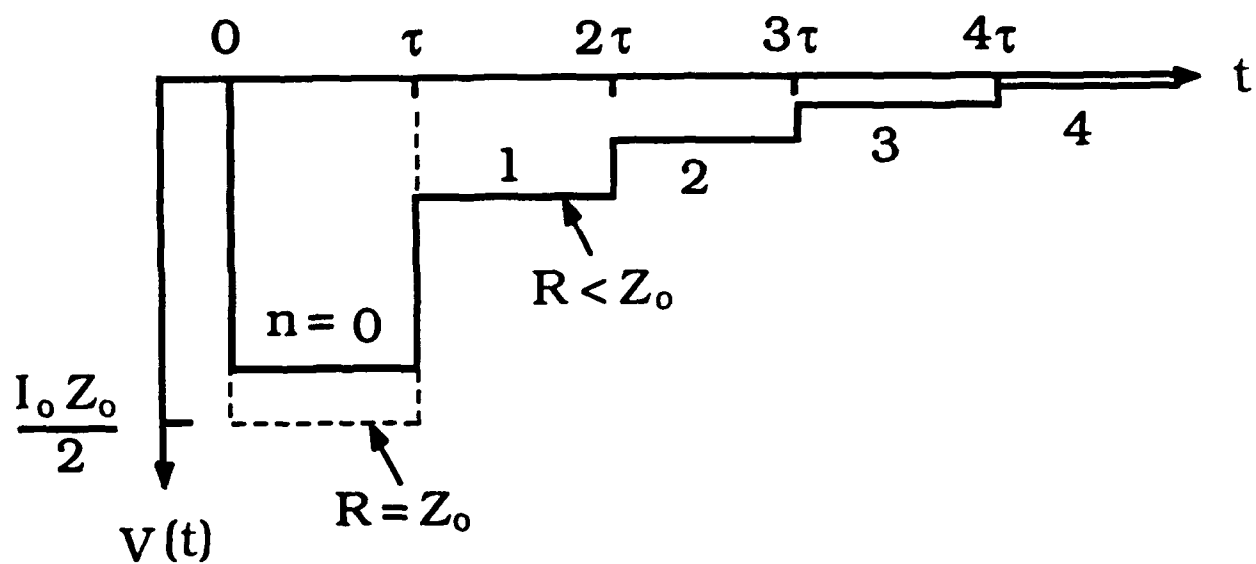Fig. 3. Depiction of output voltage waveforms produced by the current charged transmission line with an ideal opening switch, showing matched and mismatched cases.

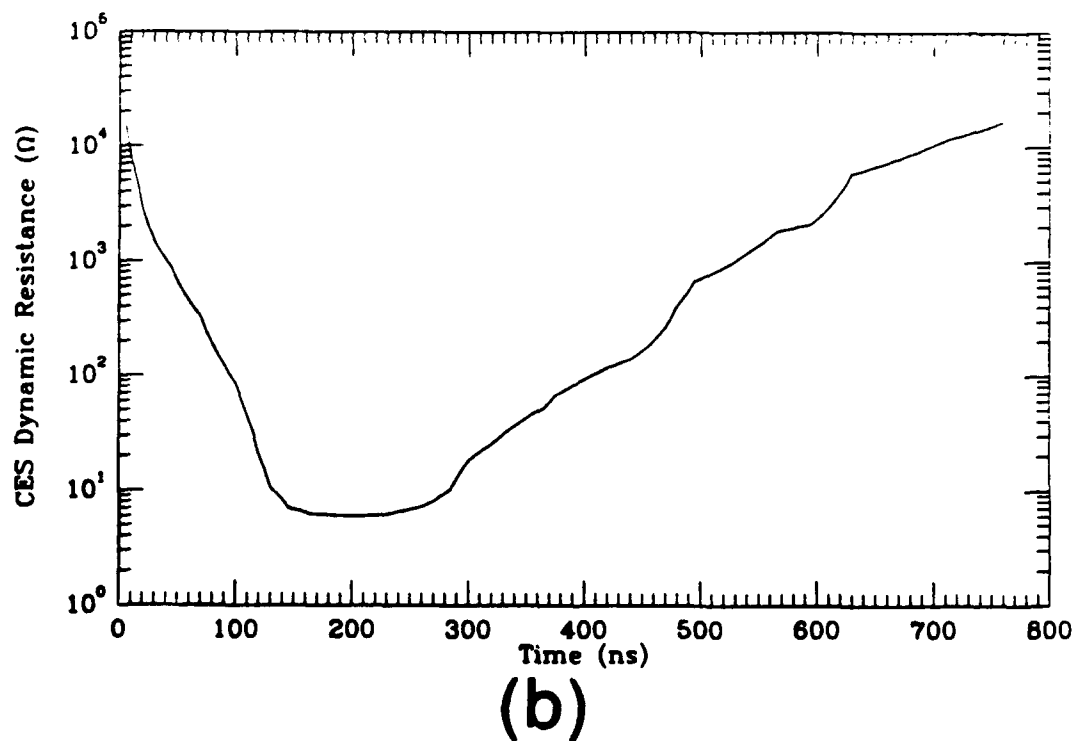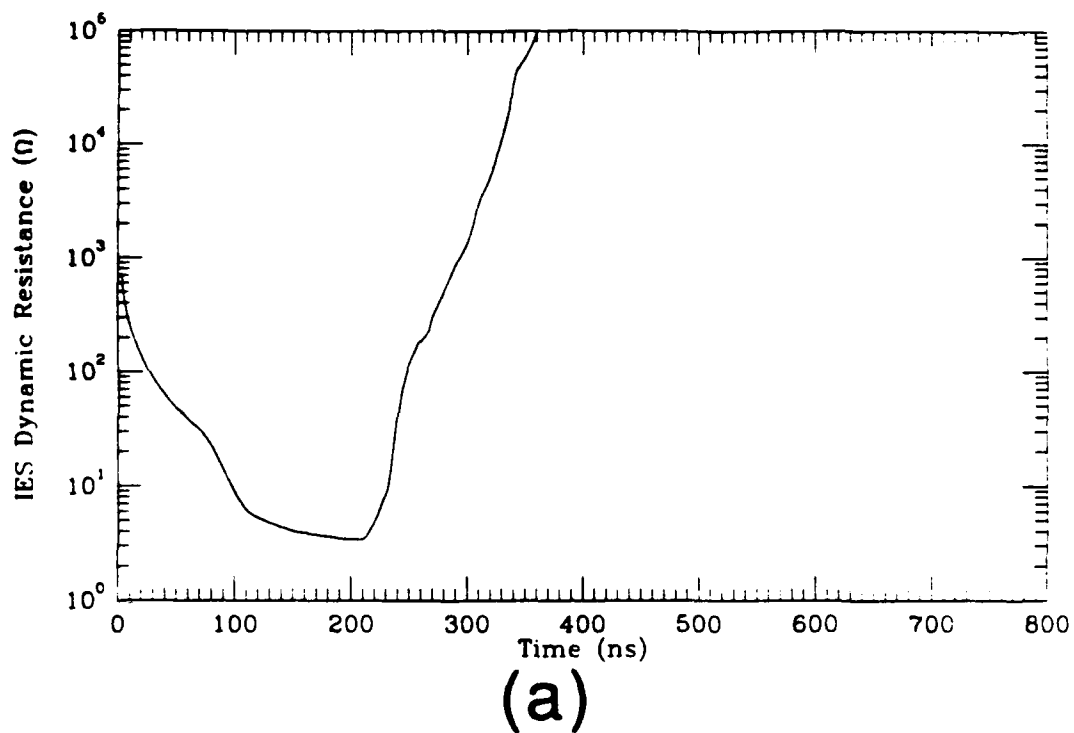Fig. 4. The 5 mm GaAs cube p-i-n diode switch dynamic resistance in two different pulse power systems at 700 V charging voltage. (a) The switch in the inductive energy storage pulsed power system. (b) The switch in the capacitive energy storage pulsed power system.

I.C

LASER CONTROLLED SEMICONDUCTOR SWITCH

Vishnu K. Lakdawala
Dept of Electrical & Computer Engineering
Old Dominion University
Norfolk, Virginia 23529

A Laser Controlled Semiconductor Switch

Vishnu K. Lakdawala and Karl H. Schoenbach
Department of Electrical and Computer Engineering
Old Dominion University
Norfolk, VA 23529

Abstract

A bulk optically controlled semiconductor switch (BOSS) is investigated. The switch can be turned on and off, on a nanosecond to picosecond time scale, using infrared laser radiation at two different wavelengths. Turn-on is accomplished by electron excitation from a deep copper level, and turn-off is obtained through hole excitation from ionized copper centers. External radiation is not needed to sustain the on-state conductivity. The switch material is gallium arsenide doped with silicon and compensated with copper (GaAs:Si:Cu). The deep level structure of the switch material is studied by means of Deep Level Transient Spectroscopy (DLTS) and Photo Induced Current Transient Spectroscopy (PICTS). A rate equation model is used to calculate the optimum concentrations of impurities and to obtain scaling laws for the switch. Switching studies with two lasers have shown the feasibility of the switch concept. Closing and opening on a nanosecond time scale with variable on-times was obtained at voltages below the lock-on voltage. Recent results have shown that this opening method also allows temporary quenching of the photocurrent for switch operation in the lock-on state.

A Laser Controlled Semiconductor Switch

Vishnu K Lakdawala and Karl H Schoenbach
Department of Electrical and computer Engineering
Old Dominion University
Norfolk, VA 23529

Introduction

This paper describes the research results on "A Laser Controlled Semiconductor Switch" project sponsored by SDIO/IST and managed by the ONR under contract # NOO-14-86-k-560. Dr. Karl H. Schoenbach is the Principal Investigator and Dr. Vishnu K. Lakdawala is the co-Principal Investigator. A summary of major accomplishments obtained during the past funding period is reported. Sung T. Ko and Michael S. Mazzola worked on this project as doctoral students and have successfully completed their Ph. D. degree. Randy Roush and Gordhan Barevadia are currently working towards their Master's degree on this project.

Photoconductive switches are recently gaining popularity for a number of reasons: they are inherently simple, scalable, optically controllable, and they possess capability for fast (ps) switching and high rep rate operation. They are, however, mainly used as high power closing switches. External radiation sustains the conductivity of the switch by generating electron-hole pairs. Turning off the laser radiation results in decay of conductivity with a time constant dependent upon bulk recombination of free carriers or career sweep out. This material or geometry dependent conductivity decay after laser illumination allows photoconductive switches to be used as opening switches as well as closing switches. In order to obtain short opening time, the electron-hole lifetime needs to be short. This requirement, however, results in a large carrier loss during the conduction phase. This dictates for many pulsed power applications an unacceptable expenditure of expensive laser photons.

Concept

A concept for a new type of optically controlled semiconductor switch, BOSS was introduced by Schoenbach et. al. [1]. Here, laser radiation is employed to switch into a conductive state and to quench the photoconductance on demand. In between the two laser pulses, the conductivity remains at a high level for times long compared to the laser pulse duration. The switch conductance therefore can be varied by varying the delay time between the two laser pulses in a ns to tens of μs temporal range.

Silicon doped copper compensated gallium arsenide (GaAs:Si:Cu) is used as a base material. Si is a shallow donor (0.0058 eV below conduction band) and Cu is a deep acceptor (Cu_B at 0.44 eV above valence band). With controlled diffusion of Cu in Si doped GaAs (compensation), a highly resistive crystal can be obtained. Turn-on is accomplishHx with laser radiation with

photon energy less than the bandgap energy (1.42 eV) but greater than the energy difference between the Cu_B level and the conduction band {(1.42-.44) eV}, see Fig. 1. Electrons stored in Cu_B levels will be excited into conduction band. Two step excitation of electrons through vacant Cu_B centers and electron excitation from other deep centers (not shown) will also contribute to the on-state conductivity. Holes generated from two step excitation however, will be rapidly captured through direct recombination or recombination via recombination centers. Some of the free electrons will also be captured by defects such as EL2 traps. Due to the small electron capture cross section of the Cu_B centers, a large fraction of the free electrons will stay into the conduction band for times long compared to the typical recombination time for GaAs. If the valence band is now flooded with holes photoexcited from the Cu_B centers, the free electrons will recombine quickly with the generated free holes and the conductivity of the switch will be drastically reduced. This process of "stimulated recombination" of electron-hole pairs is accomplished by irradiating the switch with a second laser pulse of photon energy less than 1 eV, but greater than 0.44 eV.

Sample Preparation

Sample preparation is one of the most crucial and important parts of the project. The crystals used in this investigation are taken from a GaAs wafer grown using the horizontal Bridgman technique. The material was originally doped with a Si density of 5×10^{16} cm^{-3}. Copper is vacuum evaporated on face to a 1 μm thickness. The sample is then placed in a diffusion furnace (arsenic rich ambient). The temperature for the diffusion and time were varied over a wide range to accomplish different levels of compensation. Detail information about the sample preparation technique is reported elsewhere [2]. Significant achievements are as follows. We have successfully demonstrated the controlled compensation of low resistivity Si doped GaAs with copper to obtain high resistivity semi-insulating crystals. Also a procedure to obtain over compensated (p-type) or under compensated (n-type) materials has been established. Sample resistivities of 10^7 ohmcm have been obtained by compensation. A non-contact laminar flow polishing system has been designed and built. This system is used to obtain extremely fine polished surfaces required before contact deposition. Au-Ge films were found to give good ohmic contacts.

Sample Characterization

Various measurements techniques used to obtain basic information about the switch materials are:

1. Hall van-der Pauw Method
2. Dark Current Measurements
3. Deep Level Transient Spectroscopy (DLTS)
4. Photo Induced Current Transient Spectroscopy (PICTS)
5. Measurement of Absorption Depth

3

A Hall van-der Pauw system has been designed and built. The system allows us to measure carrier concentration, mobility, resistivity and Hall coefficient. Dark current measurements reveal information on the deep level structure and on processes such as lock-on and avalanche breakdown. A DLTS (MDC DLS-81 system) is used to characterize the deep level structure in the low resistivity material. Basic information on various deep levels such as EL2, EL5 has been determined. The measurement technique yields data on the activation energy, concentration and cross sections on electron and hole capture of the deep levels. The used DLTS system, however, is not capable of measuring very large cross sections for strong traps (such as Cu_B) due to limited time response. A summary of results is shown in the energy level diagram of Fig. 2.

In order to characterize deep levels in high resistivity (semi-insulating) semiconductors, we have developed an experimental set up for the photo-induced current transient spectroscopy (Fig. 3). In PICTS, pulsed light is radiated on the test samples. During the turn on time of the light, the traps in the sample are filled; the photocurrent reaches a steady state level. When the light is turned off, the steady state current decreases very fast due to recombination of free carriers. After this initial fast decay, the current decays slowly due to detrapping of trapped carriers. The slow current decay is an exponential function of time [3,4], with a time constant which varies with temperature. By determining this time constant with a rate window method (Fig. 4) and plotting it in an Arrhenius plot it is possible to obtain the activation energy of the deep level. Under certain conditions, the height of the electrical signal can be used to predict the concentration of the traps.

We have characterized a semi-insulating GaAs sample using this method. As shown in Fig. 4., three deep levels with activation energies of 0.38 eV, 0.68 eV, and 0.78 eV have been identified. The levels at 0.38 and 0.78 are believed to be the native defects related to EL family. The level at 0.68 is probably due to an impurity. We are in the process of characterizing copper doped GaAs:Si. Our preliminary results indicate that this method will give us information about the copper levels in GaAs. In this way we will be able to study the copper compensation effect in GaAs:Si, which will lead to better switch sample development.

The absorption depth has been measured for a wavelength of 1064 nm by irradiating the edge of a sample and measuring the output intensity for different sample lengths. Taking multiple internal reflections into account, the equation for the transmission T is

$$T = \frac{I_T}{I_0} = \frac{(1-R)^2 e^{-\alpha d}}{1-R^2 e^{-2\alpha d}}$$

where I_0 and I_T are the incident and transmitted intensities respectively, R is the reflection coefficient, α is the absorption coefficient, and d is the sample length. Using the assumption that the majority of the light is absorbed before reaching the opposite end of the sample (αd large), the equation for the transmission reduces to

4

$$T = \frac{I_T}{I_0} \sim (1-R)^2 e^{-\alpha d}$$

The slope of the line drawn through the squares in Fig. 5 gives the approximate 1/e absorption depth for GaAs:Si:Cu. It was found to be 3 mm. The absorption depths for GaAs:Si, and undoped semi-insulating GaAs are approximately 8 mm.

Numerical Simulation

Modeling studies were made to investigate the switch behavior and also the influence of various deep traps on the photoconductivity of the switch. A rate equation model for the free electrons, holes and bound electrons in deep traps has been used. The model and the corresponding results are described in detail elsewhere [5,6,7]. The findings from the modeling studies for specific systems investigated are:

1. The turn-on phase is characterized by two time constants, one time constant which is fast, is related to direct band-to-band recombination of free carriers and recombination through deep centers (nanoseconds). The second time constant which is very slow (tens of microseconds), is related to the capture of electrons at the Cu_B level.
2. With increasing photon flux (beginning at 3×10^{25} $cm^{-2}s^{-1}$) the on-state conductivity saturates for a sample doped with Cu at a concentration of 8×10^{16} cm^{-3}.
3. For photon flux greater than 5×10^{26} $cm^{-2}s^{-1}$ two-photon ionization becomes a dominant mechanism.
4. The greater the electron occupation at Cu_B level the better the on-state conductivity. However, this leads to a degradation in turn-off characteristics of the switch.
5. For the use of the system as both a closing and opening switch, an optimum compensation ratio of 1.6 is predicted.
6. The recombination centers in the switch material controls the free carrier decay rate, however, it does not affect the turn-on transient risetime significantly.

Switching Experiments

Feasibility of the BOSS concept

A schematic of experimental set up for the photoconductivity measurements is shown in Fig. 6. Two different lasers were used to allow two consecutive laser pulses to illuminate the crystal, one for closing the switch ($\lambda = 1.06$ μm, FWHM = 26 ns, peak photon flux 5×10^{23} $cm^{-2}s^{-1}$), and the other to open it ($\lambda = 1.8$ μm, FWHM = 7 ns, photon flux 5×10^{25} $cm^{-2}s^{-1}$). The bias circuit consists of a capacitor charged to a dc-voltage and connected to the crystal by a 50 ohm cable (two way transit time = 275 ns). The load is a 50 ohm oscilloscope termination, which acts as a current viewing resistor. The current waveform is digitized by a Tektronix 7912 digitizer. Fig. 7 shows a typical photoinduced current flowing through the p-type crystal. Sample conductivity is initially induced by the 1.06 μm laser pulse. The sample conductivity is quenched

5

200 ns later by the 1.8 μm laser pulse. The results clearly demonstrates the feasibility of the BOSS concept for the p-type GaAs:Si:Cu.

The major findings from the switching experiments [8,9] are:

1. Optically controlled closing and opening can be achieved on command on a nanosecond time scale.
2. Persistent photoconductivity with a time constant as large as 30 μs has been obtained using sub-bandgap laser radiation of photon energy greater than 1 eV. The GaAs:Si:Cu switch has a conductivity decay time constant comparable to that achieved with bulk Si closing switches, but with the advantage of using a material with dark resistivity and high electron mobility.
3. Current densities as high as 10 kA/cm^2 were switched and fields as high as 20 kV/cm were held off.
4. At higher fields (greater than 10 kV/cm), a voltage "lock-on" was observed.

Optical Quenching of Lock-On Currents in GaAs:Si:Cu switches

Experiments to study the effect of infrared radiation on "lock-on" currents in photoconductive GaAs:Si:Cu switch have been performed. The experimental set up is shown in Fig. 8. The results demonstrate that infrared quenching of "lock-on" current in these switches is possible. Fig. 9 and 10 show typical results with optical quenching of the photocurrent for bias electric fields of 20 kV/cm and 875 V/cm respectively.

The significant findings are:

1. After quenching of the persistent photocurrent, the current recovers in about 25 ns to a constant level.
2. The persistent photo and dark currents are considered to be due to double injection of carriers through the ohmic contacts of the photoconductive switch.

Optical quenching of lock-on current offers the possibility to use GaAs:Si:Cu switches in high rep-rate inductive energy storage systems.

References

1.	K. H. Schoenbach, V. K. Lakdawala, R. Germer, and S. T. Ko, *"An Optically Controlled Closing and Opening Switch,"* **J. Appl. Phys.,** 63, 2460 (1988).

2.	M. S. Mazzola, *"Experimental studies of bulk optically controlled GaAs switches utilizing fast infrared quenching",* **Ph. D. Thesis,** Old Dominion University, May 1990.

3.	Ch. Hurtes, M. Boulou, A. Mitonneau, and D. Bois, *"Deep-level spectroscopy in high resistivity materials",* **Appl. Phys. Lett.,** 32 (12), 821 (1978).

4.	J. C. Balland, J. P. Zielinger, C. Noguet, and M. Tapiero, *"Investigation of deep levels in high resistivity bulk materials by photo-induced current transient spectroscopy: I. Review and analysis of some basic problems",* **J. Phys. D: Appl. Phys.,** 19, 57 (1986).

5.	S. T. Ko, *"Study of direct semiconductor materials for an optically controlled switch",* **Ph. D. Thesis,** Old Dominion University, May 1989.

6.	S. T. Ko, V. K. Lakdawala, and K. H. Schoenbach, *"Kinetics of Photoconductivity in bulk GaAs with deep traps for closing and opening switch applications"* submitted to **IEEE Trans. Quantum Electronics,** MS # 7026.

7.	S. T. Ko, V. K. Lakdawala, K. H. Schoenbach, and M. S. Mazzola, *"Influence of Copper Doping on the performance of Optically Controlled GaAs Switches,"* **J. Appl. Phys.,** 67, 1124 (1990).

8.	M. S. Mazzola, K. H. Schoenabch, V. K. Lakdawala, and S. T. Ko, *"Nanosecond Optical Quenching of of Photoconductivity in a Bulk GaAs Switch,"* **Appl. Phys. Lett.,** 55, 2102 (1989).

9.	M. S. Mazzola, K. H. Schoenbach, V. K. Lakdawala, R. Germer, G. M. Loubriel and F. J. Zutavern, *"GaAs-Photoconductive closing switches with high dark resistance and microsecond conductivity decay,"* **Appl. Phys. Lett.,** 54, 742 (1989).

10.	R. A. Roush, M. S. Mazzola, K. H. Schoenbach, and V. K. Lakdawala, *"Optical Quenching of Lock-On Currents in GaAs:Si:Cu Switches",* Proc. 19th Power Modulator Symposium, San Diego, CA, June 1990.
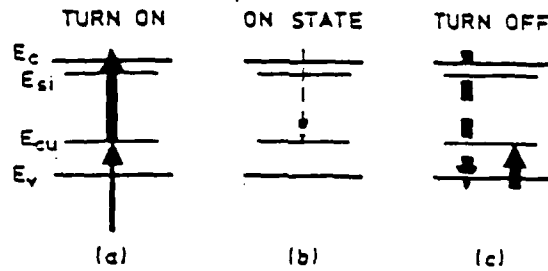
TURN ON   ON STATE   TURN OFF

E_c
E_{si}

E_{cu}
E_v

(a)   (b)   (c)

Fig. 1 Optical ionization processes (solid lines)
and recombination processes (dashed lines)
during different stages of the switch.

Si ——————— 0.0058

EL5 ——————— 0.4
(Ni, Cr) ——————— 0.54

0.64 ——————— (Cr, Fe)

EL2 ——————— 0.8

0.47 ——————— (Cu, Fe)

Density :   EI2 ; $6 \cdot 10^{15}/cm^3$
(Ni, Cr) ; $3 \cdot 10^{14}/cm^3$

EL5 : $2 \cdot 10^{15} /cm^3$
(Cr, Fe) ; $5 \cdot 10^{14} /cm^3$

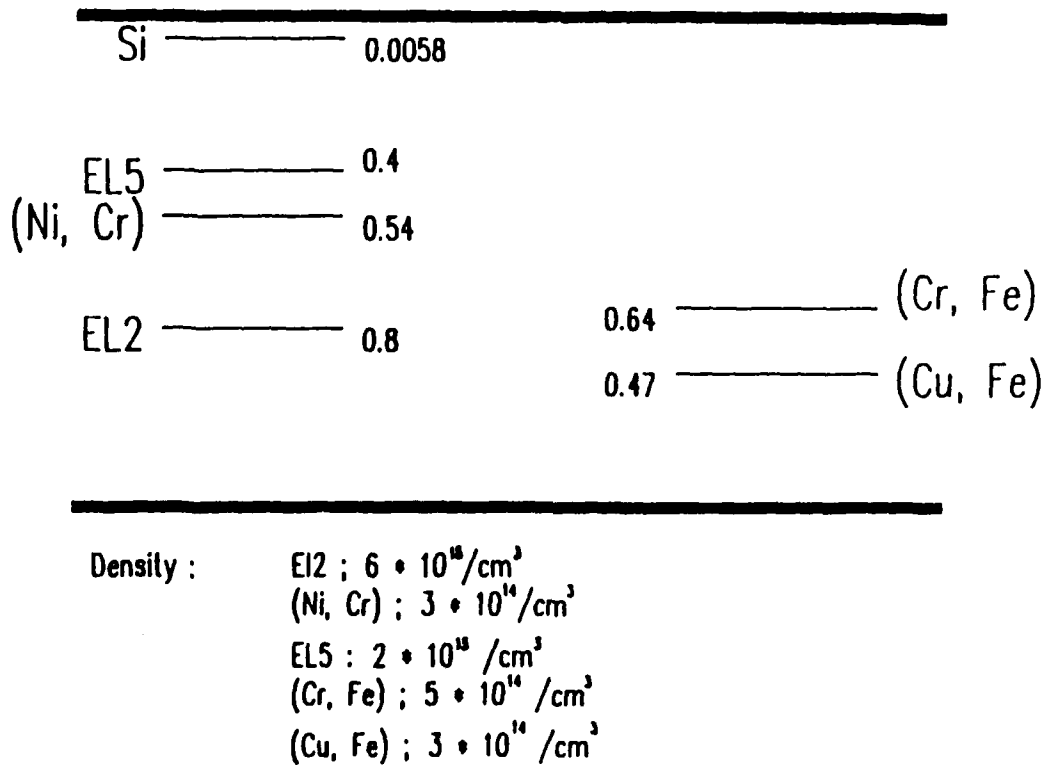(Cu, Fe) ; $3 \cdot 10^{14} /cm^3$

Fig. 2 Energy level diagram of GaAs:Si   system showing the measured deep
impurity levels and their concentration in GaAs:Si crystals.
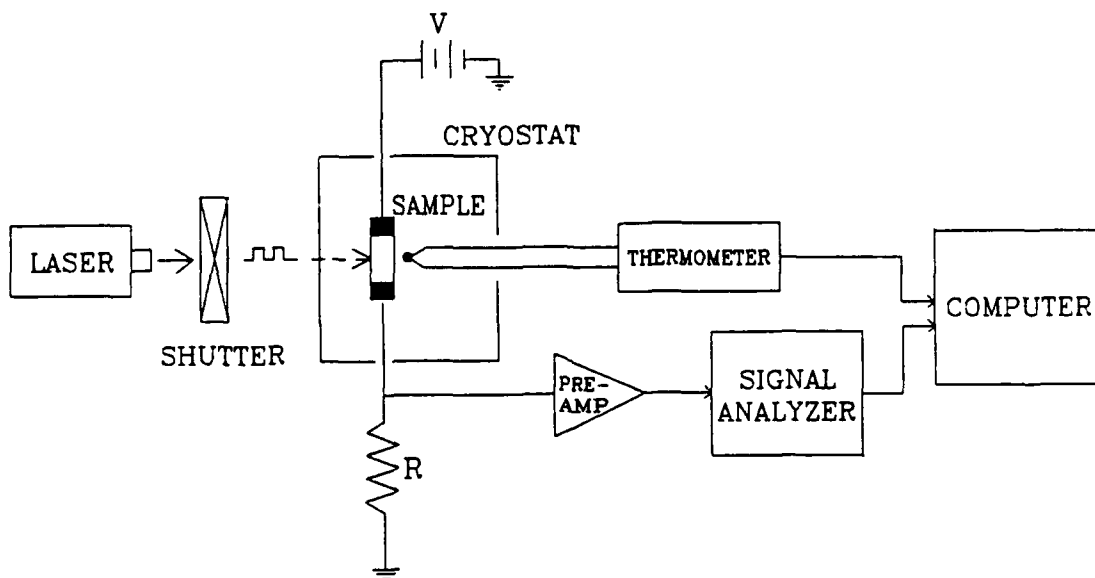
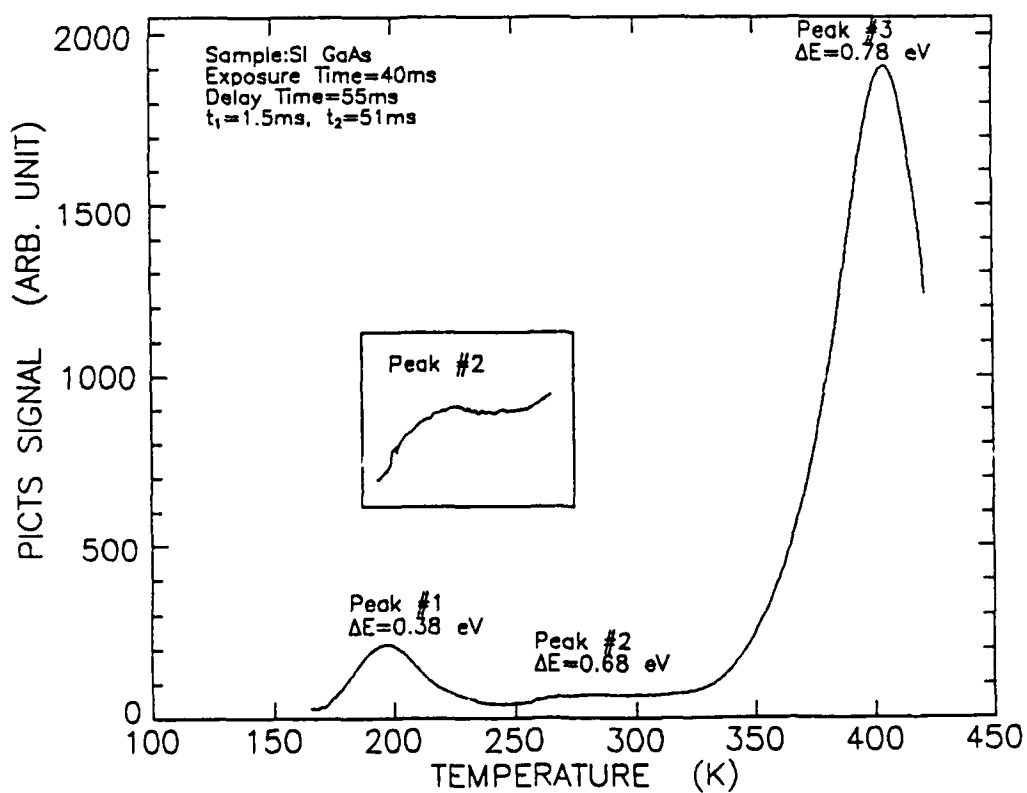Figure 3   An experimental set up for PICTS using rate window method.

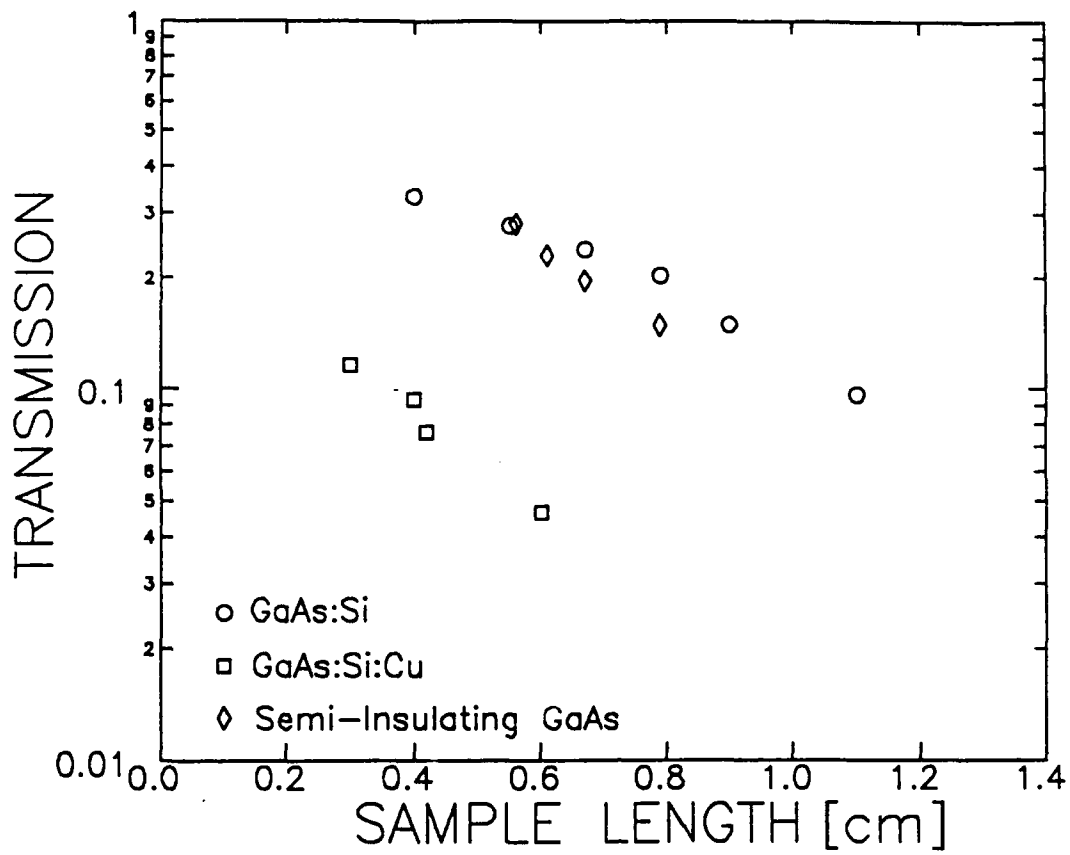Figure 4   A typical PICTS spectrum obtained on SI GaAs.

Fig. 5 Transmission of 1064 nm laser radiation vs sample
length for three types of GaAs [10]
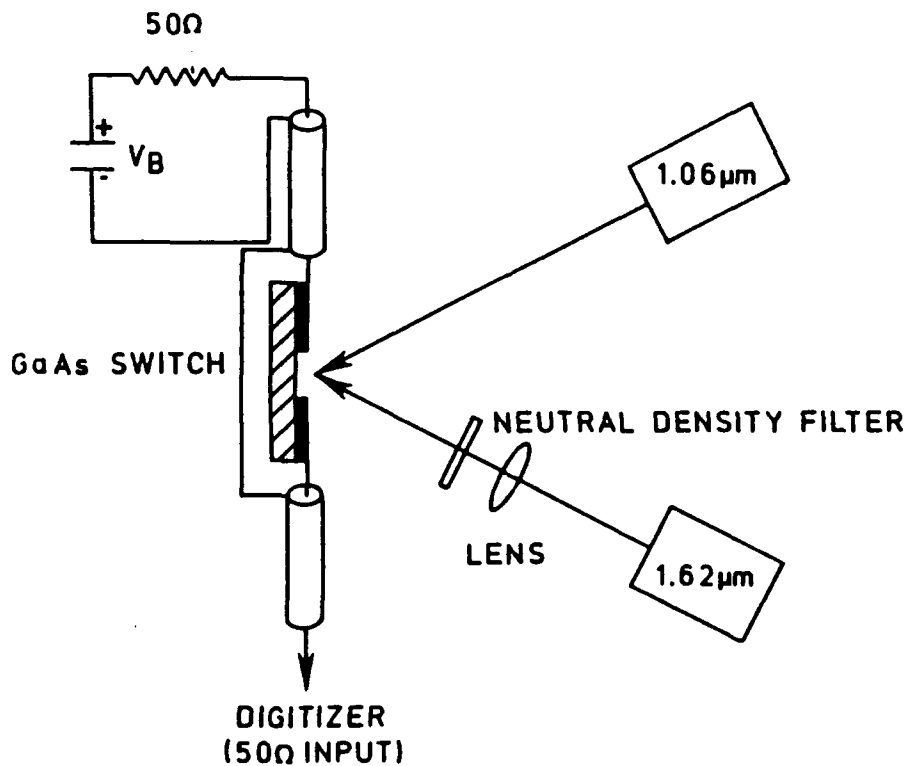
Fig. 6 Diagram illustrating the experimental setup. Note that the crystal was
illuminated on the face containing the contacts. [8]
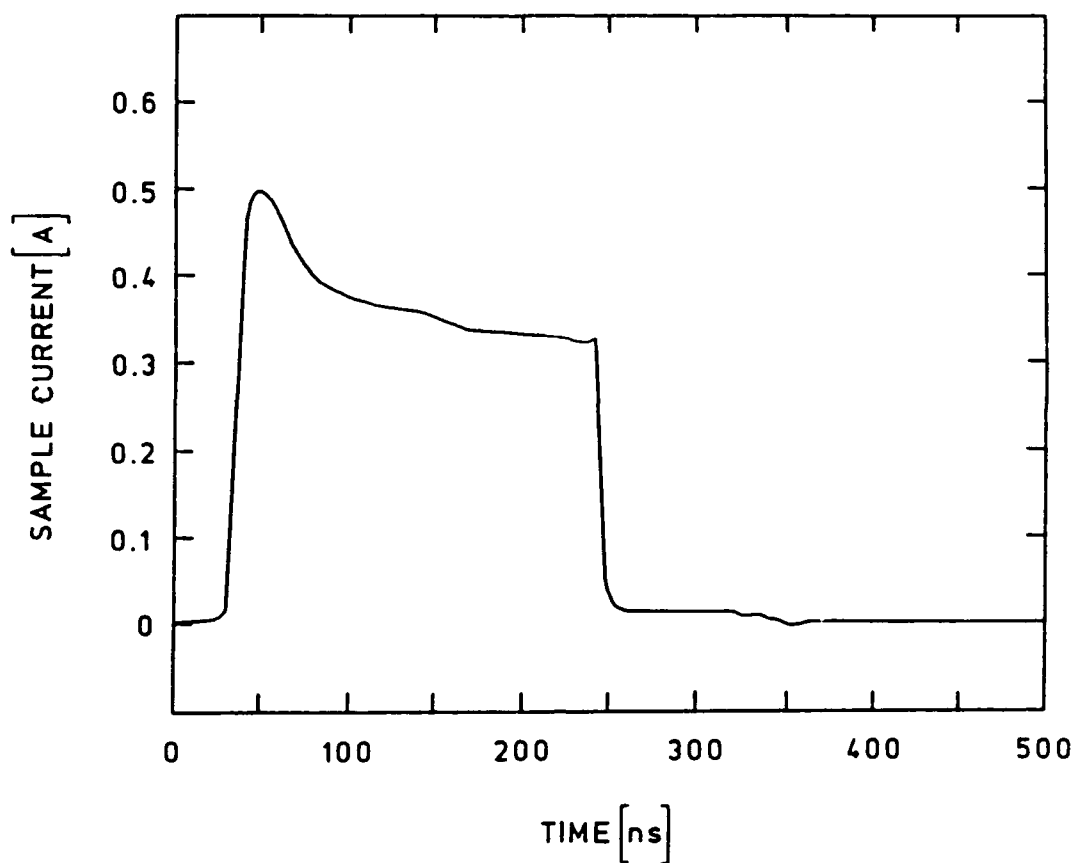
Fig. 7   Measured current flowing through the p-type crystal.
          Sample conductivity is induced initially by the 1.06 μm
          laser pulse.   The sample conductivity is quenched 200 ns
          later by the 1.8 μm laser pulse.   The initial bias
          voltage is 55 V.   [8]

Fig. 8 Experimental Set-Up [10]

Fig. 9   Optical quenching of the photocurrent in GaAs:Si:Cu
for a bias electric field of 20 kv/cm. [10]

Fig. 10   Optical quenching of the photocurrent in GaAs:Si:Cu
for a bias electric field of 875 V/cm. [10]

I.D

SEMICONDUCTOR METAL EUTECTICS FOR PULSED POWER SWITCHING

Brian Ditchek
GTE Labs Inc.
40 Sylvan Road
Waltham, MA 02254

A New Approach Towards the Development of Opening, Solid-State Pulsed Power Switches
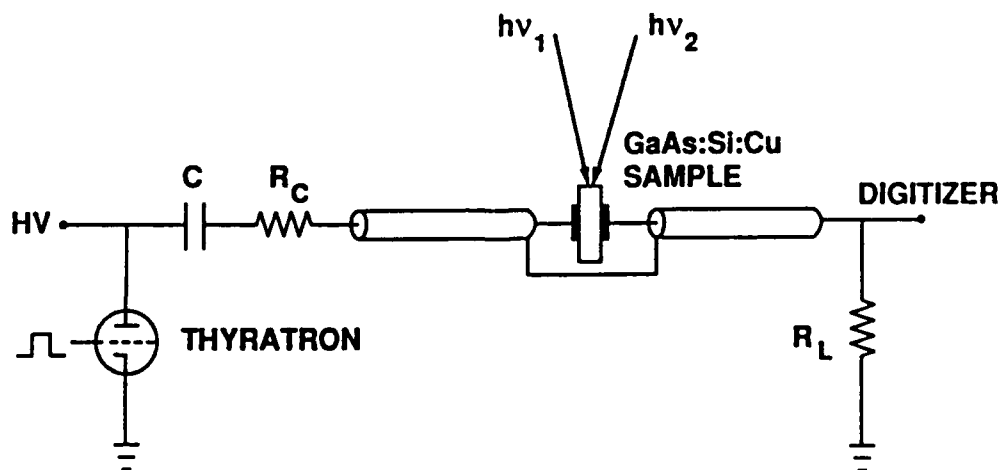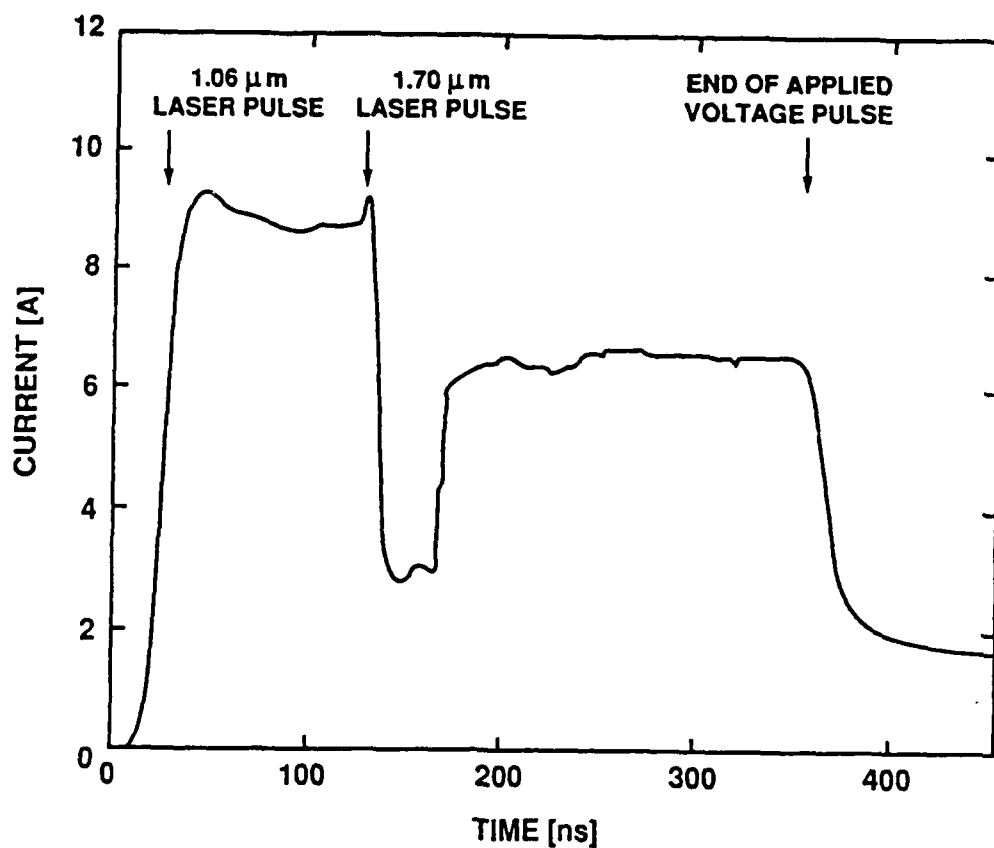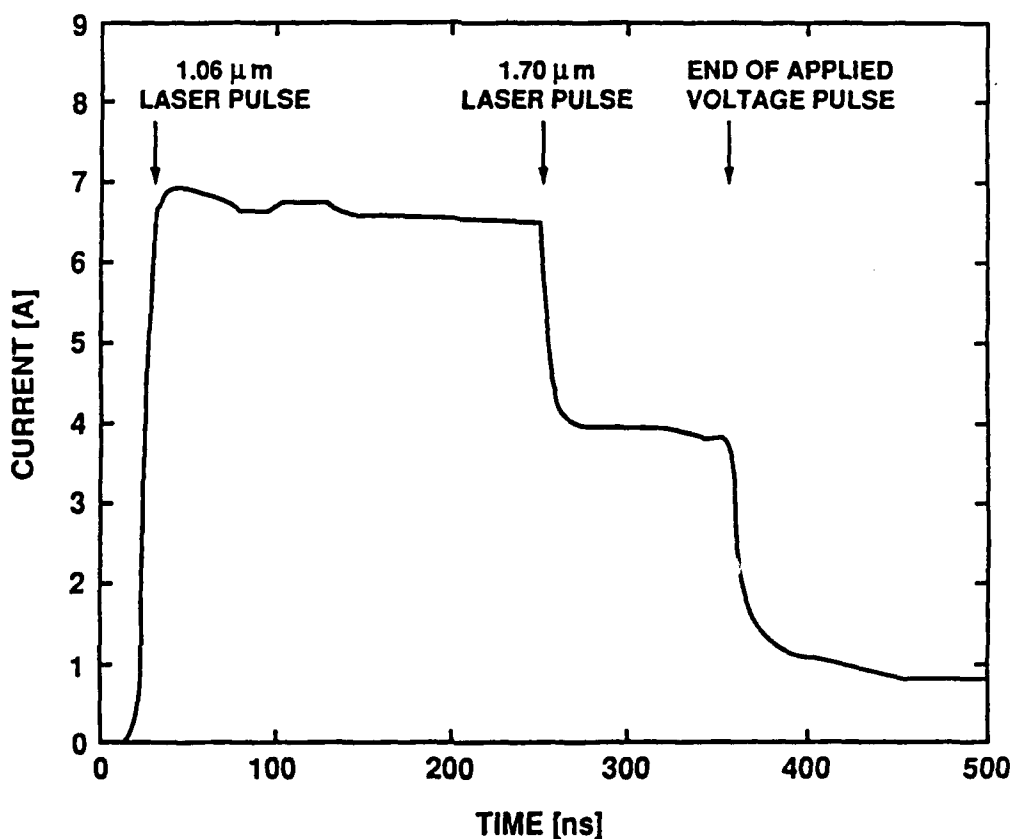
M. Levinson, B. M. Ditchek, V. Byszewski, P. G. Rossoni, and D. Matthiesen

GTE Laboratories, Incorporated, 40 Sylvan Rd., Waltham, MA 02254

and

L. Kaufman

ManLabs, Incorporated, 21 Erie Street, Cambridge, MA 02139

Abstract

A new class of transistors based on semiconductor-metal eutectic composite materials is described and their application to pulsed power switching is discussed. Their unusual resistance to avalanche breakdown has been examined by numerical modeling, and device and materials parameters which should optimize their performance have been identified. Experimental devices have shown very high breakdown voltages in agreement with the model. A search for new semiconductor-metal eutectic systems has been undertaken to identify materials which may provide further improvements. Assessments based on thermodynamic calculations for candidate systems are presented, and initial experimental results are reported.

Introduction

Extension of conventional transistor technology to the pulsed power conditioning regime would require the development of devices with "on-state" currents in excess of 1 kA and blocking voltages of 50 kV. The main obstacle to engineering such high power devices is the existence of avalanche breakdown. It is this breakdown mechanism, together with basic junction physics, that limits conventional devices of reasonable size to either high voltage or high current but not both.

This paper discusses a new class of transistors that should allow the attainment of both high voltage and high current in a single opening switch. They are based on the unique microstructure of a new kind of electronic material: semiconductor-metal eutectic composites. These materials contain arrays of rod-shaped metallic regions imbedded in a single crystal semiconductor matrix. The rods form parallel, cylindrical Schottky junctions which fill the bulk of the material. Transistor devices can be fabricated which take advantage of the unusual properties of these materials to overcome the limitations imposed by avalanche breakdown in conventional devices. This approach should lead to the development of devices which are capable of both high voltage and high current in a single switch.

We will briefly review the effects of avalanche breakdown in pulsed power opening switches based on conventional solid-state technology and describe our new approach using semiconductor-metal eutectic devices. We then discuss the "benchmark" Si-TaSi$_2$ materials system, report the performance of experimental devices, and compare them to the predictions of numerical modeling. The results highlight issues of materials and device design which must be addressed in order to achieve the goal of practical voltage-controlled pulsed power opening switches based on this technology.

Limitations of existing transistor technology

The major restriction to increased blocking voltages in conventional transistors is the mechanism of avalanche breakdown. Avalanche breakdown occurs when mobile electrons or holes in the semiconductor are accelerated by an electric field which is sufficiently large that they can gain a quantity of energy greater than the semiconductor bandgap before being scattered by other electrons or the lattice. In a scattering event with a valence band electron, this amount of energy is sufficient to raise the valence electron to the conduction band and thereby create an electron-hole pair. Each of these new charge carriers can themselves gain energy from the electric field and in turn create still more electron-hole pairs. In this way, the current increases in an extremely short time to a point that is limited only by the series resistance of the circuit. Indeed, in many cases the energy dissipated in the semiconductor by such large currents is sufficient to cause thermal runaway and destroy the device.

In semiconductor devices, internal electric fields are found in the depletion regions of rectifying junctions, which may be either p-n, metal-semiconductor (Schottky), or metal-insulator-semiconductor types. The electric field E_{max} at which avalanche breakdown occurs is determined by ionization coefficients of electrons and holes which are specific to each semiconductor material.[1] Given E_{max}, the corresponding maximum voltage V_{max} which can be supported without avalanche breakdown can be expressed for planar junctions as

$$V_{max} = (E_{max}^2 e_s / 2qN_d) - V_b.$$

where e_s is the semiconductor permittivity, q is the electronic charge, N_d is the dopant concentration, and V_b is the built-in junction potential, which will normally be negligible compared to V_{max}.

The dependence of V_{max} on doping concentration for Si is shown in Fig. 1. Because V_{max} is inversely proportional to N_d, it is clear that achieving a high breakdown voltage requires a low carrier concentration. However, a low carrier concentration means high resistivity, and so limits the current densities which can be transported without unacceptable heating. Therefore, conventional transistor technology permits either high carrier concentration, high current devices operating at low voltage, or low carrier concentration, low current devices operating at high voltage, but not high current, high voltage devices.

Our studies of semiconductor-metal eutectic devices have suggested a novel approach to designing transistors which may circumvent these restrictions. It is based on the existence of uncontacted junctions between the gate and drain of the device. The potential at each of these junctions floats in such a way as to spread the applied voltage over a greater distance than the width of a single junction. This mechanism is similar to the well known "guard ring" effect, and can limit the maximum electric field to a value which is lower than the breakdown field.

Device modeling

The semiconductor-metal eutectic transistor geometry is shown schematically in Fig. 2. The metal rods, which are arrayed perpendicular to the surface of the wafer, create rectifying Schottky junctions with the semiconductor. A gate contact, which provides a

metallic contact to the rods but maintains a blocking contact to the semiconductor, is formed between the ohmic source and drain contacts. Current flowing from the source to the drain passes through the bulk to the device, flowing in between the depletion zones surrounding the rods. An external voltage applied to the gate contact can be used to expand the depletion zones of the rods accessed by the contact and, by decreasing the volume of non-depleted semiconductor, reduce the magnitude of the source-drain current and provide transistor action.

One unique feature of this device is that the rods which lie in between the source, gate, and drain contacts are not contacted. These rods and their associated depletion regions float to potentials that are determined by the device parameters and external voltages. We have performed extensive numerical modeling of these devices to study the surprising effects of the floating rods in high voltage operation.[2]

Computer simulations of devices with and without floating rods were performed using the PISCES code. The PISCES software models two-dimensional distributions of potential and carrier concentrations for arbitrary device geometries and bias conditions. The version used was PISCES-IIB of Stanford Electronics Laboratories on a Digital VAX 11/785 mainframe computer.

Two types of simulation experiments are described. In the first the effect of floating junctions on device breakdown was studied. The second is aimed at optimizing material and device parameters for pulsed power applications.

The two basic simulation geometries are shown in Fig. 3. The conventional case, used as a control (left diagram), has one gate junction close to the source. The other case (right diagram) has six equally spaced floating rod-shaped junctions between the gate and

drain. With six floating junctions, the simulation uses the maximum number of electrodes that can be handled by the PISCES software. Simulations were specified for n-type Si with uniform impurity concentrations of 0.5 - 5 x 10^{15} cm^{-3}. PISCES-IIB allows the placement of a simple lumped resistance on a given electrode. This capability was exploited to account for floating rods. Floating rods were simulated by inserting as high a resistance as possible on the electrode and biasing it to the drain voltage.

To simulate the operation of the transistor, the source was held at 0 V, the gate electrode (the first rod) was biased to -2 V, and the drain electrode was stepped from 0 to 200 V in 10 V increments. The potential versus distance from the source is shown in Fig.4 and the maximum electric field versus drain potential is shown in Fig.5 comparing the two cases with and without floating rods.

For the conventional case without floating junctions, the potential increases parabolically with distance similarly to conventional planar junctions. The maximum electric field increases monotonically with increasing drain voltage. In the case with floating rods, the depletion zone at the gate rod expands with increasing voltage as in the conventional case, but only until it intersects the depletion zone of the first floating rod. This latter rod then floats in potential with further increases in applied voltage so that its depletion zone expands towards the next floating rod. In this way, the applied voltage is spread across successive floating rods. The electric field at the gate rod reaches a maximum when the drain voltage is sufficient to extend its depletion zone to the first floating rod. It is then clamped at this value as the drain voltage is increased. Eventually, the same maximum field is attained at the first floating rod, and so on. The actual value of this field depends on the interrod spacing and the carrier concentration, but by proper design it can be made lower than the avalanche field.

The results of this model clearly indicate that the floating rods inhibit avalanche breakdown and result in a larger depletion zone than would be found in a classical planar junction device. In a conventional device without floating rods, the maximum electric field increases as the drain voltage increases until it reaches the critical value for avalanche breakdown. With the floating rods, however, as the drain voltage is increased the field reaches a maximum that may be significantly lower than the critical field for avalanche breakdown. Thus, even as the drain voltage is increased to a value significantly beyond that required to yield avalanche breakdown in a conventional device, avalanche breakdown is avoided because the field never reaches a value sufficient to cause impact ionization. However, avalanche will eventually occur by a 'punch-through' mechanism when the depletion region expands to reach the drain contact and no additional floating rods are available to accommodate further voltage increases. Therefore, the maximum blocking voltage of the device is determined by the gate-drain spacing, rather than the carrier concentration as in conventional devices. This distance can in principal be designed to yield an arbitrarily large blocking voltage.

Further model calculations can be used to investigate the ways that these devices could be optimized for simultaneous high voltage and high current operation. This is done by holding the maximum electric field to a value less than that of the avalanche field, and calculating the corresponding carrier concentration and saturation current density for different interrod spacings. A microstructure with floating rods similar to that shown in Fig. 3 was modeled to determine the carrier concentration which yields a saturation E_{max} of 100 kV/cm. This maximum field was chosen because it is conservatively below the value that would lead to avalanche breakdown. The average electric field in the gate-drain region and the gate-drain distance needed to hold off 1000 V were also calculated. The microstructure was then scaled uniformly to different interrod spacings and rod

diameters, keeping the volume fraction of the rods constant (as would be the case with real eutectic systems).

The results are shown in Table I for interrod spacings of 4, 7, and 23 μm. Although the gate-drain distances needed to hold off 1000 V are similar in all three cases and the spatially averaged field remains nearly constant at about one-half E_{max}, the carrier concentrations and saturation current densities at zero gate bias are quite different. The highest current is found at the smallest interrod spacing.

These results are important because they indicate that semiconductor-metal eutectic transistors can be designed to hold off high voltages while at the same time having relatively high carrier concentrations and therefore high current density.

Experimental Semiconductor-Metal Eutectic Transistors

SME transistors were fabricated[3,4] using 500 μm thick Si-TaSi$_2$ wafers cut normal to the growth axis so that the TaSi$_2$ rods are perpendicular to the wafer surfaces. Carrier concentrations were 1-3 x 10^{15} cm^{-3}, and the areal rod density was about 1.6 x 10^6 cm^{-2}, yielding average interrod spacing of ~8 μm.

Wafers were thermally oxidized at 1000 C to form a 0.3 μm oxide layer. The oxide was patterned and opened to form central drain and concentric source and gate contact areas as shown in Fig. 6. The gate contact was formed using a 0.2 μm CoSi$_2$ layer which maintained a Schottky barrier to the bulk Si matrix while providing metallic contact to the TaSi$_2$ rods. Source and drain contacts consisted of annealed Au-Sb films. After

electrical measurements, some processed devices were successively thinned by mechanical polishing and remeasured, showing the effects of thickness on device performance.

The transfer characteristic of a typical eutectic device is shown in Fig. 7 (Ref. 3). All eutectic transistors show a MESFET-like characteristic. The behavior of eutectic transistors and their dependence on the contact spacing, wafer thickness and matrix carrier concentration have been extensively studied. Typical data is shown in Table II. The device characteristics shown in Fig. 7 correspond to the last entry in Table II. For the carrier concentration and interrod spacing of this device, the modeling results indicate that the maximum electric field at the rods will be less than the avalanche breakdown field of ~3 x 10^5 V/cm due to the effect of the floating rods. We therefore expect that breakdown will only occur when the depletion layer punches through to the drain contact where the electric field can increase to the breakdown value. The breakdown voltage will be given approximately by the product of the average electric field and the gate-drain distance. Modeling indicates that the average field for devices in this range of matrix carrier concentration will be about 5 x 10^4 V/cm.

Data on the devices in Table II support the modeling results and indicate that device breakdown is limited only by punch-through not avalanche breakdown. The Table includes two columns of calculated data on the effective gate-to-drain distance and the the punch-through maximum breakdown voltage based on the approximate average breakdown field expected from the model and the effective gate to drain spacings.

The difference between the actual spacing of the gate and drain contacts on the wafer surface and the effective spacing of the two contacts is related to rod divergence.[4] The TaSi2 rods are not perfectly parallel, with a maximum divergence of about +/- 6°. This

divergence results in an effective gate-drain distance at the backside of the wafer which is shorter than the actual contact spacing by a factor 2t*tan(6), where t is the wafer thickness. Corrected for this effect, the measured voltages are in reasonable agreement with the predicted values, although still somewhat lower in all but one case as shown in Table II. However, these numbers of up to 1000 V may be compared with the theoretical maximum breakdown voltage of ~200 V for planar Si junctions in this range of carrier concentration. The data clearly indicates that floating junction devices enable high voltages that are limited by device design restrictions more than inherent factors such as avalanche breakdown.

Devices with dimensions designed to hold-off 2000 V have been processed and testing of them is in progress. The high voltage properties are being tested using a high voltage gas discharge apparatus schematically illustrated in Fig. 8. This equipment is capable of delivering 100 ns pulses of 2 - 10 kV. Preliminary measurements on a device show breakdown at lower than the intended 2000 V and passage of 5 A of current. The test is an indication that at these high voltages, surface breakdown may limit the device. Because the $TaSi_2$ rods extend through the thickness of the device, the applied potentials appear at both top and bottom surfaces, as well as in the interior. This suggests that surface passivation of both surfaces may be required before testing. Surface breakdown issues will have to be examined in future studies.

Materials Issues

Despite the promising results described above, there are three factors which render the "benchmark" Si-$TaSi_2$ system less than ideal for pulsed power applications. First, the Schottky barrier height characteristic of the Si-$TaSi_2$ junction is only 0.62 eV. This

relatively low barrier gives rise to leakage currents under reverse gate bias that are higher than desirable (several orders of magnitude more than a Si p-n junction under similar conditions, for example). Furthermore, leakage increases rapidly with increasing temperature (such as that due to power loading) or carrier concentration. Identification of SME materials systems with higher Schottky barrier heights would clearly be advantageous.

Second, based on the modeling results presented in Table I, reduction of interrod spacing should lead to higher saturation current density of the transistor switch. In the eutectic solidification process the interrod spacing varies inversely as the square root of the solidification rate, with a proportionality constant that is specific to each materials system. The interrod spacing of ~8 μm used in the devices discussed in Table II was achieved at close to the maximum practical growth rate using the Czochralski technique. It would therefore be difficult to obtain smaller spacings in the Si-TaSi$_2$ system.

Third, the small divergence of the rods from parallel complicates the device design process, as discussed above, and leads to either a reduction in wafer thickness, and therefore current switching ability, or the blocking voltage.

Complete realization of the promise of this new device technology for pulsed power may require the development of new materials with optimized properties. We have been addressing these issues using two different approaches. First, we are reconsidering the basic physical parameters that determine the average interrod spacing and alignment of the rods during Czochralski growth. Our studies indicate that melt convection has a substantial effect on both of these parameters. They suggest that more control over convection in the melt may lead to finer, better aligned rod structures.

Second, we are investigating GaAs-based eutectics because they are expected to have higher Schottky barrier heights than their Si counterparts, (greater than half the bandgap, 0.72 eV) and because they might also have finer microstructures at practical growth rates. Since the existence and properties of GaAs-based SME materials are largely unknown, our first task has been the computation of phase diagrams to identify candidate systems for further investigation. This effort is being followed by experimental testing and analysis. A list of promising eutectic compositions and temperatures predicted by these phase diagram calculations (performed by ManLabs, Inc.) is given in Table III. The GaAs - metal diboride systems are particularly intriguing since growth of these systems may be relatively simple compared to those containing metallic arsenides. With metal arsenides, compositional control can be problematic due to As loss from the melt. The lack of arsenic in the metal diborides resolves this problem.

A micrograph of a Bridgman-grown GaAs-GdAs eutectic grown at 3.5 cm/h is shown in Fig.9. It contains a higher volume fraction of the metallic phase then the benchmark Si-TaSi$_2$ system and an average interrod spacing of about 15 μm. Growth at the same 20 cm/h rate as the Si-TaSi$_2$ would be expected to reduce the average interrod spacing to about 6 μm, just slightly finer than the Si-TaSi$_2$ used for devices.

Conclusions

The unique properties of semiconductor-metal eutectic materials can be exploited to yield a new class of transistors. These devices hold great promise for the development of high voltage, high current, voltage controlled pulsed power switches. We have demonstrated experimental devices with breakdown voltages far in excess of those

expected for planar junction devices made from similar semiconductor material. We have also explored the physics of these devices by numerical modeling to identify the mechanisms which lead to elevated blocking voltages. The origins of these effects are now understood. This modeling work has been extended to address the optimization of materials and device parameters needed to achieve both high voltage and high current capability in the same device.

Continuing efforts are aimed at the fabrication and testing of new devices based on modeling results. Further work involves the identification and development of new materials systems which should provide additional performance improvements.

REFERENCES

1. S. M. Sze, <u>Physics of Semiconductor Devices, 2nd Ed.</u> (John Wiley and Sons, New York, 1981), ch. 2.

2. M. Levinson, P. Rossoni, F. Rock and B.M.Ditchek, Electronics Letters, 26, 777 (1990).

3. B. M. Ditchek, T. R. Middleton, R. G. Rossoni, and B. G. Yacobi, Appl. Phys. Lett. <u>52</u>, 1147 (1988).

4. B. M. Ditchek and B. G. Yacobi, Japan. J. Appl. Phys. <u>27</u>, L2155 (1988).

Table I

DEVICE PARAMETERS
MAXIMUM FIELD $E_{max} = 10^5$ V/cm

Rod spacing (μm)	Avg. Field at E_{max} (V/cm)	S-D distance for $V_{max}=1000$ V (μm)	N_D (cm^{-3})	J_S (A/cm^2)
4	5.08×10^4	200	5.9×10^{15}	6500
7	5.37×10^4	186	3.3×10^{15}	3300
23	5.44×10^4	184	1.0×10^{15}	870

Table II

MEASURED BREAKDOWN VOLTAGES

Carrier Concentration (10^{15} cm^{-3})	Thickness (μm)	G-D Distance (μm)	Effective G-D Distance (μm)	V_{max} (predict.) (V)	V_{max} (meas.) (V)
3	500	137	33	50	165
3	250	137	85	350	425
3	125	137	111	600	555
2	500	150	46	90	230
2	250	150	98	250	490
2	125	150	124	500	620
1	250	180	128	500	640
1	125	180	154	700	770
1	250	62	10	40	50
1	125	250	224	1000	1120

FIGURE CAPTIONS

Fig. 1. Breakdown voltage vs. doping concentration (after Sze, Ref. 1).

Fig. 2. Semiconductor-metal eutectic transistor geometry.

Fig. 3. Geometries for PISCES simulations: left,no floating rods; right, six floating rods.

Fig. 4. Potential vs. distance from the source calculated for the geometry of Fig. 3 at a drain voltage of 200 V. 1) no floating rods. 2) with floating rods.

Fig. 5. Maximum electric field vs. drain voltage for the geometry of Fig. 3 showing the field clamping effect of the floating rods. 1) no floating rods. 2) with floating rods.

Fig. 6. Micrograph of semiconductor-metal eutectic transistor, showing source and gate contacts surrounding the central drain contact.

Fig. 7. Transfer characteristic of a typical device.

Fig. 8. High voltage pulse apparatus.

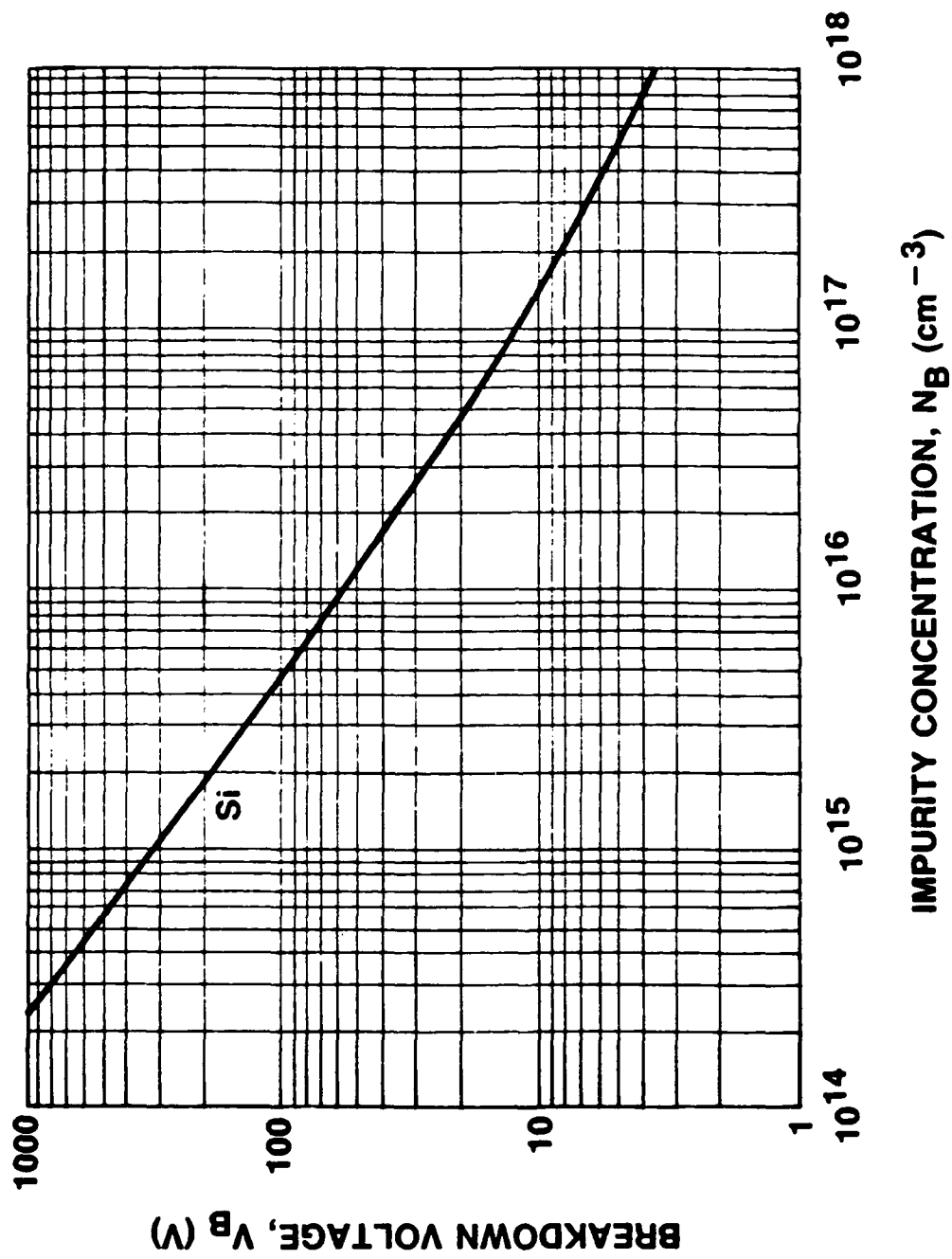Fig. 9. Cross-section of GaAs-GdAs eutectic composite.

Fig. 1. Breakdown voltage vs. doping concentration (after Sze, Ref. 1).

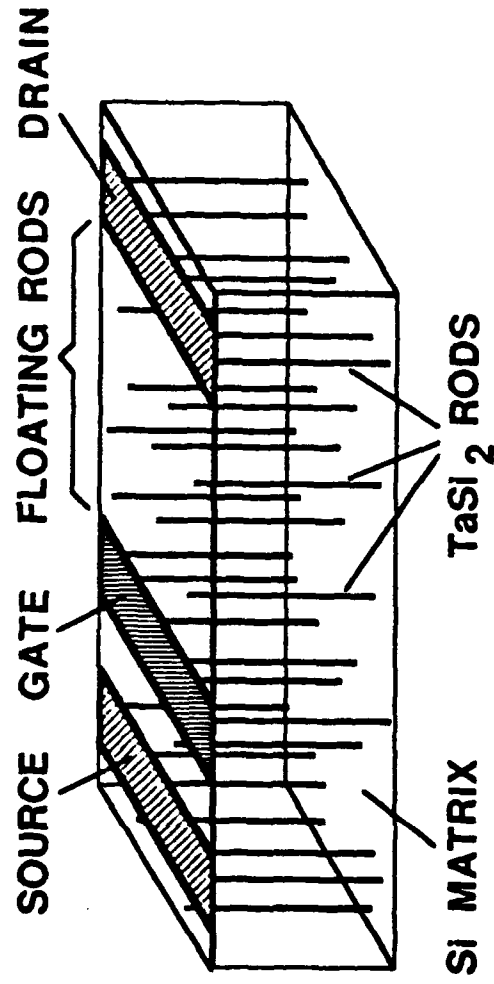# SEMICONDUCTOR-METAL EUTECTIC COMPOSITE TRANSISTOR

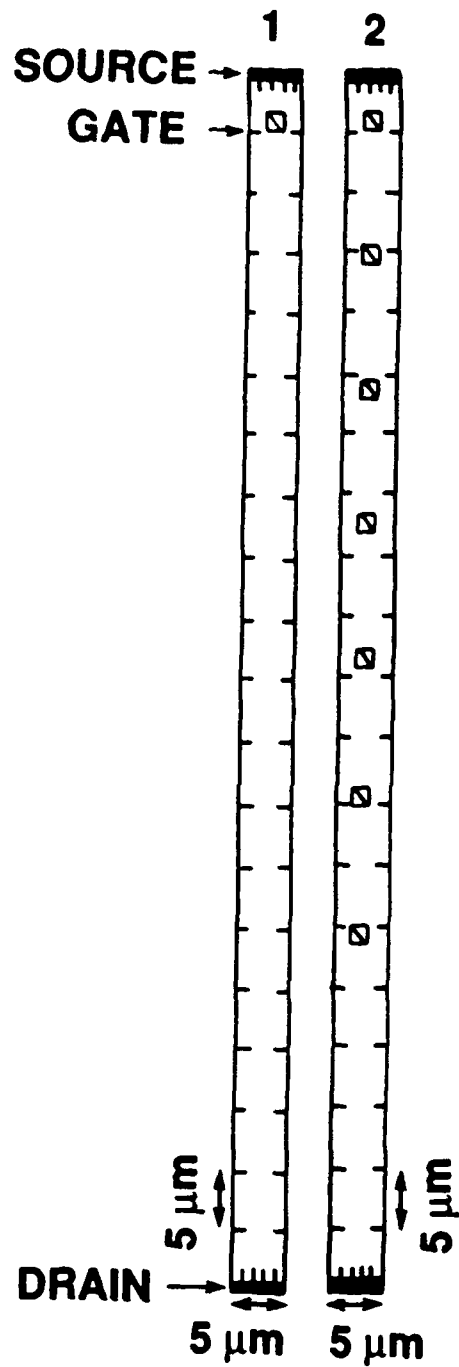Fig. 2. Semiconductor-metal eutectic transistor geometry.

Fig. 3. Geometries for PISCES simulations: left, no floating rods; right, six floating rods.
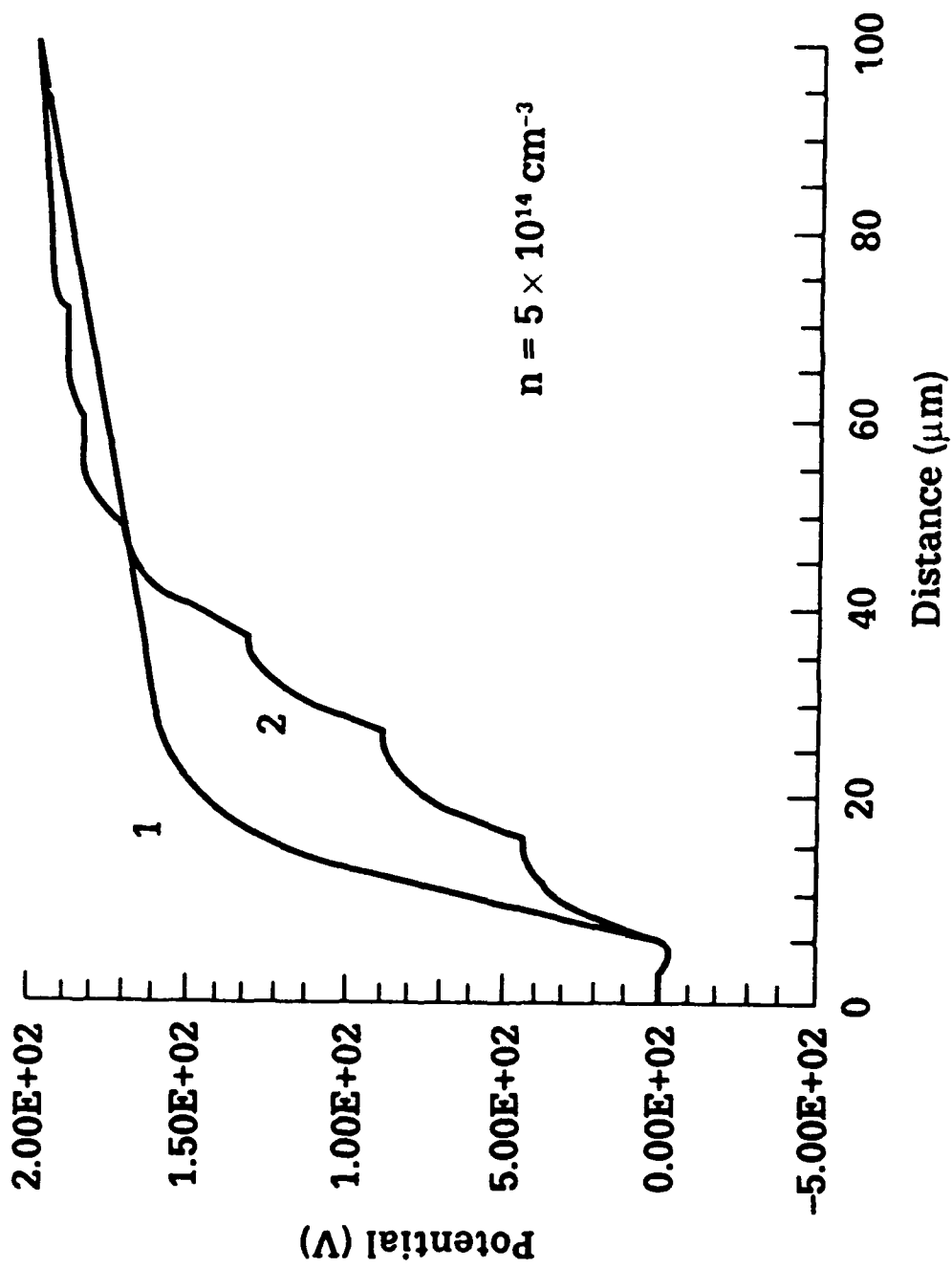
Fig. 4. Potential vs. distance from the source calculated for the geometry of Fig. 3 at a drain voltage of 200 V. 1) no floating rods. 2) with floating rods.
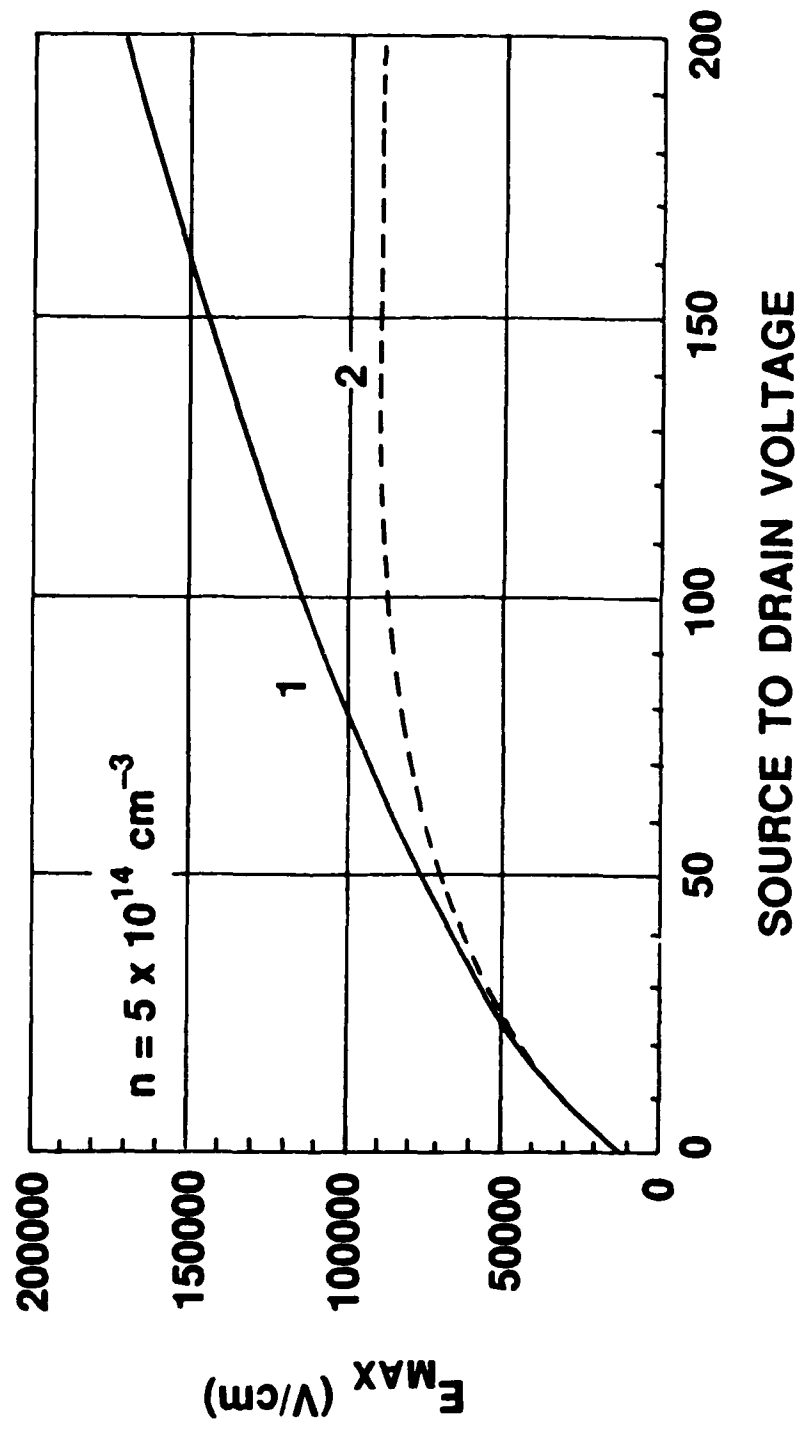
Fig. 5. Maximum electric field vs. drain voltage for the geometry of Fig. 3 showing the field clamping effect of the floating rods. 1) no floating rods. 2) with floating rods.
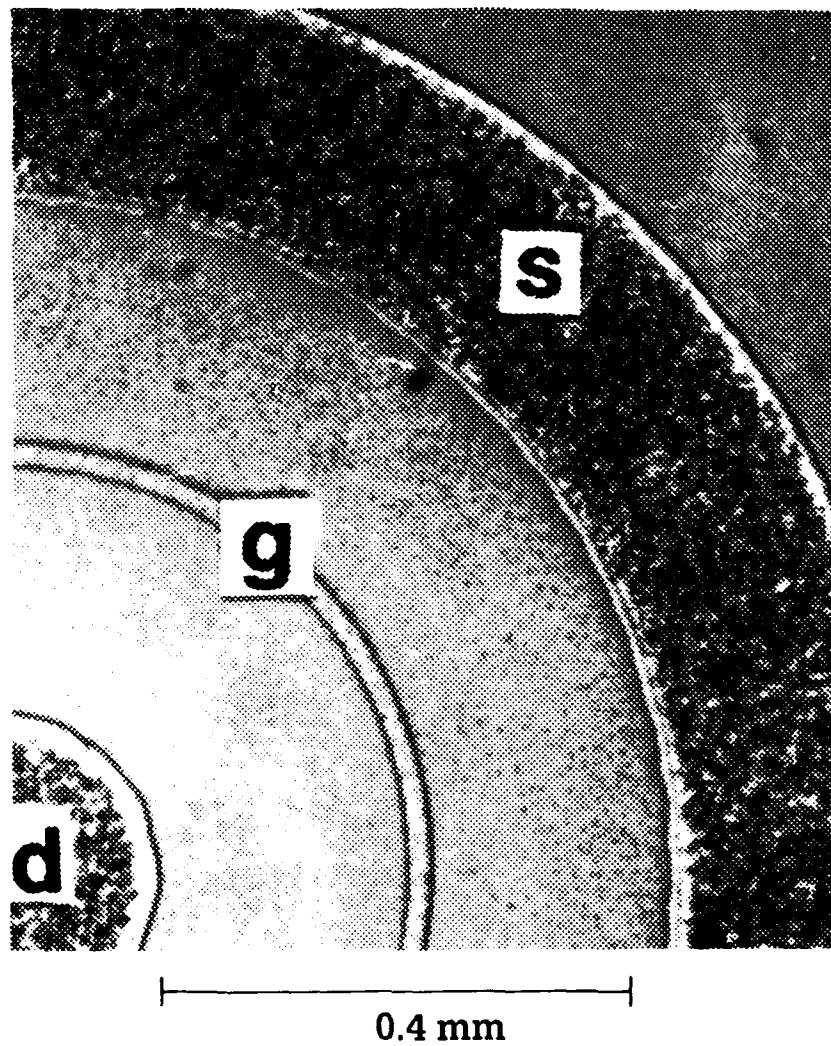
Figure 6. Micrograph of semiconductor-metal eutectic transistor, showing source and gate contacts surrounding the central drain contact.
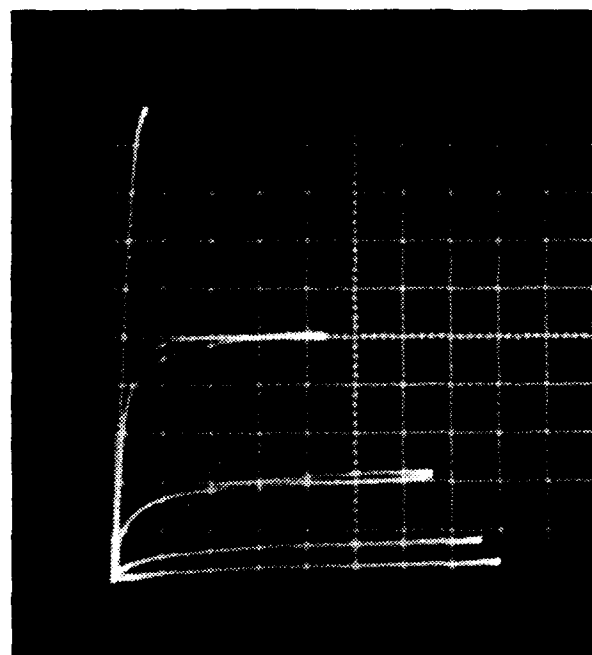
1 mA/Vert. Div.

100 V/Horiz. Div.

5 V/Step

g_m 0.2 mS/Div.

Figure 7. Transfer characteristics of a typical device.
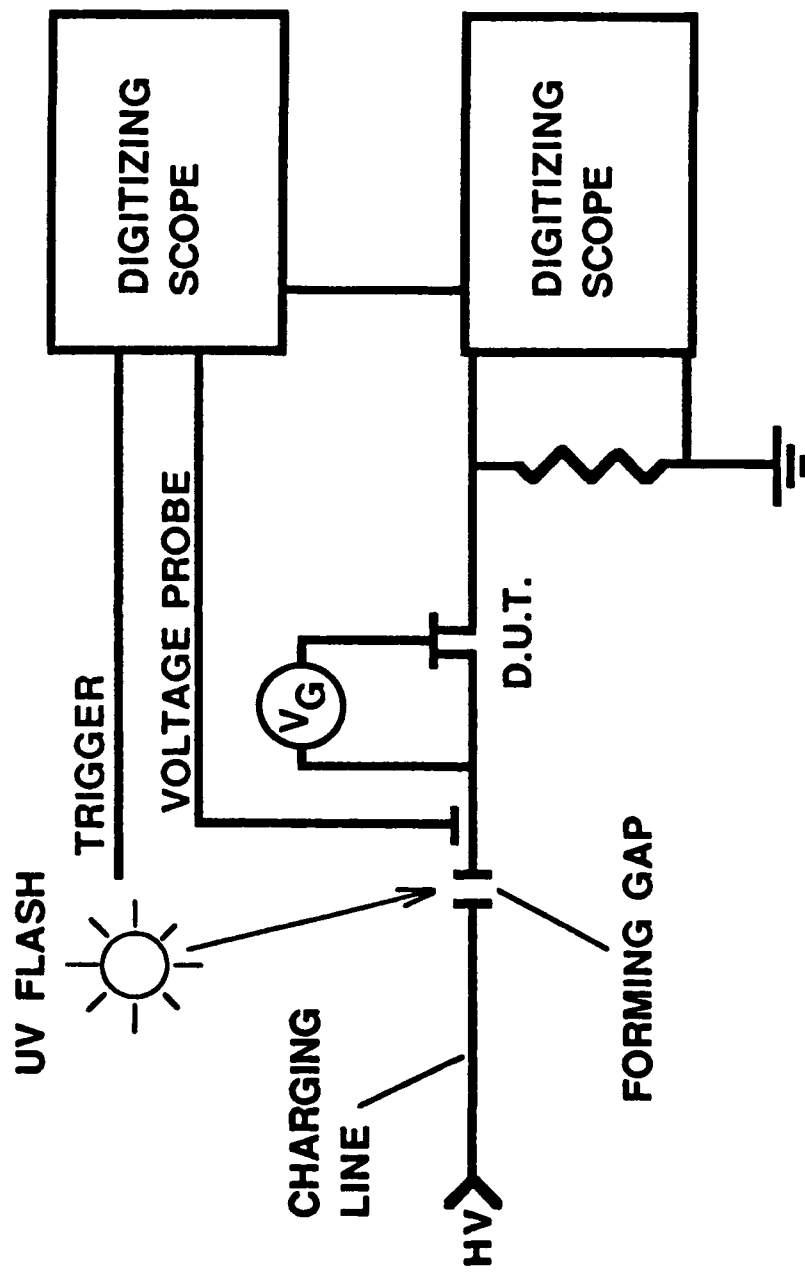
Fig. 8. High voltage pulse apparatus.

GaAs-GdAs Eutectic

Figure 9. Cross-section of GaAs-GdAs eutectic composite.

PULSED SURFACE FLASHOVER CHARACTERISTICS ALONG ALUMINA AND SILICON IN VACUUM

Tangali Sudarshan
Dept of Electrical & Computer Engineering
University of South Carolina
Columbia, SC 29208

INVESTIGATION OF PULSED SURFACE FLASHOVER PHENOMENA ALONG DIELECTRIC AND PHOTOCONDUCTING MATEIRALS

P. I.: Tangali S. Sudarshan
Graduate Students: R. G. Bommakanti, S. H. Nam,
K. Foo, J. Gamble, S. Menon
Department of Electrical & Computer Engineering
University of South Carolina
Columbia, SC 29208

Main Goals of Research
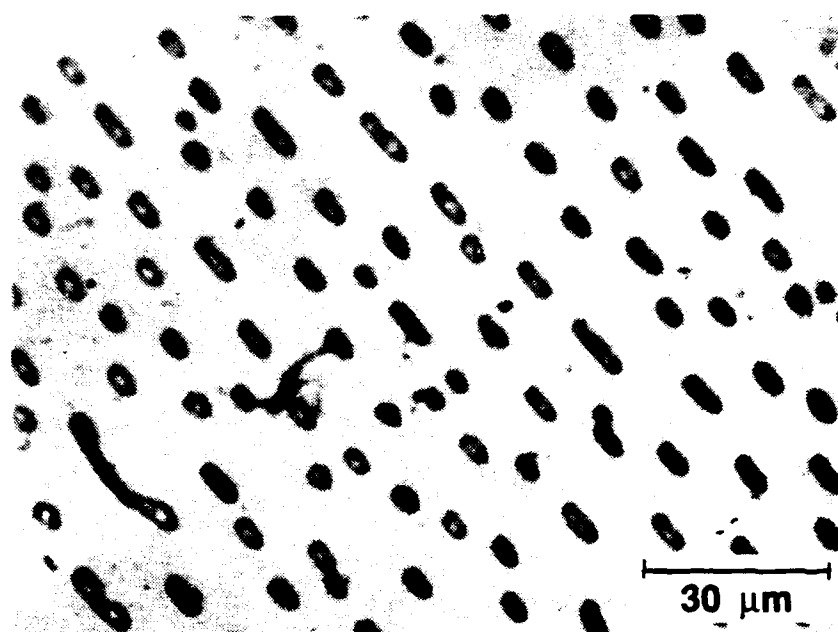
The research project addresses three main issues regarding the *surface breakdown* of Alumina (Al_2O_3) ceramics and photoconducting Si, both critical materials in pulse power switching devices:

(1) Identify key parameters at the microscopic level which influence breakdown. To accomplish this goal, the surface structural (microstructural features) and chemical imperfections were altered in a determined way by careful mechanical and chemical treatments. By this technique, the density of surface defects and hence the band gap characteristics can be altered.

(2) Gain deeper understanding of the mechanisms in the pre-breakdown conduction and discharge development phases of surface breakdown. To accomplish this goal, coordinated, time resolved (~1 ns) measurements of applied voltage, conduction current, pre-breakdown and breakdown luminosity and x-ray emission have been carried out. In addition, optical and scanning electron microscopes, and an intensified gatable 2d CID camera has been employed.

(3) Identify techniques and procedures to improve the breakdown strength of materials. The above has been accomplished by the development of precise surface preparation techniques, geometric profiles, and selection of low surface defect materials.

Introduction

The work is divided into three parts:

(i)   Study of dielectric materials in vacuum.
(ii) Study of photoconducting materials in vacuum.
(iii) Study of low-energy laser initiated switching of compressed N_2 gas gap bridged by PMMA insulators.

Results and Discussion

I. Dielectric materials in vacuum: The studies were carried out on 99.9% polycrystalline Al_2O_3, single crystal SiO_2, and PMMA, using 0.5/15 μs impulse voltage excitation, in an ambient of 15 μTorr vacuum. Figures 1 and 2 show the schematic of the experimental setup and the voltage conditioning procedures.

Figure 3 shows the discharge luminosity and current profiles for a 0.25 micron finish alumina which is subjected to abrasive polishing resulting in surface damage and a high density of surface defects. It is to be noted in Fig. 3(a) that the luminosity (photon emission) precedes the discharge current (electron avalanche) by a few nanoseconds. The luminosity profile has an initial slowly varying component followed by a steeply rising portion in the first few breakdowns. With successive breakdowns, the slowly varying portion decreases in duration and almost disappears after a few shots, and the delay between the onset of light and current signals also decreases as shown in Fig. 3(b). It is to be noted that the temporal profiles of current and luminosity are vastly different and that both change dynamically in the first few breakdowns. These and other results, based on a systematic study, point to the important role of carrier trapping and recombination processes, within the localized levels of the forbidden band gap, due to the presence of surface defects [JAP 66(5), Sept. 1989] These results suggest that surface breakdown is based on a solid-state model, controlled by defects and imperfections, characteristic of the insulator surface.

The pulsed flashover performance is strongly influenced by the mechanical grinding and polishing operations. Three different surface finishes of 99.9% Al_2O_3 are studied:

(a) 0.8 micron; as fired.

(b) 0.25 micron; here the sample was ground on a wheel using diamond abrasive. This high temperature, high pressure process is mutative, resulting in inter- and trans-granular fracture surface features.

(c) 0.05 micron; uses a low pressure, room temperature polishing using a slurry. The damaged layer produced in (b) is removed substantially, resulting in a smooth surface with a shallower damage layer.

The results are shown in Table 1. The flashover strengths of the ground samples (0.25 μ) are lower than the as-fired samples by ~50% while the strengths of the polished surfaces are intermediate between the two. The results are attributed to sub-surface defects (fracture) induced by mechanical grinding for 0.25 μ and partial removal of damage for the 0.05 μ surfaces. The temporal luminosity and current profiles are characteristic of a trapping mechanism due to defects [JAP, 67 (11), June 1990]. The results suggest that the surface insulating properties, as influenced by the microstructural features, are strongly dependent

on the precise mode of material removal during grinding and polishing operations, and hence cannot simply be correlated to the gross surface topography.

The performance of single crystal quartz (SiO_2) shows improvement over some polycrystalline alumina. In conjunction with the above tests, for the first time, pulsed x-ray measurements were carried out which correlated well with the breakdown characteristics. Table 2 shows the breakdown and x-ray data for quartz specimens with the piezoelectric axis parallel (X-cut) and perpendicular (Z-cut) to the applied field E. The Z-cut samples exhibit superior performance over X-cut and have a lower incidence of pre-breakdown x-ray emission. Fig. 4 shows the pre-breakdown emission. Fig. 5 shows x-ray emission both during the pre-breakdown and breakdown phases. The x-ray emission studies were also carried out for alumina samples as shown in Table 3. Here, tx_{pbd} refers to the time for the onset of pre-breakdown x-ray emission from voltage zero. The results indicate that specimens with high pre-breakdown x-ray activity exhibit lower voltage hold-off and vice versa. The strong correlation of the pre-breakdown x-ray emission activity with the insulator hold-off voltage represents a valuable diagnostic tool in the practical choice of insulators for pulse power [1990 DEIV proceedings]. The superior performance of Z-cut quartz (>170 kV/cm) exceeds anything that has been reported in the literature for straight cylindrical samples.

A novel technique for comparing the insulating properties of different dielectric surfaces, using an SEM, has been developed [1990 CEIDP proceedings]. An insulator bombarded by an energetic e-beam in an SEM becomes negatively charged. The surface, thus charged, acts as a mirror for a low energy e-beam. The objective lens of the SEM can be imaged (mirror). The mirror diameter is inversely proportional to the dielectric constant ε_r of the surface. Fig. 6 shows a typical mirror. Table 4 shows the results of two different surfaces of Al_2O_3. The larger mirror diameter implies lower ε_r and larger band gap, and hence a larger breakdown voltage. The one-to-one correspondence between the SEM mirror data and surface breakdown strength proves the potential of this technique as a ND tool to study surface defects, dielectric constant, band gap, and importantly, the breakdown strength.

Table 5 shows a comparison between dc and pulsed breakdown voltages, for 1 cm long PMMA insulators, having different geometric profiles. For straight cylindrical and conical frustrum shapes, the pulsed breakdown strength is significantly higher than the dc values. However, for other shapes (e.g., bevel at the cathode or electrode covering samples), the higher dc vs. the pulsed breakdown strength is attributed to time dependent surface charging due to surface defects. From an engineering point of view it is important to note that designs offering superior dc voltage hold-off do not necessarily offer high pulse withstand.

II. Photoconducting Silicon in vacuum: The studies were carried out on high purity Si (resistivity >30 kΩ cm) in the form of circular cylinders (2.5 cm dia. x 1 cm long), using 0.39/10 μs impulse voltage excitation in an ambient of ~1 μ Torr vacuum. The <111> direction of the crystal was parallel to the axis of the cylindrical specimen along which the external electric field was applied. Specimens with and without metal contacts were studied in a quasi-uniform field as shown in Fig. 7.

Fig. 8 shows typical waveforms revealing 3 distinct phases leading to flashover [*IEEE Trans on E. Insul.*, Dec. 89]. The phase I prebreakdown current has one of three distinguishing characteristics, depending on the type of contacts and previous history. They are, for specimens with metal contacts:
(a) Ohmic dominant where the current peak I_p is proportional to voltage peak V_p,
(b) Space charge limited (SCL) dominant where Ip α V_p^2, or
(c) Pure SCL current observed for specimen without metal contacts.

Fig. 9 shows typical SCL dominant current response. When the SCL dominant phase I current reaches a threshold value, significant increase in photonic emission results, as indicated by Point A in Fig. 10. The current increases significantly at point B, accompanied by an increase in light emission and partial voltage collapse, indicating the onset of phase II. In this phase, $I_p \alpha$ $V_p^{7.3}$. At higher voltages, phase II leads to phase III, characterized by complete voltage collapse and increase in current and light emission to their peak values. When the phase I current reaches a critical value of 0.55 A, and if the photon emission occurs near the voltage peak, breakdown (phase II or III) ensues. Based on these experimental results, the flashover voltage has been successfully computed from an analytical model, as shown in Table 6, for the three different cases of phase I current.

The influence of chemical and mechanical imperfections on the surfaces of high purity Si is studied. The imperfections were deliberately altered on the specimen contact and cylindrical surfaces. Table 7 shows surface preparations for the five different specimens studied. The mechanical polishing of the contacts for specimen 2 involved final polish of the end surfaces with 0.05 μm alumina. The chemo-mechanical polishing of the contacts of the other specimens involved final polish of the contacts with 0.05 μm colloidal Silica suspended in KOH. For specimens 4 and 5, even the cylindrical surfaces were chemo-mechanically polished. The etch indicates chemical etching in a 3:5:3 mixture of HF-HNO3-CH3COOH solution. After the surfaces were prepared, the specimens were cleaned either in water or by using the RCA procedure (HF based to remove impurities), a standard industry procedure to etch IC Silicon wafers. Sample 5 was oxidized as a final step, which involved heating the entire specimen at 1100°C for 120 minutes in a dry O_2 ambient, to produce a surface layer of SiO_2.

Table 8 shows the phase I luminosity and breakdown voltage inception values for samples 1 to 5. Chemo-mechanical polishing of the contacts and RCA cleaning results in significant improvements in the onset of phase II and phase III voltages (sample 3). Further, chemo-mechanical polishing of the cylindrical surface (along which breakdown occurs) followed by RCA cleaning results in the highest phase II and phase III voltages. Compared to a mechanically polished contact (sample 2), the improvements are by a factor of ~3 and 2.5, respectively [1990 CEIDP Proceedings]. Another important observation from Table 8 is that the higher the onset voltage for the initiation of light activity in the phase I pre-breakdown phase (V_{iL}), the higher the phase II and phase III inception voltages. Thus, the onset of light activity in the prebreakdown phase is an important forecaster of the device failure voltage and hence a significant ND tool.

The onset of partial collapse in voltage (phase II) is strongly correlated with the injection of carriers from emission spots on the cathode as shown by the micrograph of the cathode in Fig. 11. Fig. 12 shows light emission from injection spots on the anode and cathode, captured by a gatable, intensified, 2d CID camera. It demonstrates that charge injection in phase II is clearly a bulk process, whereas, as Fig. 13 shows, phase III or complete breakdown is a surface process.

The results indicate that irreversible device damage sets in at the onset of phase II partial breakdown (Figs. 11 and 12), corresponding to the development of injection spots. These light emitting injection spots, which are characteristic microplasmas, are believed to be caused by avalanche breakdown at an inversion layer formed near the cathode contact (IEEE Tr. on Electron. Devices).

Based on our experimental observations, involving fast electrical and optical diagnostics, optical micrographs, and 2d imaging, we have proposed an innovative model to describe surface breakdown of photoconducting Silicon.

III. Laser initiated switching of compressed N_2 gas gaps: The effect of insulator (plexiglas) diameter (1, 4, and 6 cms) and pressure (0.1 to 0.4 Mpa) were studied using coordinated measurements of discharge current and luminosity, with nanosecond response time. Delay times to the onset of discharge from laser initiation and the threshold laser initiated breakdown voltage were also measured. The results indicate that the insulator surface impedes the development of the discharge in both the avalanche (onset) and streamer phases of breakdown. The results also indicate that a surface breakdown can be initiated using a low energy laser (90 µJ) with very low jitter. The results are presented and discussed in detail in a journal article: IEEE Tr. on Plasma Science, 17(4), pp. 588-94, Aug. 1989.

List of Publications from the SDIO/ONR supported Research

1. "Observation of Three Distinct Phases Leading to Pulsed Surface Flashover Along Silicon in Vacuum", with S.H. Nam, *13th Int. Symp. on Discharges and Electrical Insulation in Vacuum*, Paris, 1988. Also published in the *IEEE Trans. on Electrical Insulation*, Vol. 24, No. 6, pp.979-83, 1989.

2. "Studies on the self and laser initiated discharge characteristics at dielectric/gas interfaces", with K. Foo, *IEEE Trans. on Plasma Science*, 17(4), pp.588-94, Aug. 1989.

3. "Effect of Leakage Current and Light Emission on Surface Flashover along Silicon in Vacuum", with S.H. Nam, *6th Intl. Symp. on High Voltage Engineering*, Aug. 1989, New Orleans.

4. "Influence of Insulator Surface Finish on the Pulsed Surface Flashover performance", with Bommakanti, *7th Pulsed Power Conference*, pp.828-31, June 1989, Monterey, California.

5. "Pre-breakdown (leakage) and Breakdown Currents and Light Emission Related to Surface Flashover Along Silicon in Vacuum", with Nam, pp.362-64, *IBID*.

6. "Trap Dominated Breakdown Processes in an Insulator Bridged Vacuum Gap", with Bommakanti, *J. of Applied Physics*, 66(5), pp.2091-99, Sept. 1989.

7. "Influence of Mechanical Grinding and Polishing Operations of Brittle Polycrystalline Alumina on the Pulsed Surface Flashover Performance", with Bommakanti, *J. of applied Physics*, 67 (11), pp.6991-97, June 1990.

8. "Pulsed Surface Flashover Performance of Monocrystalline SiO_2 Bridged Vacuum Gaps", with Bommakanti and Le Gressus, *XIV Int. Symp. on Discharges and Electrical Insulation in Vacuum*", Santa Fe, NM, Sept. 1990.

9. "An SEM Technique for Investigating the Insulating Properties of Dielectric Surfaces", with Bommakanti and Le Gressus, *Conf. on Electrical Insulation and Dielectric Phen.*, Oct. 1990.

10. "Pulsed Voltage Pre-breakdown observations on Silicon in Vacuum", with Gamble and Faust, *Conf. on Electrical Insulation and Dielectric Phen.*, Oct. 1990.

11. *"New Findings of Pulsed Surface Breakdown Along Silicon in Vacuum"*, with S.H. Nam, Accepted *IEEE Trans. on Electron Devices.*

12. *"Measurement of Electrical and Optical Avalanches Near Solid Insulators in High pressure (up to 0.3 MPa) Nitrogen Gas"*, with S. M. Mahajan, Submitted to the J. of Applied Physics.

Students Supported under the Contract.

1) Three Ph.D Students - graduated.

2) Four M.S. Students - two graduated.

3) Three Undergraduate Research Assistants.

EXPERIMENTAL
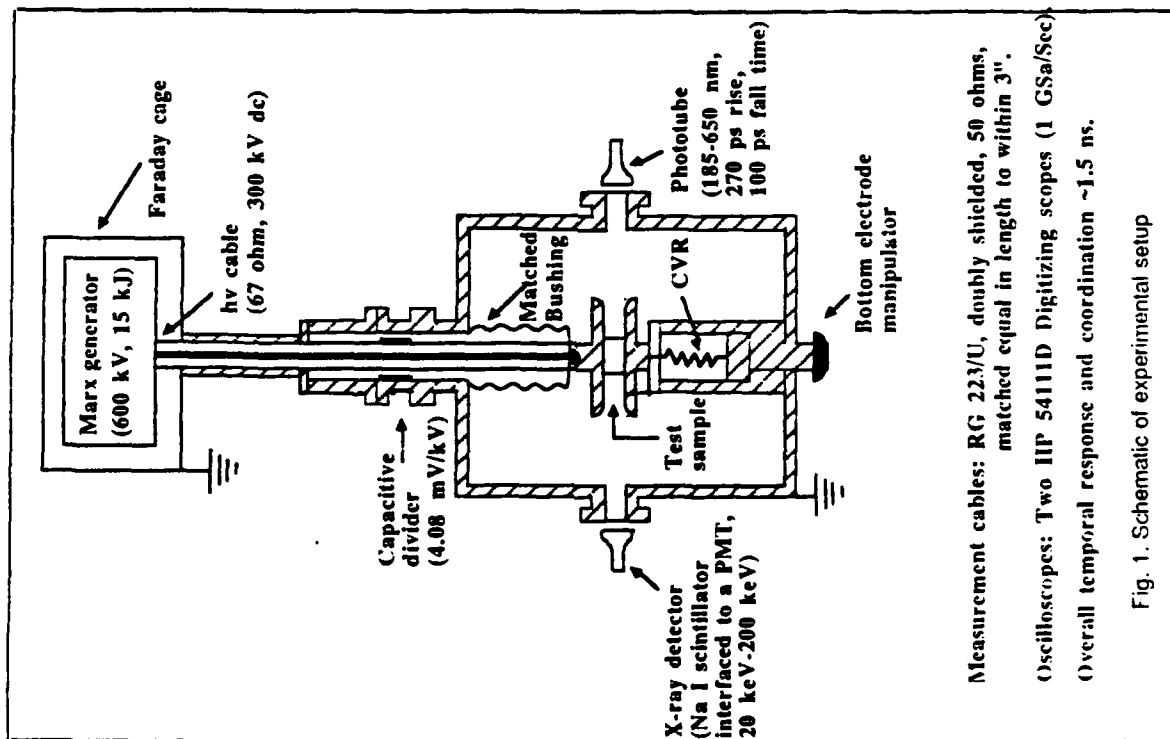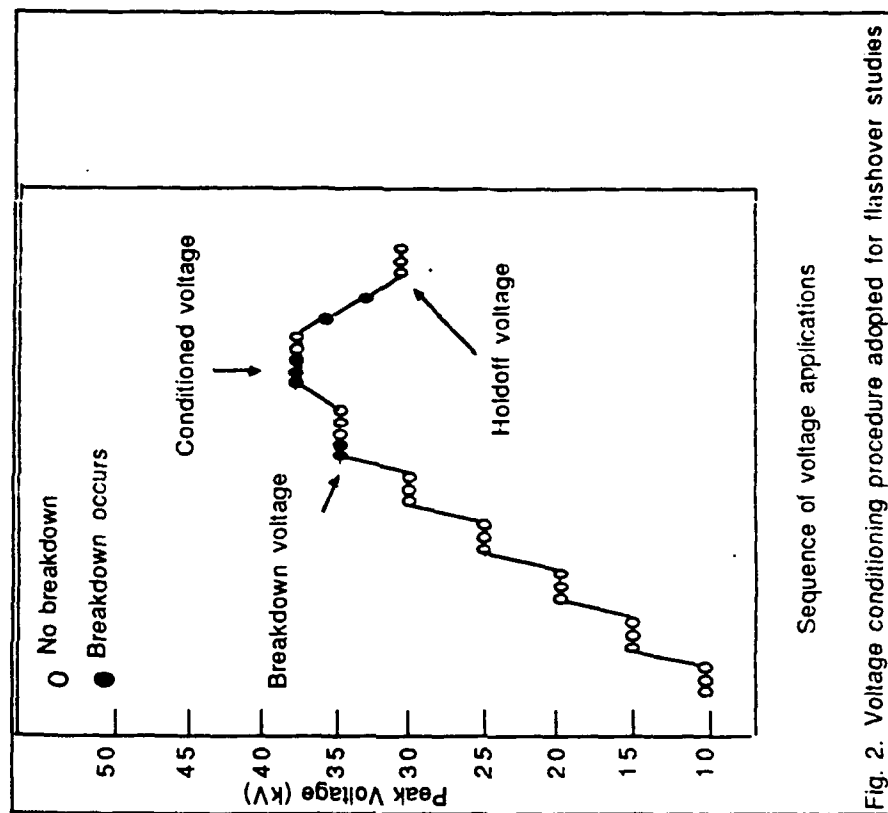
Fig. 2. Voltage conditioning procedure adopted for flashover studies

Measurement cables: RG 223/U, doubly shielded, 50 ohms, matched equal in length to within 3".

Oscilloscopes: Two HP 54111D Digitizing scopes (1 GSa/Sec).

Overall temporal response and coordination ~1.5 ns.

Fig. 1. Schematic of experimental setup
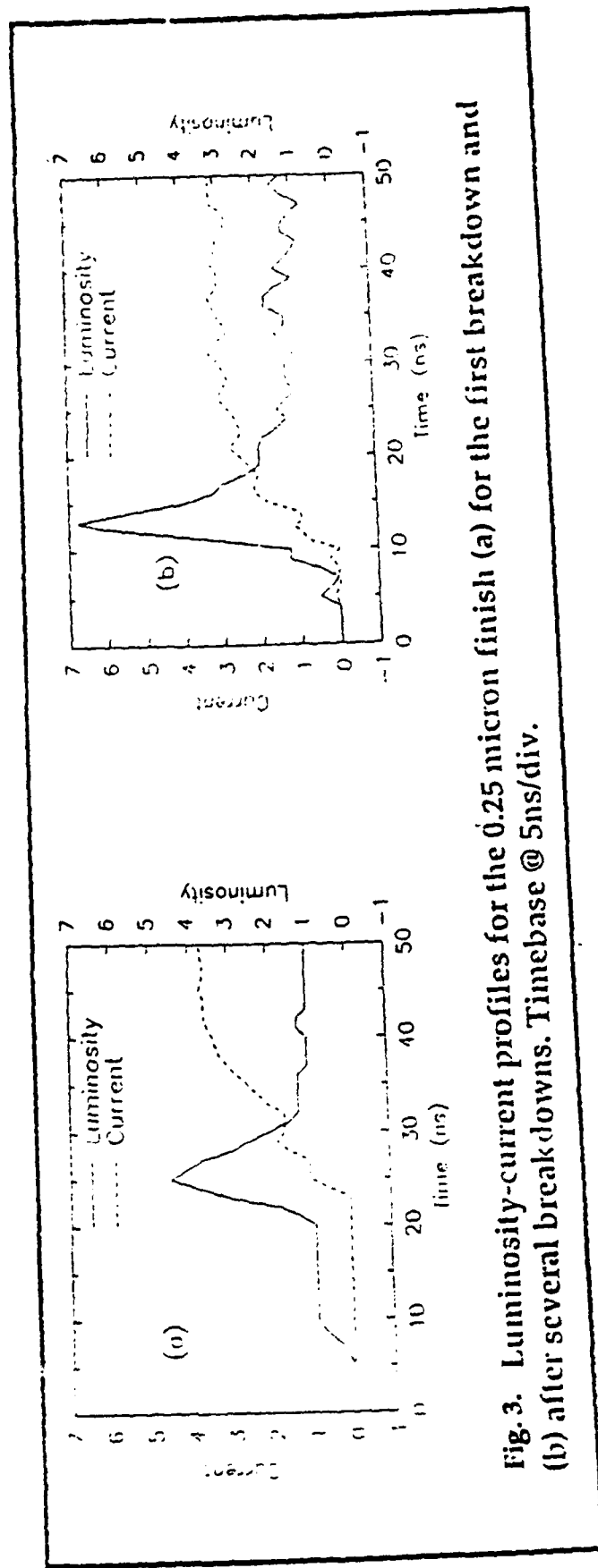
Fig. 3. Luminosity-current profiles for the 0.25 micron finish (a) for the first breakdown and (b) after several breakdowns. Timebase @ 5ns/div.
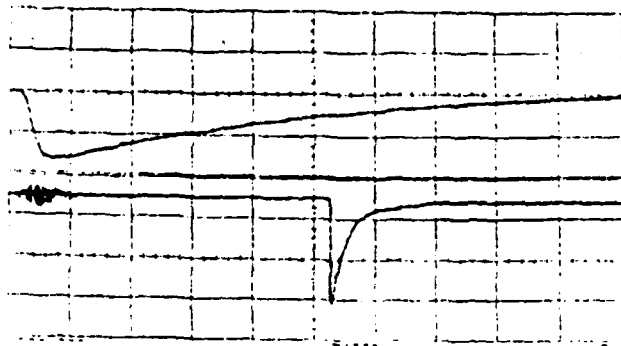
Prebreakdown x-ray activity only

Fig. 4   Oscillogram showing x-ray emission without the occurrence of breakdown. Time @ 1.0 μs/div, Upper trace: Voltage @ 83 kV/div, Lower trace: x-ray detector output @ 100 mV/div.
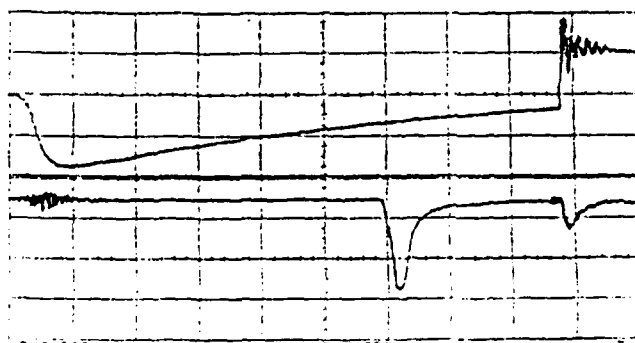
Prebreakdown and breakdown x-ray activity

Fig. 5   Oscillogram showing x-ray emission both during the prebreakdown and breakdown phases. Time @ 0.75 μs/div, Upper trace: Voltage @ 63 kV/div, Lower trace: x-ray detector output @ 100 mV/div.

Fig.6. SEM image of the microscope beam aperture
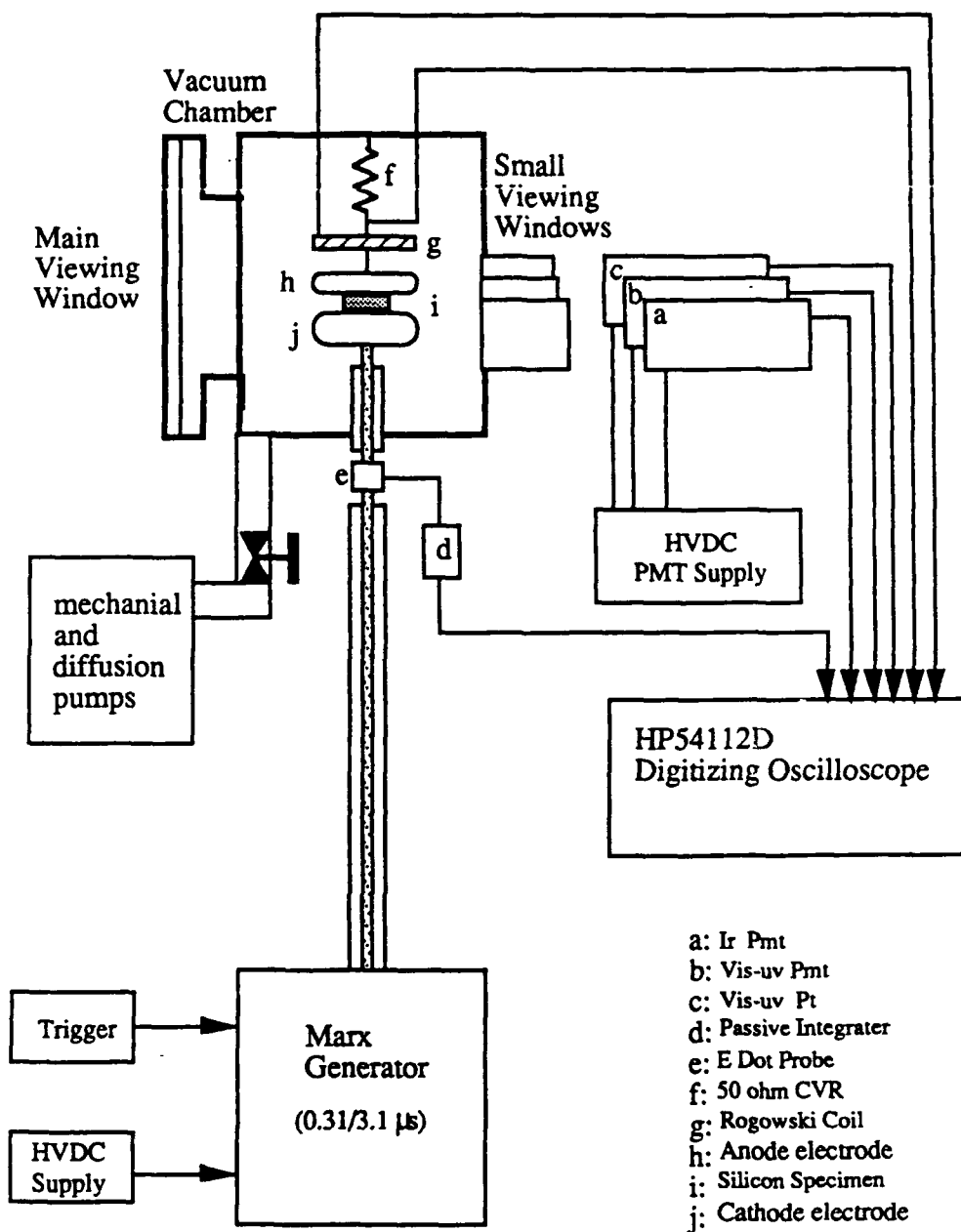
Figure 7 Experimental Test System
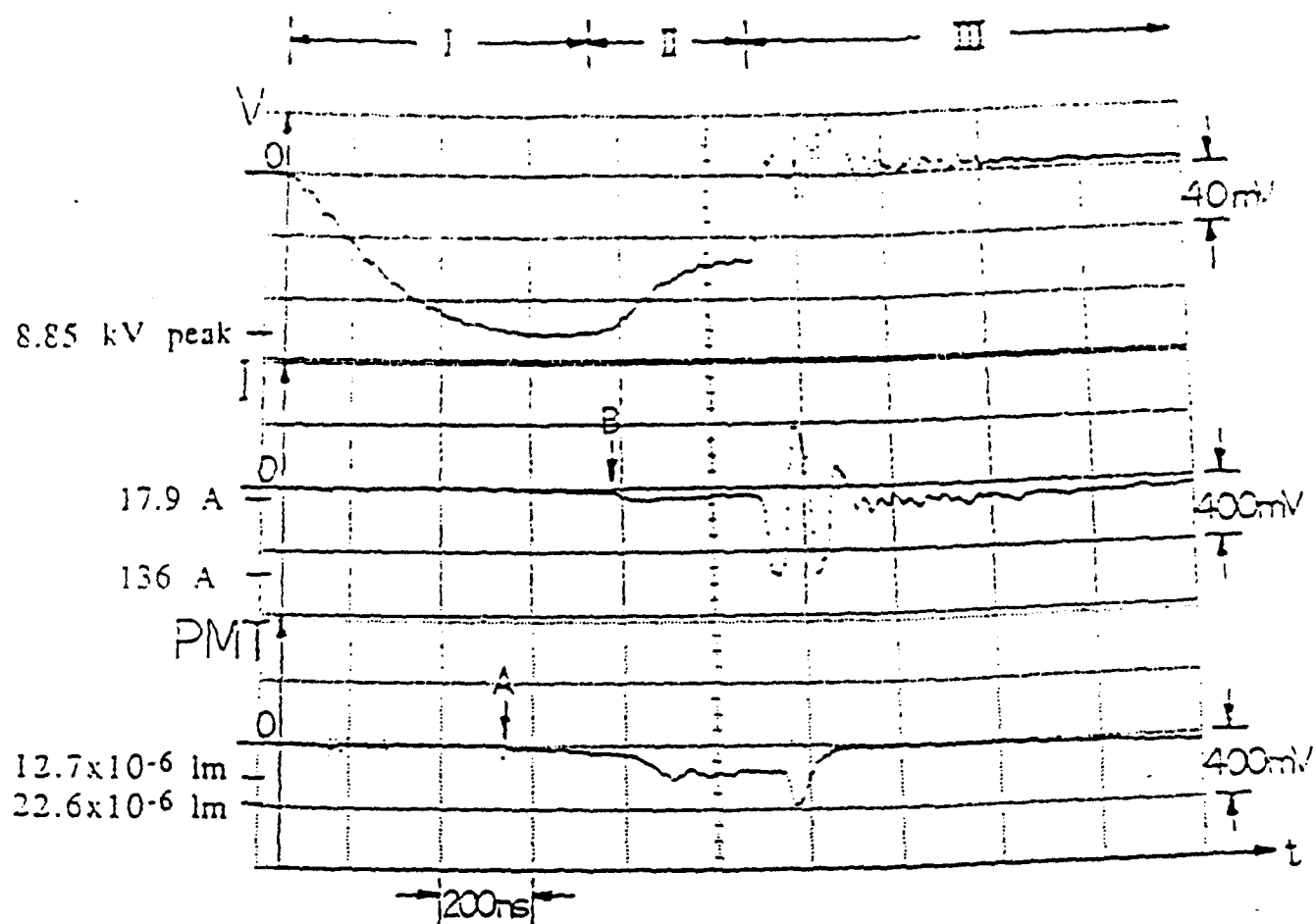
A : Onset of photonic activity.
B : Onset of phase II.

Fig. 8.   Three distinct processes leading to flashover along high
purity silicon with end gold contacts. Notice that the onset of
photonic activity (A) starts before the phase II current (B). Also the
amplitude of PMT signal during phase III is only ~2 times higher
than phase II PMT amplitude. This is not true for current.
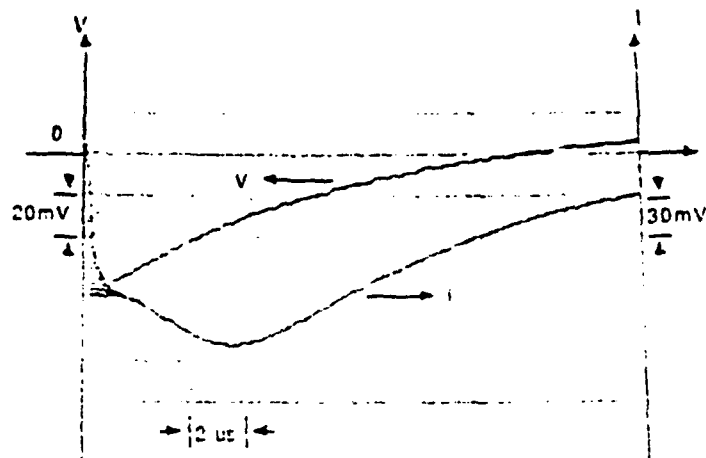
Fig. 9.   Voltage (5.56 kV peak) and phase I leakage current (0.56 A peak) for a specimen with gold contact. Phase shift between V and I peaks is ~5 us.
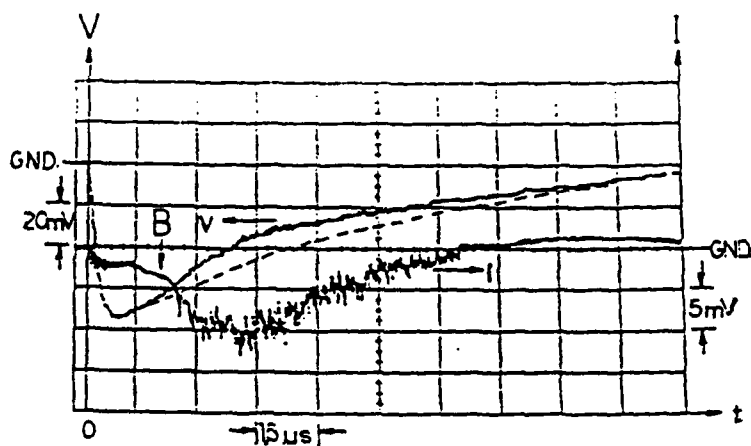
a) Impulse voltage (6.49 kV peak) and phase II current (3.15 A peak).
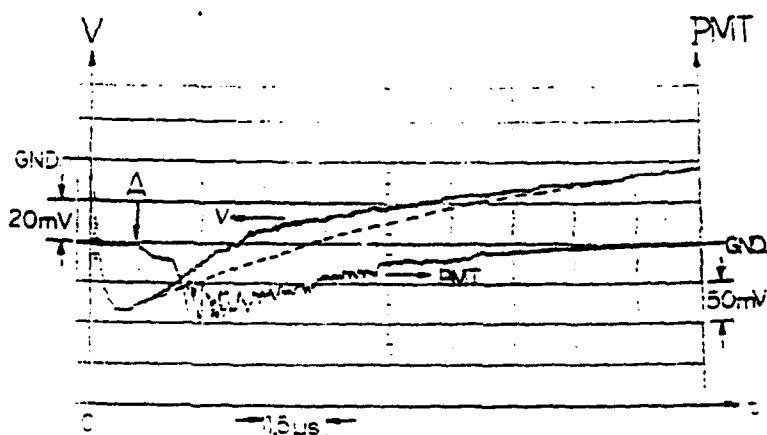
b) Impulse voltage (6.49 kV peak) and corresponding PMT signal (~5.89x10⁻⁶ lm peak).

Fig. 10   Voltage, current, and PMT responses in phase II. A and B indicate the onset of photon emission and Phase II process, respectively.   The dashed line indicates expected voltage signal without deformation.
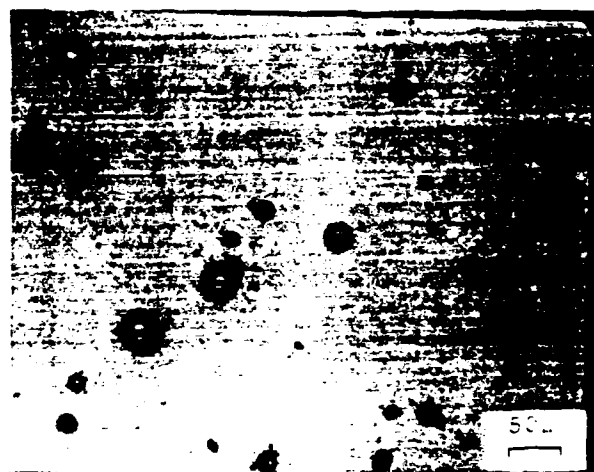
Fig.11. Micrograph of the cathode showing injection spots

CATHODE

ANODE
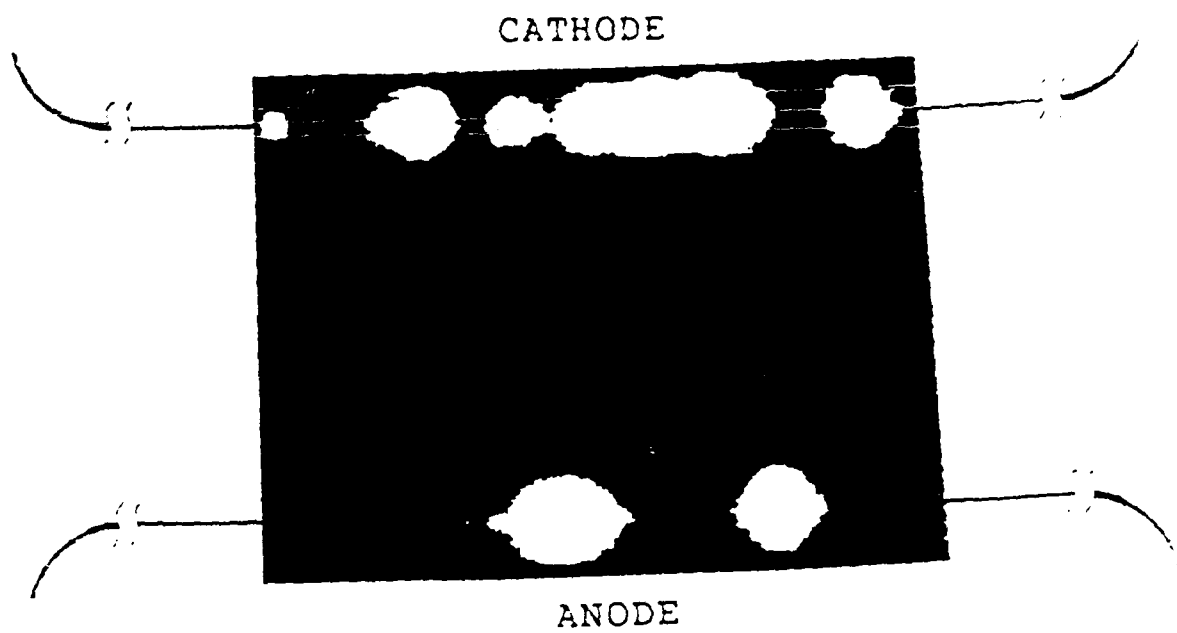
Fig. 12   Light emission from injection spots recorded using a 2d
           CID camera.
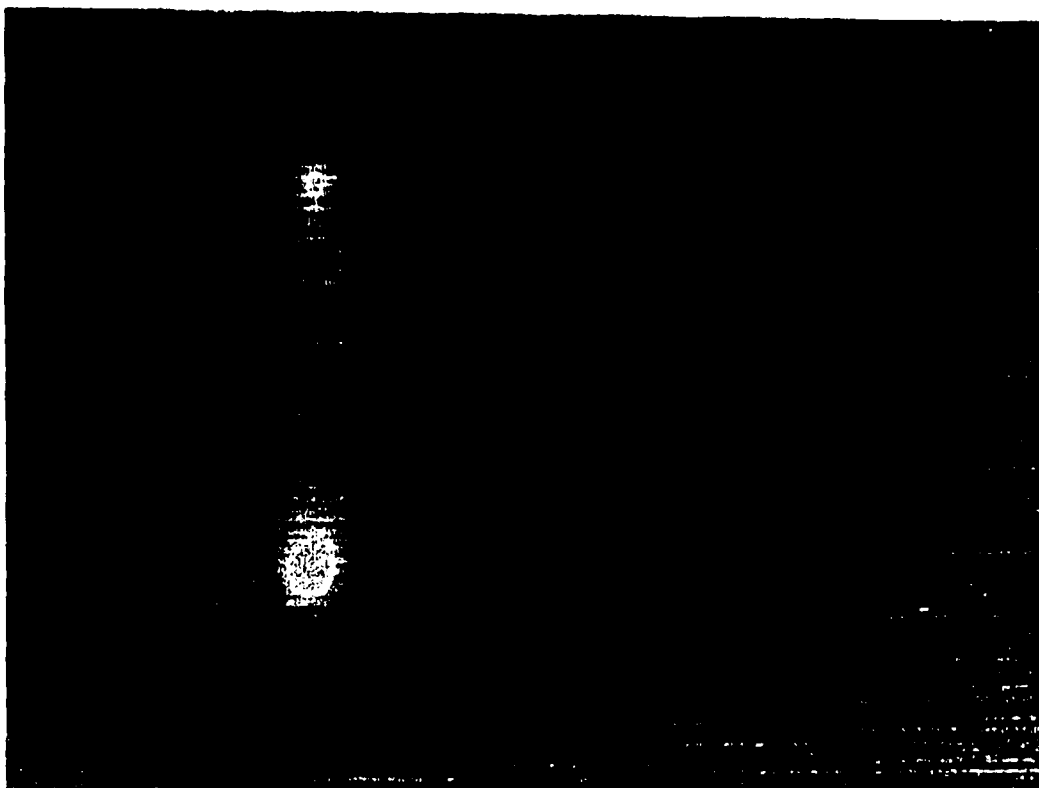
Fig. 13   Complete breakdown (phase III) along the surface of Si
            recorded using a 2d CID camera.

Table 1. Effect of surface finish on the pulsed surface flashover performance for 99.9% pure RW-99 polycrystalline alumina. σ is the standard deviation.

Surface finish in microns	Breakdown voltage V_{bd} in kV (mean ± σ)	Conditioned voltage V_c in kV (mean ± σ)	Holdoff voltage V_{ho} in kV (mean ± σ)
0.80	95 ± 14	115 ± 18	111 ± 13
0.25	43 ± 8	59 ± 8	41 ± 7
0.05	86 ± 1	87 ± 3	79 ± 8

Table 2

Pulsed surface flashover performance and prebreakdown x-ray emission results for X-cut and Z-cut quartz

Type of quartz	Initial Test			After 24 hour rest period			Prebreakdown x-ray results	
	V_{bd} (kV)	V_c (kV)	V_{ho} (kV)	V_{bd} (kV)	V_c (kV)	V_{ho} (kV)	Frequency of [1] x-ray emission	Typical [2] txpbd
X-cut	93 ± 10	124 ± 21	122 ± 19	>170	>170	>170	10 %	5 µs
Z-cut	95 ± 15	>170	>170	>170	>170	>170	2 %	10 µs

1   Frequency of prebreakdown x-ray emission $=\dfrac{\text{Voltage applications during which prebreakdown activity was observed}}{\text{Total no. of voltage applications}}$

2   Value is the most frequently observed over nearly 100 voltage applications

Table 3. Pulsed surface flashover performance and prebreakdown x-ray emission results for the alumina samples

Surface finish of alumina sample	Initial Test			After 24 hour rest period			Prebreakdown x-ray results	
	V_{bd} (kV)	V_c (kV)	V_{ho} (kV)	V_{bd} (kV)	V_c (kV)	V_{ho} (kV)	Frequency of [1] x-ray emission	Typical [2] txpbd
0.8 μm	120	130	128	> 170	> 170	> 170	4 %	7 μs
0.25 μm	68	70	60	60	60	47	60 %	0.4 μs

1 Frequency of prebreakdown x-ray emission $=$ $\dfrac{\text{Voltage applications during which prebreakdown activity was observed}}{\text{Total no. of voltage applications}}$

2 Value is the most frequently observed over nearly 100 voltage applications

Table 4. Comparison of the results of the SEM experiment and the pulsed surface flashover experiments.

Surface finish	SEM results (mirror radius)	Surface flashover results (Breakdown voltage)
As-fired	410 μm	130 kV
0.8 μm	21 μm	95 kV

Table 5. Influence of insulator geometry on the pulsed and dc surface flashover in insulator bridged vacuum gaps
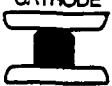
Sample geometry ▢ METAL ■ PMMA	Impulse (0.15/20 μs) stress			dc stress	
	V_{bd} (kV)	V_c (kV)	V_{ho} (kV)	V_1 (kV)	V_c (kV)
CATHODE / ANODE	70	95	90	35	58
CATHODE / ANODE	58	71	68	>100	>100
CATHODE / ANODE	70	70	68	40	58
CATHODE / ANODE	90	108	100	>100	>100
CATHODE / ANODE	100	100	100	>100	>100
CATHODE / ANODE	111	>150	>150	42.5	>80
CATHODE / ANODE	>150	>150	>150	56.5	59

Table 6

Current (Contact)	Flashover voltage (kV)	
	Experimental	Computational
Ohmic (Gold)	9.5	7.37
Ohmic + Charge Injection (Gold)	6.5	6.7
Charge Injection (No Contacts)	18	18.16

Specimen	Surface finish		Cleaning	Other
	Contact	Cylindrical		
#1	chemo	etch	water	—
#2	mech	etch	water	—
#3	chemo	etch	RCA	—
#4	chemo	chemo	RCA	—
#5	chemo	chemo	RCA	oxidized

Table-7.   Summary of Specimen Surface Preparation

TABLE 8
Luminosity and Breakdown inception voltages
(Voltages are in kV)

specimen	contact finish	V_{iL}	V_{i2}	V_{i3}	Comment
#2	mechanical	4.0	8.0	13	water cleaned
#1	chemo	4.0	14.5	22	water cleaned
#3	chemo	11.5	22	25	RCA cleaned cylindrical surface
#4	chemo	10.5	26.5	33	chemo-mech. Polished + RCA
#5	chemo	23	-	23	same as #4 and oxidized

V_{iL} : Luminosity inception voltage
V_{i2} : Phase II inception voltage
V_{i3} : Phase III inception voltage

PHOTOCONDUCTIVE SWITCHING AND BREAKDOWN
INVESTIGATED WITH ELECTRO-OPTIC IMAGING

William Donaldson
Laboratory for Laser Energetics
250 East River Road
Rochester, NY 14623-1299

PHOTOCONDUCTIVE SWITCHING AND BREAKDOWN
INVESTIGATION WITH ELECTRO-OPTIC IMAGING

W. Donaldson

LABORATORY FOR LASER ENERGETICS
University of Rochester
250 East River Road
Rochester, NY 14623-1299

INTRODUCTION

The goal of this program was to develop diagnostic techniques for measuring electric fields on the surfaces of semiconductors to identify the mechanisms leading to surface breakdown. The primary diagnostic that was employed relied on the Pockels effect which mixes the electric field on a semiconductor surface with that of an incident optical pulse in a nonlinear crystal, rotating the polarization of the optical pulse. This rotation can be detected and used to extract the surface electric field. Since the optical probe pulse has a duration of 100 ps (the sampling time of the measurement), this technique has very high bandwidth. This diagnostic allows us to study the physics of semiconductors subjected to high fields. The results of this research should aid in developing techniques for the reduction of surface breakdown on solid-state switches and an understanding of the physics of photoconductive switches of potential use for SDIO-directed energy weapons.

The simultaneous requirements of speed and high voltage capability can place narrow constraints on the pulse power switches. Optimizing both of these performance parameters results in significant electric fields between electrodes, possibly leading to surface breakdown. A particularly interesting class of such high-power switches, semiconductor photoconductors, have become increasingly useful for pulsed-power applications where high voltage must be switched on a short time scale. Photoconductive switches can switch tens of kilovolts with picosecond rise times. A variety of devices make use of the high-speed, high-voltage devices. They have been used for microwave

1

generation, in Pockels cell drivers, and in innovative accelerator designs.[1,2] Although various semiconductors have been investigated for use as switches, Silicon and GaAs are the most popular materials for use in high-power photoconductive switches. GaAs is particularly suited for high-voltage switches as its high resistivity ($\rho > 10^7$ Ωcm) makes it less susceptible to thermal runaway than the more conductive Si. This is very important, as the electric field, and therefore, the leakage current between electrodes on a semiconductor photoconductive switch can be significant at field strengths of 10–50 kV/cm. A more significant concern is that the switches will preferentially breakdown along the surface between electrodes at these field strengths. Surface breakdown is the primary failure mode for photoconductive switches and places a limit on their operation. It would be advantageous to approach the bulk breakdown threshold of 200 kV/cm. The threshold voltage for surface breakdown is the maximum operating voltage for a photoconductive switch. This problem is compounded by the need to shorten the electrode gap to increase switching speed, thus increasing the electric field across the switch for a given bias voltage. Engineering considerations, such as the need to improve switch reliability, and the desire to explain certain physical phenomena associated with high-voltage switching, have motivated the investigation of the dynamics of photoconductivity. Despite their relevance to switch engineering, the mechanisms of surface breakdown and photoconductivity are not well understood. A detailed measurement of the surface electric field between the electrodes would be very useful in studying the phenomenon of surface breakdown.

To better understand the physics of photoconductivity and surface breakdown, it is necessary to monitor a photoconductive switch during the switching and breakdown processes. This is usually done by looking at the switched output waveform with a conventional or sampling oscilloscope. However, for switching speeds on the order of a picosecond, oscilloscopes do not have sufficient bandwidth to temporally resolve the switch rise time. Temporal resolution is greatly improved if the switched output is sampled electro-optically. This is a technique that uses optical probes to measure fast electrical

2

transients.[3] Briefly, the birefringence of an electro-optic crystal, placed in the vicinity of an electronic circuit, is modified by stray electric fields surrounding the circuit. The electric field can be measured by probing the electro-optic crystal with a fast, polarized optical pulse and monitoring the change in polarization. The duration of the optical pulse determines the bandwidth of the system. This technique has been used to measure the picosecond and subpicosecond response of electronic devices.[4] (The effective bandwidth of the electro-optic sampling technique is limited to about 1 THz due to absorption in the electro-optic sampling crystal.) The switched output transient behavior can be measured and temporally resolved using electro-optic sampling. Such a measurement of the output waveform yields information about the temporal evolution of the voltage at the output electrode of the switch, but gives no information about the evolution of the electric field within the electrode gap itself. The electric field in the contact gap must be changing rapidly in both time and space. By combining electro-optic sampling, short-pulse lasers, and imaging technology, an ultrafast, 2-D, electro-optic imaging system was developed that can monitor rapid variations of the electric field over an extended region. This system can produce maps of the surface electric field between contacts on photoconductive switches that can be used to determine the electric field configuration for different contact shapes, separation, and preparation. Electrodes can be designed to minimize surface breakdown and, hence, maximize switch operating voltage. Moreover, the surface electric field is related to the internal field in the semiconductor because the tangential component of the electric field is continuous across a dielectric interface. The internal field is modified by the presence of carriers in the contact gap. Thus, surface field imaging can be used to investigate the behavior of charge carriers within the semiconductor.

The physics of photoconductivity can be studied by monitoring the influence of photogenerated carriers on the surface field. Switch performance parameters, such as switching efficiency, carrier transport, and switching speed, were measured by this optical technique. In addition, the formation of a surface arc during breakdown can be observed

3

through its disturbance of the electric field in the gap. Surface field maps could also be useful in the design of other high-field devices, not just photoconductive switches. Integrated circuits, while low bias devices, require contacts to be closely spaced resulting in high fields between electrodes. Surface field maps of entire LSI circuits could be obtained with the electro-optic imaging system and be used to pinpoint possible breakdown points.

The work on this project progressed through an number of phases. The first requirement was to show that surface fields could be mapped with the electro-optic sampling technique. Thus we looked at static fields to see geometric and contact effects. The next phase was to show that the field could be imaged with a detector array rather than a single detector. This allowed the mapping of multiple spatial events with a single laser pulse. Finally, the system was upgraded to use 2-D detectors and single-shot imaging. The dynamics of both photoconductivity and surface breakdown were measured.

MEASUREMENT TECHNIQUE: STATIC 2-D AND DYNAMIC 1-D IMAGING

An electro-optic crystal placed in the fringing electric field above the semiconductor surface experiences a change in its birefringence as a function of the electric field. The change in the birefringence is monitored by probing the crystal with polarized light as shown in Fig. 1. The light passes through a polarizer; a wave plate, to provide an adjustable bias to the transmission; the electro-optic (e-o) crystal; and then reflects off a dielectric mirror to retrace its path. Because of the wave plate and the static birefringence of the e-o crystal, the polarizer is effectively crossed with respect to itself. This effect can be viewed as the mixing of a dc electric field and an optical field in a crystal to produce a new optical field with its polarization rotated with respect to the original optical field. When the crystal is placed between crossed polarizers, the transmission is given by:

$$T = \sin^2\left\{ [(K E \ell) + \phi]/2 \right\} \qquad (1)$$

where E is the magnitude of the dc electric field; ℓ is the optical path length through the crystal; ϕ is a constant optical rotation due to the wave plate and static birefringence of the crystal; and K is a constant that depends on material parameters, the crystal orientation, and the frequency of the optical field.[5] By choosing the type of crystal and its orientation, the Pockels effect can be made sensitive to only one spatial component of the applied electric field.

A dielectric mirror is bonded directly to the e-o crystal and the entire assembly is placed directly on top of the surface to be monitored. The surface typically has two rectangular electrodes separated by a fixed distance. The e-o crystal was $LiTaO_3$. Its optic axis was perpendicular both to the direction of light propagation and the edges of the electrodes. Thus the optic axis was orientated along the electric field lines and the Pockels effect was sensitive to only the component of the electric field perpendicular to the electrode edges.

The principle assumption of this work is that the measured electric will not be uniform over the surface being measured. The initial measurements investigated the low voltage quasi-static configuration of the surface electric field. A piece of $LiTaO_3$ was placed across evaporated metal contacts on both silicon and gallium arsenide. A time varying potential was placed across the contacts that induced a modulation of the birefringence of the $LiTaO_3$ in both space and time via the Pockels effect. A tightly focused cw HeNe laser, with a spot size of approximately 40 μm, probed the change in birefringence. The spatial profile was obtained by translating the e-o crystal and semiconductor such that different points were illuminated by the laser beam. The low voltage applied to these devices produced very weak modulation of the the optical signal requiring that the signal be extracted with phase-sensitive detection. This experiment demonstrated that we could spatially resolve the surface electric field on the surface of the semiconductor.

The data acquired as described above had two serious drawbacks. It lacked temporal resolution and required that the beam be scanned across the device to acquire the total spatial variation of the field. Such conditions are incompatible with the need to record spatially non-local, transient events typical of a surface breakdown and photoconductivity. The ability to time resolve events came with the introduction of short-pulse laser probes. A single-light pulse from a frequency-doubled, mode-locked, amplified Nd:YAG laser sampled the electric field only while it traversed the sampling crystal (~150 ps). At field strengths that are comparable with the field necessary to cause the direction of the polarization vector in the sampling crystal to change by one-half wave (~1–10 kV/mm), the image can be acquired with a single optical pulse. Otherwise, the optical modulation would be too weak to be extracted without the aid of extensive signal processing. (A primary requirement of the diagnostic we developed was that it be able to acquire images of a single event.) With short-pulse lasers, it is possible to take 100-ps snapshots of any given event. A series of sequential snapshots, can be taken to record the temporal variation in the field. Thus, we can make a movie of the temporal change in the field.

The spatial variation in the surface field can be monitored by illuminating the entire area of interest. Instead of using a single detector and scanning a tightly focused spot, a detector array captured an image of the entire field of interest, which increased the speed of data acquisition. Each detector element measured only a small portion of the electric field. The initial experiment was done with a 512-element, linear-intensified diode array. A 2-mm gap with identically prepared gold-coated, laser-annealed contacts on intrinsic silicon (7000 Ωcm) was pulsed biased with a short electrical pulse synchronized with respect to the laser pulse. The sample was illuminated with a 120-ps, 532-nm light pulse at the peak of the voltage pulse. A 50-Ω load was placed on the low side of the silicon and the leakage through the material was monitored. The lack of photoconductive switching at the load guaranteed that none of the light coupled through the dielectric mirror into the silicon. It is important that the probe light does not perturb the field. The laser illuminated a circular

6

region on the silicon surface. The detector acquired a 1-D slice of the electric field on a line joining the two electrodes midway between the ends of the electrodes. This was the first demonstration of imaging technology applied to electro-optic field measurements. Initially, the electric pulse was applied with conventional electronic devices giving a quasi-static measurement. Later the electrical pulse was applied with a second photoconductive switch to give better time resolution.

ANALYSIS OF EARLY EXPERIMENTS

The static electric field distribution produced by the coplanar electrodes used in these experiments was not uniform. It is a common field configuration encountered when fabricating devices on wafers (e.g., coplanar transmission lines between transistors in VLSI circuits or photoconductive switches fabricated on wafer substrates). The field lines in a plane perpendicular to the surface are shown in Fig. 2(b). They may be derived from the simple case illustrated in Fig. 2(a) by the operation of the conformal transformation[6]:

$$z = 2 \ln\left(\left\{ [1 + \sin(w)]^{1/2} + [b_z + \sin(w)]^{1/2} \right\} / (b_z - 1)^{1/2} \right) . \qquad (2)$$

Followed by the second transformation:

$$z' = wd - \ln\left(\left\{ [1 + \sin(iz + \pi/2 - iw_g)]^{1/2} + [b_z + \sin(iz + \pi/2 - iw_g)]^{1/2} \right\} / [b_z - 1]^{1/2} \right). \qquad (3)$$

Where:

$$b_z = 2 \coth^2(\pi \, l_c / 2 \, l_s) - 1 = \sim 1 , \qquad (4)$$

w_g is the normalized gap width; l_c is the electrode length; and l_s the substrate thickness.

These transformations fold the electrode end faces out into the coplanar geometry. The second transformation is only valid if the transformed plane is at infinite distance from the first plane because the electric field lines must be normal to the second plane. However, if the electrodes are sufficiently far apart, the deviation from normal incidence is

7

negligible. The transformation defines the expected value of the electric field throughout the volume of the semiconductor provided that the measurement is not taken near the corners of the electrodes. The fringing field outside of the semiconductor can be inferred from electromagnetic theory (i.e., the surface electric field is continuous across a dielectric interface). Thus the coplanar electrode configuration provides a reasonable test of our ability to map electric field configurations.

From the known electric field configurations in Fig. 2(a), the electric field in Fig. 2(b) can be calculated. For the type of e-o crystal that was used in this experiment, the electric field along the y axis in Fig. 2(b) was measured. Figure 3 shows the field in the plane of the interface. The features are exactly as expected. Above the contacts the electric field is normal to the surface; therefore, the field along the y axis is zero. At the edge of the contacts the field lines bunch-up due to the attraction of charges on the opposing electrodes. However, this is not what is actually measured. What is actually measured is:

$$\int_{IA} \int E_y(x,y)\partial\ell\partial A \qquad (5)$$

This integral (ℓ) is over the thickness of the e-o crystal and is clearly dependent on that thickness. Figure 4 shows the integrated detected signal as a function of the e-o crystal thickness. The uppermost curve indicates what happens if the crystal is so thick that the integral extends over all the field lines. The surface features are completely obscured because the total integrated flux is conserved between the electrodes. Alternatively, if the crystal is too thin, then the modulation imparted to the light signal becomes very small, since the amount of rotation is proportional to the optical path length in the crystal. However, the high dielectric of the e-o crystal will trap most of the field lines, reducing the peaking of the contacts. Additionally, smearing of the detected signal is also incorporated

into the calculation of the curves in Fig. 4. The signal must be averaged over either the laser spot size or the size of the detector element on which it is imaged. In Eq. (5) this is represented by the integral over the illuminated area (IA).

The usefulness of this technique has been demonstrated at low voltage where the preparation of the contacts on the semiconductor has been shown to influence the dc electric field distribution. This is the work that was done with the cw probe and the phase sensitive detection. The primary purpose of the cw experiments was to demonstrate that we could detect spatial variations in the field. The electric field was essentially dc (actually a low frequency, 1 kHz, square wave). In addition to demonstrating the ability to monitor surface fields, the experiments proved to be a reliable method of characterizing the contacts. Figure 5 shows a cross-sectional view of the field along the center line between the contact pads on GaAs. The figure shows the general features that are expected, the bunching at the contacts, and the tailing off at the electrodes. The sampling crystal was thick with respect to the electrode separation. Therefore, the peaks exhibit a significant amount of smearing. What is most interesting is the asymmetry of the electric field. The contacts were identically prepared, so no asymmetry was expected from the material properties of the sample. When the polarity of the applied bias was reversed, the asymmetric field distribution also reversed. This indicated the contacts were not ohmic with respect to the different carrier species (electrons and holes). It was also noted that as the contacts became more ohmic, the peaking at the edges decreased. Semiconductors, with their mobile charge carriers, that can move in response to the applied field, would not be expected to ridgely conform to the field distribution described above. The cw data also showed that a full 2-D map of the electric field could be acquired. Figure 6 is an 3-D plot of the electro-optic image of the electric field on a silicon switch.

Time-resolved data was taken to determine the time scale on which the asymmetry illustrated in the cw data evolved. The data was taken by grounding one of the electrodes on a sample prepared on high-resistivity silicon ($\rho = 7$ kΩcm). The dielectric relaxation

9

time of this material is given by the product, $\rho\varepsilon$, where ε is the dielectric constant of the silicon. Thus on time scales <7 ns we expect to see transient behavior of the silicon in response to an applied electric field. A photoconductive switch was used to pulse bias the test structure on a 100-ps time scale. One electrode was grounded and the other was attached to a terminated 50-Ω line driven by a photoconductive switch. The switch was triggered with a 1.06-μm light pulse from a Nd:YAG regenerative amplifier. A 0.532-μm pulse, derived by frequency doubling a portion of the 1.06-μm pulse, probed the LiTaO$_3$ crystal on the second photoconductive gap, which was not triggered. An optical delay line in the path of the 1.06-μm light provided a variable time delay between the voltage and probe.

The optical image of the electric field was measured with a gated diode array at various time delays between the pump and probe. Figure 7 shows three traces of the surface electric field of a device with a 2-mm gap pulsed with a 1-kV voltage pulse at various time delays. The units of vertical axis are in percent modulation of the light signal (i.e., the signal obtained with the voltage on, minus the signal with the voltage off, divided by the signal with the voltage off). Thus the acquired signal was relatively immune to variations in the illumination profile. At very early times (A), very little voltage has built up but the device appears to be symmetric in response to the electric field. Curve (B), 166 ps later, shows that a significant voltage has built up across the device and the field is still symmetric. At 166 ps later still (C), the voltage is still rising but the field shows a definite asymmetry. The simple explanation of this data is that at early times the electrical inertia of the silicon prevents it from reacting to the field. The device then behaves as if it were a perfect dielectric, and the field rises symmetrically on both electrodes. Later, as the charge carriers in the silicon begin to rearrange in response to the field, the field itself is modified by the charges in the silicon.

Although the applied fields were less than those necessary to cause breakdown, some features about the semiconductors could readily be discerned from the electro-optic

imaging data. The contacts were asymmetric with respect to the applied voltage. With some combinations of materials and contact preparation, one contact had a higher field enhancement at the edge than the other. The enhancement shifted as the polarity of the applied voltage reversed. Such field enhancements are probably due to differences in the injection of holes and electrons at the contacts. They may play an important part in initiating breakdown. Also, the field profiles were undoubtedly affected by the uniformity of probe illumination. This problem has been dealt with in the 2-D imaging system described in the next section.

2-D ELECTRO-OPTIC SAMPLING

The logical extension of the earlier single-point, time-averaged, and 1-D time-resolved probes has produced the current 2-D, time-resolved electro-optic imaging system which can obtain surface field maps in real time with picosecond temporal resolution.[7,8] If the probe beam only illuminates a small portion of the crystal, the electric field only in that region will be measured. If the entire crystal is illuminated by the probe beam, the electric field at every point in the crystal will be interrogated. The probe beam will then be imprinted with an optical analog of the spatial electric field distribution in the crystal. Spatial variations in the field can be recorded with a video camera without requiring translation of the sampling point across the crystal. This is the essential operating principle of the 2-D electro-optic probe. The electric field in the crystal is sampled only when the probe pulse is present. In effect, the electric field is "frozen" by the probe "strobe" so that a snapshot of the instantaneous electric field is taken. Two different probe geometries were used and the pump/probe roles of the fundamental and second harmonic of Nd:YAG could be reversed. Figure 1 shows the surface field probe set up to measure the field of a photoconductive switch of a surface device type, i.e., the metallic contacts are in the same plane on the surface of a semiconductor substrate. Figure 8 shows the probe set up to measure the field of a bulk photoconductive switch, which has contacts on opposite faces

11

of a rectangular slab of a semiconductor. The geometry shown in Fig. 8 had the advantage of a much simpler (i.e., spatially uniform) field distribution. For either type of switch, probe operation is the same, only the IR pump geometry is different. When a bias voltage is applied to the metallic contacts, an electric field is established between the contacts. There is a fringing field which extends above the surface of the semiconductor. The e-o crystal is placed directly on top of the switch, covering the contact gap completely. The crystal is immersed in the fringing electric field of the contacts above the surface of the semiconductor, and its birefringence is altered by this surface field. The optical probe is polarized and directed onto the crystal and test switch. The probe beam diameter is greater than the contact gap so that the entire contact gap is illuminated. The beam traverses the crystal and is reflected back onto itself by the dielectric mirror on the semiconductor side of the crystal. While the probe beam is in the crystal, the beam's polarization is modulated by the electrically induced crystal birefringence so that the polarization of the back-reflected beam is altered with respect to the incoming beam. Any component of the back-reflected beam with polarization different from the incoming beam will be rejected by the polarizer. Each point in the rejected beam has sampled the local birefringence of the corresponding point in the crystal. Thus, the intensity of the rejected beam is an optical replica of the electrically induced birefringence pattern in the crystal. The back-reflected beam is imaged onto a 2-D diode array that records the back-reflected beam's intensity profile. Each pixel in the array image has a corresponding point in the crystal. As the optical probe makes a double pass through the polarizer, the crystal can be considered to be between two crossed polarizers. The second polarizer is crossed because of the action of the $\lambda/4$ plate and the LiTaO$_3$ birefringence. The intensity at any given point in the cross section of the back-reflected beam will depend on the sine squared of the polarization rotation experienced by that particular beam element as it traverses the crystal. The transmission to a detector element (i,j) can be written:

$$T_{ij}(V) = I_{ij}(V)/I'_{ij} = \sin^2\left[(\alpha_{ij}E_{ij} + \beta_{ij})\right] \qquad (6)$$

where $I_{ij}(V)$ is the light intensity measured at camera pixel (i,j) when a voltage V is applied to the electrodes; I'_{ij} is the intensity that appears at the camera if 100% of the light is imaged onto the camera without bias voltage applied; E_{ij} is the magnitude of the local electric field; α_{ij} is a constant for a given point (i,j) which relates the electro-optic coefficient[5] to the local electric field and whose value depends on material parameters, optical path length in the crystal, electrode geometry, and frequency of applied optical field; and β_{ij} is a constant optical rotation due to static birefringence in the crystal and $\lambda/4$ wave plate. The $\lambda/4$ plate chooses where the probe beam sits on the sine-squared transmission curve with no voltage applied. By comparing the intensity at the camera with and without voltage applied, the rotation due to the electric field can be determined. This is a much more sophisticated procedure than the simple percent modulation done with the earlier work.

α_{ij} is determined by taking a series of images at fixed voltages and fitting them to Eq. (6). The e-o crystal used was y-cut $LiTaO_3$ that was 0.5 mm thick. It was cut to completely cover the contact gap of the switch being studied. The top surface of the $LiTaO_3$ was antireflection coated to prevent spurious back reflection and improve transmission through the crystal. The bottom surface was coated with the a dielectric mirror that had a reflectivity of 99.3% at 532 nm. A conventional oscilloscope attached to the load side of the switch studied revealed that the green light caused a voltage pulse equal to about 10^{-6} times the applied bias voltage to be switched to the load. This is negligible: the probe effectively does not excite the switch. The $LiTaO_3$ optic axis (z axis) was perpendicular to the contact edges and parallel to the applied electric field. In this geometry, the crystal is sensitive primarily to the electric field component parallel to the $LiTaO_3$ optic axis. The complete probe system is shown in Fig. 9.

13

The laser source is a Nd:YAG regenerative amplifier seeded by a Nd:YAG mode-locked oscillator with a wavelength of 1064 nm and a pulse width of 150 ps. The mode-locked pulses are amplified to approximately 300 µJ and switched out of the laser with a double Pockels cell arrangement to yield pulses that have a prepulse to main pulse contrast ratio of at least 4000:1.[9] The pulse repetition rate is 30 Hz. The infrared beam from the amplifier is first upcollimated and then split, 90% for switching use and 10% for second-harmonic generation. This green beam is upcollimated and serves as the probe beam. The green beam diameter is 1.25 cm, which completely illuminated the electrode gaps that were studied. The back-reflected green probe beam pulses are imaged onto a 512 x 512 element CID camera. The CID camera is interfaced to a personal computer through a video frame grabber supplying a digital image of the modulated probe beam. Images are digitized with 8-bit resolution. The camera response was measured to be linear with applied light intensity over the range of intensity used in this experiment. As the green probe was only 140 ps in duration, the switch surface field is sampled only during a short window in time. If an infrared excitation pulse illuminated the switch during this window, the switch field could be sampled during the photoconductive collapse. For surface switches, as in Fig. 1, this is accomplished by directing a pump pulse onto the switch gap collinear with the probe pulse. The surface switches can be studied with both the IR pump with a visible probe and the visible pump with IR probe. Sampling crystals with different coatings were used as were the relative amounts optical energy directed to the second harmonic crystal. For the bulk switches, the infrared illuminates the switch directly through the metallic mesh contacts. By sweeping the 140-ps sampling window through the photoconductively induced event, the switch surface field can be monitored as it evolves in time. This is actually 512 x 512 separate, parallel pump-probe experiments, each probing a different spatial region in the electrode gap. The sampling window is moved in time by changing the length of an optical delay line in the pump beamline. As the pump and probe are derived from the same laser pulse and timed optically, there is no jitter.

14

For the probe to operate in real time, i.e., without averaging, data must be collected with a single laser pulse. As the system operates in the high-field regime, the electric field applied to the e-o crystal causes the optical polarization vector of the probe pulse to change by a significant fraction of $\pi/2(>2\%)$. At these fields, the change in transmission to the camera is large with respect to the shot-to-shot noise in the laser pulse. Thus, the electro-optic images can be acquired without averaging. This is essential to image random events such as surface breakdown. To ensure that the camera sees only one laser pulse, the camera and laser are synchronized to the same electronic oscillator, with a pulse from the camera triggering the firing of the laser. The overall energy of every laser pulse is measured with a fast diode. Any pulse that is not within 10% of a reference value is rejected and the measurement is repeated.

The field data must be extracted from the raw camera image. The values of α_{ij} and β_{ij} for each point (i,j) must be determined so that given the transmission T_{ij}, the field E_{ij} can be determined. The crystal is not illuminated uniformly because the probe beam has a Gaussian spatial profile. This must be considered in the analysis of the data. Therefore, before the field can be determined, the raw image must be normalized with respect to the beam profile, so that the transmissivity and not the transmitted intensity is used.

To calculate the transmissivity, each image acquired by the camera is normalized to a stored reference image. This reference image is the average of four frames taken with the quarter-wave plate set for maximum transmission. The light intensity is adjusted so that the most intense pixel is just within the 8-bit camera resolution; i.e., no points in the detector field are saturated. This reference image contains I'_{ij} for each point (i,j), as in Eq. (6). Images normalized with respect to this reference are scaled to the maximum signal and represent $I_{ij}(V)/I'_{ij}$.

The values of α_{ij} and β_{ij} are obtained by calibrating the response of the probe to applied electric field. A quasi-dc, i.e, long compared to the light pulse, bias voltage is applied to the contacts by a computer controlled high-voltage pulser. The amplitude of the

15

applied voltage pulse is well below the breakdown threshold. The initial data that was taken with the 2-D imaging system was reduced to a 32 x 32 format by averaging over pixels. This array size reduction is done so that image acquisitior., processing, and display can be done with a PC rather than a workstation and in real time, i.e., without any post-processing. This allows for rapid scanning of camera images. The bias voltage is varied from 0–9.5 kV in 500 V increments. An image was taken at each voltage. The transmission curve [Eq. (6)] for each of the 1024 elements of the reduced image was determined experimentally by this procedure. α_{ij} and β_{ij} were obtained by performing a least squares fit of the experimental transmission curve to Eq. (6) for each element in the reduced image. Figure 9 shows this dc calibration for one element of the reduced image. The biasing is chosen such that all points lie within one-half cycle of the transmission curve. Due to the sinusoidal nature of Eq. (6), it is sometimes necessary to reduce sensitivity to see large effects. The current system takes full 512 x 512 images at 4 voltage settings and uses that data to calculate the least squares fit.

After correcting for the probe beam spatial profile and calibrating the crystal response, the surface electric field information can be decoded from the raw images from the camera. To measure the field, a frame is first acquired with high-voltage bias on and then with the bias off. The images are scaled by cross-referencing the raw image pixel (with voltage on) value and the corresponding reference pixel (voltage off) value and using a look-up table to determine the scaled image pixel value. The zero bias image is used to remove the contribution of the static birefringence, β_{ij}. The lookup table associates each pair of points in the reference and voltage images with a value corresponding to the product $\alpha_{ij}E_{ij}$. The scaled pixel image is divided by α_{ij}, as determined by the dc calibration described earlier, to yield E_{ij}. The field, E_{ij}, is given in units of "equivalent electrode voltage," or EEV, which means that the ρoint (i,j) is responding to the applied electric field as if a voltage E_{ij} were applied to the electrodes. Although the electrode bias voltage may be constant, the local field E_{ij} may be nonuniform due to the presence of carriers or

16

bending of field lines due to the geometry of the electrodes. An underlying assumption of this work is that the field between the contacts will be nonuniform. The resulting field map of the electric field has an 8-bit range and can be displayed as a false-color image on a monitor or the digital image can be manipulated to produce field contour plots, 3-D plots, or field cross sections at a particular line across the switch. The optical system is capable of producing images with a spatial resolution of 3 μm per pixel. Therefore, the electric field can be measured with this type of spatial resolution. It requires that the above calibration procedure be applied to the entire 512 x 512 array. The minimum electric field sensitivity is approximately 200 V/cm and can be adjusted by rotating the quarter-wave plate before the LiTaO$_3$.

CHARACTERIZATION OF PHOTOCONDUCTIVE SWITCHING

Silicon and GaAs photoconductive switches have been studied with the majority of the work done with GaAs. The Si switches are surface devices, as in Fig. 1. The GaAs switches are bulk devices, as in Fig. 7, as well as surface devices. Figures 10 and 11 show typical raw, unnormalized, field images obtained with the electro-optic imaging system. Figure 10 shows successive lineouts of the surface field over a 3-mm gap Si switch taken through the center of the switch parallel to the contact edge. The switch gap has been illuminated by the IR pump pulse. Time is relative to the position of the IR optical delay line. The surface electric field begins collapsing at the onset of photoconductive switching and has collapsed completely within 300 ps, consistent with the ~200-ps pulse width of the laser. Figure 10 illustrates the ability of the system to monitor the surface field in the switch gap during switch operation, and the ability to measure switching parameters like switch rise time, using the field across the electrode gap. The field collapse is spatially uniform. This is typical of the imaging we saw in silicon. The field collapses as the light pulse is applied and shows no oscillation or recovery. Figure 11 shows the result of nonuniform IR illumination on the Si switch surface field. The center of the switch gap

17

was illuminated with a pinpoint (~40 μm) spot of infrared laser energy. This local illumination photogenerates carriers only in a small region at the gap center. These carriers migrate outward, collapsing the surface field as they drift. Figure 11 illustrates that ability of the system to map nonuniform fields and to observe carrier migration within the switch gap. One significant feature of the field on the coplanar silicon switch is that we have not detected the significant field enhancements at the contact edge we would have suspected from the geometry. This may be due to a number of factors including: the presence of ohmic contact, the conductivity of the substrate, and the averaging of the dielectric crystal.

The primary physical system investigated was the collapse of the electric field in a GaAs photoconductive switch both bulk and planar. GaAs has a band gap of 1.42 eV. Photoexcitation of an electron into the conduction band with the IR pump (λ = 1064 nm, 1.17 eV) is due to the mid-gap donor EL2. At 532 nm, the excitation is direct band-to-band electron-hole generation.[10] The bulk switches were fabricated by the U.S. Army Electronic Technology and Device Laboratory by depositing circular contacts of NiAu:Ge on opposite faces of a blocks of intrinsic GaAs 0.6 to 1 cm thick. The GaAs was high resistivity material ($\rho \sim 10^7$ cm) supplied by MA-COM. The absorption coefficient was measured to be 1.39 cm^{-1} at 1.06 μm. The center region of the contact was perforated with holes to allow light to pass through into the bulk of the GaAs. This resulted in a nonuniform carrier density profile that decreased exponentially across the switch. The contact preparation was also varied with the 6-mm thick switches having an ion implantation under the metallization to make ohmic contacts; the other samples had contacts deposited on bare GaAs. Skin effect conduction may be ignored. This switch design is of interest for its applicability to the coaxial geometry[11] and for its relative immunity to surface breakdown, because a surface arc must travel out to the edge, down the side and back into the center—a very long physical path. This design is also useful because parallel contact geometry allows for uniform fields which facilitate extraction of absolute field values. The coplanar geometry, by contrast, has a much more complicated field pattern.

18

To access the fields between the contacts, this design has been modified by cutting the GaAs in a plane passing through the center of the contacts. Connection to the external circuit was made by pressure contacting copper electrodes coated with indium along the outside circumference of the NiAu:Ge electrodes. The Cu electrodes were bored out so that IR light could reach the switch contacts. By placing a dielectric beam splitter in the IR pump beam, approximately 50% of the IR light could be directed onto each electrode. Either of these beams could be blocked to investigate asymmetries in the response of the photoconductor. The arrival time of the two beams at the switch was adjusted to within 300 ps by monitoring the arrival of the switch pulse at the load with a 1-GHz analog oscilloscope. The dielectric beam splitter was mounted on a kinematic mount so that it could be removed and the full IR laser energy could be applied to one side of the switch. Thus, five illumination schemes were employed, considering that full energy could be applied to either the ground or high-voltage contact.

Figures 12–15 show data taken for a 6-mm-thick ion-implanted GaAs bulk switch. The images taken were normalized and scaled to equivalent electrode voltage (EEV). Figure 12 shows a 3-D plot of the surface field on a 6-mm GaAs switch illuminated through both contacts 800 ps after initial illumination. Outside the region between the contacts, the field falls abruptly to zero because there is no tangential component of the electric field at the surface of a conductor. Noise spikes in that region of the image have been artificially suppressed. The left edge of the image corresponds to the negative high-voltage contact, and the right side to the ground contact. The active area in the center is 6 mm wide, and the front and back edges of the image are 10 mm apart and correspond to the edges of the deposited electrodes. Initially, the image was uniform between the contacts. The infrared light has caused the field to collapse. The center section of the image is where the 2-mm-wide pump beam illuminated the GaAs. Note that the field has collapsed over most of the active region to a value of ~0.3 kV EEV, although the bias voltage is 5 kV. The field collapses uniformly on the ground side of the image but it has

areas of significant enhancement on the high-voltage side. There are two significant high-voltage spikes of ~3 kV EEV even though most of the switch field has collapsed. These spikes are located at the very edges of the high-voltage contact [review Fig. 7 for contact geometry]. A survey of all the images that have been acquired reveals that this is a general feature independent of the type of contact. There is always an enhancement at the high-voltage contact. The enhancement can be alleviated at the perforated region of the contact by illuminating with more IR light but the collapse is never as complete as on the ground side.

Figures 13 and 14 show a series of axonometric plots of the field above a 6-mm GaAs switch. These illustrate the progressive collapse of the surface field in time for two different bias voltages. Both contacts were illuminated with IR. In Fig. 12 the switch bias was 5 kV; in Fig. 13, 9 kV. The field is given in EEV; the true field is EEV divided by the gap distance, which in this case is 6 mm. The time is relative to the IR translation stage position; 0 ps is ~200 ps before the arrival of the IR pulse and the stage can scan out to 1 ns after IR illumination begins. At 0 ps, the field across the switch is essentially uniform, as expected. As time progresses, the field collapses. For 5 kV bias, the collapse is almost complete, except for the enhancement near the contacts. At 9 kV, the situation is much different; the field collapses only to 3 kV EEV. There is still a field of ~3 kV/cm across the switch, 1200 ps after illumination.

Figure 15 shows a series of lineouts from surface field images of the 6-mm GaAs switch, taken through the center of the image, perpendicular to the contact faces. These illustrate the progressive collapse of the surface field in time for various illumination schemes. Switch bias was 8 kV. Single-side illumination is characterized by a wave front that propagates across the switch. In Figs. 15(a) and 15(b), the field collapses from the illuminated contact to the nonilluminated contact in time as the region of conduction propagates from the region of photogeneration. In Fig. 15(c), both sides were illuminated. For both-side illumination, the field collapses more quickly and to a lower final value than

20

for single-side illumination, as in Figs. 15(a) and 15(b). The rise time is faster and the efficiency is higher for illumination through both contacts. This is an important engineering consideration. The field enhancement exhibited in Figs. 12, 13, and 14 can also be observed in these lineouts.

Some of these observations can be made more quantitative by defining an electro-optic switching efficiency. A standard measure of switching efficiency would be what fraction of the dc bias is switched to the load. A perfectly efficient switch would be driven completely conductive and the bias voltage would appear across the load. No electric field would remain across the switch electrodes. The electric field across the switch can be imaged electro-optically, and an electro-optic switching efficiency, η, can be defined:

$$\eta = \sum_N \eta_{ij} = (1/N) \sum_N \left[E'_{ij} - E_{ij}(t) / E'_{ij} \right], \tag{7}$$

where the summation is over the total number of active pixels (pixels outside the electrode gap have been ignored); E'_{ij} is the electro-optic image element with no IR light present; and $E_{ij}(t)$ is the electro-optic image element at a time delay t as determined by Eq. (7). The restrictions on the summation are that if

$$0 > E'_{ij} - E_{ij}(t), \tag{8}$$

corresponding to a field enhancement, η, was set equal to zero (i.e., it was considered to be an element that had not undergone switching) and if

$$E'_{ij} - E_{ij}(t) > E'_{ij}, \tag{9}$$

implying a negative oscillation in the surface electric field, the efficiency at that point, η, was set equal to one. The parameter, η, is a measure of how much of the dc field has been switched. η would equal the real switch efficiency if it were possible to integrate through

21

the entire switch volume. This is impossible for these experiments. The quantity η tells us what is happening at one plane in a 3-D device. It is difficult to relate quantitatively to the total switched current at the load. However, it is the best available measure we have of the internal dynamics of the photoconductive switch. Figure 16 shows the electro-optic efficiency as a function of the setting of the optical delay line for several applied fields in the case of two-side illumination. The most striking feature of this graph is that the switching efficiency drops as the field increases. Figure 17 shows this trend continues with single-side illumination at two different intensities. In particular, at an illumination intensity of 2.1 mJ/cm^2, there is sufficient light to switch a field of 6.7 kV/cm with 90% efficiency. At the same intensity, a field of 15 kV/cm is switched with only 40% efficiency. Figure 16(a) shows that increasing the intensity to 3.8 mJ/cm^2 increases the efficiency to only 50% at 15 kV/cm. The rise time of the switch also decreases as the light intensity is increased.

PHOTOCONDUCTIVE SWITCHING: LOCK-ON

GaAs surface switches were also investigated using the surface geometry. The principle focus of this work was the investigation of Lock-on behavior in GaAs. In GaAs the photo-generated electron hole pairs should recombine in about 1 ns. This should limit the duration of electrical pulse delivered with GaAs switches. Lock-on is the phenomenon where GaAs switches remain in the conducting state for a long time (hundreds of nanoseconds) after the optical excitation. The bias field has to be greater than a threshold value of 3 to 8 kV/cm depending on the material preparation. Typically, there will be a voltage drop across the switch in this state equal to the gap length times the threshold field. The lock-on behavior has several interesting features. Lock-on can be triggered with very low light levels and it has the potential for producing long duration from GaAs switches. However, lock-on is not well understood and the electro-optic imaging system can explore its physical dynamics.

22

The switches used in this study were supplied by Sandia National Laboratory. They were 2.5 mm wide and had a gap of 2.5 mm. The switches had an electron mobility of 7000 cm^2/volt-sec, an impurity concentration of 10^7 cm^{-3}, and a lock-on threshold of 4 kV/cm. To eliminate any complicating effects due to impurity concentrations the photoconductive switching was done with 532-nm light ,which has an energy greater than band gap. This necessitated converting the optics to interchange the pump and probe. Because lock-on is a phenomenon which occurs several nanoseconds after optical trigger pulse, the measurements were taken out to 6 ns after the trigger.

The measurements reveal a very complicated behavior. If one looks at the electric field averaged over the whole switch, the two distinct patterns emerge. Below the threshold for lock-on, the field collapses uniformly in roughly the full width half maximum (FWHM) of the laser pulse. The rapid collapse is followed by a rapid recovery of the order of a few hundred picosecond followed by a slower recovery to the initial bias field in about 5 ns. This trend is illustrated in Fig. 18. This is the average electric field along a line parallel to contact and through the center of the switch.

Above the threshold for lock-on the behavior is much more complicated. The field collapses and starts to recover as in below threshold case. However, at about 1 ns the begins to collapse again. The second collapse of the electric field across the switch is much slower than first optically induced collapse. It is also not monotonic. An oscillatory structure is superimposed on the decay of the electric field. This second decrease in the electric field is apparently associated with the lock-on state. Oscilloscope traces for a current probe at the output of the switch indicated that conduction through the switch continued longer than would be expected from that determined by the recombination of the electron-hole pairs. Figure 19. which is similar to Fig. 18, illustrates the gross features described above.

This graph reveals only a small portion of the complex behavior of these devices. Figures 20, 21, and 22 show three different electro-optic images at different times after

23

illumination. The images have been manipulated such a dark region in the active switch area indicates the absence of an electric field greater than 2 kV/cm. A white region indicates the presence of an electric field greater than 2 kV/cm. The areas above the metallic contacts have arbitrarily be set to white. Figure 20 shows the electric field at the peak of the photo-induced conductivity. The active area of the switch is uniformly black, indicating complete switching, and the edges of the contacts are clearly delineated. At time beginning about 1 ns after complete switching has occurred the electric field develops an 2-D structure. In some places the field has collapsed and in other places it has increased to values which may even be greater than the original applied field. In Fig. 21, which occurs 1.8 ns after Fig. 20 the electric field is concentrated near the high voltage contact. A region of low field, which could indicate the presence of carriers in the underlying semiconductor, extends out from the low voltage contact. Although the fields are changing everywhere there is a preponderance of images where the electric field is enhances at the high voltage contact. Figure 22 show another state that the field can evolve into. A region of low field or high conductivity extends from the low voltage contact to the high voltage contact. Note that this region is only about 25% of the active area of the switch. This may indicate that the current is being carried in channels through the switch in the lock-on regime. This could seriously degrade switch performance in the long term.

SURFACE BREAKDOWN STUDIES

In the course of testing the 2.5 mm GaAs switches, it was noticed that the switches were damaged by surface arcing at applied voltages above 7 kV. An experiment was set up to observe the surface breakdown. A the sample was biased with a 400 ns, 9.5 kV voltage pulsed that could be at a variable time with respect to the laser pulse. The 532 nm second harmonic was used to probe the electric field. The electric field was probed at times starting from before the voltage pulse was applied to the end of the voltage pulse at 2 ns intervals. Since the switch was breaking down during the voltage pulse, it was hoped that

24

at least one of the electro-optic images would capture the switch in a breakdown event. To guarantee that the switch was not damaged by the arcing, a high-power IR laser pulse illuminates the switch 5 ns after the green light probes the field. This pulse was to truncate the field. There must be some time delay between when the voltage pulse is applied and when the switch breaks down. This time should be of the order of the gap (25 cm) divided by the electron velocity (10^7 cm/sec). This is a few tens of nanoseconds. To verify when a breakdown event occurred, the voltage across the switch and the current through the switch were monitored with a transient digitizer for each shot. Judging for the physical damage induced on the switch surface, arcing did occur. The current probe showed that photo-induced current spike was followed a broader secondary current spike. It was not clear whether the secondary spike was caused by the lock-on effect or surface arc. The carriers in GaAs recombine so quickly, it is possible for the switch to close and re-open before the voltage pulse ended. This would allow a surface breakdown to happen even though the field had been briefly truncate. In either case, the interesting event occurred after the probe pulse had sampled the electric field.

To clarify the situation, a silicon photoconductive switch was placed in parallel with the GaAs. This switch was used to truncate the voltage pulse. Silicon has a long recombination time, therefore it is guaranteed to hold the voltage across both switches at zero after it has been triggered. In this configuration, no secondary current peaks were observed and there was no physical damage due to surface arcs. It is clear that the surface arcs were caused by the optical switching. This is plausible when viewed in the context of the experiments and theory, described below, on photoconductive switches biased just below arcing threshold. There are field enhancements at the contacts and, at least in the experimental case, the enhancements propagate out from the contacts and seem to evolve into current channels. At higher voltages the enhancements will be larger and the channels may constrict more. This could lead to filamentation and the arcing.

ANALYSIS

A number of important features about how GaAs photoconductive switches operate can be discerned from this work. The first is that the electric field is enhanced at the negative high voltage electrode and collapses most slowly there. This type of behavior was seen in both types of contacts tested. Similar behavior has been predicted to occur at both contacts for uniformly illuminated silicon switches with ohmic contacts.[12] The field enhancement, in that case, was shown to be due to rapid carrier sweep-out at the ohmic contacts. In particular, the enhancement was strongest under the solid portion of the high voltage contact. A corresponding enhancement was not observed on the ground side electrode (positive with respect to the high-voltage pulse). The enhancement could be reduced in the perforated region by increasing the light incident on the high voltage contact. This enhancement was seen in all samples and showed some increase with the numbers of shots applied to the sample. Some of the nonuniform enhancement may have been associated with the long term degradation of the contact ($>2 \times 10^4$ shots). The degradation was due to arcing from the perforated region to the solid region of the Ni:AuGe contact. The arcing only occurred if the GaAs was switched.

It was seen that the switching efficiency of GaAs decreased with increasing voltage. Increasing the number of carriers by increasing the IR illumination energy by a factor of ~2 did not significantly improve the electro-optic switching efficiency. This suggested that this was predominantly a field effect. This was confirmed by the observation that, for constant bias voltage, the switching efficiency increased with increasing electrode spacing. The switching efficiency should not be a function of the bias voltage if the mobility is not a function of field. The switch was mounted in a transmission line geometry. The voltage switched to the load, V_L, is given by the expression:

$$V_L = (Z/2Z + r) \ V_{BIAS},$$ (10)

where r is the switch resistance, V_{BIAS} is the bias voltage, and Z is the impedance of the bias and load cables, which was 50 Ω for these experiments. The switch resistance, r, is given by

$$r = \text{(voltage across switch/switch current)} = (El/JA) , \qquad (11)$$

where J is the total current density, l is the electrode gap spacing, and A is the illuminated area of the contact. J can be written $J = ne\mu E$, where n is the density of photogenerated carriers, e is the electronic charge, and μ is the sum of carrier mobility for bipolar conduction carrier mobility. The relative amount of voltage switched to the load, V_L/V_{BIAS}, is then:

$$V_L/V_{BIAS} = Z/[2Z + (l/Ane\mu)] . \qquad (12)$$

There is no explicit field dependence in Eq. (12). Field dependence can only enter through the mobility, μ. Equation (12) can be verified by measuring the current at the load, I_L, versus bias voltage. Since

$$I_L = V_L/Z = [1/2Z + (l/Ane\mu)] V_{BIAS} . \qquad (13)$$

It should be a linear function of V_{BIAS} for a given carrier density (i.e., optical illumination). Figure 23 illustrates results of measurements of I_L versus V_{BIAS} for various optical energies. The linear relationship between I_L and V_{BIAS} is verified for bias voltage up to 5 kV, as shown in Fig. 23(a). Figure 23(b) gives I-V curves for bias voltages up to 9 kV. The I-V curves deviate from linear behavior at high bias (>6 kV): the switch resistance increases as the bias increases. This deviation from linearity coincides with the onset of negative differential resistance (NDR) in GaAs.[13] In the NDR regime, the analysis leading to Eq. (13) does not hold. We should not expect and do not see a continuation of the linearity between voltage and current. It must be emphasized that the measurements of the current shown in Fig. 23 lack the temporal resolution of the electro-

optic sampling. They cannot reveal temporal structure in the leading edge of the pulse. Thus there is at least circumstantial evidence to suggest the observed decrease in switching efficiency with increasing voltage may be due to NDR. Above 4 kV/cm, the electron drift velocity in GaAs decreases as the electric field increases. Since the current is proportional to the drift velocity, this represents an effective increase in switch resistance. This observation has important implications for the use of photoconductive switches in pulsed power applications. In many cases, the trend has been to push the breakdown limit in these devices to achieve the highest switch electrical energy for the minimum optical energy. These results indicate that switches with longer gaps, and lower field may be more efficient in terms of switched voltage to pump energy, at least in the purely photoconductive mode of switching at pulse durations of 1 ns or less.

A computer model of photoconductive switch behavior that is based on the semiconductor device equations has been developed to explore the nonlinear behavior of photoconductive switches. The time-dependent, drift-diffusion equations and carrier continuity equations were appropriately modified to represent a photoconductor in operation. The coupling between carrier drift and electric field is completed through Poisson's equation. The model equations are solved numerically with boundary conditions and operating parameters that are consistent with high-speed switching of a practical, high-voltage, photoconductive switch in an external circuit. High-field, non-linear effects, such as negative differential resistance (NDR) in GaAs, are included in the model. Computer simulations of transient photoconductivity in high-power GaAs and Si switches were done for various bias voltage and optical illumination conditions for which we measured electro-optic images.

MODEL FORMULATION

On the time scale of ultrafast, high-power photoconductive switch operation, picoseconds to nanoseconds, transient photoconductivity is governed by the generation,

28

recombination, and transport of carriers. Hot electron effects, drift velocity overshoot, and other non-equilibrium processes such as inter-valley transfer of electrons are significant on a subpicosecond, or femtosecond time scale, and need not be included in a model of high-voltage switch operation on a picosecond time scale. For example, the carrier mobility, μ, is assumed to have reached its steady-state value so that DC measurements that depend on the drift velocity versus field relationship, e.g., an I-V curve, are valid.

Using the drift-diffusion/carrier continuity model, Iverson has previously modeled photoconductors operating in a non-switching, or small-signal, mode where the potential across the switch does not vary appreciably,[14] and the switching, or large-signal mode, where the bias voltage across the photoconductor is quickly switched to an external load.[12] This photoconductive switching model dealt with large-scale, practical high-power switches, but did not include non-linear carrier mobility. Weiner *et al.* have also presented a solution to the semiconductor equations in high-bias switches for the linear mobility regime.[15] This model did not include carrier diffusion. White *et al.*[16] have constructed a computer model of high-bias photoconductive switching, numerically solving the drift-diffusion/carrier continuity relations, that includes non-linear mobility, but this model deals only with micron-scale device lengths and relatively low bias voltages (< 1 kV) and is not capable of simulating a more realistic, cm-scale device with multikilovolt bias voltage. Sano and Shibata have presented a very complete, 3-D model of ultrafast switches in microstrip lines,[17] but this model is limited to 100 μm size devices and total simulation times of only a few ps by computer memory requirements and results were only presented for a 2.5 V bias voltage. To best knowledge, the model presented here is the first numerical solution of the semiconductor device equations capable of simulating ultrafast photoconductive switches under operating conditions consistent with realistic pulsed-power applications that includes non-linear carrier mobility.

The carrier continuity equations for the electron density, n(r,t), and hole density, p(r,t), are

$$\frac{\partial n(r,t)}{\partial t} = G(r,t) - R_n(r,t) + \frac{1}{e} \nabla \cdot J_n(r,t) \tag{14}$$

$$\frac{\partial p(r,t)}{\partial t} = G(r,t) - R_p(r,t) - \frac{1}{e} \nabla \cdot J_p(r,t) , \tag{15}$$

where $G(r,t)$ is the electron-hole pair generation rate, $R_n(r,t)$ and $R_p(r,t)$ are the electron and hole reduction rates, and $J_n(r,t)$ and $J_p(r,t)$ are the electron and hole current densities. The current densities are given by the drift-diffusion model as

$$J_n(r,t) = e\mu_n(r,t)n(r,t)E(r,t) + e\, D_n\nabla n(r,t) \tag{16}$$

$$J_h(r,t) = e\mu_h(r,t)p(r,t)E(r,t) - e\, D_h\nabla p(r,t) , \tag{17}$$

where E is the electric field, $\mu_n(r,t)$ and $\mu_p(r,t)$ are the electron and hole mobilities, and D_n and D_p are the electron and hole diffusion coefficients given by the Einstein relations as

$$D_n(r,t) = \mu_n(r,t)\frac{kT}{e} \tag{18}$$

$$D_p(r,t) = \mu_p(r,t)\frac{kT}{e} . \tag{19}$$

$\mu_n(r,t)$ and $\mu_p(r,t)$ are functions of space and time through the field dependence of the mobility.

The total charge density, $\rho(r,t)$, is given by the sum of the electron and hole densities as

$$\rho(r,t) = e[\, p(r,t) - n(r,t)] . \tag{20}$$

The electric field, $E(r,t)$, is written in terms of the electric potential, $\Psi(r,t)$, as

$$E(r,t) = - \nabla\Psi(r,t) . \tag{21}$$

Poisson's equation couples the electric field to the carrier densities through the electric potential, Ψ, and is written in quasi-static form

$$\nabla^2\Psi(x,t) = - \frac{\rho(r,t)}{\varepsilon} = - \frac{e}{\varepsilon}[\, p(r,t) - n(r,t)] . \tag{22}$$

30

where ε is the dielectric constant of the switch material, which is treated as a scalar constant.

Photoconductive switches are simulated as 1-D devices in terms of current flow and effects perpendicular to the applied bias field are of second order and may be neglected. Thus, the vector r becomes the scalar x. Also, as the photogenerated, or excess densities, are typically many orders of magnitude greater than the thermal equilibrium densities, the carrier densities in Eqs. (14–22) can be considered to be the excess densities, with the small thermal equilibrium values of the electron and hole densities neglected. This system is solved for the particular functions, $R(x,t)$ and $G(x,t)$, and initial values and boundary conditions appropriate for photoconductive switch operation.

Diffusion of carriers is included in the model even though the applied bias voltage is vastly greater than the thermal voltage, $\frac{kT}{e}$, which is $\cong 0.03$ V at room temperature. It would appear that the drift component of the current would dwarf the diffusion term. However, as the electric field collapses to a very low value when the switch closes, the diffusion current can become comparable to the drift current. Also, diffusion is significant if very large carrier density gradients develop, as is expected to happen near the switch electrodes.

The function $G(x,t)$ represents the optical generation of carriers. Its form depended on the particular illumination scheme that was simulated. In all cases, the number of carriers created was assumed proportional to the optical energy absorbed and the optical pulse was assumed to have a normalized Gaussian temporal profile. In general, $G(x,t)$ can be written

$$G(x,t) = \phi(x) \frac{N_0}{a\sqrt{2\pi}} e^{-\frac{(t-3a)^2}{2a^2}} \tag{23}$$

31

where N_0 is the total number of photons in the optical pulse, a is the temporal variance of the optical pulse ($a = \dfrac{fwhm}{2\sqrt{\ln(4)}}$), and $\phi(x)$ will depend on the particular spatial illumination scheme. Overhead, or broadside, illumination, and end-on, through the contact, illumination were simulated. For end-on illumination, t in Eq. (23) is replaced by $t \rightarrow t - x/c$ to represent a Gaussian pulse propagating through the switch from $x = 0$, or $t \rightarrow t - (\ell - x)/c$ for a light pulse propagating from $x = \ell$. The amount 3a is subtracted from t to shift the peak optical intensity away from $t = 0$ so that illumination begins at ~1% of the peak intensity. For uniform overhead illumination, $\phi(x)$ is given by

$$\phi(x) = \frac{1}{\ell w d} \tag{24}$$

where A is the area of the conducting region of the switch, and ℓA is equal to the conducting volume.

For a normalized Gaussian spatial profile,

$$\phi(x) = \frac{1}{b\sqrt{2\pi}} \frac{1}{A} e^{-\frac{(x-ctr)^2}{2b^2}} \tag{25}$$

where b is the spatial variance of the optical beam, and ctr is the center of the illumination. Asymmetric illumination can be simulated by giving ctr a value other than $\ell/2$. For end-on illumination through $x = 0$, $\phi(x)$ is written

$$\phi(x) = \frac{\sigma}{w d} e^{-\sigma x} \tag{26}$$

where σ is the absorption coefficient of the semiconductor for the optical pulse. For illumination through $x = \ell$, x in Eq. (26) is replaced by $x \rightarrow \ell - x$.

The function $R(x,t)$ represents the reduction of carriers through recombination processes. A simple expression is used for $R(x,t)$ where

$$R_h(x,t) = \frac{p(x,t)}{\tau} \tag{27}$$

32

$$R_n(x,t) = \frac{n(x,t)}{\tau} \qquad (28)$$

with τ as the carrier recombination time.

The electric field dependence of the carrier mobility is included in the model. It is necessary to include this non-linear effect to properly simulate photoconductive switching at high-bias fields. The field-mobility relation for GaAs used by Horio *et al.*[18] was used in this model. For Si, the relationship given by Sze was used.[19]

The switch electrodes are located at $x = 0$ and $x = \ell$. The contact at $x = 0$ is connected to ground through the load resistor. The high-voltage bias is applied at $x = \ell$. The contacts are assumed to be perfectly ohmic, with infinite surface recombination velocity. The carrier densities at ohmic contacts will be the thermal equilibrium values; the excess densities will be zero.[20] The switch is assumed to be in thermal equilibrium before illumination at $t = 0$, so the excess densities are zero at $t = 0$. These conditions can be summarized

$$n(o,t) = n(\ell,t) \equiv 0 \qquad (29)$$

$$p(o,t) = p(\ell,t) \equiv 0 \qquad (30)$$

$$n(x,0) = p(x,0) \equiv 0. \qquad (31)$$

The electric field is assumed to be continuous across the contact boundary, as is the current density, in general. For special simulations of no current injection at the contacts, the contact current is set equal to zero.

The electric potential boundary conditions are somewhat more complicated. A derivation of boundary conditions on the electric potential, Ψ, is used which accurately represents the operation of a high-speed photoconductive switch. This formulation follows closely that given by Iverson.[12]

$$\frac{\partial}{\partial t}\Psi(\ell,t) = \frac{e}{\varepsilon}\left\{ \int_0^\ell E(x,t)[\mu_n(x,t)n(x,t)+\mu_p(x,t)p(x,t)]\partial x \right\}$$

33

$$-\frac{\ell}{\varepsilon AR}[\Psi(x,t) - V_o] \,. \tag{32}$$

Equation (32) gives a mixed, global boundary condition for $\Psi(\ell,t)$ which must be integrated with the transport equations. This boundary condition correctly accounts for the integrated displacement current and is, thus, valid for high-speed switching simulation.

The equations are first put into a discrete form using a finite difference representations. Centered difference representations[21] are used for the density gradients, second derivative of the potential, and potential gradient. The divergence of the current density in the continuity equations is represented using an upwind-differencing scheme.[22] The spatial discretization is carried out on a uniform mesh, dividing the domain $(0,\ell)$ into 500 equally spaced mesh points. A fully explicit, forward time finite difference scheme is used for the time derivatives in the continuity equations

BULK SWITCH MODELING

The switching of the bulk GaAs switches with gridded electrodes obtained from the U.S. Army Electronic Technology and Device Laboratory was simulated. For these switches, illumination through the electrode grid was modelled by a propagating Gaussian optical pulse using the generation functions described earlier. The program parameters were: $\ell = 0.6$ cm or $\ell = 1$ cm; the conducting area, $A = 0.1$ cm; $\varepsilon_r = 13.1$; and the absorption coefficient, $\sigma = 1.39$ cm. These parameters were chosen to represent the actual switches that were used in experiments. The value of A was the measured optical beam size. σ was measured at LLE for the samples provided. The applied optical pulse energy was 100 μJ resulting in carrier densities of $\sim 10^{16}/\text{cm}^3$. The optical pulse variance was 200 ps.

A spatial profile of the electric field for one side illumination at various times and an applied bias voltage of -9 kV is shown in Fig. 24. The electric field collapses in time from the ground contact to the negative high-voltage contact as the optical pulse propagates

34

through the switch. The field is seen to "compress" as it collapses, forming a field peak at the contact opposite illumination. This simulation is consistent with the electric field profiles obtained experimentally for this illumination scheme with the electro-optic imaging system. The field is compressed until, at 1200 ps, NDR effects take over. This results in a sharp field gradient and rise in the field at the contact. This agrees well with the experimental results in Fig. 15(b).

Illumination through both the ground and negative high-voltage electrodes was also simulated. The calculated electric field profiles showed uniform collapse as in Fig. 15(c). The simulated switching with two-side illumination was considerably more efficient than one-side illumination, with more complete field collapse and faster rise time, also in agreement with the experimental observations. The observed field peaking at the contact was not reproduced in the simulations. But we believe that is due to geometric considerations.

The gridded contacts on the switch had areas of bare GaAs and thus could not represent ohmic contacts. To simulate this, the boundary conditions on the current density were altered to represent contacts that would not pass electrical current. Two-side illuminated switches with non-injecting contacts were simulated. The calculated electric field profiles for this case showed the same uniform field collapse as the injecting case except for an extreme field peak at the negative high-voltage electrode. This peak is ~20 times the applied bias field. As the electrode is gridded, there will be some areas of the electrodes that are metallized and pass current and open areas that do not. The simulations suggest that there will be a significant potential difference between the injecting and non-injecting regions. This explains the observed arcing between the non-metallized and metallized areas. The simulations only show peaking at the contacts if the contacts are noninjecting. Experimentally we observed that increasing the light under the contacts reduces the field enhancement there. This is also in agreement with the simulation.

The observed decrease in the electro-optic switch efficiency was not recreated in the simulations. They do not show significant field remaining across the switch after several nanoseconds. On the basis of this computer model, the observed decrease in electro-optic switch efficiency is not due to negative differential resistance in the photoconductive switch. The failure of the program to recreate the reduced switching efficiency is most probably due to the fact that the gridded electrode switches do not lend themselves to a 1-D analysis. To properly simulate the bulk switches with gridded electrodes, it would be necessary to model the conducting and non-conducting channels created by the electrode grid. There is probably considerable vertical structure that effects the field profile, as well. Simulation of these effects would require a 3-D model, which would be practical only if a supercomputer were available. Also, the field probe can only access the switch field at the switch surface and the surface field may not be a true measure of the internal field structure for switches with such considerable vertical structure.

LOCK-ON MODELING

The computer program cannot fully describe the behavior we are observing in the surface GaAs switches biased above the lock-on threshold. The model is only 1-D and therefore cannot explain two-dimensional phenomenon like channeling. In addition, lock-on requires some mechanism for generating carriers to carry the current after the initial photogenerated carriers decay. No such mechanism has been incorporated into our model. Given these limitations the model does a spectacular job of modeling the experiments. Using the experimental Gaussian illumination profile, the model shows the field collapses in the center of the switch first. The speed of the electric field collapse accelerates when the local electric field falls below the threshold for NDR. Figure 25 shows the simulated electric field across the switch. The field roughly follows the Gaussian distribution of carriers until the NDR threshold is reached in the center. Then the filed at the edges remains high while the center collapses. In Fig. 26, the same simulation is carried out to

36

longer times. (Note the logarithmic vertical scale.) When the condition arises that the local electric field is increasing (above the NDR threshold) and the local carrier density is decreasing, regions of enhanced field called Gunn domains nucleate. The model shows that these domains nucleate primarily at the negative high voltage contact as we see experimentally. It is likely that the enhanced field at the negative high voltage contact shown in Fig. 26 is a manifestation of a Gunn domain.

The secondary collapse of electric filed is not duplicated in these experiments for the reasons stated above. It would be easy to conceive of adding a mechanism such as avalanche carrier generation or field dependent ionization of traps which operates in these high field region to generate the addition carriers.

CONCLUSION

The electro-optic imaging system is now in full operation. It has been used to observe the dynamics of photoconductive switching in Si and GaAs. Silicon has been found to be a rather simple photoconductive material. The field collapses with the integral of absorbed optical energy. There are no anomalies in the field profile after switching. GaAs is much more complex. Both side illuminated and through the contact illuminated switches have been studied. GaAs has two distinct regions of operation. At biases below about 3–6 kV/cm (depending on material preparation), the switch behaves like silicon. Above 6 kV/cm, the electric field across the switch exhibits transient anomalies. Specifically, in both geometries, there are field enhancements at the contacts. The negative contact generally has the greatest field enhancements. These transients may be implicated the failure mechanism of these switches. GaAs switches can withstand at least 40 kV/cm, under 10 psi SF_6 when they are not triggered. However, at 28 kV/cm they will undergo surface breakdown after they have been triggered. Current channeling and local field enhancements, which have been identified by the electro-optic imaging system, may be

responsible for arcing. Theoretical modelling has identified the Gunn effect as the prime factor leading to the field enhancements.
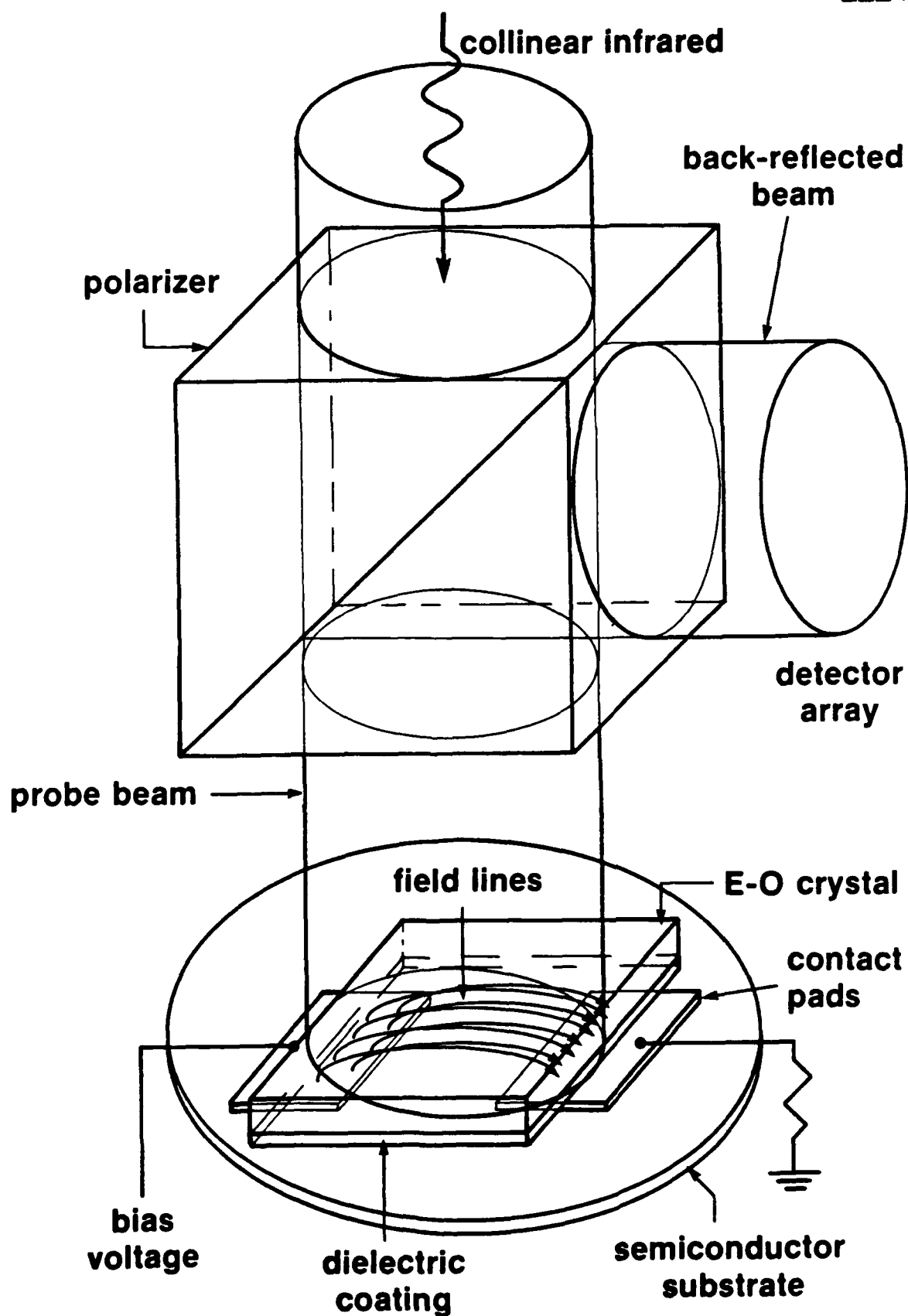
ACKNOWLEDGMENT

REFERENCES

1. G. Mourou, W. H. Knox, and S. Williamson, Picosecond Optoelectronic Devices, Chap. 7 (Academic Press, New York, 1984), pp. 219–248.

2. C. Bamber, W. Donaldson, T. Juhasz, L. Kingsley, and A. C. Melissinos, Part. Accel. 23, 255 (1988).

3. J. A. Valdmanis, G. Mourou, and C. W. Gabel, Appl. Phys. Lett. 41, 211 (1982).

4. K. Meyer, M. Pessot, G. Mourou, R. Grondin, and S. Chamoun, Appl. Phys. Lett. 53, 2254 (1988).

5. A. Yariv, Quantum Electronics, 2nd Ed (John Wiley & Sons, New York, 1975), p. 340.

6. P. M. Hall, Thin Solid Films 1, 277 (1967).

7. Z. H. Zhu, J-P. Weber, S. Y. Wang, and S. Wang, Appl. Phys. Lett. 49, 432 (1986).

8. Y. H. Lo, Z. H. Zhu, C. L. Pan, S. Y. Wang, and S. Wang, Appl. Phys. Lett. 50, 1125 (1987).

9. I. N. Duling III, T. Norris, T. Sizer II, P. Bado, and G. A. Mourou, J. Opt. Soc. Am. B 2, 616 (1985).

10. T. Burke, M. Weiner, L. Bovino, and R. Youmans, Digest of Technical Papers, 6th IEEE Pulse Power Conference, ed. B. Bernstein and P. Turchi (IEEE, New York, NY, 1987), p. 283.

11. L. Bovino, T. Burke, R. Youmans, M. Weiner, and J. Carter, Digest of Technical Papers, 5th IEEE Pulse Power Conference, ed. P. Turchi and M. F. Rose (IEEE, New York, NY, 1985), p. 242.

12. A. Evan Iverson, Trans. Soc. Comput. Simulation 5, 175 (1988)

13. S. M. Sze, Physics of Semiconductor Devices (John Wiley & Sons, New York, NY, 1981), p. 44.

14. A. E. Iverson and D. L. Smith, IEEE Trans. Electron Devices 34, 2098 (1987).

15. M. Weiner, L. Bolvino, R. Youmans, and T. Burke, <u>J. Appl. Phys.</u> <u>60</u>, 823 (1986).

16. W. T. White, C. G. Dease, M. D. Pocha, and G. H. Khanaka, "Modeling GaAs High Voltage Photoconductive Switches in One Spatial Dimension," <u>IEEE Trans. Electron Devices</u>, to be published (November 1990).

17. E. Sano and T. Shibata, <u>IEEE J. Quantum Electron.</u> <u>26</u>, 372 (1990).

18. K. Horio, T. Ikoma, and H. Yanai, <u>IEEE Trans. Electron Devices</u> <u>33</u>, 1242 (1986).

19. Sze, op. cit., p. 325.

20. Sze, op. cit., p. 56.

21. P. J. Roache, <u>Computational Fluid Dynamics</u> (Hermosa, Albuquerque, 1982), p. 20.

22. Ibid, p. 72.

The electric field above contacts on surface devices can be imaged electro-optically

collinear infrared

back-reflected beam

polarizer

detector array

probe beam

field lines

E-O crystal

contact pads

bias voltage

dielectric coating

semiconductor substrate

Z767

Figure 1

Conformal Mapping of Parallel-to-Coplanar Electrodes

$w = u + iv$

(a)

$z' = x' + iy'$

(b)
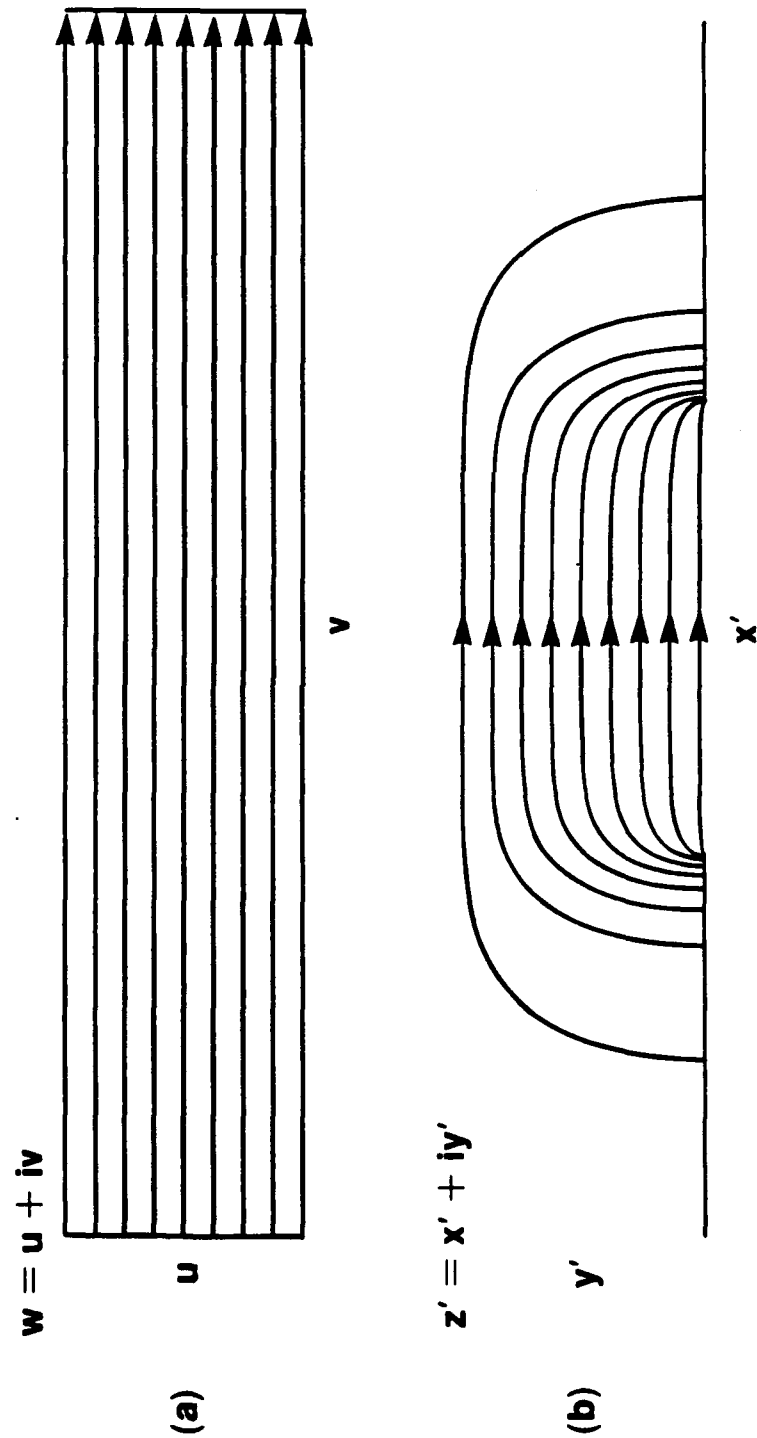
Z434

Figure 2

Electric Field in the Plane of Coplanar Electrodes
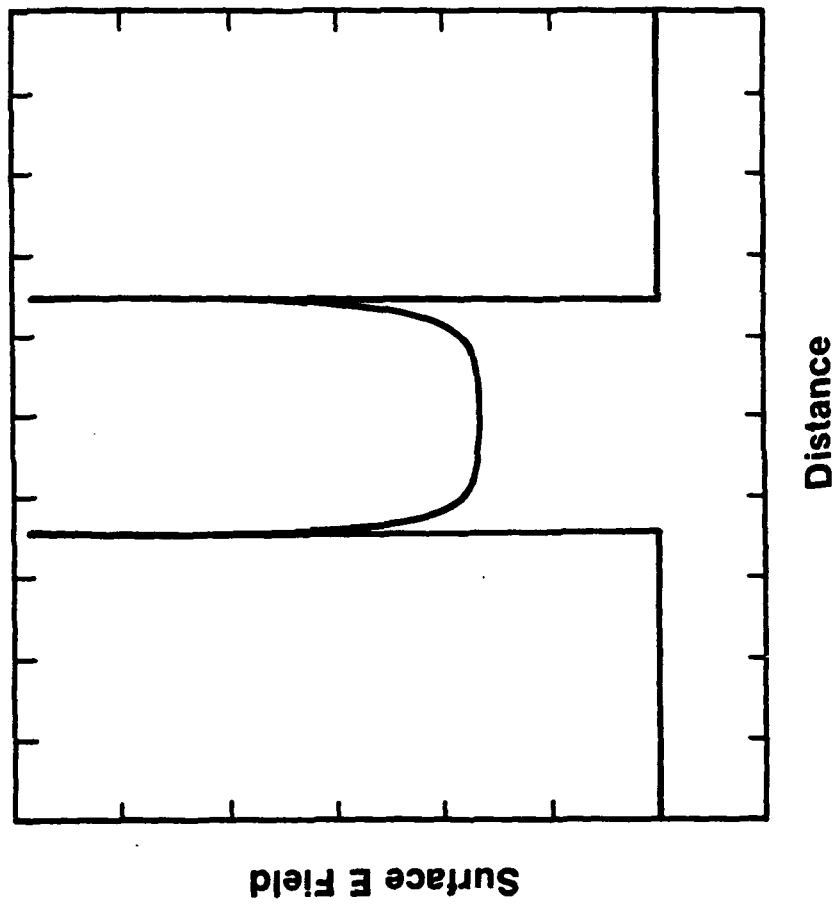
Figure 3

Z435

Integrated Surface Electric-Field Profile

UR
LLE

1/2 of Field Lines

Distance
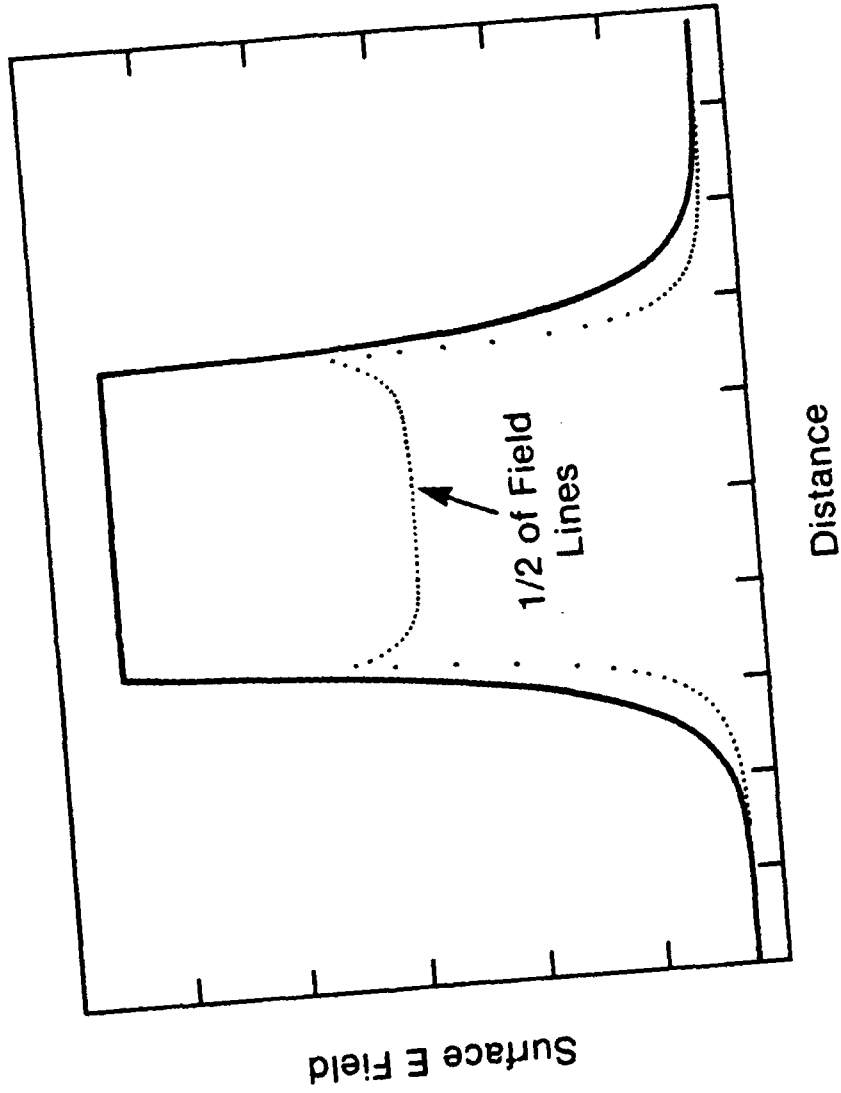
Surface E Field

Figure 4

Z428
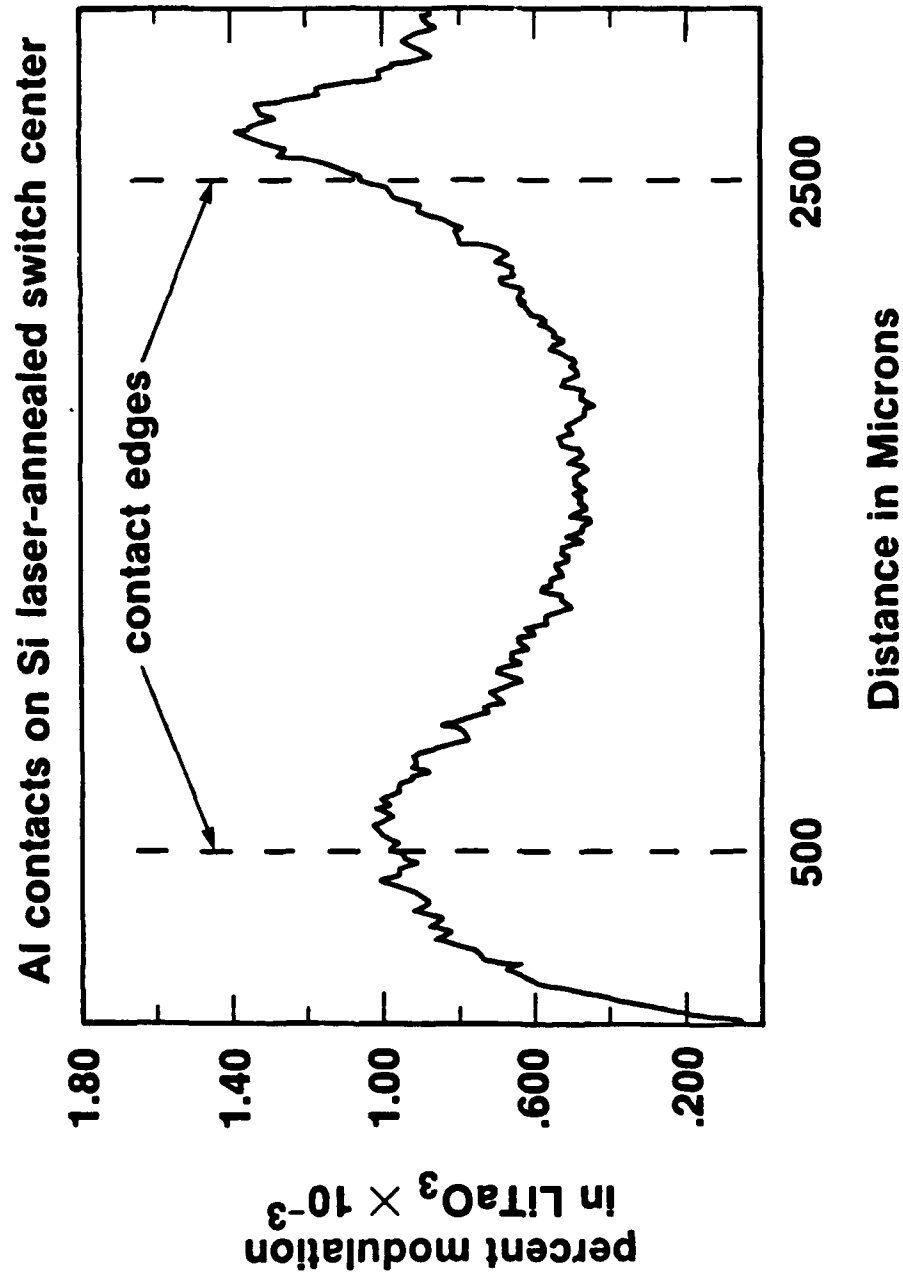
Figure 5

Surface Field and Contact Arrangement
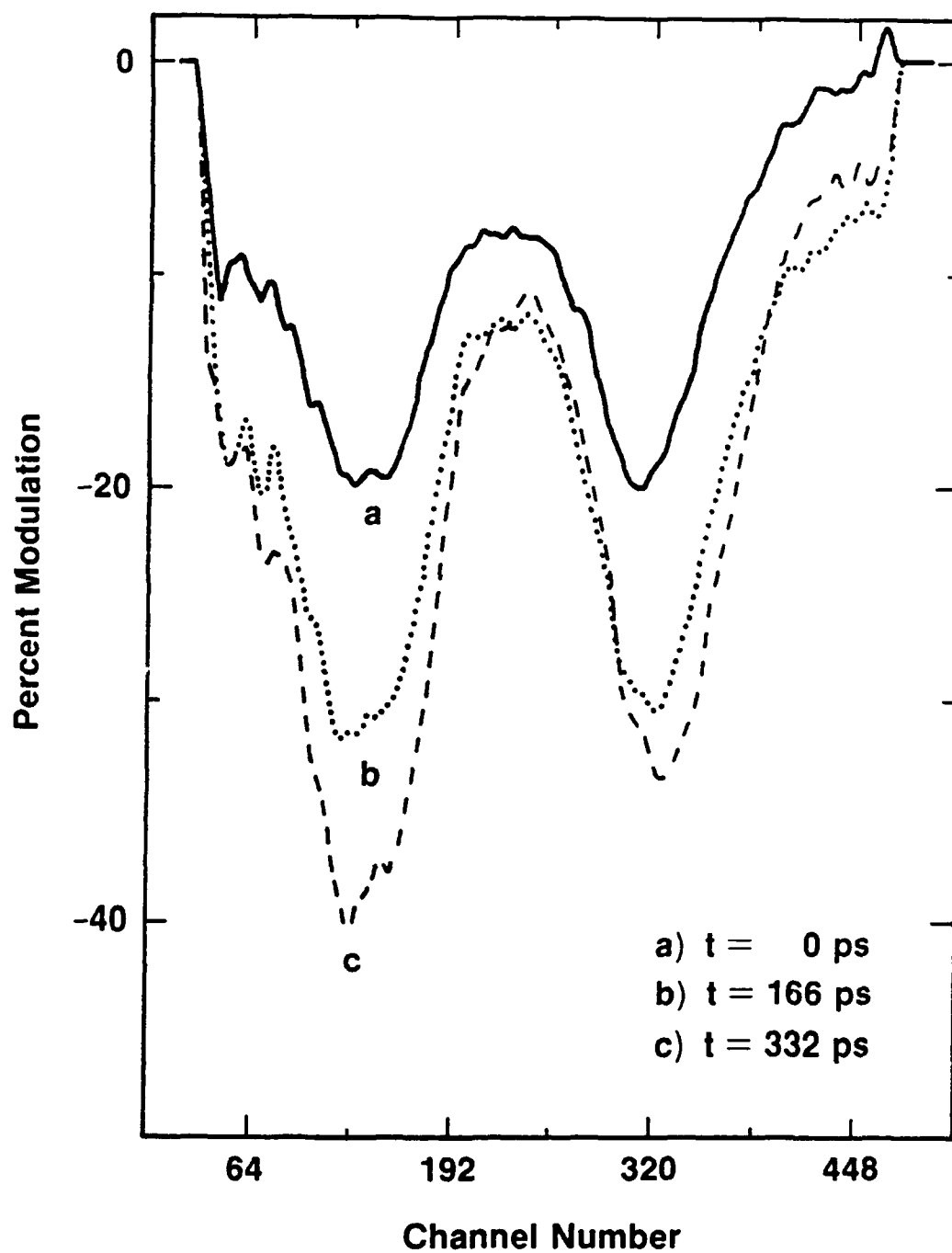
contact pads

photoconductive switch
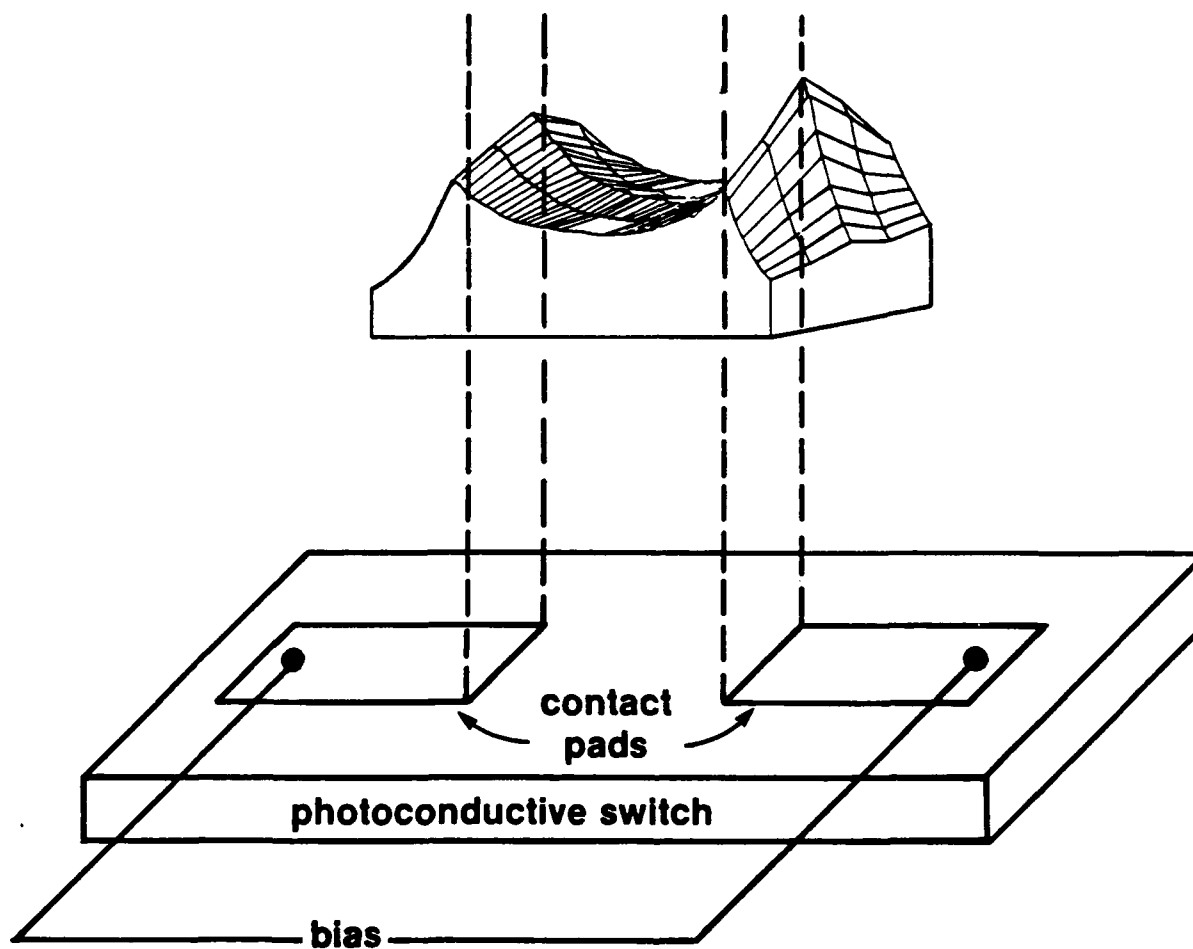
bias

Z267

Figure 6

Surface Electric Field on Si versus Time
Bias 1 kV; Gap 2 mm

Figure 7

The field above GaAs bulk power switches can be mapped

green probe beam
$\lambda = 532$ nm

back-reflected beam

to diode array

polarizer

infrared pump beam
$\lambda = 1064$ nm

splitter

LiTaO$_3$ crystal

metallic mesh contact

reflective coating

R_{load}
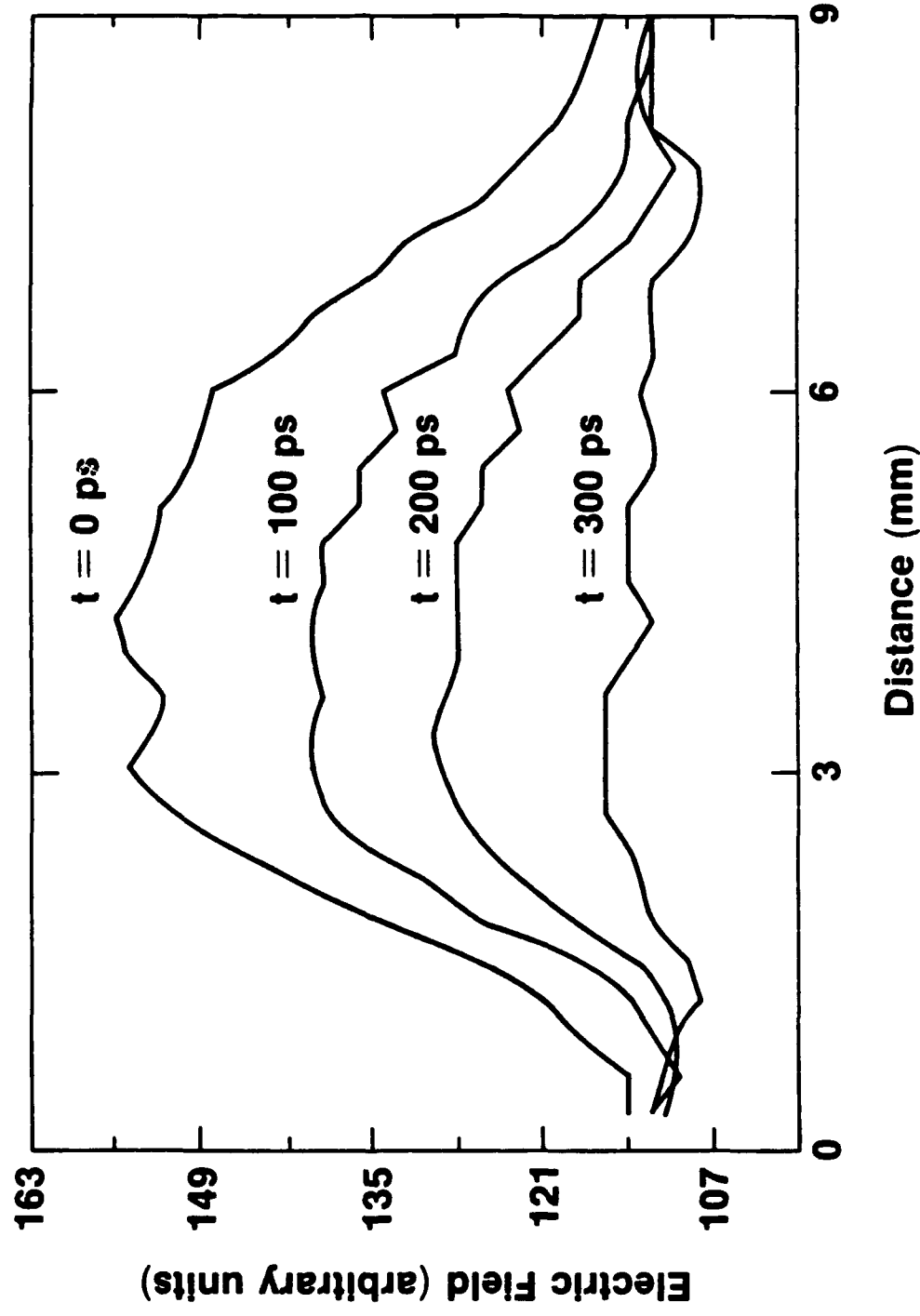
GaAs switch

bias voltage

Z814
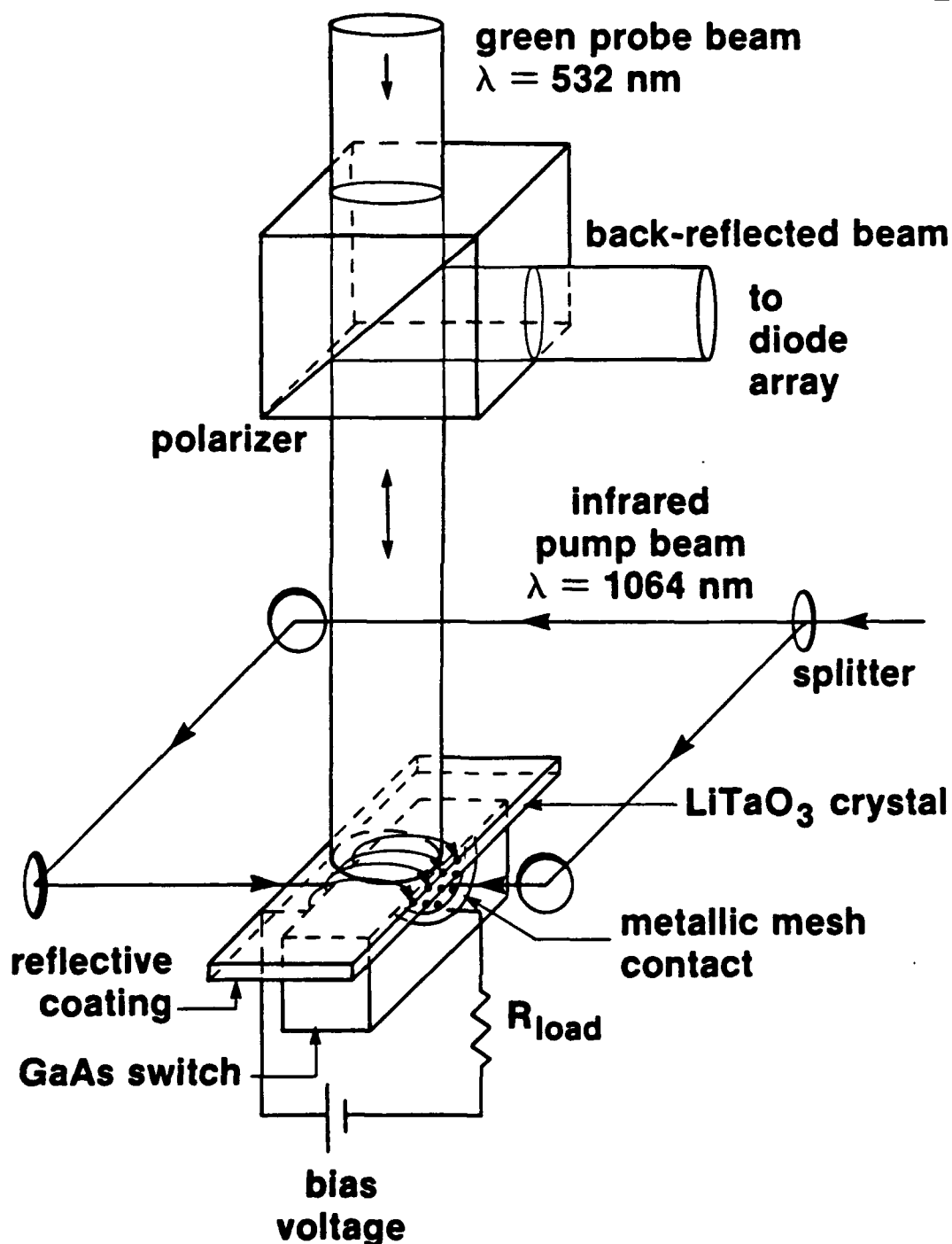
Figure 8

The electro-optic imaging system combines short-pulse lasers and two-dimensional imaging technology
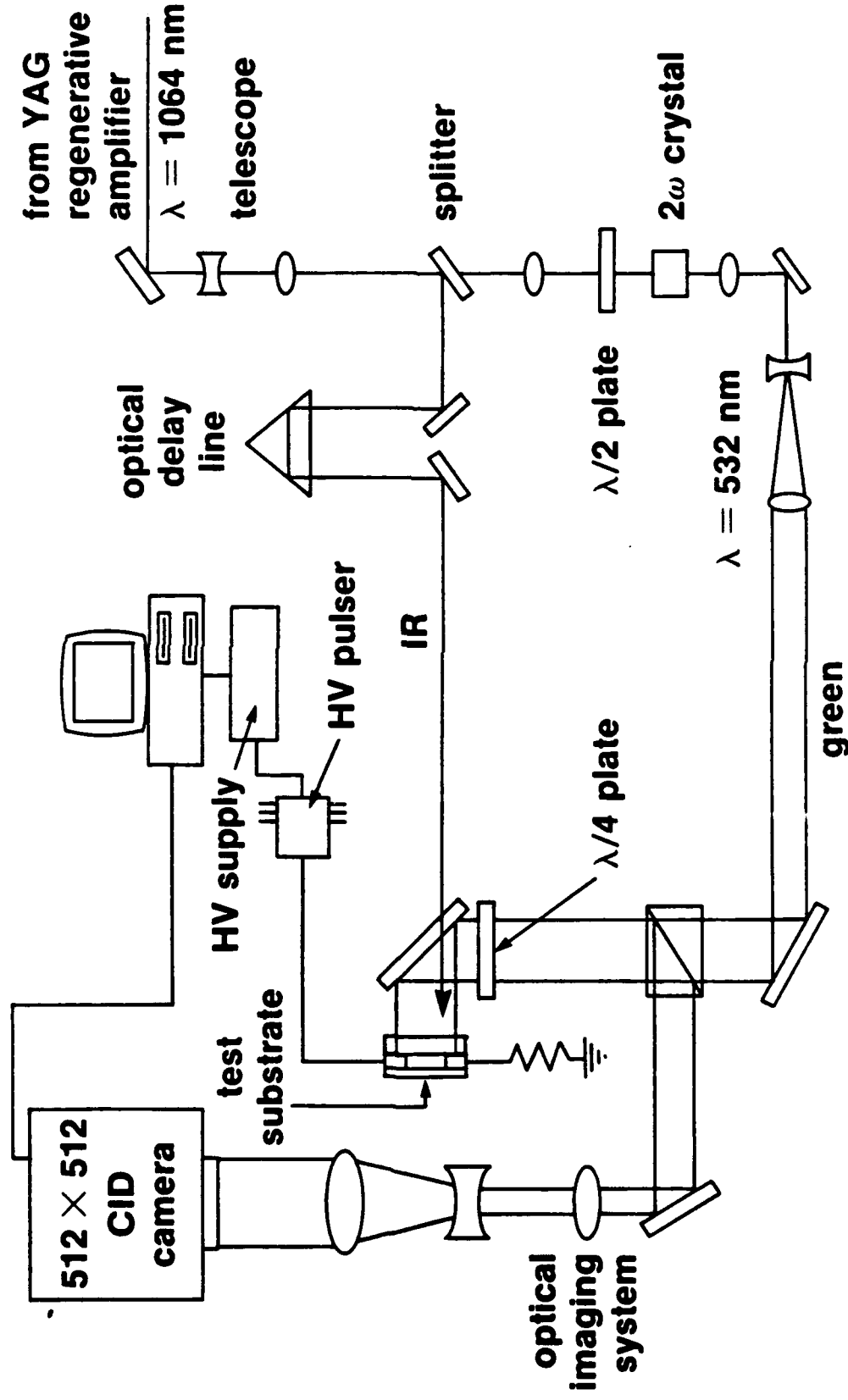
Figure 9

Z768

The collapse of the electric field above a photoconductive switch can be monitored
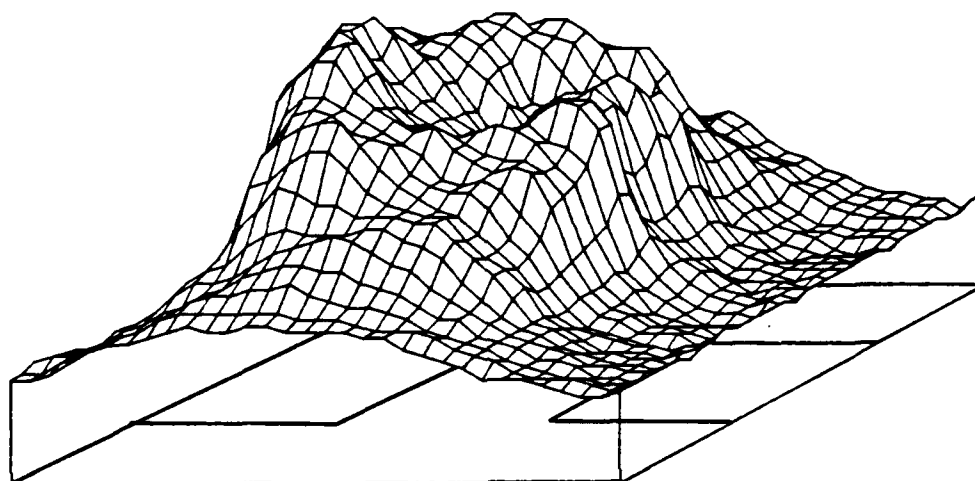

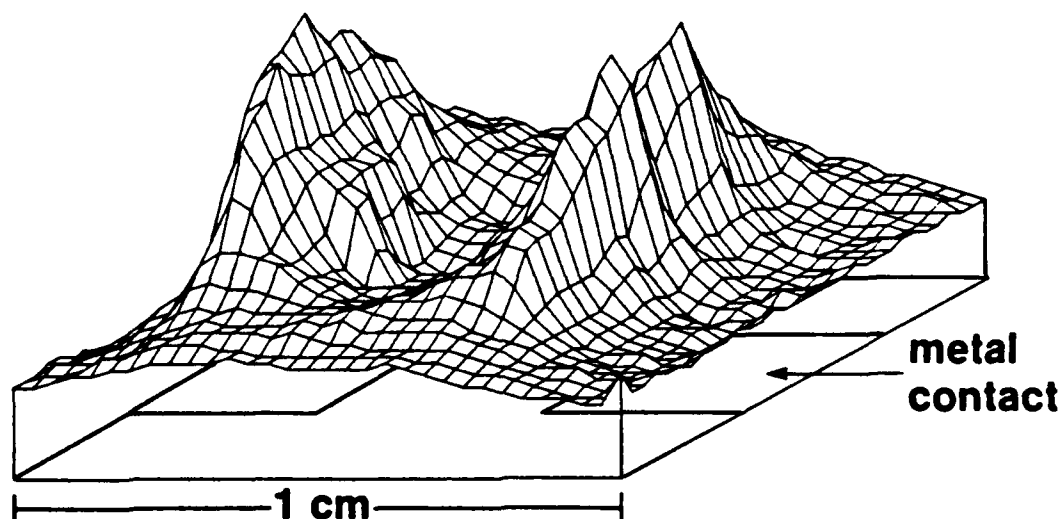silicon substrate, 3-mm contact gap, 5.8-kV bias

Local, transient events within the switch contact gap can be recorded

UR
LLE

Before IR illumination

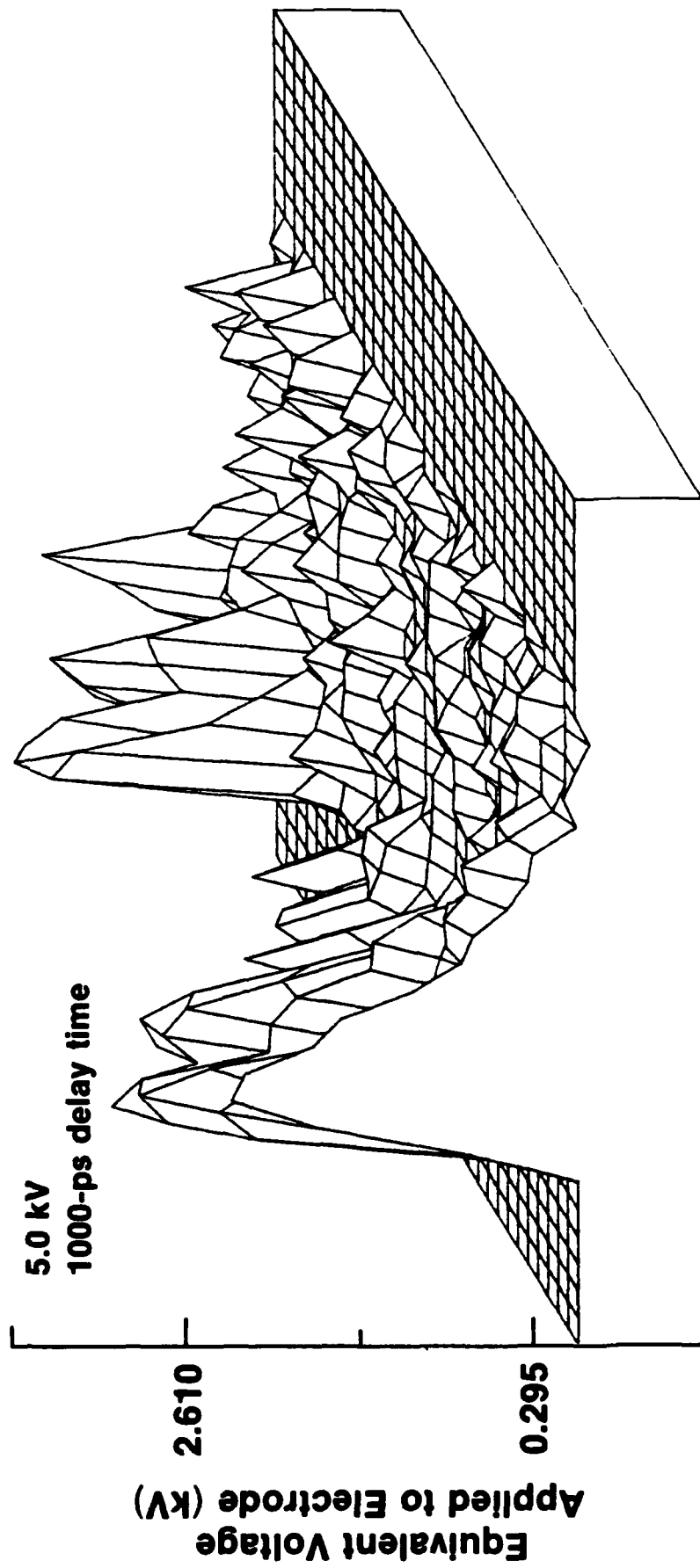**1 ns after IR point illumination**

metal
contact

|——————1 cm——————|

Z792

Figure 11

6 mm GaAs Illuminated from Both Sides with 1.9 mJ/cm^2

UR
LLE

5.0 kV
1000-ps delay time

2.610

0.295

Equivalent Voltage Applied to Electrode (kV)
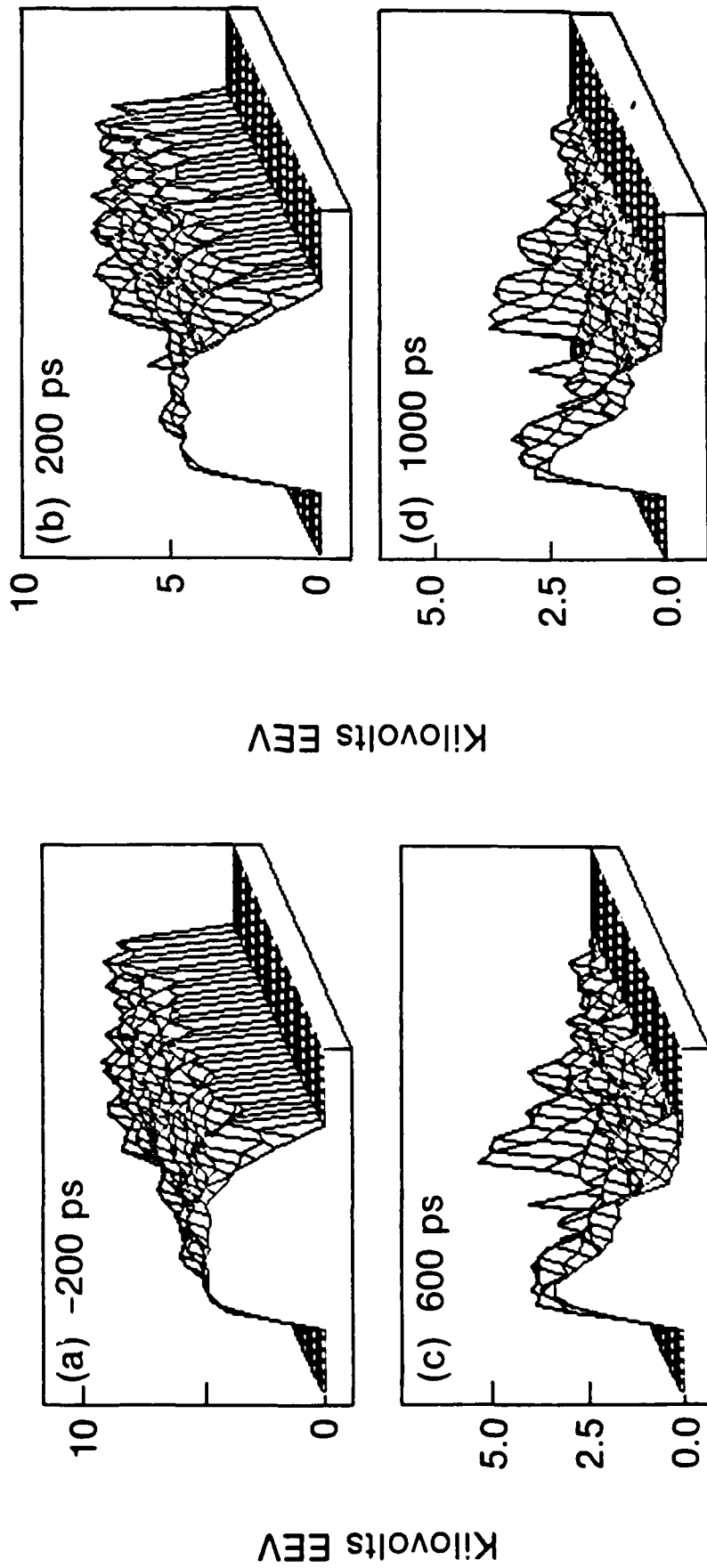
Figure 12

Z809

The electric field above a bulk GaAs power switch was imaged during switch operation

UR
LLE

5-kV bias
6-mm contact gap

(a) −200 ps

(b) 200 ps

(c) 600 ps
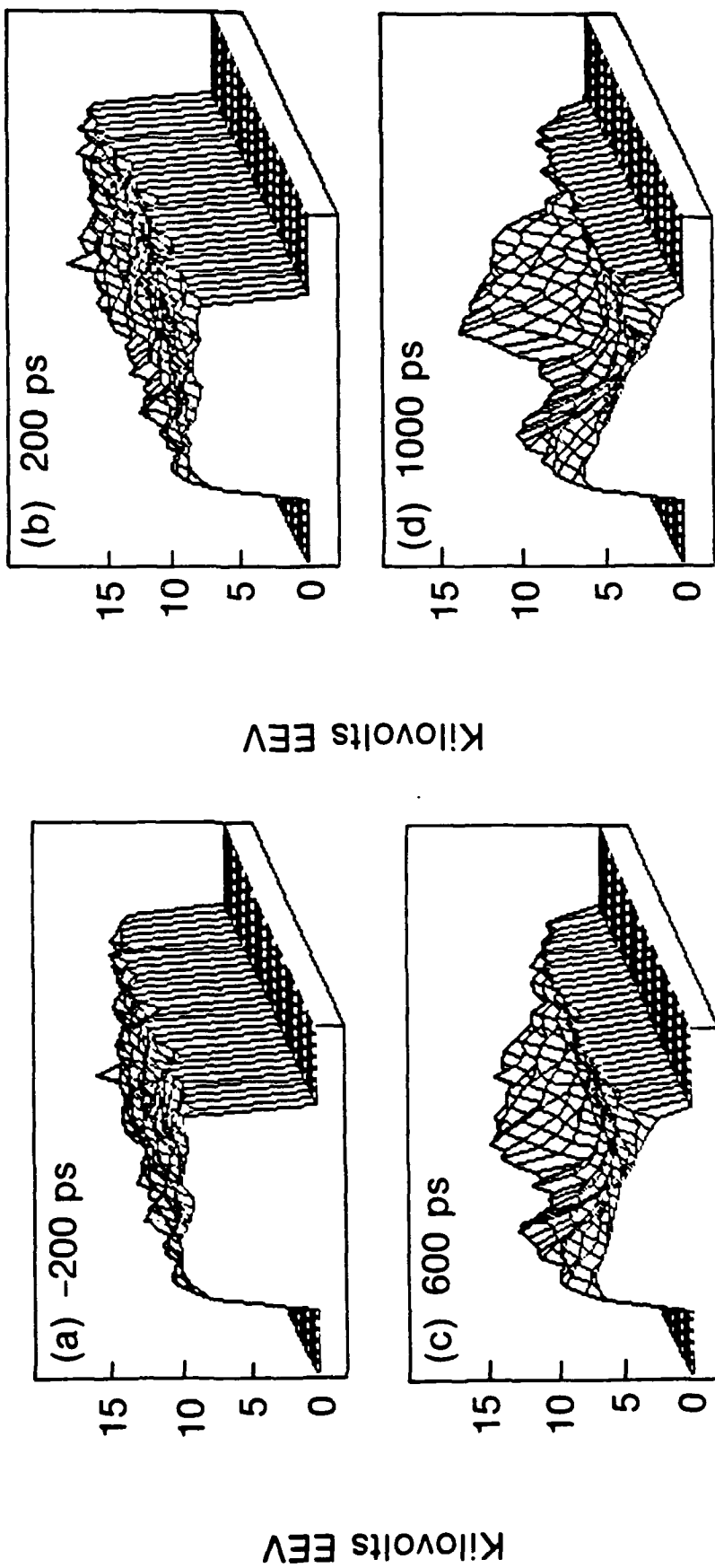
(d) 1000 ps

Kilovolts EEV

Kilovolts EEV

Ground Side Right

Figure 13

Z831

Two-dimensional field maps reveal interesting behavior of GaAs power switch at high bias voltage
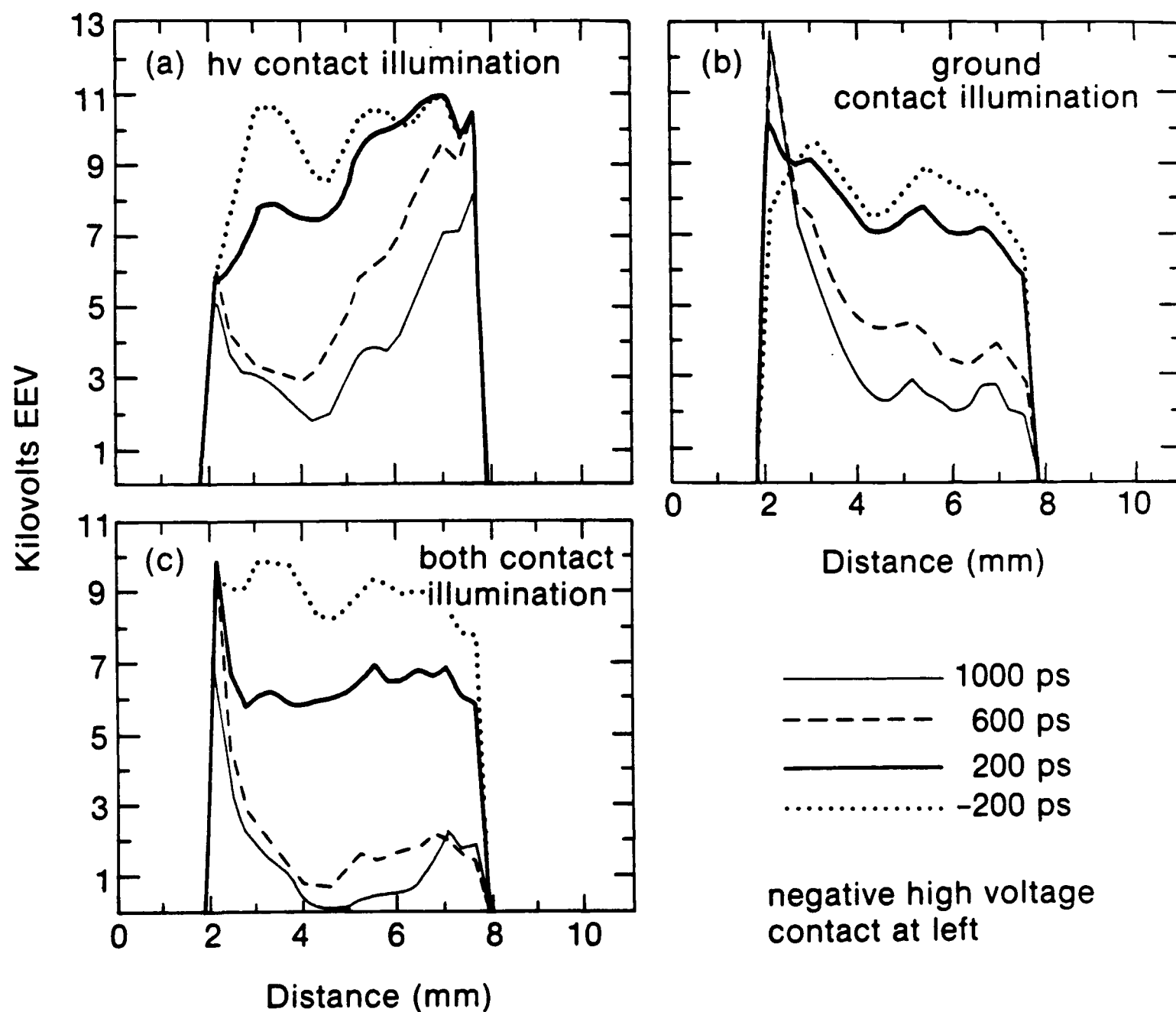
9-kV bias
6-mm contact gap

Ground Side Right

Figure 14

Z830

The field above GaAs power switches collapses differently for different illumination schemes

UR
LLE

Figure 15

Z834

Electro-Optic Switching Efficiency in a 6-mm GaAs Photoconductive Switch
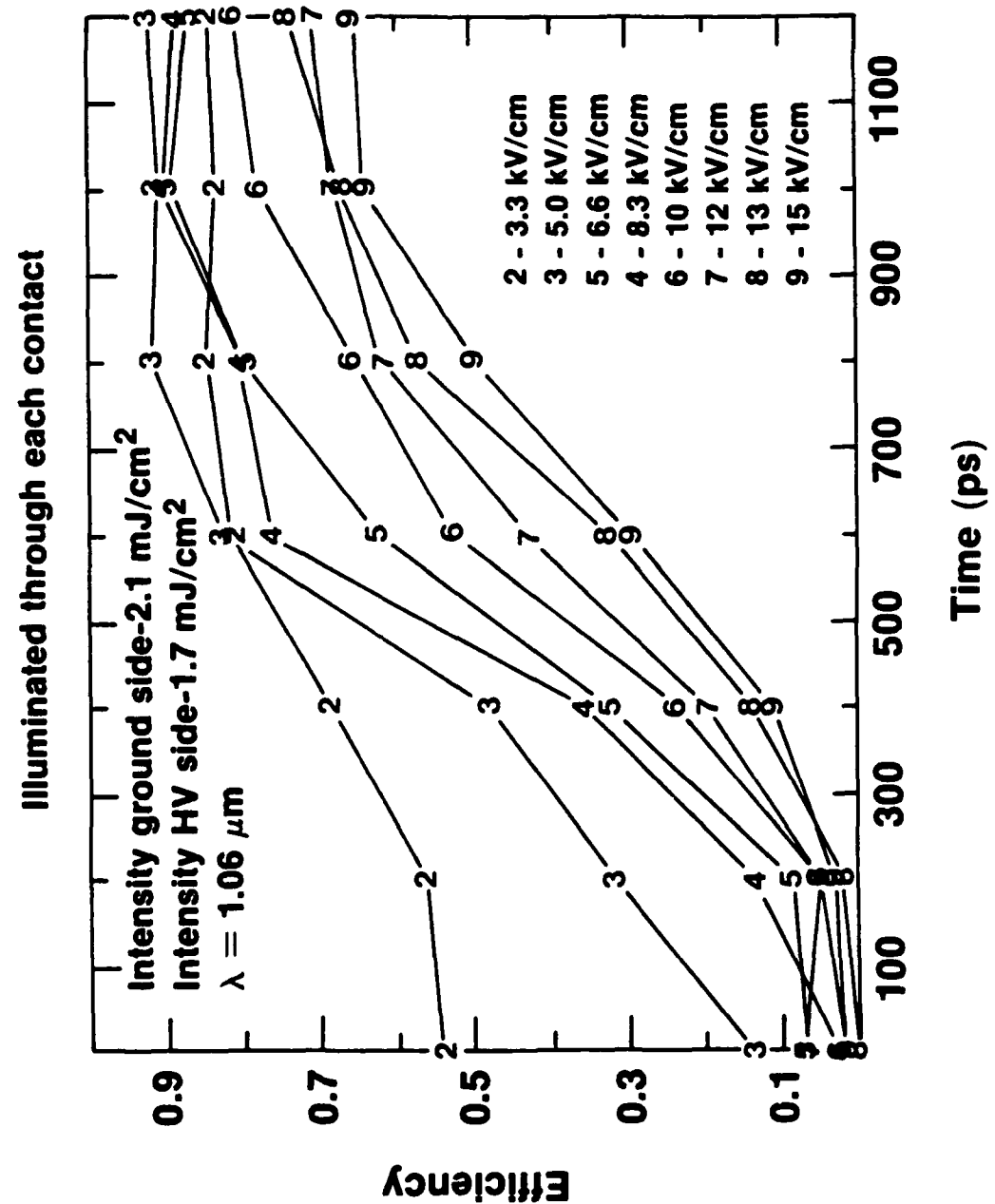
Figure 16

The switching efficiency of power switches can be measured electro-optically

(a) Intensity = 3.8 mJ/cm²

(b) Intensity = 2.1 mJ/cm²

Time (ps)

Efficiency

1 - 1.7 kV/cm   4 - 6.6 kV/cm   7 - 12 kV/cm
2 - 3.3 kV/cm   5 - 8.3 kV/cm   8 - 13 kV/cm
3 - 5.0 kV/cm   6 - 10 kV/cm   9 - 15 kV/cm

Figure 17

Z806

UR
LLE

GaAs Surface Switch
Average E-Field at Center - 2 kV bias

Electric Field (EEV)

3.00

1.00

Time (ns)

1.00   3.00   5.00
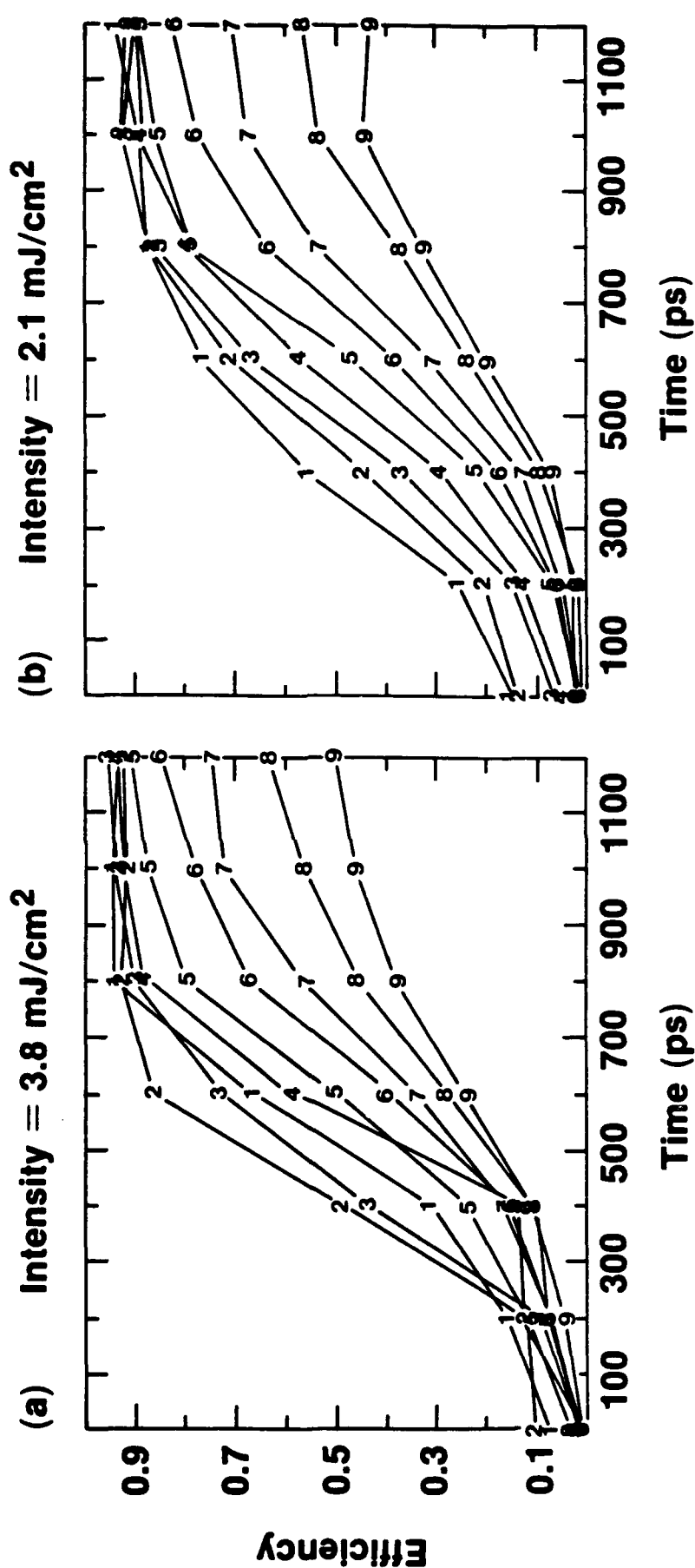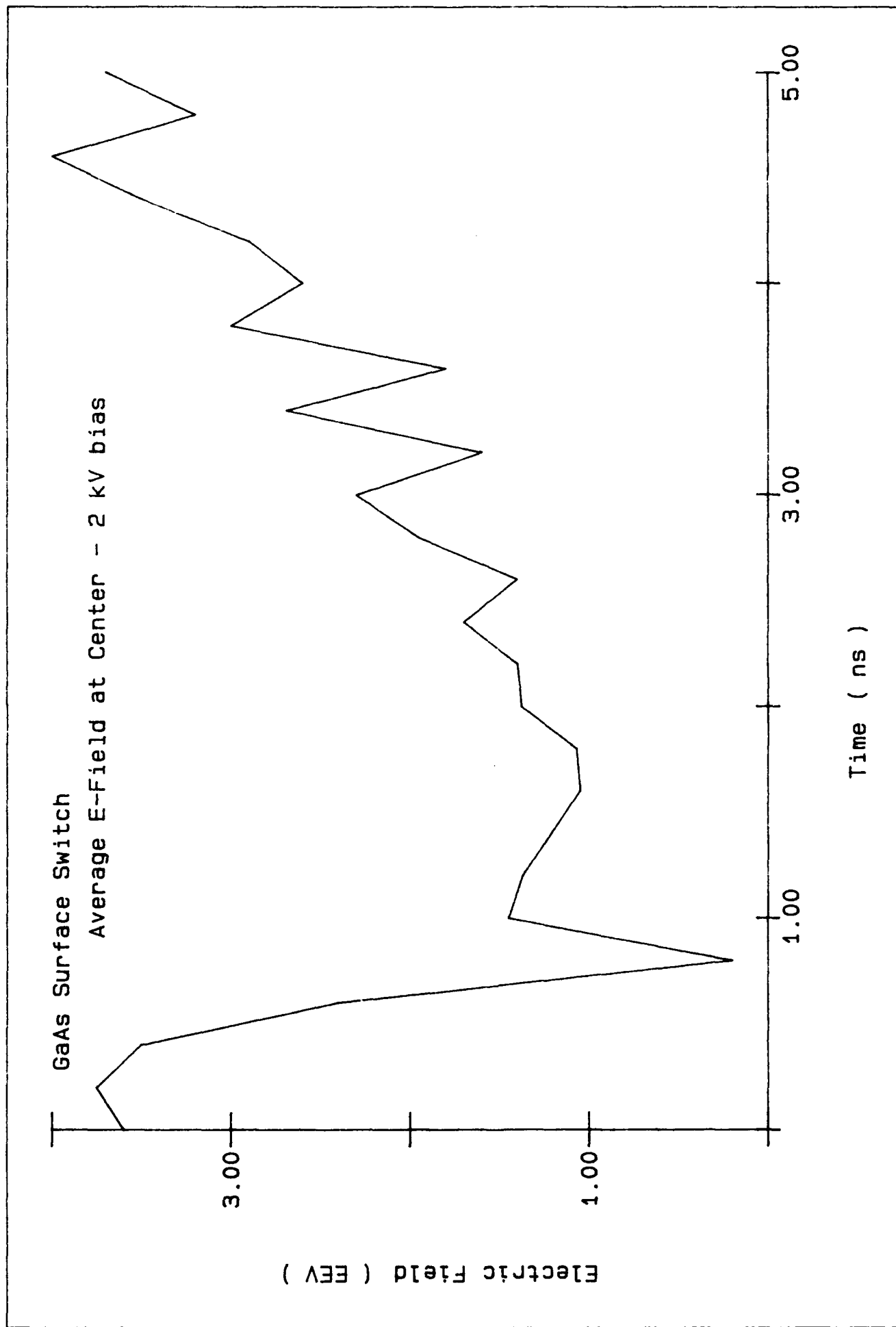
Figure 18

GaAs Surface Switch
Average E-Field at Center - 6 kV bias

Electric field (EEV)

Time (ns)
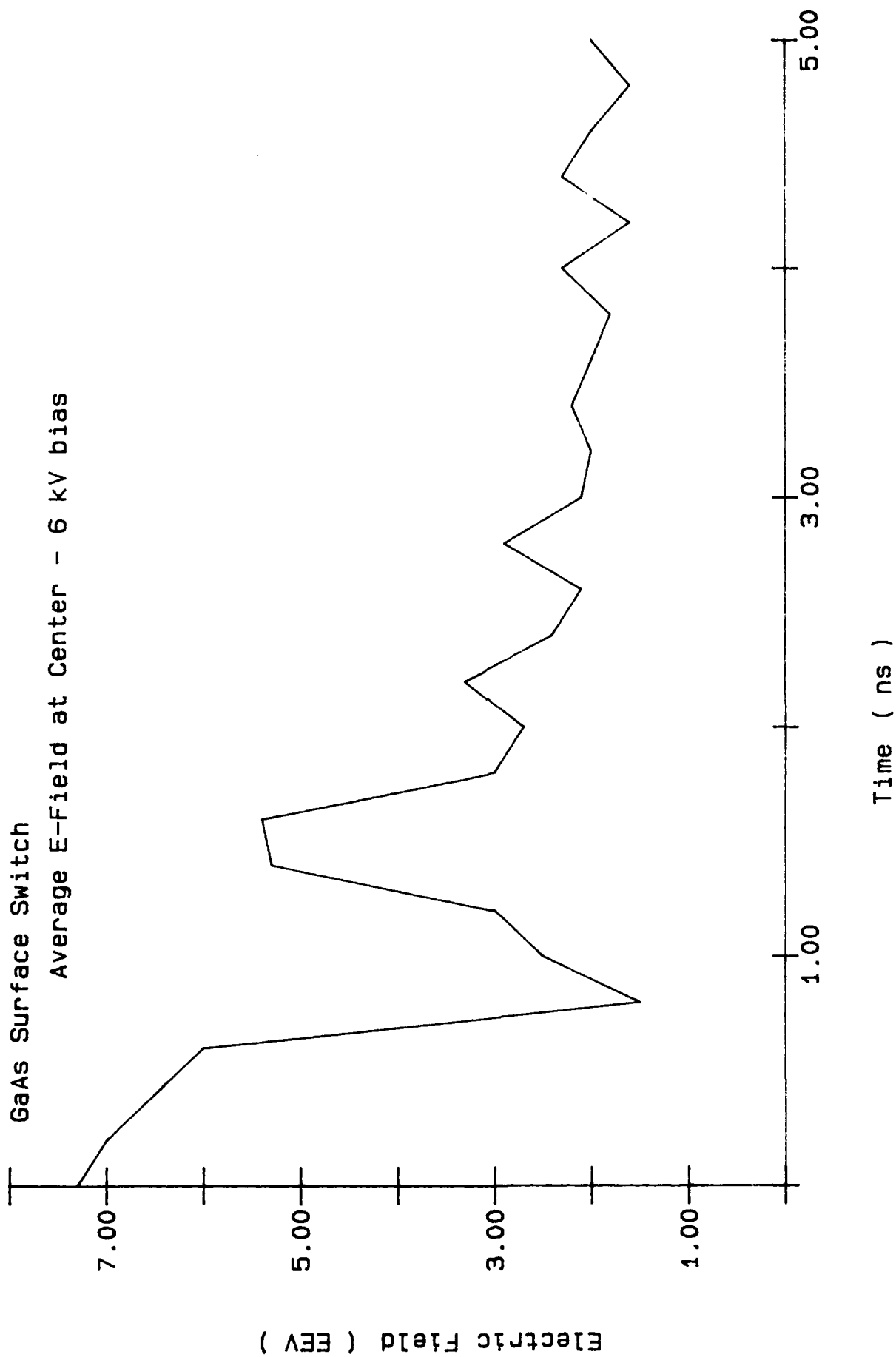
Figure 19

In the linear mode, the current is uniform in a photoconductive switch
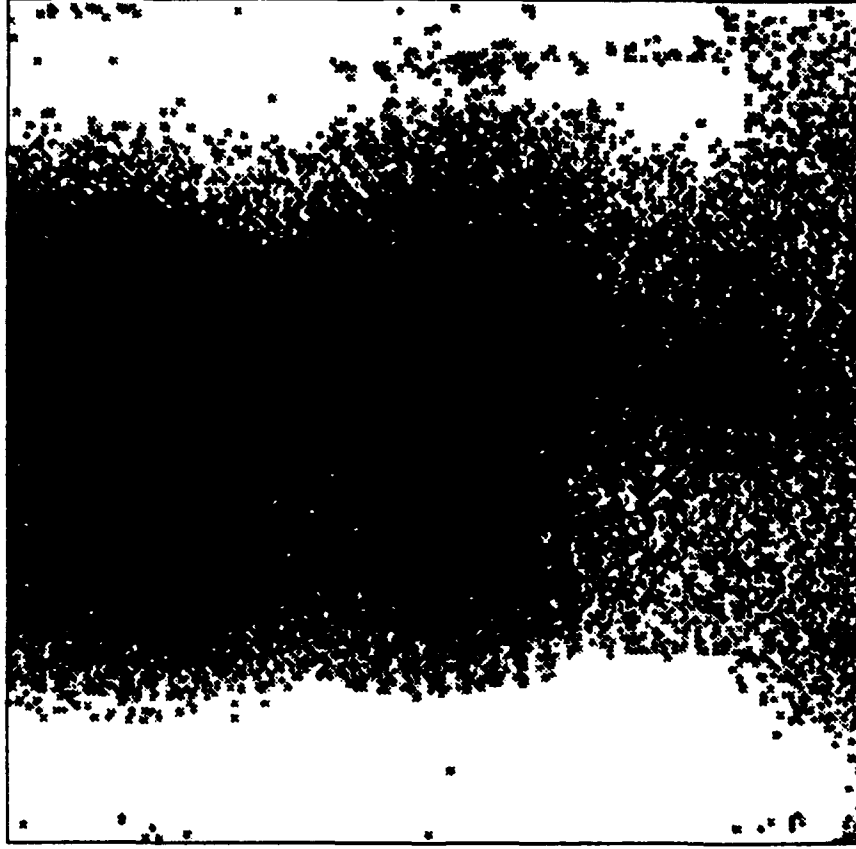
Figure 20

6 kV across
2.5 mm @ 2 ns

UR
LLE
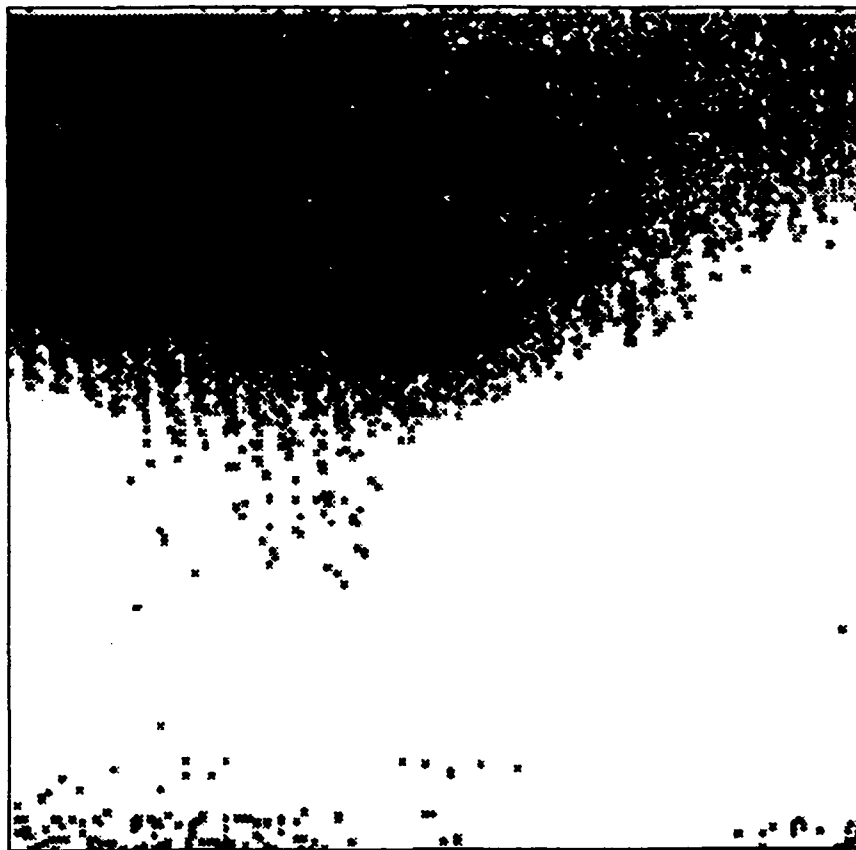
Figure 21

In lock-on mode, the current is confined to channels

UR
LLE

Figure 22

Switch current versus bias voltage
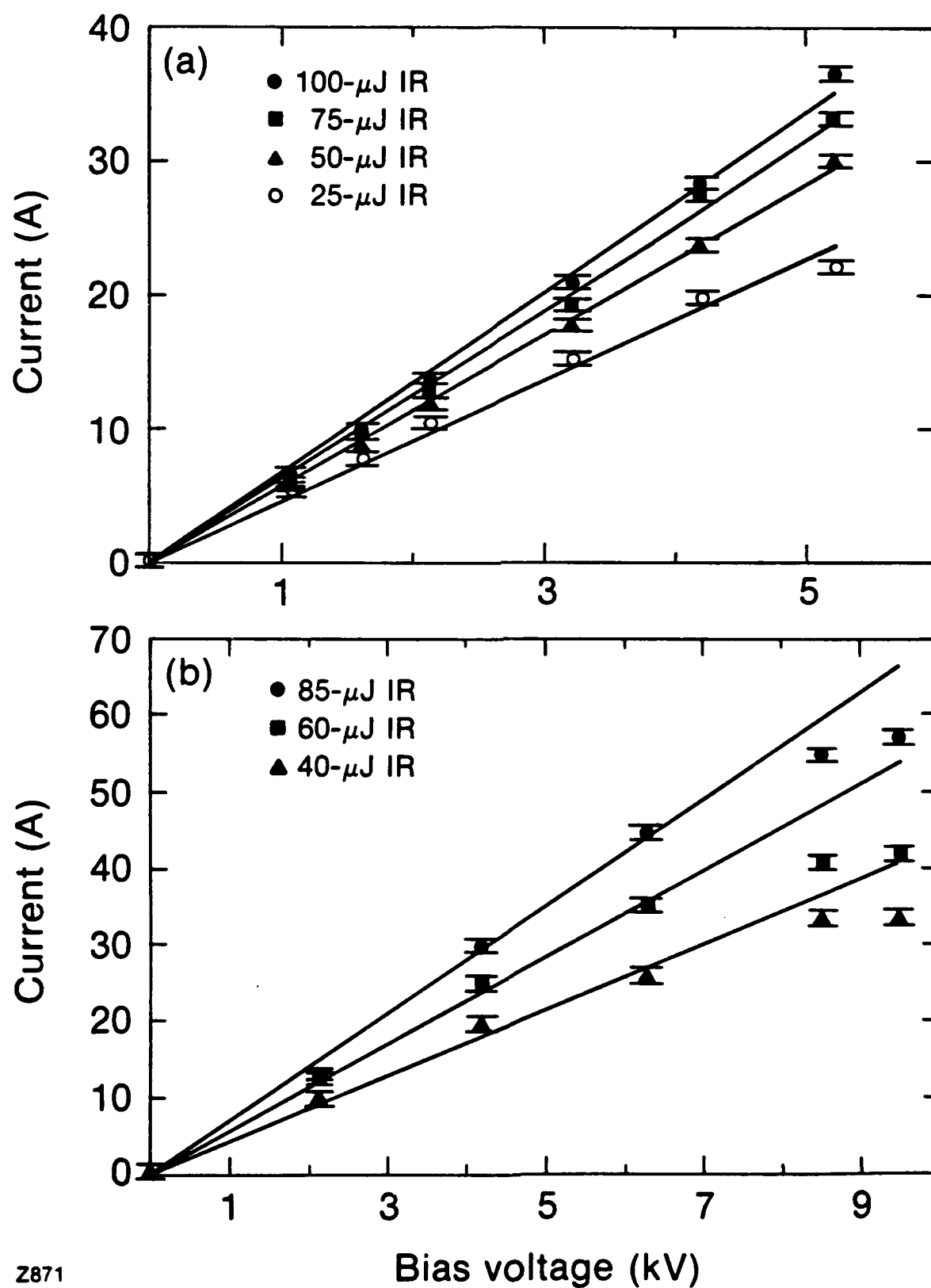
Figure 23

GaAs Illuminated Through Ground Side Contact
Initial Electric Field – 9 kV/cm

Electric Field (kV/cm)

Distance (cm)
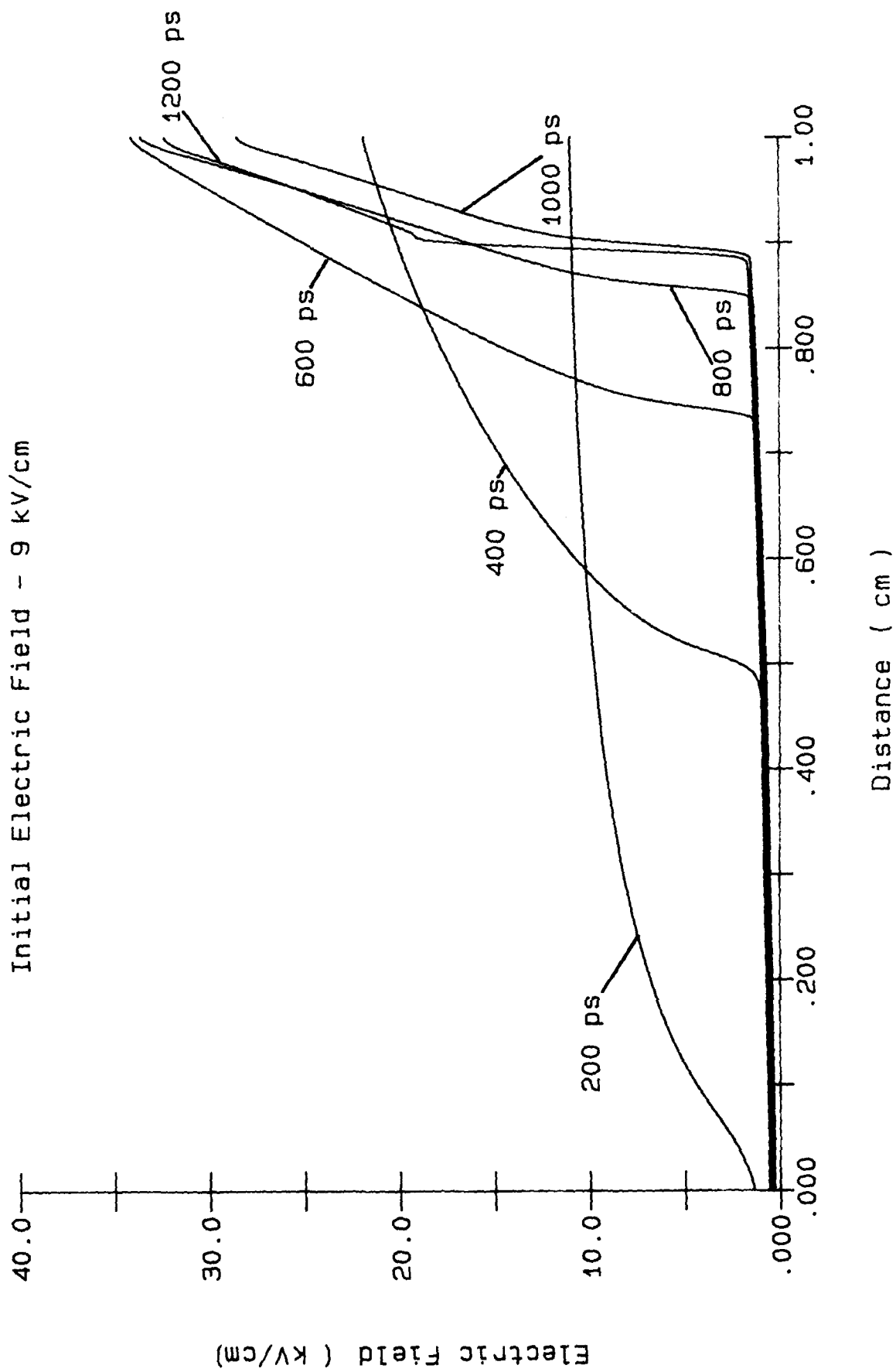
Figure 24

GaAs Surface Switch
Initial Electric Field – 24 kV/cm

40 ps
160 ps
240 ps

280 ps

320 ps

Electric Field (kV/cm)

25.0

15.0

5.00

.050   .150   .250

Distance (cm)
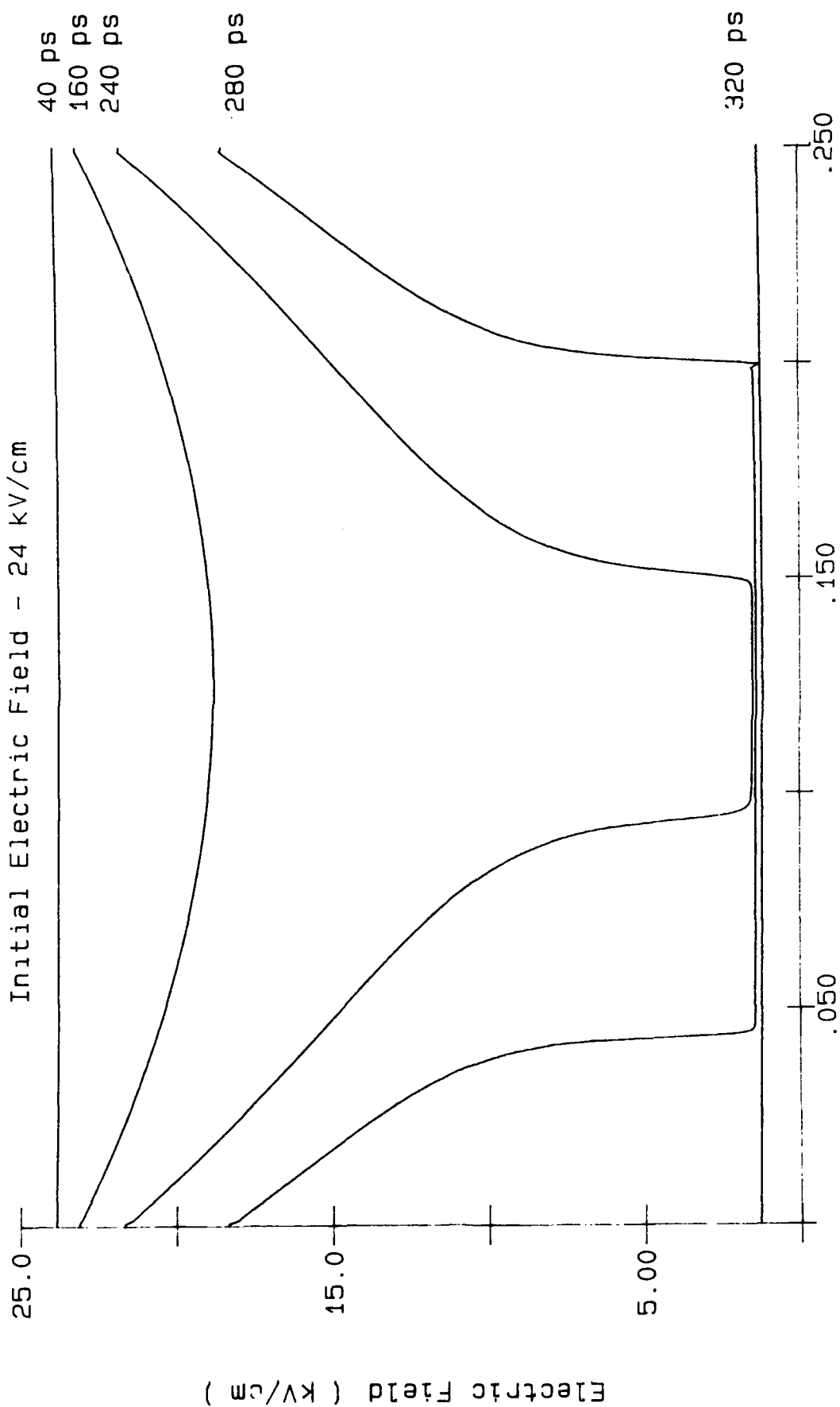
Figure 25

GaAs Surface Switch
Initial Electric Field – 24 kV/cm
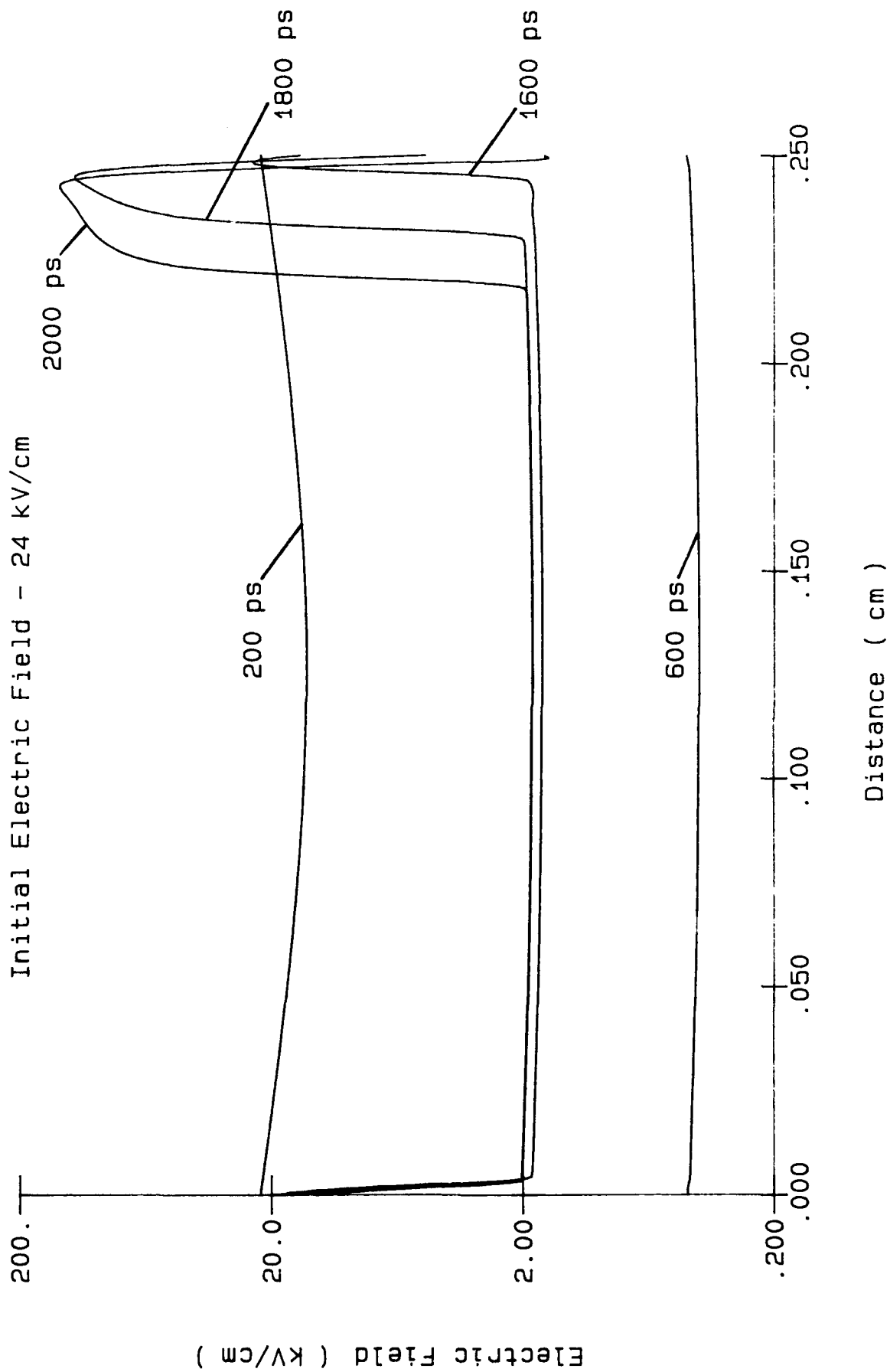
Figure 26

PHYSICAL MECHANISMS OF SURFACE FLASHOVER ON SILICON

Frazer Williams
Dept of Electrical Engineering
University of Nebraska
Lincoln, NE 68588

SURFACE FLASHOVER OF SILICON

F.E. Peterkin, T. Ridolfi, L. L. Buresh,
B.J. Hankla, D.K. Scott, and P.F. Williams
Department of Electrical Engineering
University of Nebraska-Lincoln
Lincoln, NE 68588-0511

W.C. Nunnally, and B.L. Thomas
Center for Energy Conversion Research
University of Texas at Arlington
Arlington, TX 76019

ABSTRACT

The development of high voltage semiconductor devices has been hampered by the occurrence of flashover at the surface of the semiconductor. The physical mechanisms responsible for this phenomenon are not understood. We present new empirical information which clarifies the processes responsible for surface flashover in a vacuum ambient by showing clearly that in flashover current flows primarily inside the semiconductor surface rather than in the ambient. This observation is in fundamental disagreement with the standard model for vacuum flashover of insulator surfaces.

SURFACE FLASHOVER OF SILICON

F.E. Peterkin, T. Ridolfi, L. L. Buresh,
B.J. Hankla, D.K. Scott, and P.F. Williams
Department of Electrical Engineering
University of Nebraska-Lincoln
Lincoln, NE 68588-0511

W.C. Nunnally, and B.L. Thomas
Center for Energy Conversion Research
University of Texas at Arlington
Arlington, TX 76019

There has been considerable interest recently in the application of semiconductors to high voltage switching technology.[1-21] A primary problem is that in most cases the switches flashover at the surface under average applied fields much less than the bulk breakdown field of the semiconductor. This problem has plagued the development of high voltage solid state devices for more than 30 years,[22] but the physical basis for this flashover phenomenon is still not understood.[15, 23-29]

In this paper we present new empirical information about surface flashover of silicon in a vacuum ambient which shows that in breakdown the current is carried primarily inside the semiconductor. This observation shows that the physical processes responsible for flashover of silicon are fundamentally different than those assumed in the standard model for flashover of insulators.[30][31] When breakdown occurs we observe, as have other workers, visible emission from a plasma in the ambient just outside the silicon surface. This plasma may influence the course of the breakdown, but it does not appear to be the cause of the breakdown event. This evidence supports the earlier suggestion

of Williams and Peterkin[25] that surface flashover might be caused by carrier accumulation at the semiconductor surface as a result of electric-field-induced band bending, and that of Thomas and Nunnally[29] that current filamentation in the semiconductor surface plays an important role in the process.

I. EXPERIMENTAL SETUP

Fig. 1 shows the experimental setup we used. For all results reported here the sample was a rectangular prism of nominally intrinsic silicon with long dimension 10 mm. The other two dimensions varied a little between samples and were about 7 x 2 mm. The samples were weakly n-type, with a resistivity as measured with a four-point probe of 1.3-1.6 kΩ-cm, implying a carrier density of about 3×10^{12} cm^{-3}. All samples were ground flat, etched chemically with an HF-based etching solution, washed in deionized water, and blown dry with nitrogen. The etchant polished the sample chemically, leaving a shiny surface with considerable "orange peel." The sample under test was mounted between two parallel-plane copper electrodes, and contact was made by bonding an indium solder alloy (Indium Corp. Alloy #1E) directly to the silicon using an ultrasonic soldering iron. Low-voltage I-V curves of samples prepared this way were straight lines with slope corresponding to a sample resistivity of about 1.4 kΩ-cm. The assembly was then indium soldered to a holder in the vacuum cell. The cell was evacuated with a small turbomolec-

ular pump and was typically operated at a vacuum of about 10^{-7} Torr.

Voltage was applied to the sample in pulses. The pulse generator consisted of a laser-triggered spark gap which discharged a length of 50 Ω coaxial cable into a matched 50 Ω resistor, labeled R_1 in Fig. 1. When fired without the sample in place, the generator produced rectangular pulses of magnitude up to about 35 kV with pulse length determined by the length of the charged coaxial cable. The pulse risetime depended on voltage, and was 15-20 ns for a 30 kV pulse. Jitter was typically 2-3 ns. One electrode of the sample cell was connected to the generator as shown, and the other was connected to a 50 Ω termination, labeled R_2. For all data reported here, a 30 kV voltage pulse was applied across the 10 mm length of the sample, making the average applied field 30 kV/cm. Capacitive divider voltage probes, labeled P_1, P_2, and P_3 monitored the voltage on the charged electrode of the laser-triggered spark gap, and on both sides of the sample. When used with a Tektronix 7834 oscilloscope, these probes had overall risetimes of about 1, 1, and 2 ns respectively. The total sample current could be determined from probe P_3 by dividing the output voltage by 50 Ω. The current in R_1 was monitored using P_4 to measure the voltage across a section of the distributed load.

Optical access to the front and back of the sample was provided by 4.5 and 2 inch diameter fused quartz windows, labeled W_1

and W_2, respectively. The sample was mounted so that the broad faces of the sample were visible through the two windows. A locally-constructed shutter camera and a Hammamatsu C979 streak camera were used to record the temporal and spatial development of optical events in the sample chamber. Both cameras were capable of near single-photon detection sensitivity. The shutter camera had a minimum shutter time of about 5 ns. The time resolution of the streak camera depended on the streak speed and the width of the entrance slit, and varied from less than 1 ns to about 15 ns. The time scales of the electrical and optical diagnostics could be synchronized to within about ±1 ns, but in many cases the effective time synchronization was limited by the temporal resolution of the camera. In most experiments a spherical mirror, labeled M_1, was placed behind W_2 to provide an inverted image of the back side of the sample which could be recorded by the cameras simultaneously with the image from the front side. The effective optical aperture for all photos was determined by the focusing lens, and was $f/8$.

II. EXPERIMENTAL RESULTS

Fig. 2 shows a sequence of shutter photographs of the emission recorded during flashover, and a typical breakdown current oscillogram. The sample had undergone fewer than 30 shots. Except for changes in the delay between the arrival of the voltage pulse and the onset of the rapid current rise signaling

breakdown, photos and current traces from samples which had undergone many more shots (up to 1000) were similar. In many cases the "aged" samples developed preferred breakdown paths whereas the breakdown path for "new" samples varied randomly from shot-to-shot. Both front and rear views are shown in Fig. 2, with the rear view being inverted by the optical system. The positions of the edges of the sample for both views are indicated in the figure by white dotted lines. The shutter camera was capable of acquiring only one photo at a time, so these photographs are each of a different shot. There was substantial shot-to-shot variation, but the photos are representative of the sequence of events. The shutter time was ≈5 ns, and the time when each photograph was taken is shown in the representative current trace in Fig. 2d.

Fig. 3 shows streak photographs of two breakdown events. The horizontal dimension of the photos just spans the length of the sample, and time increases downward. In order to see events from the entire surface of the sample, a cylindrical lens was used to focus emission into a narrow, slit-shaped region. Since no entrance slit was used, the time resolution was determined from the dimensions of this region and was about ±4% of full scale or 3.5 and 14 ns for Figs. 3a and 3b respectively. In Fig. 3a a spherical mirror was used behind the sample to record the emission from both broad faces. Since the image of the rear face is inverted, a front moving from left to right appears to move

from right to left. This feature helps to separate events occurring on the two faces. In Fig. 3b emission is seen from only the front face because the rear mirror was blocked.

The first optical event observable in Figs. 2a and 3a is a small spot of light appearing near the cathode about 20 ns after the arrival of the voltage pulse at the sample. By reversing the polarity of the applied voltage pulse we verified that the spot is associated with the cathode and not with a specific contact on the sample. In all cases for which we have data, this first emission appeared _after_ (typically ≈ 10 ns) the start of the rapid current rise signaling breakdown. Within 10-50 ns after the appearance of the cathode spot, emission spreads to other areas of the sample surface, moving roughly as a wavefront with a speed in the range $1 - 5 \times 10^7$ cm/sec. As seen in Fig. 3b, the motion was often sporadic, and the luminosity was non-uniformly distributed across the sample surface. Emission also often appeared in midgap, initially unconnected to either electrode. Fig. 2b shows a shutter photograph of such an event. Shutter photographs such as those shown in Fig. 2 show that the emission is localized to one, or at most a few, channels.

Fig. 4 shows typical oscillograms of the current in a sample during the earliest stage of breakdown, as measured by P_3. The trace in Fig. 4a was obtained from a "new" sample (< 10 shots), and that in 4b from an "aged" sample which had been subjected to ≈ 1200 shots. The first prominent peak in both traces is due to

capacitive coupling, and provides a convenient time marker since it results from the arrival of the voltage pulse at the sample. For the "new" sample, a rapid current increase signaling break-down occurred within 10 ns of the arrival of the voltage pulse at the sample. For the "aged" sample, on the other hand, a current rising slowly from about 2.7 to more than 6 A flowed for $\approx$60 ns before the rapid current rise signaling breakdown appeared. For "aged" samples the delay time to breakdown varied randomly from shot to shot over a typical range of 100 ns or more. It is interesting that for a series of consecutive shots the portions of the current traces before the rapid current rise signaling breakdown were quite repeatable. On one such sample, these por-tions could not be distinguished from each other for traces from ten consecutive shots.

The initial sample current of 2.7 A seen in Fig. 4b is that expected from a sample with a volume resistivity of 2.3 kΩ-cm. Low-voltage I-V curves of the same sample, both when "new" and "aged" were straight lines with slope corresponding to a resis-tivity of 1.4 kΩ-cm. This discrepancy may be due to the con-tacts, or it may reflect the thermal carrier generation rate. Current limitation due to the contacts would be consistent with our observation of luminous emission from the cathodic contact, and with the results of Donaldson et. al.[10] who found the elec-tric field in a silicon sample under similar conditions to be non-uniform along the gap axis, with the largest field near the

contacts.

The increase in breakdown delay with number of breakdown events evident in Fig. 4 was seen in all samples we studied. For one sample, after about 1000 shots breakdown almost never occurred during the 250 ns charging pulse. The "aging" effect could be partially reversed. The delay could be reduced substantially by simply leaving the sample under vacuum ($\approx 10^{-7}$ Torr) overnight, or by admitting dry grade N_2, O_2, or atmospheric air to the cell. For these treatments, the sample could usually be "aged" again through the application of several hundred additional shots. The sample could sometimes be cycled in this way several times.

The effect on breakdown of exposure to air is shown in Fig. 5, where the delay times to breakdown are plotted for 50 consecutive shots for an "aged" sample which had already undergone about 700 shots. The delay for these shots is highly variable. Also shown in the figure are the delays for the following 50 shots obtained after the sample had been exposed to atmospheric air for two days. The delay is much less variable, and is clearly less on the average than before exposure to the air.

We observed an interesting effect of illumination on the breakdown of "aged" samples. In one such sample, breakdown almost never occurred in the absence of illumination during the ≈ 250 ns voltage pulse. We carried out experiments in which a

small portion of the laser beam used to trigger the laser-triggered spark gap in the main pulse generator was used to illuminate diffusely the front surface of the sample. A portion of the main beam was split off, attenuated, and directed into a diffuser. The light scattered from the diffuser uniformly illuminated the front surface of the sample located inside the test cell. The laser pulse was about 15 ns long and struck the sample 10-20 ns before the arrival of the high voltage pulse. For intercepted illumination energy greater than some value which we estimate to be about 1 μJ, breakdown occurred within 5 ns of the arrival of the high voltage pulse at the sample. By reducing the energy below this value, the breakdown delay could be increased continuously. For a fixed laser illumination energy, the jitter in the breakdown delay was less than 5 ns. Surprisingly, it appeared that the 1064 nm fundamental wavelength of the Nd:YAG laser was more efficient at inducing breakdown than was the 532 nm second harmonic.

CW illumination from an incandescent 40 W light bulb in a desk lamp could also be used to decrease the breakdown delay time in an "aged" sample. For the sample shown in Fig. 5 after it had been "aged" and "rejuvenated" several times the delay was constant at 50 ± 5 ns. For full rated voltage on the lamp, breakdown occurred within 10 ns of the arrival of the high voltage pulse at the sample. The delay could be continuously increased by decreasing the lamp voltage.

III. DISCUSSION

In the commonly accepted model, surface flashover of insula-
tors in a vacuum occurs as a result of breakdown of gas desorbed
from the surface of the insulator.[30][31] Electrons emitted from
the cathode are responsible for desorbing this gas and for ioniz-
ing it through electron impact excitation, and the flashover
current flows in the resulting plasma. Our results show very
clearly that this model does not describe flashover of our sili-
con samples. Besides ionizing the atoms of the desorbed gas,
electron impact excitation also produces light emission, and such
emission is observed coincidentally with significant current flow
in vacuum flashover of insulators.[32] Microdischarges, a related
phenomenon, are observed in pre-breakdown activity of vacuum
gaps.[33] These discharges are thought to result from gas ejected
from the electrodes. Visible emission is observed from these
discharges for currents of the order of 10 μA.

In all cases for which we have data, breakdown started and a
current of several tens of amperes flowed before the appearance
of any visible emission at all. Further, the sample current typ-
ically rose to a value >300 A before emission appeared outside
the region of the cathode spot, and remained between 300-400 A
for 30-50 ns before the gap between the electrodes was bridged
with luminescence. Such currents could not flow through a gas
discharge as assumed in the standard model without inducing visi-
ble emission. Thus, the standard surface flashover model cannot

describe flashover of our silicon samples.

Where is the current flowing? It is unlikely that currents of this magnitude could be carried by a beam of ballistic electrons in the vacuum. Transition radiation is generally observed at the anode of vacuum gaps for prebreakdown currents greater than about 1 mA/cm^2.[34] We do not see such a emission from the anode of our gap, even though the current is many orders of magnitude larger than the reported threshold for emission of transition radiation. We conclude, therefore, that most of the current must flow in the semiconductor.

The mechanisms responsible for this current flow are not as clearly indicated. Williams and Peterkin have proposed the following model of surface breakdown in silicon.[25] Initially there is a thin, conductive layer at the surface of the silicon sample. This layer is similar to the inversion layer in MOSFET transistors, and is produced by carrier accumulation at the surface as the result of band bending induced by a normal electric field.[35] The source of this field might be charge in an insulating surface layer (either fixed charge associated with surface states or impurities in a native oxide layer), or charge bound to the surface of the layer (perhaps through the action of electron impact). When voltage is applied to the sample a thermal runaway process ensues in which ohmic heating of the conductive layer increases conductivity through increased thermal carrier generation. The ohmic heating increases in turn, leading to

thermal run-away and breakdown. Although there are some difficulties, the results we report here are generally consistent with this model.

The question of the origin of the optical emission seen in the photographs presented here naturally arises. The most likely source is luminescence from gas evaporated from the semiconductor surface as the result of heating. Emission would result from electrical breakdown of the low pressure gas or, possibly, from excitation associated with the evaporation event. A preliminary examination of the spectrum of the optical emission showed that it consists of discrete lines. The only line we were able to clearly identify was the $H\alpha$ line of atomic hydrogen. Each shot caused a pressure rise in the cell corresponding to a liberation of 10^{14}-10^{15} atoms or molecules. Analysis of the gas with a residual gas analyzer showed mass components corresponding to H, H_2, C, O, OH, H_2O, N_2 or Si, and SiO. There were also a number of components which we believe to correspond to hydrocarbon compounds.

A simple calculation[25] shows that a uniform (non-filamentary) heating process is unlikely to induce breakdown through thermal runaway at the surface on a time scale consistent with our results for "new" samples. For example, if heat flow out of the surface conduction layer is neglected, and a surface carrier density of 2×10^{17} cm^{-3} assumed, then for an applied field of 30 kV/cm and other parameters the same as the room

temperature bulk values for silicon, ohmic heating would result in a rate of temperature rise of about 2.5×10^{10} °C/sec. If we arbitrarily assume that breakdown occurs when the surface temperature has increased by 500 °C, we would predict a breakdown time of about 20 ns. While this figure might be considered consistent with the 5-10 ns delay we observe from "new" samples, it is about the shortest that can be produced using reasonable values of the parameters involved, and more realistic estimates of the effect of heat conduction out of the surface layer and of reduced carrier mobility due to the surface, elevated temperature, and high carrier densities would certainly increase it.

The localized nature of the observed optical emission implies that the gas is evaporated from channels on the silicon surface, and suggests that current filamentation occurs inside the semiconductor. The assumption of filamentary current conduction in the silicon is consistent with surface damage patterns seen after a number of breakdown events, and is strongly supported by electron photomicrographs to be presented elsewhere of samples after flashover. Thomas and Nunnally have developed a model of breakdown in which it is assumed that current flows in thin filaments at the surface of the silicon,[29] and they show that simple resistance heating in the filaments can account for breakdown on the time scale we observe.

On the basis of these considerations, we propose that the following sequence of events is responsible for inducing

breakdown at the surface of our samples. First, a layer of enhanced conductivity exists at the surface of the silicon, as discussed by Williams and Peterkin.[25] When voltage is applied to the sample, current flows in this layer, resulting in roughly uniform heating. After some time, current constriction begins near the cathode, and current in this region becomes localized to one or more thin filaments. The enhanced conductivity at the tip of each filament induces increased heating there, and causes the filament to grow in length. Breakdown is complete when one or more filaments reach the opposite electrode.

The current trace from the "aged" sample shown in Fig. 4b is consistent with this model. The slowly increasing current observed during the first 60 ns of the voltage pulse is due partly to bulk conduction, and partly to conduction in the assumed surface layer. The rate of rise of current is much too rapid to be due to heating of the bulk material, and is probably due to heating in the surface layer. The observation that the current traces from consecutive shots were quite reproducible during this time is consistent with this uniform heating interpretation. About 65-70 ns after the start of the voltage pulse current we believe that constriction began near the cathode, and one or more current filaments started growing towards the anode. At this time, the current began to increase much more rapidly, and about 10 ns later visible emission appeared from the cathode region.

Current traces such as that in Fig. 2d are also consistent with our model. After an initial fast rise, the current rise slows and then becomes noticeably flat at a value corresponding to negligible sample resistance and complete breakdown. The delay time from the application of the voltage pulse until complete breakdown could usually be determined from such current traces to within 5-10 ns. In all cases for which we have data, this time of complete breakdown coincided to within about 10 ns with the time when the visible emission first continuously bridged the gap. Assuming the visible filament to be an indicator of the position of the underlying current filament(s), this observation supports the important role in breakdown played by current filamentation, as postulated by Thomas and Nunnally.[29]

The physical mechanisms responsible for the optical triggering of breakdown which we observe remain unclear. Enloe and Gilgenbach have reported the optical induction of breakdown of a stressed insulator,[36] but it is clear that this is a different effect than that which we observe for two reasons. First, we observe induction of flashover by 1064 nm laser radiation with a threshold fluence of less than 1 $\mu J/cm^2$, and even by the radiation from a 40 W incandescent light bulb; whereas Enloe and Gilgenbach report a threshold fluence of about 10 mJ/cm^2 of 248 nm radiation. They show that the effect they observe is the result of multiphoton ionization of and subsequent electron emission from the surface of the insulator. It is very difficult to

explain the much lower threshold fluence we observe with near infrared light in terms of such a mechanism. Second, for the effect reported by Enloe and Gilgenbach flashover results from the charging of the insulator surface. Even if some charging process were operative in our case, the accumulated surface charge would be minimal bacause the dielectric relaxation time of our silicon samples is of the order of 1 ns.

The results we report suggest that the triggering of breakdown is the result of enhanced conductivity near the surface of the sample, which would be consistent with our proposed model. The observation that near infra-red is more efficient than visible light in inducing the effect is surprising, however. Perhaps in the "aged" samples the surface is damaged sufficiently that light absorbed in the top layer does not contribute substantially to the conductivity. The infra-red light would penetrate more deeply to undamaged material and result in a greater increase in current density.

The physical reasons for the "aging" effect seen in Fig. 4 also remain unclear. The most likely explanation of the effect is that a surface layer, probably an oxide, plays an important role in the breakdown. Charging of this layer could result in the surface-normal fields postulated by Williams and Peterkin.[25] Repeated flashover events might remove this layer and damage the silicon surface, thereby reducing the conductivity of this surface layer and delaying the onset of breakdown. The

procedures for reversing "aging" would tend to regrow this oxide layer on the damaged surface. An alternate explanation is based on surface damage. Each breakdown event damages some portion of the surface of the silicon. Damage would reduce carrier mobility in the inversion layer and could introduce carrier traps. Both effects would reduce the surface heating rate, thereby increasing the delay to breakdown. This latter explanation is consistent with the difference we observe between the effects of visible and infrared illumination on breakdown.

IV. SUMMARY

Our results clearly show that the standard model of surface flashover of insulators in vacuum[30][31] does not describe surface flashover of silicon in a vacuum ambient. The physical mechanism(s) responsible for flashover of silicon are not indicated as clearly, but it appears that breakdown proceeds through heating of the silicon surface, followed by current constriction in this layer and the growth of current filaments. These results support and extend the general models proposed by Williams and Peterkin,[25] and by Thomas and Nunnally.[29]

V. ACKNOWLEDGEMENTS

We have had a number of useful conversations with B.J. Ganguly and A. Garscadden regarding preparation of silicon samples, vacuum systems, and analysis of optical emission spectra.

We thank A.J. Gibbs for helpful advice on chemical etching of silicon, and N.J. Ianno and G.G. Myer for advice on several aspects of silicon processing techniques. We also thank R.A. Dougal and M.A. Gundersen for helpful discussions regarding high-current, vacuum and low-pressure discharges respectively.

REFERENCES

1. D.H. Auston, "Picosecond Optoelectronic Switching and Gating in Silicon," Appl. Phys. Lett. 26, 101 (1975).

2. A. Antonetti, M.M. Mally, G. Mourou, and A. Orszag, "High Power Switching with Picosecond Precision," Opt. Commun. 23, 453 (1977).

3. O.S.F. Zucker, J.R. Long, V.L. Smith, D.J. Page, and P.L. Hower, "Experimental Demonstration of High-Power Fast-Rise-Time Switching in Silicon Junction Semiconductors", Appl. Phys. Lett. 29, 261 (1976).

4. W.C. Nunnally and R.B. Hammond, "Photoconductive Power Switches," Los Alamos National Laboratory Report, LA-9759-MS (1983).

5. W.C. Nunnally, "Accelerator Applications of Photoconductive Power Switches," Los Alamos National Laboratory Report, LA-9760-MS (1983).

6. W.C. Nunnally and R.B. Hammond, "Optoelectronic Switch for Pulsed Power," in Picosecond Optoelectronic Devices, C.H. Lee ed. (Academic, New York, 1983).

7. W.C. Nunnally and R.B. Hammond, "80-MW Photoconductor Power Switch," Appl. Phys. Lett. 44, 980 (1984).

8. W.C. Nunnally, "Photoconductive Power Switches, a Review," in Digest of Technical Papers, 5th Pulsed Power Conference, M.F. Rose and P.J. Turchi eds. (IEEE, New York, 1985), pp. 235-241.

9. W.R. Donaldson and G. Mourou, "Improved Contacts on Intrinsic Silicon for High Voltage Photoconductive Switching," in Digest of Technical Papers, 5th Pulsed Power Conference, M.F. Rose and P.J. Turchi eds. (IEEE, New York, 1985), pp. 590-593.

10. W. Donaldson, G. Mourou, L. Kingsley, and C. Bamber, "Characterization of High-Voltage Photoconductive Switches," in Digest of Technical Papers, 6th Pulsed Power Conference, P.J. Turchi and B.H. Bernstein eds. (IEEE, New York, 1987), pp. 141-144.

11. L. Bovino, R. Youmans, M. Weiner, and T. Burke, in IEEE Conf. Record of the 17th Power Modulator Symp., Seattle, 1986, p. 219.

12. J.D. Morse and M.D. Pocha, in IEEE Conf. Record of the 17th Power Modulator Symp., Seattle, 1986, p. 211.

13. M.S. Litz, G.A. Huttlin, D.P. Davis, S. Krimchansky, L.J. Bovino, and W.C. Nunnally, "Photoconductive Switching of a Blumlein Pulser," in Digest of Technical Papers, 6th Pulsed Power Conference, P.J. Turchi and B.H. Bernstein eds. (IEEE,

New York, 1987), pp. 153-156.

14. R.M. Goeller, M.C. Thompson, R.B. Hammond, and R.A. Lemons, "Investigation of Cryogenic Photoconductive Power Switches," in Digest of Technical Papers, 6th Pulsed Power Conference, P.J. Turchi and B.H. Bernstein eds. (IEEE, New York, 1987), pp. 157-160.

15. G.M. Loubriel, M.W. O'Malley, and F.J. Zutavern, "Toward Pulsed Power Uses for Photoconductive Semiconductor Switches: Closing Switches," in Digest of Technical Papers, 6th IEEE Pulsed Power Conference, P.J. Turchi and B.H. Bernstein eds. (IEEE, New York, 1987), pp. 145-148.

16. F.J. Zutavern, G.M. Loubriel, and M.W. O'Malley, "Recent Developments in Opening Photoconductive Semiconductor Switches," in Digest of Technical Papers, 6th Pulsed Power Conference, P.J. Turchi and B.H. Bernstein eds. (IEEE, New York, 1987), pp. 577-580.

17. B. Senitzky, R.D. Schrimpf, and W.J. Kerwin, "Efficiency of Photoconductive Switches," J. Appl. Phys. 62, 4798 (1987).

18. R.K.F. Germer, K.H. Schoenbach, and S.G.E. Pronko, "A Bulk Optically Controlled Semiconductor Switch," J. Appl. Phys. 64, 913 (1988).

19. M.S. Mazzola, K.H. Schoenbach, V.K. Lakdawala, and S.T. Ko, "Nanosecond Optical Quenching of Photoconductivity in a Bulk

GaAs Switch," Appl. Phys. Lett. 55, 2102 (1989).

20. K.H. Schoenbach, V.K. Lakdawala, D.C. Stoudt, T.F. Smith, and R.P. Brinkmann, "Electron-Beam-Controlled High-Power Semiconductor Switches", IEEE Trans. Electron Dev. T-ED36, 1793 (1989).

21. M.S. Choi, J.H. Hur, and M.A. Gundersen, "Optoelectronic Bistability in Gallium Phosphide," Appl. Phys. Lett. 52, 1563 (1988).

22. C.G.B. Garrett and W.H. Brattain, "Some Experiments on, and a Theory of Surface Breakdown," J. Appl. Phys. 27, 299 (1956).

23. C.G.B. Garrett and W.H. Brattain, "Physical Theory of Semiconductor Surfaces," Phys. Rev. 99, 376 (1955).

24. B.L. Thomas and W.C. Nunnally, "Investigation of Surface Flashover in Silicon Photoconductive Power Switches," in Digest of Technical Papers, 6th Pulsed Power Conference, P.J. Turchi and B.H. Bernstein eds. (IEEE, New York, 1987), pp. 149-152.

25. P.F. Williams and F.E. Peterkin, "A Mechanism for Surface Flashover of Semiconductors," in Digest of Technical Papers, 7th Pulsed Power Conference, B.H. Bernstein and J.P. Shannon eds., (IEEE, New York, 1989), pp. 890-892.

26. B.L. Thomas and W.C. Nunnally, "Recent Developments in the

Investigation of Surface Flashover on Silicon Photoconductive Power Switches," in _Digest of Technical Papers_, _7th Pulsed Power Conference_, B.H. Bernstein and J.P. Shannon eds., (IEEE, New York, 1989), pp. 893-896.

27. S.H. Nam and T.S. Sudarshan, "Observation of Three Distinct Phases Leading to Pulsed Surface Flashover along Silicon in Vacuum," in _Proc_. _XIIIth Int_. _Symp_. _on Discharges and Elect_. _Insulation in Vacuum_, Paris, 1988, pp. 527-530.

28. S.H. Nam and T.S. Sudarshan, "Effect of Leakage Current and Light Emission on Surface Flashover along Silicon in Vacuum," in _Digest of Technical Papers_, _7th Pulsed Power Conference_, B.H. Bernstein and J.P. Shannon eds., (IEEE, New York, 1989), pp. 362-364.

29. B.L. Thomas, _Surface Flashover in Silicon Photoconductive Power Switches_, PhD Dissertation, University of Texas at Arlington, Arlington, TX, 1989.

30. R.A. Anderson and J.P. Brainard, "Mechanism of Pulsed Surface Flashover Involving Electron-Stimulated Desorption," J. Appl. Phys. _51_, 1414 (1980)

31. R.A. Latham, _High Voltage Vacuum Insulation_: _The Physical Basis_, (Academic, London, 1981), pp 229-240.

32. J.D. Cross, "High Speed Photography of Surface Flashover in Vacuum," IEEE Trans. Electr. Insul. _EI_-_13_, 145 (1978).

33. P.A. Chatterton, "Vacuum Breakdown," in Electrical Breakdown of Gases, J.M. Meek and J.D. Craggs eds. (Wiley, New York, 1978).

34. C.J. Bennette, L.W. Swanson, and R.W. Strayer, "Visible Radiation from Metal Anodes Preceding Electrical Breakdown," J. Appl. Phys. 35, 3054 (1964).

35. See for example E.H. Nicollilan and J.R. Brews, MOS Physics and Technology (Wiley, New York, 1982).

36. C.L. Enloe and R.M. Gilgenbach, "Microscopic and Macroscopic Material Property Effects on Ultraviolet-Laser-Induced Flashover of Angled Insulators in Vacuum," IEEE Trans. Plasma Sci. 16, 379 (1988).

FIGURE CAPTIONS

1. Schematic diagram of the experimental setup.

2. Shutter photographs (a, b, and c) and a representative
    current trace (d) showing the progress of surface flashover
    in a vacuum ambient on a silicon sample which had undergone
    < 30 shots. The applied voltage during the pulse was 30 kV
    across a 1 cm sample. Each photograph is from a different
    shot, and the current trace is that recorded for the photo in
    c). The timing of each photo is shown by the vertical arrows
    in the current trace. A spherical mirror was used behind the
    sample to provide a simultaneous record of events on both the
    front and rear faces of the sample. The image from the rear
    face is inverted. In the photos, the upper photo is from the
    front face, the lower from the rear. In each photo, the
    boundaries of the sample are indicated by the white, dotted
    lines.

3. Streak photographs and corresponding current traces of two
    breakdown events. The horizontal axis of the photos
    corresponds to the spatial dimension along the inter-
    electrode axis, and the vertical to the temporal dimension,
    with time increasing downwards. The vertical edges of the
    photos correspond to the positions of the two contacts to the
    sample, and a cylindrical lens was used to concentrate emis-
    sion to a thin line corresponding to ±4%, or about 0.7

division on each photo. The timing synchronization between photo and current trace is accurate to within this uncertainty.

a) Streak photo and current trace showing the early stage of breakdown. The white, dotted line is an artifact introduced to help in determining timing synchronization with the current trace. A spherical mirror was used behind to sample to provide a record of events on both faces of the sample simultaneously. Both images were focussed to a single line by the cylindrical lens. The image from the rear surface is inverted, making the front appear to travel in the opposite direction to that which it actually travelled. Fronts are seen on both faces in this photo, both emanating from the cathodic contact (on the left in the photo of the front surface). It is clear that visible emission first appeared some 10-15 ns after the onset of the rapid current rise leading to breakdown.

b) Lower temporal resolution streak photo and current trace showing the entire course of a breakdown event. In this case the rear mirror was blocked, and only emission from the front face is recorded. As in a), the cathodic contact was on the left.

4. Current traces of breakdown events in a) a "new" sample which had undergone < 10 shots, and b) and an "aged" sample which

had undergone ≈1200 shots. The initial peak is due to capa-
citive coupling and reflects the arrival of the voltage pulse
at the sample.

5. Plot showing the delay between the application of the voltage
pulse and the onset of the rapid current rise signaling
breakdown for 100 consecutive shots from a sample which had
already undergone about 700 shots. At the point indicated by
the vertical arrow experimentation was suspended, and room
air was admitted to the cell. After two days the cell was
then evacuated again, and the delay for 50 more shots
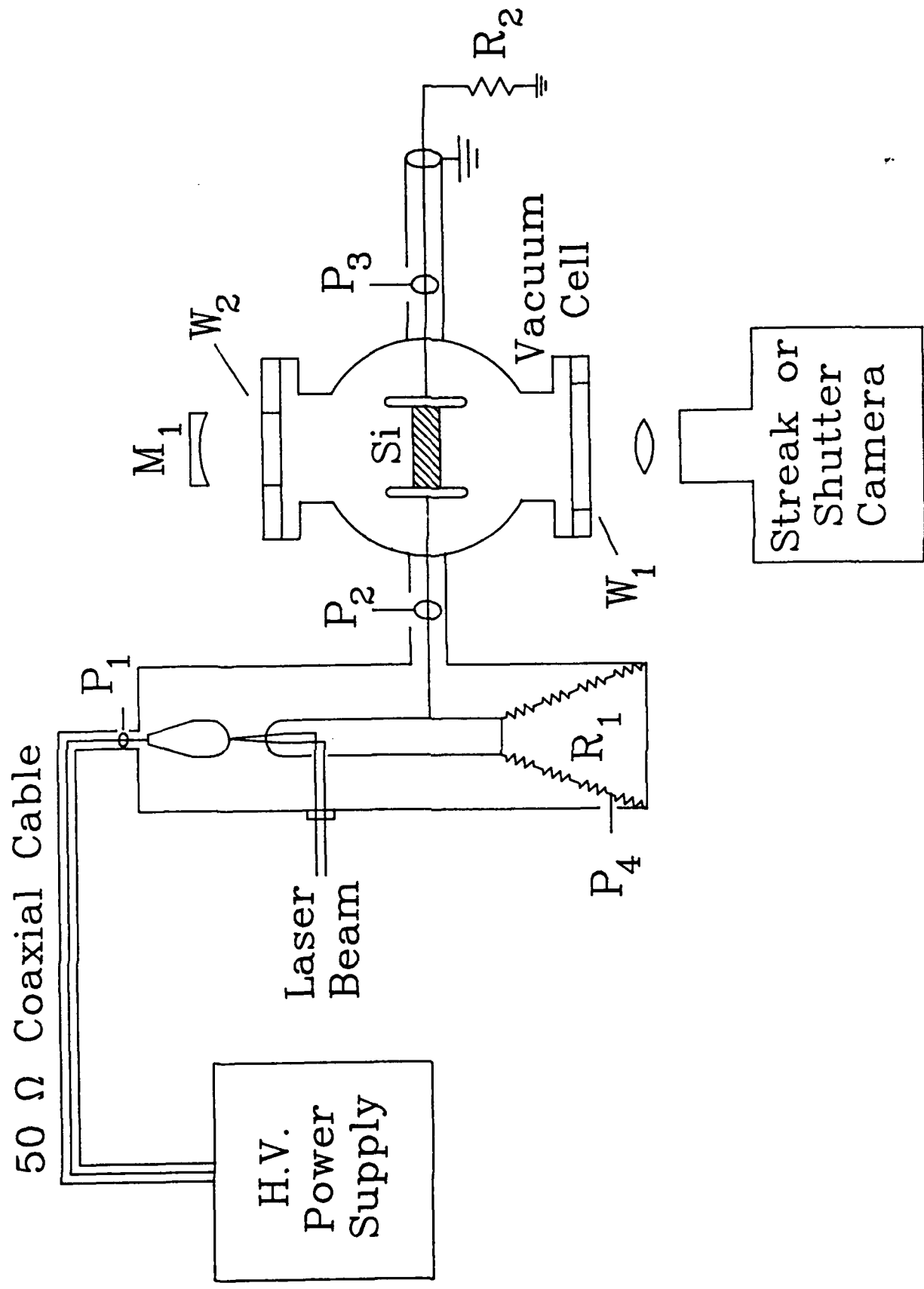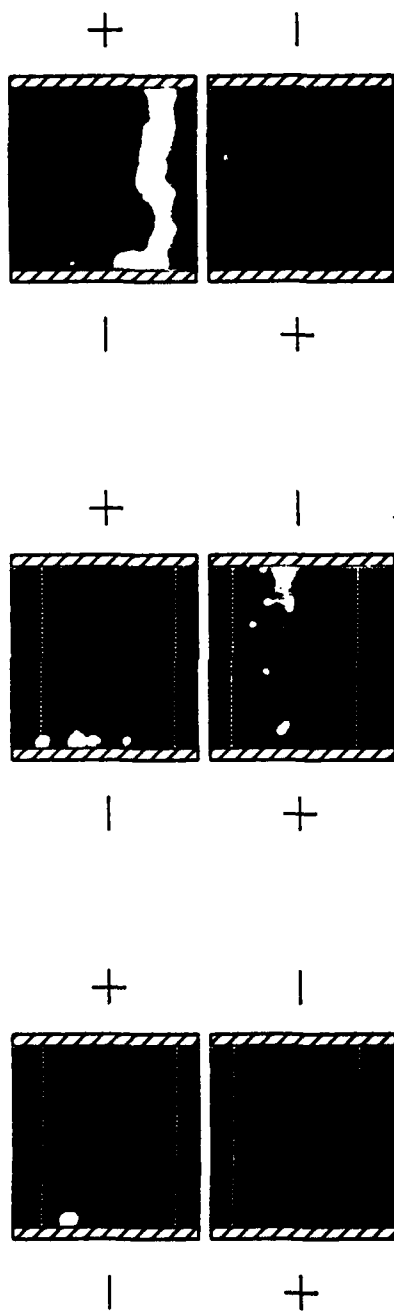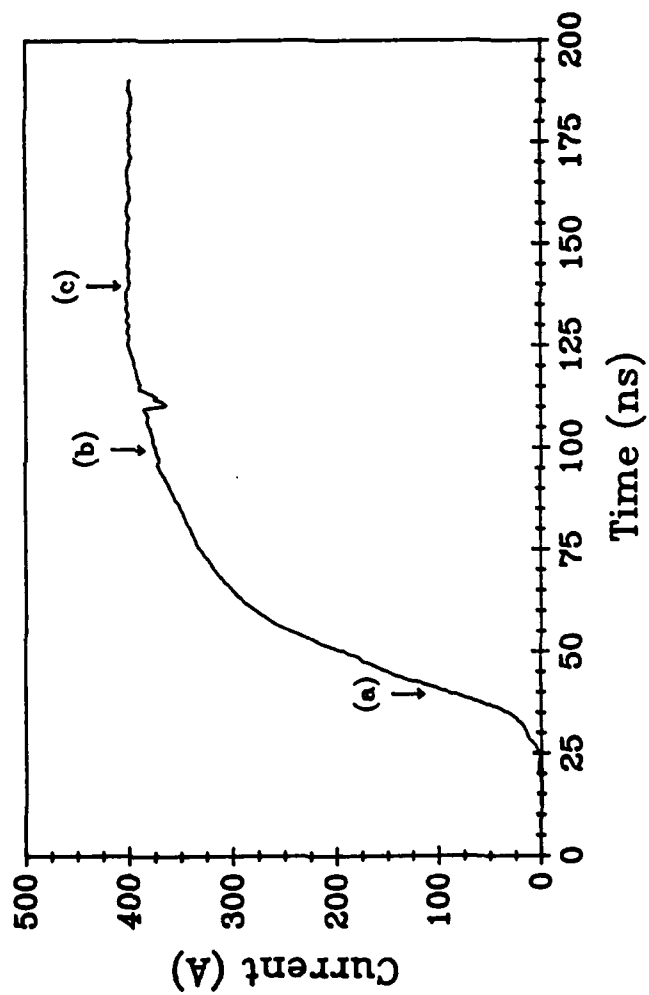recorded.

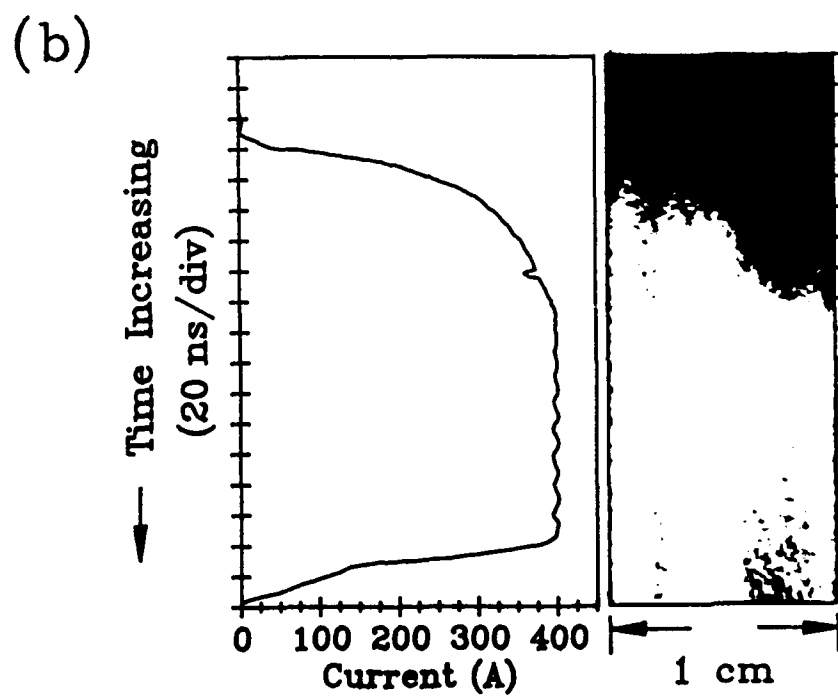Figure 1

(a)   (b)   (c)

(d)

Figure 2

(a)

Time Increasing
(5 ns /div)

Current (A)

1 cm

(b)

Time Increasing
(20 ns/div)

Current (A)

1 cm

Figure 3

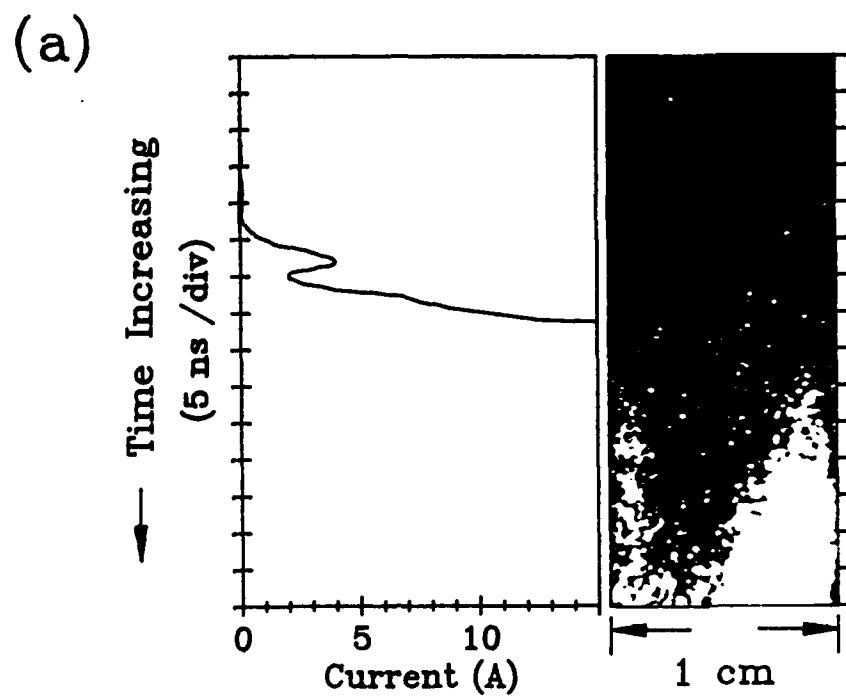Figure 4

Two day atmospheric exposure

Delay to Breakdown (ns)

Event Number
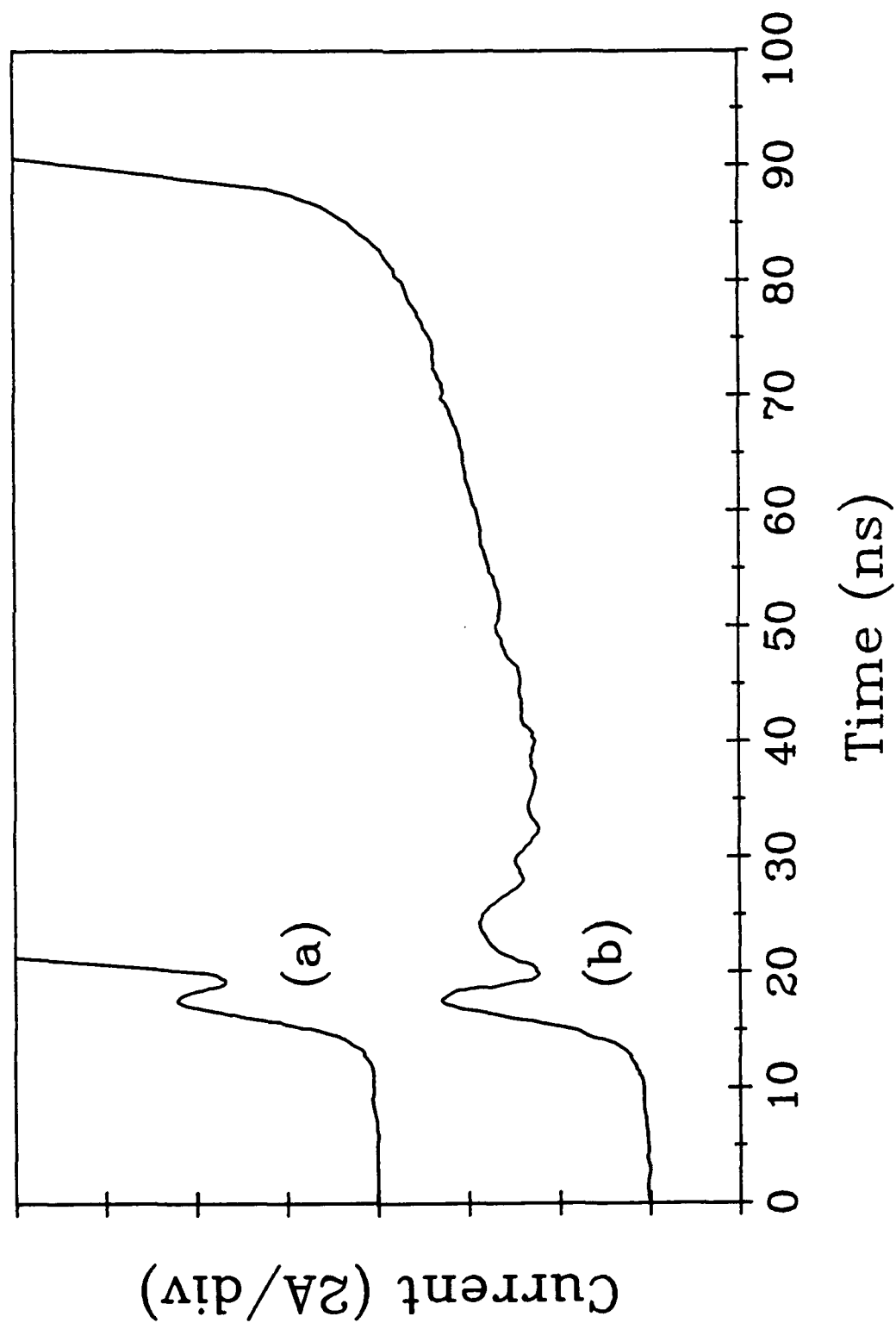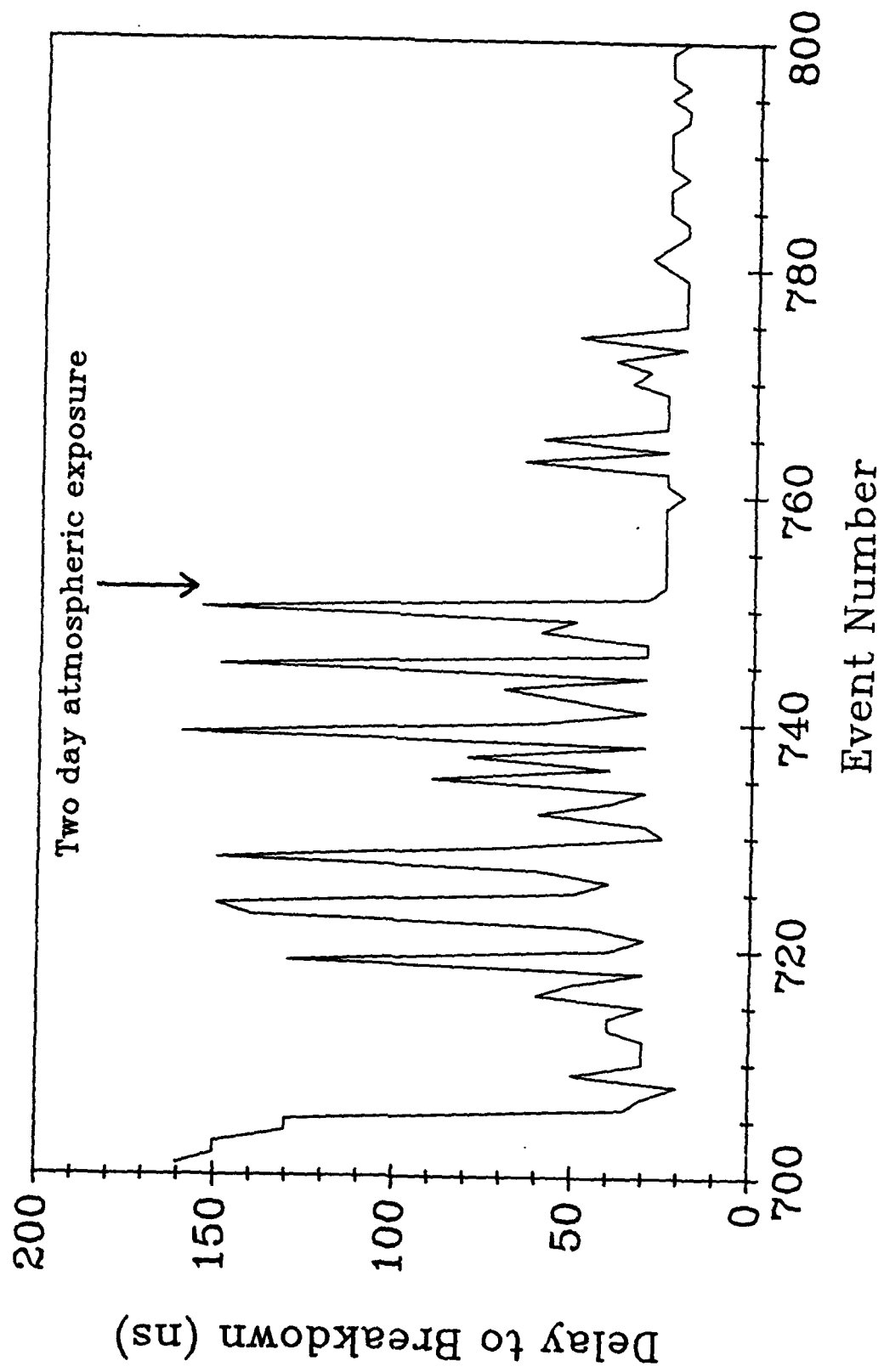
Figure 5

SOME PLASMA PHYSICS ASPECTS OF PULSED POWER

Alan Garscadden
AF Wright Aeronautical Laboratory
Wright Patterson AFB
Ohio 45433-6563

RESEARCH RESULTS FROM THE USC PULSE POWER APPLIED PHYSICS PROGRAM

Martin Gundersen
Dept of Elec. Eng-Electrophysics
SSC-420, MC 0484
Los Angeles, CA 90089

A REVIEW OF SOME RECENT USC PULSED POWER PHYSICS RESEARCH

M. A. Gundersen

Contributors include

Gas Phase

W. Hartmann, G. Kirkman, H. Bauer, R. Liou, H. Figueroa, Y. Hsu

Solid State

J. H. Hur, P. Hadizad, S. G. Hummel, K. M. Dzurko, P. D Dapkus, C.W. Myles (TTU), and H. R. Fetterman (UCLA)

University of Southern California

Los Angeles CA 90089-0484

INTRODUCTION

The USC program has active solid state and gas phase research activities. These are described separately, and some of the recent results are summarized below. The most important single result of the last few years is probably the delineation of the cathode emission mechanism in the pseudospark and back-lighted thyratron (BLT) – the super-emissive cathode.

GAS PHASE EFFORT

By way of review, a schematic of a typical BLT is shown in Figure 1. Two cylindrical cap electrodes face one another end-on and hold off the applied high voltage across a narrow gap. The device envelope contains a low pressure (< 0.5 torr) gas, such as hydrogen, nitrogen or argon.
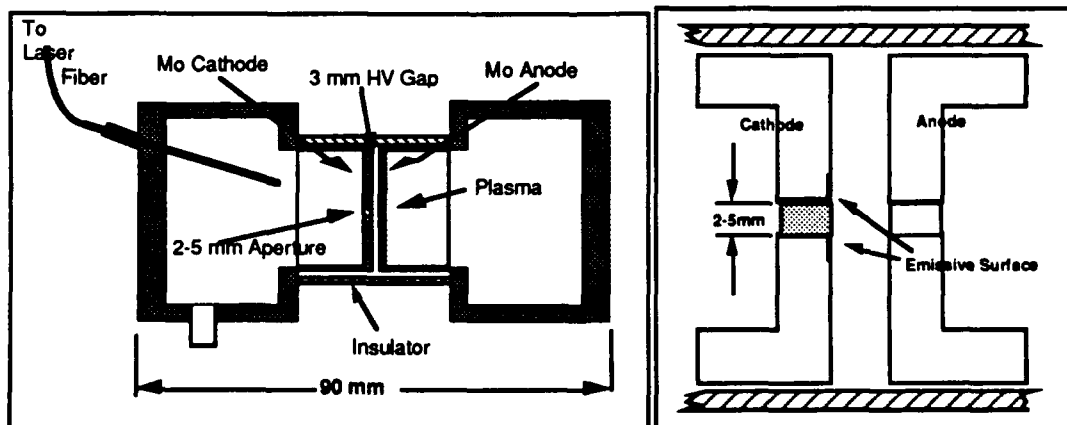

Figure 1. Structure of a BLT switch with optical triggering through an optical fiber. The switch is filled with low pressure (0.01-0.3 Torr typical) gas and is triggered by unfocused UV light incident on the back of the cathode surface. Right. Detail of super-emissive cathode electrode structure indicating the region that is ion-heated. The super-emissive area is approximately 1 cm².

1

Electrons generated by the trigger pulse – optical or electrical – pass through the small aperature in the cathode and initiate the discharge.

The BLT and pseudospark have been shown to operate with a self-heated **super emissive cathode producing electron emission current densities >10kA/cm^2**. The high cathode emission (>> externally heated cathodes) and current densities obtained in a <u>non-arcing</u> mode and with a simple, robust structure, strongly encourage consideration of new applications. The emission is observed to occur over a surface area ≈ 1 cm^2, and the cathode operates without forming an arc. This is in contrast to the high current densities achieved over very small areas in field emission devices and the high, yet rather disruptive, currents achieved in arc discharges. Although in the past comparable but localized current densities have been achieved through the formation of filamentary arcs, devices used for applications (e.g. spark gaps, felt cathodes, and field emission devices) tend to be limited. Problems associated with arc discharges include the melting, sputtering and cratering of electrode material, and addition of electrode material to the arc plasma. This new cathode supports currents that formerly required arc-type devices, such as spark gaps. It appears feasible to extend performance to devices requiring peak currents over 100,000 A, and these results suggest that high brightness cathode design may be significantly improved.

Super-emissive Cathode

The pseudo-spark and back lighted thyratron operate with a large-area (~1cm^2) superemissive cathode (~10^4 A/cm^2). The discharge is a superdense glow with a cross-section of the order of 1cm^2, rather than an arc. Streak camera recordings show that the plasma extends radially outward from the center aperture and is homogeneous. Studies of the cathode with a scanning electron microscope indicate that the discharge produces a uniform surface melting. The data supports the mechanism wherein the cathode surface is heated to the melting point by an intense ion beam present during the avalanche phase of discharge. This high temperature, together with the high field across the cathode sheath, is responsible for the extremely large and uniform field-enchanced thermionic emission over a large area.

Evidence for the anomalously large cathode emission includes scanning electron microscope pictures and streak camera data. Cathodes studied with a scanning electron microscope following operation at 6-8KA, ~1msec pulse length, 10^5 pulses in a low-pressure (~27Pa) H$_2$ discharge show evidence of melting of a thin surface layer within a radius of ~4mm, indicating that the discharge is a superdense glow with a cross-section area of the order of 1cm^2, rather than an arc. The cracks on the cathode surface also indicate that the surface has been melted, probably to a depth of several micrometers, within a very short time interval, subsequently undergoing a very rapid quenching due to heat conduction into the cold bulk material of the cathode. Streak camera recording shows that the plasma extends radially outward from the center aperture and is homogeneous and it is straightforward to clearly distinguish between arcing and glow modes.

Previous studies show that a mechanism, wherein the cathode surface is heated by an intense ion beam present during the avalanche phase of a discharge, is responsible for the

2

cathode emission. In the avalanche phase this ion beam will have an energy related to the initial voltage of the electrode gap, while during the steady-state phase the beam will have a lower energy related to the cathode fall voltage. An ion beam with 10-20MW/cm^2 lasting ~100 nsec was shown to be sufficient to heat a thin surface layer (several mm deep) to a temperature near the melting point of Mo. A high field (~10^{8}V/cm) could exists at the surface in the plasma sheath. The combination of high temperature and field can be a possibility for this extremely large field-enchanced thermionic emission after the initial cathode surface heating.

The USC project has demonstrated several new applications of the BLT device. These include:

Marx bank operation

This is important because it is a proof of principal experiment that demonstrates a method of optical control that is potentially very important for high power modulators. If modulators controled through optical fibers can be used for large systems with many modulators, the methodology for design will change.

The BLT-based Marx bank offers attractive possibilities for improved pulsed power performance for a number of applications. The BLT has been implemented in a Marx bank at USC, and has demonstrated switching of > 100 kV, with unsophisticated BLT switches. There are various possibilities for implementation. For example, high current can be straightforwardly achieved in a small device, and improved isolation can be obtained by optical triggering. At USC a small, single aperture device has been operated that switched 81.6 kA peak current in a relatively short ($\approx$ 400 nsec) ringing pulse ($\approx$ 75% reverse current) at 20 kV. Of related importance is that the USC results do not show arc-type behavior during this experiment.

Modeling of the BLT plasma

Temperature, energy, and densities of two electron distribution function components, including an isoptropic "bulk" part and an anisotropic beam, have been analyzed for a hydrogen pseudospark and/or back-lighted thyratron switch plasma with peak electron density of 1-3x10^{15} cm^{-3} and peak current density of 10^4 A/cm^2. Estimates of a very small cathode fall width during the conduction phase and high electric field strengths lead to injection of an electron beam with energies $\geq$100 eV and density of 10^{13}-10^{14} cm^{-3} into a Maxwellian "bulk" plasma. Collisional and radiative processes of monoenergetic beam electrons, "bulk" plasma electrons and ions, and atomic hydrogen are modeled by a set of rate equations and line intensity ratios are compared with measurements. Under these high current conditions, for an initial density $n_{H2}\approx$10^{16} cm^{-3} the evaluated "bulk" plasma parameters are electron density of 1-3x10^{15} cm^{-3} and electron temperature of 0.8-1 eV, the estimated "beam" density is $\approx$ 10^{13} - 10^{14} cm^{-3}. These results suggest the possibility of producing in a simple way a very high density electron beam.

The purpose of this work is to develop models that provide quantitative information about electron temperature, energy, and density of two electron components, i.e. an isoptropic and anisotropic one, in either a pseudospark or a back-lighted thyratron (BLT)

switch plasma during the conduction phase. It is of interest to understand the plasma responsible for conducting such a large current and current densities in a glow plasma, both for the purpose of understanding the inherent limitations of the switch, and in determining new applications for the plasma and the cathode. The knowledge of the velocity distribution is important to analyze transport properties such as conductivity, radiative processes and the production of particle beams. A quantitative knowledge of the plasma physics, parameters and properties will be useful for applications that include the production of particle beams, plasma based particle accelerators and plasma lens devices.

In a high voltage ($\approx$10 - 50 kV between electrodes) pseudospark operating with hydrogen gas, the initial density of molecular hydrogen n_{H2} is typically 10^{16} cm^{-3}, and the peak electron density was measured as 1-5x10^{15} cm^{-3}. In earlier work it was found that a typical hydrogen thyratron "bulk" plasma with an initial density $n_{H2}=10^{16}$ cm^{-3} is Maxwellian with electron temperature of 1eV, electron density of about 5x10^{14} cm^{-3} and dissociation degree of 0.2. In this paper, calculations are performed for a single gap geometry of a typical BLT or pseudospark and for external circuits with about 0.25-1 μs time to maximum current. Consideration of the current density and electric field strength lead to the assumption of a cathode fall produced electron beam and are discussed below. Electron densities of 1-5x10^{15} cm^{-3} and an estimated electron temperature of about 1 eV cause a very small cathode fall width of several μm during the conduction phase which results in a high electric field inside the cathode fall which is estimated to about 10^6 V/cm. Hence, because the device geometry is confined and the cathode fall is close to the "bulk" conducting region, it is necessary to consider a strong anisotropic electron component, e.g. an electron beam. Considering only electron-electron encounters the mean free path of electrons with initial energies of 100 eV is estimated to be $\approx$ 1-5 cm for ionization degrees of 0.1 - 0.5. Because the gap spacing is much smaller than this mean free path, injected electrons will not become thermalized during the gap penetration, i.e., their distribution function becomes not too broadened and is therefore assumed to be a Dirac delta function in energy.

The model thus consists of two electron groups: a monoenergetic electron beam, which penetrates a Maxwellian "bulk" plasma, directly excites and ionizes atomic hydrogen, and a 'background' Maxwellian "bulk" plasma. Collisional processes of both electron-groups with hydrogen ions and atoms and radiative transitions are considered. Re-absorbtion of spectral lines is modeled by the radiation escape factors. Calculations are performed for different initial densities of atomic hydrogen and for optically thick and thin Lyman series. The solution of the appropriate set of rate equations yields the population of atomic levels and the "bulk" electron density as a function of electron beam density and energy and electron temperature of the "bulk" plasma. It is shown that a steady state assumption fails for the process of impact-ionization due to a pulse beam electrons with a pulse duration of 100-300 ns. Once the beam dissapears the relaxation of excited states occurs immediately and a steady state condition is applied to the remaining "bulk" plasma. Comparision of calculated and measured line intensity ratios of H_α and H_β lines yields the "bulk" electron temperature and electron density.

Distribution function at the anode
(arbitrary units)

Distribution function at the anode
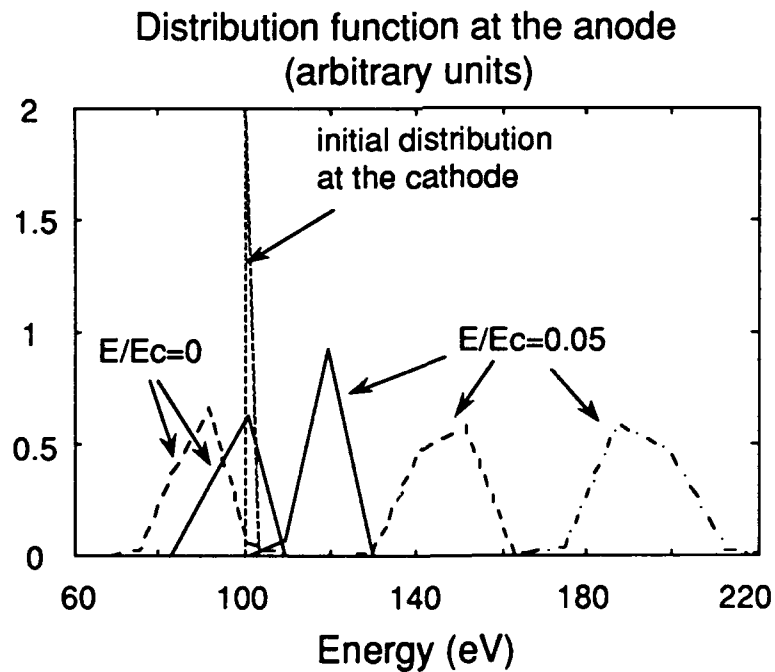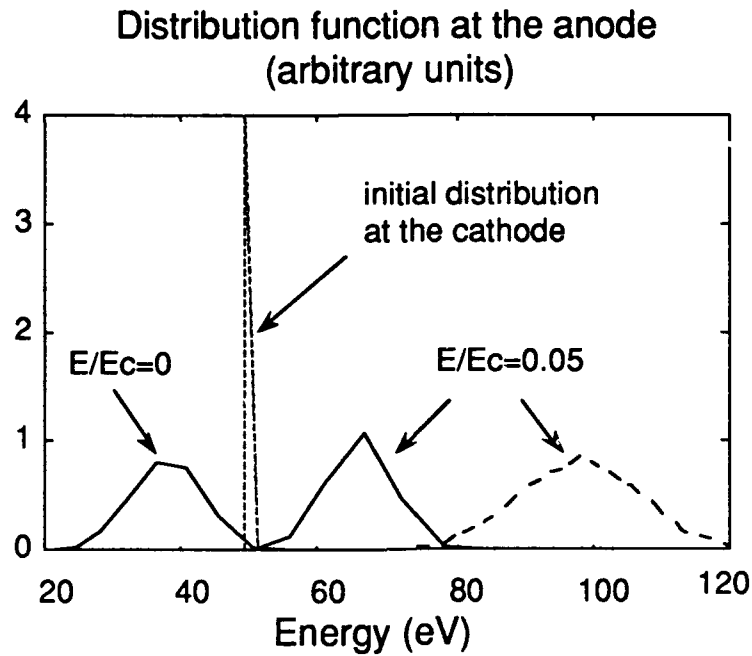## (arbitrary units)

Figure 2. Distribution function of injected electrons, initial energy of 50 (atove) and 100 eV (below) at anode after 3 mm penetration of "bulk" plasma for different values of the electric field E and "bulk" densities n. Solid line: $n = 1 \times 10^{15}$ cm^{-3}, dashed line: $n = 2.5 \times 10^{15}$ · dash-dot line: $n = 5 \times 10^{15}$.

A result of this is the prediction of a new electron beam source. An analysis Of the transport of an electron beam that is produced during the conductive phase operation in the cathode fall of a pseudospark or back lighted thyratron for applications that require a high

5

brightness electron source was performed (Fig. 2). The beam is estimated to traverse the device without thermalization if the plasma density is $\leq 2.5 \times 10^{15}$ cm^{-3}. High brightness electron sources are necessary for various new plasma based devices, and these results encourage consideration of this electron beam as a new candidate for applications including microwave generation sources, electron sources for accelerators and plasma based accelerators which require improved cathodes.

High current and high voltage operation

We report successful operation of flashlamp-switched multiple-stage back-lighted thyratrons at very high pulsed power levels, including 100 kV stand-off voltage and >70 kA switched peak current. Simultaneous optical triggering of each gap for precision timing, and plasma triggering, are also discussed. The results suggest that fairly simple multiple-gap configurations of the device will be useful for applications such as multiple high power modulator systems for accelerators.

Although operation of a single-stage 100-kV thyratron has been reported by Mancebo, this interesting switch has not been implemented as a commercially engineered device. Multiple-stage commercial switches have been reported for reliable operation at voltages up to ~250 kV. The size of these high-voltage multiple-stage thyratrons is proportional to the number of grids required and other factors. The BLT switches described are simpler and smaller than these multiple-stage thyratrons.

Current Quenching

Current quenching during the conductive phase limits peak conduction current in certain thyratron switches. The quenching phenomenon also occurs in the pseudospark. However, a remarkable feature is that current quenching is observed only below currents of $\approx$ 2-3 kA, near the onset of super-emissive behavior, and thus in the pseudospark is not an upper limit to high current operation.

One high current effect that has been observed in certain thyratrons is current quenching, or the sudden breaking of current during conduction. Although current quenching is well known for thyratrons, the effect is not well understood. Mechanisms for quenching have been proposed including gas heating, ion pumping, pinch effect, pumping of the grid-anode space, cathode double sheath, and plasma instabilities. The quenching phenomenon is also a function of thyratron design and geometry, and different quenching mechanisms may occur under different circumstances. Thyratron quenching is typically observed to occur at current densities of $\approx$ several 100 A/cm^2, limiting charge transfer to ~10^{-3} As/cm^2 without arcing. Quenching can thus impose an *upper* limit for the charge transferred in a single shot in conventional hydrogen thyratrons.

In contrast to this behavior it is found that quenching sets a *lower* limit for the charge to be transferred in the pseudospark. Quenching is observed for pressures between 15 and 40 Pa H$_2$, and discharge current $\approx$ 1-2 kA. Above these limits no quenching is observed, although the discharge still is a spatially homogeneous glow.

6

The initial phase of the discharge is a transient hollow cathode discharge (hcd) from the back of the cathode. This is followed by a transitional phase where the electron beam emerging from the hcd produces an expanding plasma column on the axis of the discharge geometry. A third phase occurs when the radially expanding plasma column reaches the wall of the cathode hole, thus electrically shielding the hollow cathode space from the main anode-cathode gap. In this last phase, the cathode surface facing the anode has to take over the discharge current and conduct very high current – the super-emissive phase.

The early transient part of the discharge can be characterized as beam-dominated due to the high voltage drop in the cathode fall and the low collisional scattering rate for beam electrons, and ionization is then governed by beam electron collisions. As the electron density increases, the cathode fall voltage drop decreases, and the bulk plasma begins to contribute to the electron current. As the secondary electron emission coefficient at the cathode surface falls below unity, the discharge becomes unstable in regard to the current transport capability of the plasma. We can roughly distinguish between two cases:

i) The bulk plasma ion current density is larger than the ion flux that can be provided by ionizing processes. Hence, a double layer will build up in the bulk plasma, resulting in an internal voltage drop that compensates the externally applied voltage and thus reduces the total discharge current to a value that is in in agreement with the ionization rate and thermal drift of the ions and electrons. Quenching of the discharge current is thus caused by ion pumping within the bulk plasma, and it's limited capability to provide a sufficient flux of ions by ionization processes.

ii) The plasma boundary can provide a sufficient ion current density due to a high ionization rate and a high flux of ions from the bulk plasma, but runs out of neutrals due to an excessively high ion pumping rate at the range of current densities considered here; this holds if the supply of neutrals from the cathode surface is insufficient (which could also happen in the case i)). Hence, current quenching is caused by ion pumping with an ion depletion occuring in the plasma boundary region of the discharge. Quenching may thus be expected because ion pumping is unavoidable in low-pressure, high-current density glow discharges, including all thyratron-type of discharges working in a diffuse glow mode. Heating of the cathode surface may be expected to produce neutral hydrogen, which for the pseudospark will tend to replenish neutral gas.

New applications: millimeter wave generation

Experimental demonstration of 100 GHz radiation from BLT.

We have measured the radiation produced in Ka band (26.5-40 GHz) and W band (75-110 GHz) and find strong signals during period of the formation of the discharge. We have also measured the electron beam current and plasma density in this discharge. A theoretical analysis is given to describe the beam-plasma interactions that may occur in this discharge, however a more detailed analysis and additional experimental studies are required to determine precisely the emission mechanism.

The experimental set up for the millimeter wavelength radiation and electron beam measurements is shown in figure 3. Radiation is measured using horn antennas and detector combinations for the two bands. The total current through the discharge is measured using a 5 mΩ current viewing resistor, and the electron beam current is measured using a fast Faraday cup. All time resolved measurements are taken using a fast transient digitizer and plug in amplifier with 500MHz bandwidth. The discharge current signal was used as a trigger to allow for the correlation of all signals on a common time axis. The electron density in this discharge was measured spectroscopically using the stark broadened Balmer beta emission line of hydrogen.

The time resolved measurements of the emissions in Ka and W band are shown in figure 3 correlated to the discharge current through the device. The microwave signals are observed during the formation of the discharge plasma when the electron beam is present. The lower frequency signal is observed first -- when the plasma density and frequency are lower.

The transmission of the radiation through acrylic plates of 25, 50 and 75 mm thickness was measured. The attenuation was observed to correlate well with published measurements for these materials for K and W band radiation.

The plasma densities in pseudospark and back-lighted thyratron switches have been observed to be of the order of 10^{14} to 10^{15} cm^{-3} when switching peak currents of a few kA. The plasma density increases rapidly during the current rise and then slowly decays after current maximum. At the beam and plasma densities measured we expect to observe radiation at the plasma frequency given approximately by 9000 $n_e^{1/2}$ Hz where n_e is the bulk plasma density. Radiation is therefore expected to be produced at about 100 GHz during the formation of the discharge plasma when the electron beam is present. In the experiments described above higher frequency radiation may have been produced that was not measurable by our detectors.

Several models exist for producing mm-wavelength radiation at frequencies >100GHz using the beam plasma interactions in the BLT. The generation mechanism depends on the spectrum of plasma electrostatic waves excited in a plasma by an incident electron beam. The case of a beam incident on a plasma is similar to that of a beam-beam interaction; the plasma can be considered to be a beam with zero directed velocity. The dispersion relation in the case of a beam-plasma interaction is that of the two stream instability

$$\frac{w_{p1}^2}{w^2} + \frac{w_{p2}^2}{(w - k_z u)^2} = 1,$$ where the target plasma has frequency w_{p1} and the

beam, of velocity u, has frequency w_{p2}, where $w_p^2 = 4\pi n e^2/m$, and n is the charge density.

Higher frequency radiation may be produced by using the two beam-plasma interaction, and a higher plasma density will produce higher frequency radiation. This can be obtained by operating the BLT at higher voltages and discharge currents. In the experiments described above the radiation is produced during the discharge formation while

8

the plasma density is growing. The Ka band signal corresponds to a density of $\approx 2 \times 10^{13}$ cm^{-3}, W band $\approx 1 \times 10^{14}$ cm^{-3}, and it is reasonable to expect $\geq$ 140 GHz if the density increases to $>2 \times 10^{14}$ cm^{-3} with the beam still present. Thus a single BLT could be a broadband source of radiation from < 26 GHz to >140 GHz.

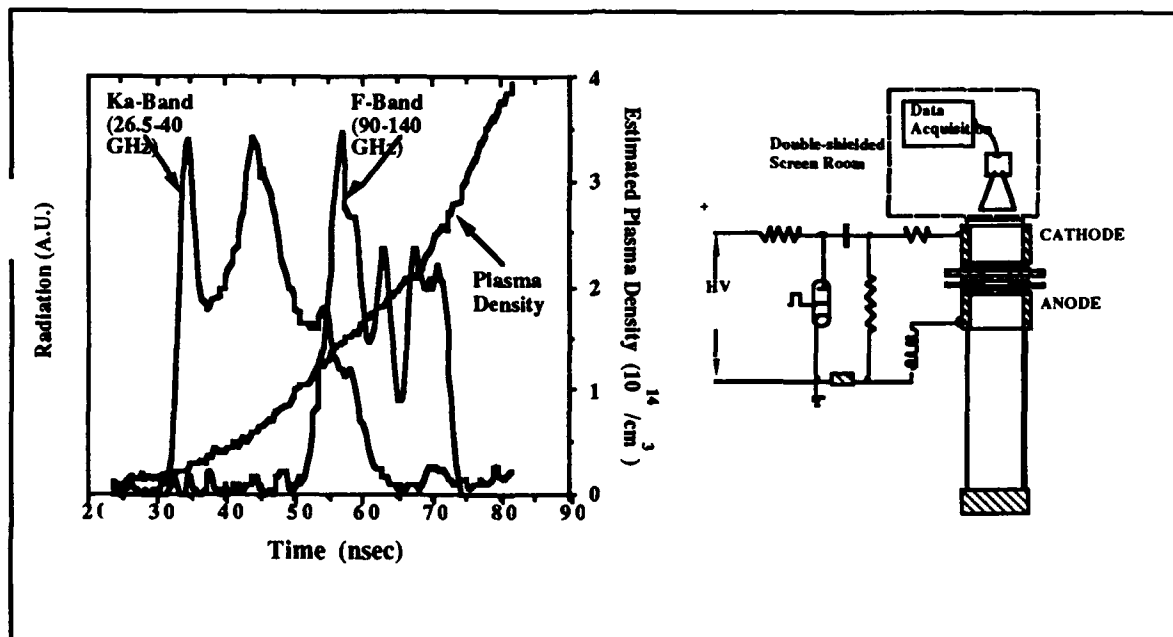

Figure 3. Experimental apparatus for preliminary results, and (left) data, including emission at > 90 GHz. Radiation and estimated plasma density versus time. The radiation power was measured in both Ka-Band (26.5-40 GHz) and F-Band (90-140 GHz). The plasma density, in an Ar background gas, is estimated from data for a hydrogen plasma and corresponding discharge current. The data show a strong correlation between plasma frequency and observed frequency of microwave and millimeter wave emission.

Transition of technology

BLT devices are being fabricated by ITT and Integrated Applied Physics inc. as well as by laboratories in Europe and Japan. Testing being undertaken at University of Texas at Arlington, Naval Surface Warfare Center Dahlgren VA, and in Europe and Japan. The BLT is being studied in Japan for laser fusion applications, and for laser isotope separation. ITT has built a BLT that has switched 30 kA at 60 kV in testing at NSWC Dahlgren. Versions of the switch are now being tested by a number of laser companies for excimer laser and other applications.

New directions and future applications

Plasma based devices are under consideration for applications include not only practical high power switches, but also advanced accelerator technology, improving accelerator beam luminosity, and as sources of electrons, ions and electromagnetic radiation. The USC effort addresses practical device implementation problems in the development of these plasma based devices, and is based on a new device with particularly

9

attractive properties for applications to plasma based accelerators, lenses, and other types of plasma sources.

These results will be of importance for new applications, including plasma based (wakefield-type) accelerators. The motivation for thinking of plasmas as a possible efficient accelerating medium lies in the fact that a plasma can support very large accelerating fields which scale as SQRT(n) where n is the plasma density. Thus, for a density of 10^{16} cm^{-3}, the maximum longitudinal accelerating field will be on the order of 10 GeV/m, which exceeds current accelerating gradients. Although there will be trade-off issues related to background collisional processes that have yet to be quantitatively determined, it appears that in order for a plasma based accelerator to be realizable, long plasma sources of several meters in length and densities higher than 10^{16} cm^{-3} will have to be developed. These plasmas will likely be pulsed. We have developed a reliable plasma source that meets many of the conditions required for a wakefield accelerator, or plasma lens – including reliability, durability, high repetition rate, shot-to-shot reproducibility, and negligible jitter. The BLT appears to be scalable to increased plasma densities without compromising performance. Applications to electromagnetic wave generation in several ways, including plasma loaded free electron lasers, other pulse generation applications, such as EMP, excimer and other laser development, will also be affected. The electron and ion beams may also be expected to be of interest for microwave, accelerator, and other technology, such as X-ray generation.

SOLID STATE EFFORT – THEORETICAL AND EXPERIMENTAL III-V BASED CONCEPTS FOR PULSED POWER APPLICATIONS

The solid state work has successfully produced an optically triggered thyristor based in GaAs, developed a model for breakdown, investigated and are developing 2 related devices, are getting at the basic limitations of GaAs for these applications, and are developing models for the physical processes that will determine device limitations. We have developed important collaborations, with Harold Fetterman of UCLA, Ch. Myles of Texas Tech, and Dan Dapkus of USC.

Theory of avalanche breakdown in $Al_xGa_{1-x}As$/GaAs heterojunction.

One promising advantage of GaAs based devices over Si based devices is that band-gap engineering can be incorporated into the device design through the use of heterojunctions. By employing a p-n $Al_xGa_{1-x}As$/GaAs heterojunction for the base region of an opto-thyristor, one can achieve a better coupling of triggering photons to the high electric field region at the base junction. Therefore, the design of a heterojunction pulsed power device requires an understanding of breakdown characteristics of p-n heterojunctions.

Avalanche breakdown was modeled by considering the electric-field-dependent impact ionization coefficients of GaAs and $Al_xGa_{1-x}As$ for all values of x. The analysis showed that as x in $Al_xGa_{1-x}As$ increased from x=0 to x≈0.45, the avalanche breakdown voltage

increased. This is the range of x for which $Al_xGa_{1-x}As$ is a direct-band-gap material. For x>0.45, the avalanche breakdown voltage decreased; thus, the maximum avalanche breakdown voltage in $Al_xGa_{1-x}As$/GaAs heterojunctions occurs for x≈0.45. Fig. 4 shows the x dependence of the avalanche breakdown voltage. The results indicate that the use of a heterojunction in the base region of a thyristor for pulsed power applications can improve the voltage blocking capability of the device.

An optically gated GaAs bipolar junction thyristor, with a semi-insulating base layer, has been studied, and the characteristics of the device as a pulsed power switch are presented. The maximum DC blocking voltage of the device was larger than 800 V, the maximum peak current in pulsed mode was higher than 300 A, and the current rate of rise was better than $1.5x10^{10}$ A/sec. These results demonstrate that GaAs based junction devices have significant potential as switching elements for pulsed power systems requiring very fast closing times.
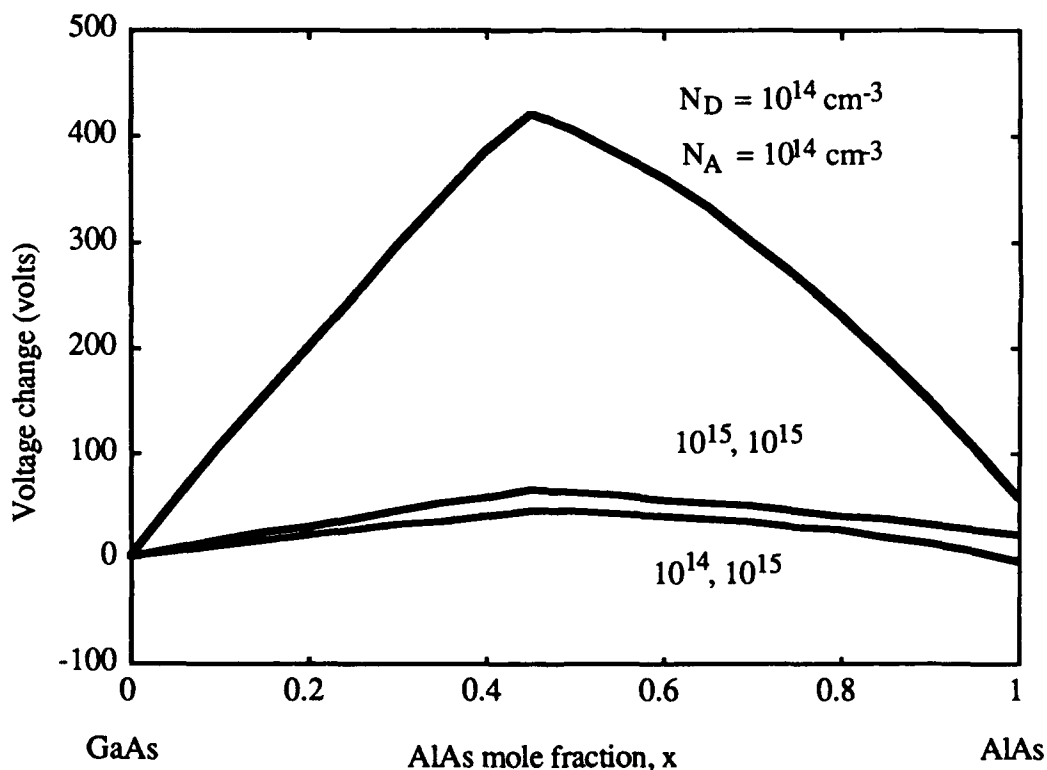

Fig. 4.   Change of avalanche breakdown voltage for p-n AlGaAs/GaAs heterojunctions as a function of AlAs mole fraction x in $Al_xGa_{1-x}As$ at T=300K. The pair of numbers for the lower two plots represents, from left to right, the donor concentration N_D, and acceptor concentration N_A. The voltage change is with respect to the homojunction value. The maximum breakdown voltage occurs for x near 0.45 which is close to the direct-to-indirect-band-gap crossover.

Demonstration of a fast GaAs pulsed power opto-thyristor

Switching devices are essential components of pulsed power systems such as high power pulsed lasers and particle accelerators. Some of the desirable properties of these switches include high blocking voltage, large peak current, large current rate of rise, low forward drop, large gating gain, gate isolation and long service life. Attractive candidates for these pulsed power switches are optically gated semiconductor switches. The III-V compound semiconductors, especially GaAs and its related ternary compounds, possess inherent material and junction properties that can provide high di/dt, and thus are attractive materials for pulsed power devices. For instance, GaAs with a larger band gap than Si can tolerate higher temperature and higher radiation energy. The larger band gap also provides larger breakdown voltage in junction devices. The direct-band-gap structure of GaAs allows efficient absorption and generation of photons, which are critical in optical gating operation. In addition, GaAs with a larger electron mobility than Si should switch faster and have lower on-resistance for the electron drift dominated devices.

Thyristors based on the GaAs/AlGaAs materials system have reported in the Soviet literature (Yu..M. Zadiranov et.al. *Sov. Phys. Tech. Phys.*, vol. 32, p. 466, 1987, for example) di/dt values of ~5×10^{10} A/sec. However, the peak currents reported in these studies were less than 10 A. An interesting observation made by these studies is that the turn-on time is shorter than the calculated transit time of carriers travelling across the base layers with saturation velocity. Although no rigorous theory exists to explain this fast turn-on of the GaAs thyristors, it is believed that the internal generation and re-absorption of photons within the base region is an important mechanism for the fast turn-on. The optoelectronic operation of these thyristors is extremely important, since it provides homogeneous turn-on of the whole device. In Si devices, it is widely accepted that the turn-on time is limited by current spreading.

In an effort to evaluate the feasibility of III-V compound based junction devices in pulsed power applications, a GaAs based opto-thyristor with a semi-insulating base layer has been studied, and the results are presented in this paper. It was found that the maximum DC blocking voltage of this device was larger than 800 volts with dark leakage current of ~12 μA. The device was able to switch a current pulse with maximum peak current of approximately 300 A and with di/dt of better than ~1.5×10^{10} A/sec.

Fig. 5 shows a cross section of the thyristor structure. A Cr-doped, Bridgman grown semi-insulating (100) GaAs substrate was used as the starting material, and the epitaxial layers in the device structure were grown by metal organic chemical vapor deposition (MOCVD). The substrate was chemically etched prior to the growth of n-barrier and p+-emitter layers on one side of the substrate. The thicknesses of these layers were both 1 μm, and the doping concentrations were ~10^{17} cm^{-3} and ~5×10^{18} cm^{-3}, respectively. The other side of the substrate was then mechanically lapped to a thickness of ~200 μm and chemomechanically polished using a combination of sodium hypochlorite and colloidal silica. The lapped and polished surface was cleaned and chemically etched, following which p-barrier and n+-emitter layers with thicknesses of 5 μm and 1 μm, and doping

12

concentrations of ~2.5x10^{17} cm^{-3} and ~10^{19} cm^{-3}, respectively, were grown. The p-barrier, semi-insulating substrate, and n-barrier layers thus form a p-i-n base of the thyristor. The n-type ohmic contact was formed by evaporating in sequence 1500 Å of Au:Ge and 400 Å of Ni. The p-type ohmic contact was formed by evaporating in sequence 100 Å of Cr and 1200 Å of Au. A 1-mm diameter, dot pattern was used for the ohmic contacts. The fabricated substrate then was cleaved to obtain individual thyristors with area of ~5x5 mm^2.
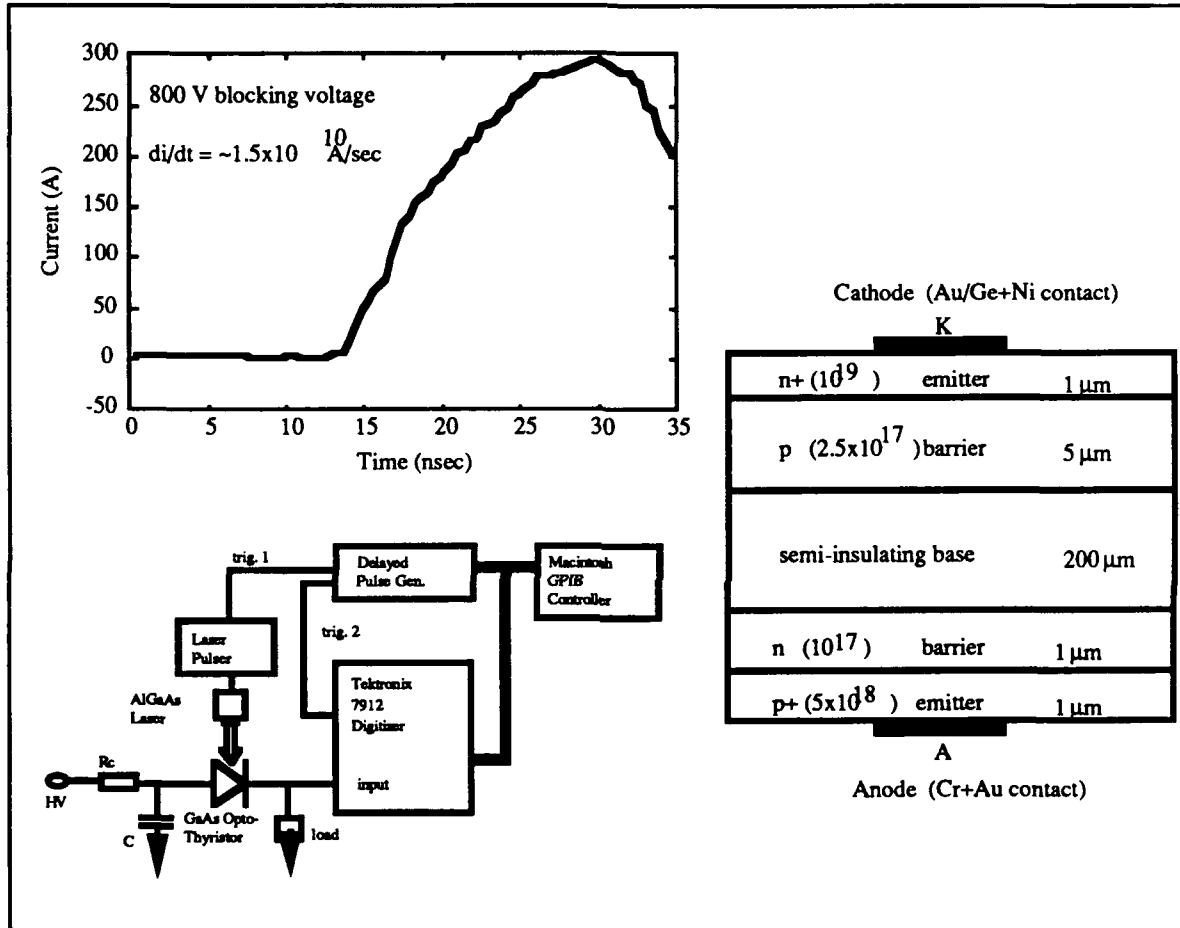

Figure 5. Right. Cross section of GaAs opto-thyristor structure with Cr-doped, Bridgman grown, semi-insulating GaAs base layer. Lower left. Circuit for measurement of the switching characteristics of the GaAs opto-thyristor. The optical gating source was an AlGaAs laser diode with an output pulse width of ~80 nsec, a peak wavelength of 848 nm, and a pulse energy of 1-2 µJ. Upper left. Typical profile of a current pulse switched with the GaAs opto-thyristor. The blocking voltage was 800 V. The storage capacitance and the load resistance were 4 nF and 5 mΩ, respectively.

The DC current-voltage (I-V) characteristics were measured for both the as-cleaved samples and the etchant-treated samples. The maximum forward blocking voltage (V_{AK}) of the as-cleaved samples was approximately 600 volts with dark leakage current of ≈ 5 µA. For the etchant-treated samples, the maximum forward blocking voltage was greater

than 800 volts with dark leakage current of ≈12 µA. This improvement in maximum blocking voltage for the etchant-treated samples over the as-cleaved samples indicates that the blocking capability depends, in part, on the edge-surface quality of the device.

The forward blocking voltage of the opto-thyristor has been compared with the breakdown voltage due to band-to-band avalanche breakdown in the base region and the punch-through in the barrier layers. For the structure under investigation, it is assumed that the electric field is constant across the semi-insulating layer of the reverse biased p-i-n base structure, and that the impact ionization would occur within this layer. An analytical evaluation gives the bulk avalanche breakdown of $V_{br}=$ ≈3700 V. The transistor effect can be taken into account reducing the device breakdown voltage as calculated to be $V_r=$ 2740 V. The measured blocking voltage of the GaAs opto-thyristor is much smaller than the calculated value. We attribute this to deep-level effects and edge breakdown.

The switching characteristics of the opto-thyristor were measured with a capacitive discharge circuit as shown schematically in Fig. 5. Care was taken in the design of the circuit to reduce the inductance which would limit the di/dt of the pulsed current. A 5-mΩ, low inductance, current viewing resistor was used to monitor the current and as the load resistor in the test circuit. A 4-nF, low inductance, disk capacitor was used as the energy storage device in the test set-up. The opto-thyristor was optically triggered with an AlGaAs laser diode. The laser diode was operated in single pulse mode with a laser pulse energy of typically 1-2 µJ, and a pulse width of ~80 nsec. The peak lasing wavelength was 848 nm.

Fig. 5 also shows a typical profile of a current pulse switched with the opto-thyristor. At a blocking voltage of 800 volts, the peak of the switched current was approximately 300 A with di/dt of ~1.5x10^{10} A/sec. An analysis indicates that the inductance in a series-RLC circuit is ~30 nH. With C=4 nF and L=30 nH, the resistance in the circuit must be less than 0.5 Ω in order to obtain a peak current of ~300 A. This suggests that the effective on-resistance of the device is less than 0.5 Ω.

The observed forward drop field corresponds to that observed for bulk semi-insulating GaAs under high current, "lock-on" conditions, and suggests that the thick base region exhibits a lock-on characteristics similar to bulk GaAs.

An optically gated GaAs thyristor was developed specifically for pulsed power applications, with emphasis on di/dt. The devices were fabricated by employing MOCVD grown epitaxial layers on both sides of a semi-insulating substrate. Devices that were etched after cleavage were able to block voltages greater than 800 volts, and were able to conduct peak currents as high as 300 A. The di/dt's for these devices were better than 1.5x10^{10} A/sec. The edge breakdown seems to limit the blocking voltage and the device lifetime. The forward drop was ~100 V and is believed to be determined by the lock-on effect occurring in the thick base region of the device.

Further investigation is necessary to reduce the edge breakdown effects such that the blocking voltage of the device is determined by the bulk avalanche breakdown voltage. Future work will involve isolating the device from the wafer edges with a guard ring

14

around the device and passivating the surface, and positively bevelling the device edges to reduce the electric field at the edges. Possible problems of ohmic contacts at high current levels and other failure mechanisms will also be studied. We conclude that the results presented in this report demonstrate that the GaAs based opto-thyristor has significant potential as a pulsed power device, and that the optoelectronic properties may significantly improve the di/dt capability of the thyristor switching.

Theoretical considerations and fabrication principles for the design and development of GaAs based "Static Induction" transistors and thyristors for pulsed power applications are presented. Compared to silicon SITs, lower on-resistance and faster switching speeds are expected. Devices are being fabricated based on implementation of chemically etched "recessed-gate" Schottky structures for improved blocking voltage capability.

A thyristor- like optoelectronic switch with high current density, based in GaP, was investigated. The switch is based on the optoelectronic bistability exhibited by certain GaP light emitting diode-type structures at 77K. The bistability is based on the negative differential resistance that occurs during the forward biased current-voltage (I-V) characteristic. A model has been developed to explain the observed s-shape I-V characteristic and describe the dependence of the I-V characteristic on the geometry of the device, doping species and concentrations. The switching time depends on the intensity of optical gating signal, bias voltage and doping concentrations. The device has high current density capability ($\sim 10^4$ A/cm^2), can be triggered optically, and its geometry and doping concentrations can be readily controlled and varied. The model has a general applicability to III-V based pulsed power switches.

PUBLICATIONS SINCE 1988

"Phonon assisted indirect recombination of bound excitons in N-doped GaP, including near resonant processes," H. Dai, M.A. Gundersen, C. W. Myles and P. G. Snyder, Phys. Rev. B 37, 1205 (1988).

"High power pseudospark and BLT switches," K. Frank, E. Boggasch, J. Christiansen, A. Goertler, W. Hartmann, C. Kozlik, G. Kirkman, C. G. Braun, V. Dominic, M.A. Gundersen, H. Riege and G. Mechtersheimer, IEEE Trans. Plasma Science, Vol. 16 (2), 317 (1988).

"Fiber optic triggered high-power low-pressure glow discharge switches," C.G. Braun, W. Hartmann, V. Dominic, G. Kirkman, M. Gundersen and G. McDuff, IEEE Trans. Electron Devices, Vol. 35, (4), 559 (1988).

"A flashlamp triggered high power thyratron type switch with remarkable plasma characteristics," G. Kirkman, W. Hartmann, and M.A. Gundersen, App. Phys. Lett. 52, 613 (1988).

"An optoelectronic bistability in gallium phosphide," M.S. Choi, J.H. Jur, and M.A. Gundersen, App. Phys. Lett. 52 (19), 1563 (1988).

"Origin of anomalous emission in superdense glow discharge," W. Hartmann and M.A. Gundersen, Phys. Rev. Lett. 60, (23), 2371 (1988).

"Evidence for large area super-emission into a high current glow discharge," W. Hartmann, V. Dominic, G.F. Kirkman, and M.A. Gundersen, App. Phys. Lett. 53 (18), 1699 (1988).

"A super-emissive self heated cathode for high power applications," W. Hartmann, G. F. Kirkman, V. Dominic, and M.A. Gundersen, IEEE Trans. Elect. Dev. 36 (4), 825 (1989).

"An analysis of the anomalous high current cathode emission in pseudo-spark and BLT switches," W. Hartmann, V. Dominic, G. Kirkman, and M. A. Gundersen, J. Appl. Phys. **65** (11), 4388 (1989).

"Phonon assisted recombination in GaAs/AlGaAs multiple-quantum-well structures", H. H. Dai, M. S. Choi, M. A. Gundersen, H. C. Lee, P. D. Dapkus and C.W. Myles, J. App. Phys. **66** (6), 2538 (1989).

"A short review of plasma science for pulse power switches", M. A. Gundersen, submitted to IEEE Trans. Plasma Sci. (invited).

"An optically gated, glow switch Marx bank," R. Liou, H. Figueroa, Y. Hsu, G. Kirkman, and M. A. Gundersen, IEEE Trans. Elec. Devices. **37**, 1591 (1990).

"A two component model for the electron distribution function in a high current pseudospark or back-lighted thyratron," H. Bauer, G. Kirkman, and M. A. Gundersen accepted for publication in IEEE Trans. Plasma Sci., **18** (2), (1990).

"Avalanche breakdown in p-n AlGaAs/GaAs heterojunctions," J. H. Hur, C. W. Myles and M. A. Gundersen, J. Appl. Phys. **67** (11), 1 (1990).

"High current plasma based electron source," H. R. Bauer and M. A. Gundersen, accepted for publication in Appl. Phys. Lett.

"Penetration and equilibration of electrons in a hydrogen pseudospark-type plasma", H. R. Bauer and M. A. Gundersen, accepted for publication in J. Appl. Phys.

"GaAs based opto-thyristor for pulsed power applications," J. H. Hur, P. Hadizad, S. G. Hummel, K. M. Dzurko, P. D. Dapkus, M. A. Gundersen and H. R. Fetterman, IEEE Trans. on Elec. Dev. submitted.

Book

M. A. Gundersen, Editor, with G. Schaefer, "The Physics and Applications of Pseudosparks," a 1989 NATO Advanced Research Workshop, to be published by Plenum Press.

Book Chapters

"Studies of fundamental processes in thyratrons," D. A. Erwin, C. G. Braun, J. A. Kunc and M.A. Gundersen, to be published in "Advances in Pulsed Power Technology Volume II: Gas Discharge Closing Switches," to be published by Plenum Press.

"The back-lighted thyratron," G. F. Kirkman and M. A. Gundersen, to be published in "Advances in Pulsed Power Technology Volume II: Gas Discharge Closing Switches," to be published by Plenum Press.

"Plasma based concepts based on the pseudospark and BLT," M. A. Gundersen, to appear in "The Physics and Applications of Pseudosparks", a 1989 NATO Advanced Research Workshop, to be published by Plenum Press.

"A two-electron-group model for a high current pseudospark or back-lighted thyratron plasma," H. Bauer, G. Kirkman, and M. A. Gundersen, to appear in "The Physics and Applications of Pseudosparks," a 1989 NATO Advanced Research Workshop, to be published by Plenum Press.

"An analysis of the high curent glow discharge operation of the BLT switch," G. Kirkman-Amemiya, R. L. Liou, T. Y. Hsu, and M. A. Gundersen, to appear in "The Physics and Applications of Pseudosparks," a 1989 NATO Advanced Research Workshop, to be published by Plenum Press.

"Cathode-related processes in high-current density, low pressure glow discharges," W. Hartmann and M. A. Gundersen, to appear in "The Physics and Applications of Pseudosparks," a 1989 NATO Advanced Research Workshop, to be published by Plenum Press.

16

"A review of the back-lighted thyratron physics and applications," M. A. Gundersen, to appear in "Laser Interaction and Related Plasma Phenomena, 9", to be published by Plenum Press.

OTHER PUBLICATIONS

"Summary of the workshop for research issues in power conditioning," M.A. Gundersen, editor, University of Southern California (1986).

"Fundamental processes in high current glow discharge switches," M.A. Gundersen, J.A. Kunc, D. Erwin, and C. Braun, Proceedings Elektronenröhren und Vakuumelectronic, NTG-Fachberichte 95, 94 (1986).

"Research issues in power conditioning," M.A. Gundersen, R. DeWitt, A.K. Hyder, C.R. Jones, J.A. Kunc, M.J. Kushner, E.P. Muntz, G. Schaefer, and P.F. Williams, Proceedings, 1986 Seventeenth Power Modulator Symposium, Hyatt Seattle, Seattle, Washington, June 23-25, 1986.

"A linear thyratron for developmental research," C.G. Braun, D.A. Erwin, G.F. Kirkman, and M.A. Gundersen, Proceedings, 1986 Seventeenth Power Modulator Symposium, Hyatt Seattle, Seattle, Washington, June 23-25, 1986.

"High power hollow electrode thyratron-type switches," K. Frank, E. Boggasch, J. Christiansen, A. Goertler, W. Hartmann, C. Kozlik, G. Kirkman, C. G. Braun, V. Dominic, H. Riege and M.A. Gundersen, Proceedings, Sixth IEEE Pulsed Power Conference, 213, June (1987).

"Switch developments could enhance pulsed laser performance," S. Spencer Merz and M.A. Gundersen, Laser Focus, May (1988).

"Preliminary results from the III-V pulsed power device research program at USC," M.A. Gundersen, Proceedings of the Semiconductor Switch Workshop, Norfolk, Virginia, May 23-24, 1988.

"A review of high power hollow electrode thyratron-type switches," M.A. Gundersen, Proceedings of the 1988 IEEE International Conference on Plasma Science, Seattle, Washington, June 6-8, 1988 (invited).

"Studies of Fundamental Processes in High Power Switches," W. Hartmann, G. Kirkman, V. Dominic and M. Gundersen, Proceedings of the European Particle Accelerator Conference, Rome, Italy, June 7-11, 1988.

"High power hollow cathode glow discharge switches," W. Hartmann, G. Kirkman, V. Dominic, M. A. Gundersen, and S.S. Merz, IEEE Conference Record of the Proceedings of the 1988 Eighteenth Power Modulator Symposium, 175, Hilton Head, South Carolina, June 20-22 1988.

"High current cold cathode glow discharge switch," G. Kirkman, W. Hartmann, T.Y. Hsu, R.L. Liou, P. Ingwersen, M. Gundersen and S.S. Merz, Proceedings of the 1988 IEEE International Electron Devices Meeting, San Francisco, California, December 11-14, 1988.

"A plasma lens candidate with highly stable properties," G.F. Kirkman, H.Figueroa, and M.A. Gundersen, Proceedings of the 1989 Workshop on Advanced Accelerator Concepts, Lake Arrowhead, California, Jan. 9-13, 1989.

"High -power thyratron-type switch for laser applications," G. Kirkman, W. Hartmann, T.Y. Hsu, R.L. Liou, P. Ingwersen, M. Gundersen and S.S. Merz, SPIE Proceedings 1046, Los Angeles, California, Jan. 19-20, 1989.

"New concepts for accelerator components", M.A. Gundersen, Proceedings of the Workshop on High Luminosity Asymmetric Storage Rings for B Physics, pgs 159-172, Caltech, April 25-28 1989.

"Modeling of the discharge plasma in a Back Lighted Thyratron," H. Bauer, G. Kirkman, J. Kunc, and M.A. Gundersen, Proceedings, Seventh IEEE Pulsed Power Conference, 495, Monterey, California, June 11-14, 1989.

"Design of an opening and closing GaAs static induction transistor for pulsed power applications," P. Hadizad, J.H. Hur, M.A. Gundersen, and H.R. Fetterman, Proceedings, Seventh IEEE Pulsed Power Conference, Monterey, California, 846, June 11-14, 1989.

"A large-area high-power superemissive cathode," W. Hartmann, R. Liou, G. Kirkman, V. Dominic, T.Y. Hsu, K. Shanahan, and M.A. Gundersen, Proceedings, Seventh IEEE Pulsed Power Conference, Monterey, California, 9, June 11-14, 1989.

"A GaAs-AlGaAs based thyristor, J.H. Hur, P. Hadizad, M.A. Gundersen, and H.R. Fetterman, Proceedings, Seventh IEEE Pulsed Power Conference, Monterey, California, pg. 341, June 11-14, 1989.

"Spectroscopic analysis of the BLT switch plasma," G. Kirkman and M.A. Gundersen, Proceedings, Seventh IEEE Pulsed Power Conference, 491, Monterey, California, June 11-14, 1989.

"Recent experimental studies of the BLT switch," G. Kirkman, T.Y. Hsu, R.L. Liou, and M.A. Gundersen, Proceedings, Seventh IEEE Pulsed Power Conference, Monterey, California, 1, June 11-14, 1989.

"Studies of multigap BLTs for high voltage applications," T.Y. Hsu, G. Kirkman, A. Litton, R. L. Liou, P. Ingwersen, H. Bauer, and M.A. Gundersen, Proceedings, Seventh IEEE Pulsed Power Conference, Monterey, California, 487, June 11-14, 1989.

"Avalanche breakdown in p-n AlGaAs/GaAs heterojunctions," Charles W. Myles, J.H. Hur, and M.A. Gundersen, Proceedings, Seventh IEEE Pulsed Power Conference, Monterey, California, 842, June 11-14, 1989.

"A high current density thyristor-like gallium phosphide based optoelectronic switch," S.D. Tsiapalas, J.H. Hur, M.S. Choi, and M.A. Gundersen, Proceedings, Seventh IEEE Pulsed Power Conference, Monterey, California, 426, June 11-14, 1989.

"The back-lighted thyratron", in "Optics in 1989", Optics News 15, 37 (1989), (invited).

"Some new applications for pseudosparks and BLT's," M. A. Gundersen, Transient Hollow Cathode Discharge Phenomena Workshop, Paris, Sept. 11-12, 1989.

"The high current glow discharge operation of the back-lighted thyratron and pseudospark switch," G. Kirkman-Amemiya, H. Bauer, R.L. Liou, T.Y. Hsu, H. Figueroa, and M.A. Gundersen, Transient Hollow Cathode Discharge Phenomena Workshop, Paris, Sept. 11-12, 1989.

"A Marx generator using back lighted switches", R. Liou, H. Figueroa, Y. Hsu, G. Kirkman-Amemiya and M.A. Gundersen, Proceedings, 1989 High Voltage Workshop, Myrtle Beach SC, October 17-19, 1989.

"A review of the back-lighted thyratron physics and applications," M. A. Gundersen, Proceedings, 9th Intl. Workshop on Laser Interaction and Related Plasma Phenomena, Monterey, CA, Nov. 6-10, 1989 (invited).

"GaAs based opto-thyristor for pulsed power applications," J. H. Hur, P. Hadizad, S. G. Hummel, K.M. Dzurko, P. D. Dapkus, M. A. Gundersen, and H. R. Fetterman, Proceedings, IEDM 1989.

"High current back lighted thyratron switches," G. Kirkman-Amemiya, T. Y. Hsu, R. L. Liou, and M. A. Gundersen, Proceedings of the International Magnetic Pulse Compression Workshop, Granilbakken, Lake Tahoe, Feb. 12-14, 1990.

"High-power multiple-gap back-lighted thyratrons," T. Y. Hsu, G. Kirkman, R. L. Liou, H. Figueroa, and M. A. Gundersen, Nineteenth Power Modulator Symposium, San Diego, California, June 26-28, 1990.

"Avalanche breakdown characteristics of AlGaAs/GaAs p-n heterojunctions for pulsed power applications," J. H. Hur, M. A. Gundersen, and C. W. Myles, Nineteenth Power Modulator Symposium, San Diego, California, June 26-28, 1990.

"High-speed static induction transistor for pulsed-power applications," P. Hadizad, J. H. Hur, H. R. Fetterman, S. Hummel, and M. A. Gundersen, Nineteenth Power Modulator Symposium, San Diego, California, June 26-28, 1990.

"GaAs opto-thyristor for pulsed power applications," J. H. Hur, P. Hadizad, S. R. Hummel, P. D. Dapkus, H. R. Fetterman, and M. A. Gundersen, Nineteenth Power Modulator Symposium, San Diego, California, June 26-28, 1990.

"A study of the high-current pseudospark and back-lighted thyratron switch," G. Kirkman-Amemiya, H. Bauer, R. L. Liou, T. Y. Hsu, H. Figueroa, and M. A. Gundersen, Nineteenth Power Modulator Symposium, San Diego, California, June 26-28, 1990.

Patents:

Light initiated high power electronic switch (U.S. Patent 4,771,168, Sept. 13, 1988).

Back-lighted thyratron Marx bank (U.S. Patent 4,890,040, Dec. 26, 1989).

19

MODELING PULSE POWER PLASMA SWITCHES: HOLLOW CATHODES AND BEAMS

Mark Kushner
Gaseous Electronics Laboratory
Dept of Electrical & Computer Engineering
University of Illinois
Champaign, IL 61820

MODELING PULSE POWER PLASMA SWITCHES: HOLLOW CATHODES AND BEAMS

Hoyoung Pak and Mark J. Kushner
University of Illinois
Department of Electrical and Computer Engineering
607 E. Healey, Champaign, IL 61820

Abstract

A comprehensive model for the optically triggered pseudospark, or Back-Lit-Thytraron (BLT) is presented. The model accounts for ballistic electrons by using a multibeam-bulk formulation. The onset of a hollow cathode effect (HCE) during commutation, which has been inferred from experimental results, is predicted by the model. The majority of electrons emitted from the inner surface of the cathode are trapped by the HCE, but they do generate secondary beam and bulk electrons which may escape from the cathode. Modifications to the conventional BLT geometry are discussed.

I. Introduction

The pseudospark is a low pressure discharge ($<$ 1 Torr) which operates as a glow yet has many of the characteristics of high pressure sparks or arcs.[1-9] The pseudospark was first developed by Christiansen, et. al. as a particle beam source.[10] Subsequently, the pseudospark was configured as a high voltage switch. One variant of the pseudospark switch introduced by Gundersen et. al is optically triggered and has come to be known as the Back-Lit-Thyratron, or BLT.[1,2] Its conventional geometry consists of a hollow cathode and anode in an inverted cup structure. (See Fig. 1.) The opposing faces of the electrodes have central holes and are closely placed to obtain a high holdoff voltage according to Paschen's Law. The BLT is triggered by using the photoemission of electrons from the inner surface of the cathode generated by a UV source, typically a flashlamp or laser. This method of triggering allows the device to electrically float since the triggering light may be generated remotely and coupled into the device using conventional optics or fibers.

The nonplanar geometry of the BLT is, in fact, necessary for its unique operating characteristics. High voltage is held off by the closely spaced faces of the anode and cathode. Breakdown and avalanche, though, require a longer path length than provided by the cathode-anode spacing. The generation of photoelectrons on the inner surface of the cathode provides electrons which have a longer path to the anode. Some amount of electric field penetration into the interior of the cathode, though, is required to consistently initiate the avalanche. Optimum operation of the BLT is then a compromise between two effects. Minimizing the size of the cathode hole will minimize the the penetration of anode potential into the interior of the cathode and therefore maximize holdoff. Having a high degree of potential penetration, though, will promote switching and insure a short period of commutation.

The discussion above, though, is largely based on the vacuum

configuration of the electric potential. The BLT is inherently a multidimensional dynamic device. In particular, the generation of space charge during switching deforms the electric potential in the interior of the cathode in the vicinity of the cathode hole.[11,12] This process increases the penetration of the electric potential into the interior of the cathode and leads to a hollow cathode effect (HCE).[13] In the HCE electrons emitted from the cathode oscillate in a potential well and slow dominantly by ionizing collisions. In the BLT, the onset of a HCE generates a dense plasma within the cathode, thereby providing the means to close the switch.

Due to the transient and multidimensional nature of the BLT, constructing a viable model is problemmatic. The voltages (10's kV to 100 kV), gas pressures (< 1 Torr), electrode separations (mm's), anode depth (cm's) and switching times (10's ns to 100'ns) place the BLT in a regime where the electron energy distribution (EED) is not in equilibrium with the local electric field. The observation of both dense glows and directed beams[9,14] in pseudosparks suggest that representing the electron swarm as a single fluid may not be an adqequate description.

We are developing models to predict the triggering and switching performance of the BLT. The goal of this work is to provide a general computational design tool to both investigate the basic physics of psuedospark devices and to contribute towards optimizing their operation. In developing models for low pressure discharges many simulation techniques may be employed. From computationally less intensive to more intensive techniques, these methods range from fluid representations for the electrons and ions using the local field approximation (LFA) to Particle in Cell Simulations (PICS) which make no apriori assumptions on the EED or transport coefficients.[15,16] The former method does not adequately represent the nonequilibrium aspects of the EED. The latter method is, at the moment, too computationally taxing for our purposes. Our approach has been to conceptually separate the electrons into at least two groups; the beam and the bulk.[17,18] In this formulation, the bulk component is represented by a fluid while the beam component is ballistic in nature. This technique has recently been applied to investigating the conduction phase of the BLT.[19] We are extending the technique to investigate the beam generating capabilities of the BLT.

II. Description of the Model

In this section, our model for the BLT will be described. The basic framework of the mcdel takes responsibility for the conservation of particles; electron and ions.[11] This is performed by solving their respective continuity equations. Enhancements to the model include solving the momentum and energy equations, and accounting for electrons in the high energy tail of the EED. The basic model consists of a 2-dimensional, two fluid representation for the electrons and ions whose densities are solved for in conjunction with Poisson's equation for the local electric potential. The user may define the arrangment and dimensions of the electrodes. Our implementation of the electron and ion continuity equations are

$$\frac{dn_e}{dt} = n_e k_I N + \nabla \cdot (n_e \vec{v}_e) + \nabla \cdot (D_e \nabla n_e) + S \tag{1}$$

$$\frac{dn_i}{dt} = n_e k_I N + \nabla \cdot (n_i \vec{v}_i) + \nabla \cdot (D_i \nabla n_i). \tag{2}$$

The subscripts e and i denote electrons and ions respectively. In Eqs. 1 and 2, n is a density, k_I is the ionization rate coefficient, $\vec{v}$ is an advective velocity, D is a diffusion coeffient, and S accounts for the secondary emission of electrons from the cathode by ion bombardment and photoemission. The continuity equations are constructed using finite differences on a nonuniform cylindrical mesh having azimuthal symmetry. The equations are integrated in time using a fifth order Runge-Kutta method.

The parameter space in which a model based solely on the continuity equations is accurate depends largely on the accuracy of the transport coefficients or variables: k_i, $\vec{v}_e$, $\vec{v}_i$, $\vec{D}_e$, and $\vec{D}_i$. If p·d (pressure · electrode separation) is sufficiently large and E/N is sufficiently small, the transport coefficients may be obtained using the Local Field Approximation (LFA). In this approximation all coefficients are functions only of the instantaneous local electric field. For example, $\vec{v} = \mu \cdot \vec{E}$, where μ is the particle's mobility and E is the local electric field. In using the LFA inertial effects are ignored, and electrons have no memory of a previous velocity or trajectory. The LFA is, in fact, satisfactory in certain portions of the BLT, but is not accurate in regions where there are large gradients in the electric field and inertial effects dominate. When the LFA is not accurate, higher order moments of Boltzmann's equation must be included to account for nonequilibrium in either momentum or energy.

We included the momentum and energy equations for electrons in our model to account for inertial effects. Transport coefficients for the ions, though, are obtained using the LFA. Our implementation of the momentum equation is

$$\frac{d(n_e \vec{v}_e)}{dt} = \frac{q n_e \vec{E}}{m_e} - \vec{v}_e \nabla \cdot n_e \vec{v}_e - n_e \vec{v}_e \upsilon_c \tag{4}$$

where, m_e is the electron mass, and υ_c is the collision frequency for momentum dissipation. Our implementation of the energy equation is

$$\frac{d(n_e \bar{\epsilon})}{dt} = \vec{j} \cdot \vec{E} + \nabla \cdot \kappa \cdot \nabla T_e - \nabla \cdot (\vec{v}_e n_e \bar{\epsilon} - D_e \nabla n_e \bar{\epsilon}) - \sum_i n_e \ell_i \tag{5}$$

where $\bar{\epsilon}$ is the swarm averaged energy, j is the electron current density, T_e is the equivalent electron temperature, κ is the electron thermal conductivity and and ℓ_i is the rate of loss of energy by collisions for process i. All

coefficients in Eqs. 4 and 5 are a function of $\bar{\epsilon}$ and are obtained in the following manner.

When implementing the LFA, the energy equation reduces to

$$\frac{e^2 E^2}{m_e \nu_c} = \sum_i \mathcal{E}_i(\bar{\epsilon}) = \sum_i \Delta\epsilon_i \cdot k_i(\bar{\epsilon}) \cdot N \tag{6}$$

where k_i is the rate coefficient for process i and $\Delta\epsilon_i$ is the energy loss for that process. By solving Eq. 6 one may obtain, for the gases of interest, a unique correspondence between E/N, average energy and distribution averaged transport coefficients. That is, one may construct a function $\bar{\epsilon} = F(E/N)$, and its inverse $E/N = F^{-1}(\bar{\epsilon})$. Taking advantage of this correspondence, one can obtain transport coefficients by using their functional form obtained from the LFA but using the energy equivalent value of E/N as the arguement. For example, $\mu = \mu_{LFA}(F^{-1}(\bar{\epsilon}))$. The nonequilibrium nature of the EED is manifested by the energy equivalent E/N not being equal to the local instantaneous E/N.

Although the majority of the electrons in a pseudospark discharge are well described by swarm averaged transport coefficients, in many cases there is a ballistic component to the EED. This ballistic component represents electrons which, since their initial ionization or emission, have had few, if any, momentum transfer or energy loss collisions. Accounting for the beam component of the EED is difficult since beams may be generated at the site of any ionization or electron emission if it is adjacent to or in a region of high electric field gradients. The ballistic component beginning at any given site can be thought of as a "beamlet" which has a unique trajectory and energy. Given this uniqueness, beam electrons in the model are conceptually separated into two components; primary beams and secondary beams. The primary beams represent those electrons emitted from the cathode, either by ion bombardment or photoemission, and have not suffered inelastic collisions. Primary beam electrons which do suffer inelastic collisions are taken out of the primary beam component and placed in either a secondary beam or into the bulk electrons. The secondary beams are then treated identically to primary beams with the exception of their source of origin.

To account for the unique paths of the beam electrons, the computational grid used for the beamlets differs from that used for the bulk electrons. Conceptually each beamlet, i, follows an independent path, $\vec{s}_i$, obtained by integrating its equation of motion defined by its vector velocity. The path consists of steps of length Δs. The location of beam electrons in beamlet i at step j is s_{ij}. The velocity of beamlet i is simply

$$\vec{v}_{ij} = \int_{s_{io}}^{s_{ij}} \frac{q\vec{E}}{m_e} \frac{ds}{|\vec{v}_{ij}|} \tag{7}$$

where the integral is along the path i from the beamlet's point of origin

(s_{io}) to location s_{ij}. The paths $\vec{s}_i$ overlap the computational grid for the bulk electrons and the site on the bulk grid which underlies location s_{ij} is $\vec{r}(s_{ij})$. Since beamlets can start from any location within the BLT the energy of a beamlet is not necessarily equal to the local plasma potential, as would be the case for a beamlet which starts at the cathode. The energy of a beamlet at location s_{ij}, ϵ_{ij}, is conceptually $q(\phi(s_{ij})-\phi(s_{io}))$ where ϕ is the local electrical potential. In practice, ϵ_{ij} is obtained directly from its velocity.

All electrons emitted from the cathode are initially classified as primary beam electrons. Therefore, all electrons ultimately trace their origins to beam electrons. The coupling between the beam and bulk components is through the source term, S. The source term represents beam electrons which undergo inelastic energy loss collisions or generate secondary electrons by ionization. This source term is

$$\left[\frac{\partial n_e(\vec{r}_b)}{\partial t}\right]_b =$$

$$\sum_{i,j} \gamma_{ij} \cdot [N \cdot (\sigma_T(\epsilon_{ij}) + \sigma_I(\epsilon_{ij})) \cdot \Gamma_{ij} \cdot R_v(s_{ij})] \cdot \delta(\vec{r}_b - \vec{r}(s_{ij})) \qquad (8)$$

where the sum is over beamlets i and path locations j, σ_T is the total inelastic cross section, σ_I is the ionization cross section, Γ is the flux of beam electrons, and R_v is the ratio of the volume of the computational cell of the beam to that for the bulk electrons. γ_{ij} is a local weighting function which determines the fraction of ionizations which feed the bulk (as opposed to secondary electron beams).

When a beam electron undergoes a collision and enters the bulk component, it brings with it energy which must be accounted for in the energy equation for the bulk. This contribution is

$$\left[\frac{\partial[n_e\epsilon(\vec{r}_b)]}{\partial t}\right]_b = \sum_{i,j} \gamma_{ij} \cdot [N \cdot (\sum_k (\epsilon_{ij}-\epsilon_k) \cdot \sigma_k(\epsilon_{ij}) +$$

$$(\epsilon_{ij}-\epsilon_I) \cdot \sigma_I(\epsilon_{ij})) \cdot \Gamma_{ij} \cdot R_v(s_{ij})] \cdot \delta(\vec{r}_b - \vec{r}(s_{ij})) \qquad (8)$$

where ϵ_k is the excitation energy of process k, and ϵ_I is the ionization energy.

III. Beam Generation in Pseudospark Thyratrons

The beam-bulk model has been used to simulate electron transport during the commutation phase of switching in the BLT. We have chosen a geometry which

will demonstrate both the switching and beam generating capabilities of the BLT. The electrodes of the BLT we modeled consisted of a cylindrical hollow cathode and hollow anode with a central hole and a collection plate for the beam, as shown in Fig. 2. This geometry differs from the conventional BLT switch by the hole in the rear of the anode which allows beams to escape. In this study, the cathode is grounded, and the anode and collection plate are charged to 10 kV. The gas is hydrogen at 0.4 Torr unless stated otherwise. The anode-cathode separation are 0.4 cm, and the radii of the cathode and anode holes are 0.4 cm. We define the switch to be closed when its resistance falls to $\simeq 10\ \Omega$. Switching is initiated by illuminating the inner surface of the cathode by a laser (13 ns FWHM).

The secondary electron beam flux (displayed using a dot plot) and one of the trajectories of the primary electron beams (displayed using lines) 60 ns after illumination of the cathode are shown in Fig. 2a as a function of position. Primary beam electrons emitted from the cathode tend to become trapped inside the hollow structure with only a small fraction escaping from the cathode. Primary beam electrons oscillate within the potential trap formed by the hollow cathode, as shown in Fig. 2b, and generate both bulk and secondary beam electrons. This is the well known HCE.[13] Although switching in the model can be obtained when excluding beam electrons and eliminating high energy pendulum electrons, we do not believe this is an accurate representation. Some aspect of the HCE persists even with the bulk electrons. The high emittance beam of electrons which is detected along the axis of experimental devices consist, according to our model, dominantly of secondary electrons. The secondary electrons are generated in the vicinity of the cathode hole, and are not subject to the HCE. BLT's operating in this fashion are similar to the hollow cathode beam generators developed by Rocca et al.[20], and the hollow cathode switches investigated by Ngo et. al.[21]

The relative contributions and locations of primary and secondary beams change during triggering and commutation, as shown in Figs. 3 and 4. Here we see the relative primary (Fig. 3) and secondary (Fig. 4) beam fluxes early during triggering when the UV flux is present and just prior to switch closure. At the time of triggering the primary beams occupy a large portion of the cathode cavity. Only a small fraction of the beams escape. Secondary beams are themselves generated throughout the cathode cavity at this time and escape along the axis. Just prior to closure (approximately 50 ns after triggering for these conditions) the primary beams are generated only in the vicinity of the cathode hole. This is a result of there being significant ion bombardment only at this location. The relative intensity of primary beams emanating from near the edge of the cathode hole, though, increases. Due to the coarseness of our computation mesh, there may be missing primary beams which actually escape from the cathode. These are shown schematically as the dotted area in the figures. The total current in these beams, though, is expected to be small. The trajectories of the secondary beams do not significantly change during commutation, as shown in Fig. 4. The sites of generation of the secondary beams move somewhat closer to the central hole to reflect the migration of primary beams to these locations.

The separation of the EED into bulk and beam components may be misleading since even the bulk electrons may display beamlike behavior. The beamlike behavior is caused by rapid acceleration of the bulk electrons near the

entrance to the cathode-anode gap. The beam like behavior of the bulk electrons are shown in Fig. 5a where the beam and bulk curent densities are compared at a time intermediate between triggering and closure. The bulk flux, though directed, has an average energy of only many 10's of eV and its momentum quickly dissipates. The directed bulk flux can therefore be described as having a low emittance. The beam electrons, by definition, are ballistic in nature and have a higher emittance. The beamlike nature of the bulk electrons can be assessed from Fig. 5b where the bulk electron density and bulk flux are plotted at switch closure. The bulk electrons are somewhat somewhat diffuse in the anode region with a small proportion actually directed along the axis.

The total current and fractional current in the beam are shown in Fig. 6 as a function of time from the onset of triggering to switch closure. Early during commutation when the cathode is being illuminated, current is dominantly in the beam but that dominance dies out after the illumination ends. The fractional beam current then builds as secondary electrons are generated near the cathode hole. Beam current at switch closure is 16.7 A, representing 1.6% of the total, which agrees well with the experimental results of Kirkman and Gundersen.[22] After switch closure, the voltage begins to collapse and the fraction of current in the beam begins to decrease. The predicted time of beam generation is typically a few tens of ns on the leading edge of the current pulse, commensurate with experimental results.[9,14] The beam generating capability of the BLT depends critically on the operating pressure since the penetration distance of beams decreases with increasing pressure. This is demonstrated in Fig. 7 where the total electron density in a multi-grid BLT is plotted for pressures ranging from 0.4 to 2.0 Torr. At pressures exceeding 1 Torr, the bulk electron density fails to penetrate beyond the anode hole.

IV. Nonstandard Geometries

One of the purposes of constructing models of the sort described here is to examine new designs and parameter spaces less expensively or faster than is possible in the laboratory. With this goal in mind, we have started a study of nonstandard geometries, as shown in Fig. 7. As an example, we will briefly discuss a study of the effects of using a slot in the cathode. It is common practice in conventional thyratrons to use a slotted control grid. The purpose of the slots is to increase the cross sectional area available for current to pass through to the anode. Since the BLT does not have a control grid, the analogous strategy would be to place slots in the cathode. Ideally, these slots should be small enough to prevent penetration of the electric potential prior to triggerering, but large enough to encourage current flow during the commutation and conduction phases of operation.

The geometry in this study is the same as described above with the exception of the addition of a single annular slot in the cathode. Recall that a key feature of the BLT is the onset of the HCE in the interior of the cathode. The onset of the HCE requires that primary electrons oscillate in the potential well formed within the cathode. By placing a slot in the cathode, the onset of the HCE is somewhat disrupted. Evidence of this disruption is seen in Fig. 8 where selected trajectories of primary beamlets are shown for BLT's with and without cathode slots. A fraction of the primary beamlets

escape from the interior of the cathode by passing through the slot. An immediate consequence of the loss of these beamlets is that the production of secondary beamlets and bulk electrons is somewhat diminished, as shown in Fig. 9. Some small amount of flux is drawn through the slot as a short burst of current. Under normal conditions, the bulk electrons are drawn away from the interior of the cathode and towards the cathode hole. This diminishes the current carrying potential of the slot, as shown in the plots of electron density in Fig. 10. Near the end of commutation, the cathode slots are nearly empty.

The final result is that the slots have a negative or small effect on switch performance. Commutation is delayed slightly due to the loss of some of the initial pendulum electrons, as shown in Fig. 11. After the electron swarm translates towards the cathode hole the effects of the slot diminish and the rate of current rise is nearly unchanged from the case without the slot. In order for the cathode slot to have a beneficial effect it must be sufficiently isolated from the central hole so that the HCE is not disrupted, and so it may independently operate as a cathode hole.

V. Concluding Remarks

In conclusion we have developed a model which uses two groups of electrons, the bulk and multiple beams, to describe the transport of electrons in an optically triggered pseudospark. The onset of a hollow cathode effect during commutation, which has been inferred from experimental results, is predicted by the model. The majority of primary beam electrons are trapped by the hollow cathode effect but do generate secondary beam and bulk electrons which may escape from the cathode. Our results indicate that experimentally measured beam currents are composed primarily of secondary beam electrons.

VI. Acknowledgements

References

1. G. Kirkman and M. Gundersen, Appl. Phys. Lett. 49, 494 (1986).
2. G. Kirkman, W. Hartmann, and M. Gundersen, Appl. Phys. Lett. 52, 613 (1988).
3. K. Frank, E. Boggasch, J. Christiansen, A. Geortler, W. Hartmann, C. Kozlik, G. Kirkman, C. Braun, V. Dominic, M. Gundersen, H. Riege, and G. Mechtersheimer, IEEE Trans. Plasma Sci. 16, 317, (1988).
4. G. Mechtersheimer, R. Kohler, T. Lasser, and R. Meyer, J. Phys. E: Sci. Instrum. 19, 466 (1986).
5. D. Bloess, I. Kamber, H. Riege, G. Bittner, V. Brueckner, J. Christiansen, K. Frank, W. Hartmann, N. Lieser, C. Scheltheiss, R. Seeboeck, and W. Seudtner, Nucl. Instrum Meth. 205, 172 (1983).
6. W. Hartmann, V. Dominic, G. Kirkman and M. Gundersen, Appl. Phys. Lett. 53, 1699 (1988).
7. C. Braun, V. Dominic, G. Kirkman, W. Hartmann, M. Gundersen, and G. McDuff, IEEE Trans. Electron Devices 35, 559 (1988).
8. W. Hartmann, V. Dominic, G. F. Kirkman and M. A. Gundersen, J. App. Phys. 65, 4388 (1989)
9. W. Benken, J. Christiansen, K. Frank, H. Gundel, W. Hartmann, T. Redel and M. Stetter, Trans. Plasma Science 17, 755 (1989)
10. J. Christiansen and Ch. Schultheiss, Z. Physik A 290, 35 (1979)
11. H. Pak and M. J. Kushner, J. Appl. Phys. 66, 2325 (1989)
12. K. Mittag to appear in "Physics and Applications of Hollow Cathode Switches" edited by. M. Gundersen (Plenum, New York, 1990)
13. D. J. Sturges and H. H. Oskam, Physica 37, 457 (1967)
14. E. Boggasch and M. J. Ree, Appl. Phys. Lett. 56, 1746 (1990)
15. M. Surendra, D. B. Graves and I. J. Morey, Appl. Phys. Lett. 56, 1022 (1990).
16. M. Kushner, J. Appl. Phys. 61, 2784 (1987)
17. Ph. Belenguer and J.-P. Boeuf, Phys. Rev. A 41, 4447 (1990)
18. M. Surrendra, D. B. Graves and G. M. Jellum, Phys. Rev. A 41, 1112 (1990)
19. H. R. Bauer, G. Kirkman and M. A. Gundersen, IEEE Trans. Plasma Sci. 18, 237 (1990)
20. J. J. Rocca, B. Szapiro and T. Verhey, Appl. Phys. Lett. 50, 1334 (1987)
21. M. T. Ngo, K. Schoenbach, G. A. Gerdin and J. H. Lee, Trans. Plasma Sci. 18, 651 (1990)
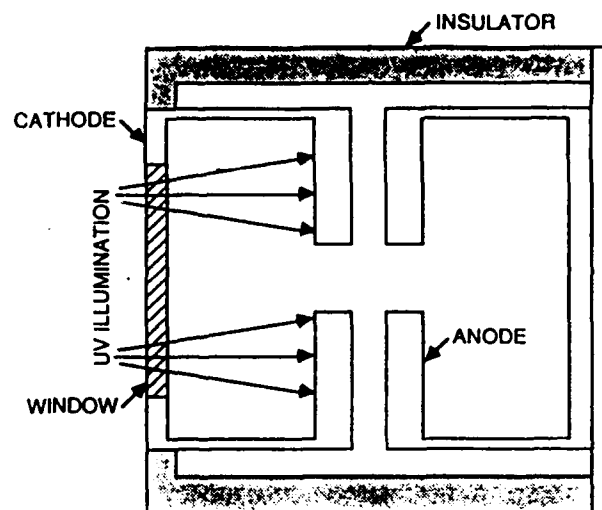22. G. Kirkman and M. Gundersen, unpublished data, 1990.

Figure 1. Schematic of the conventional optically triggered pseudospark, or Back-Lit-Thyratron (BLT). The diameter is 4-5 cm and length 5-10 cm.
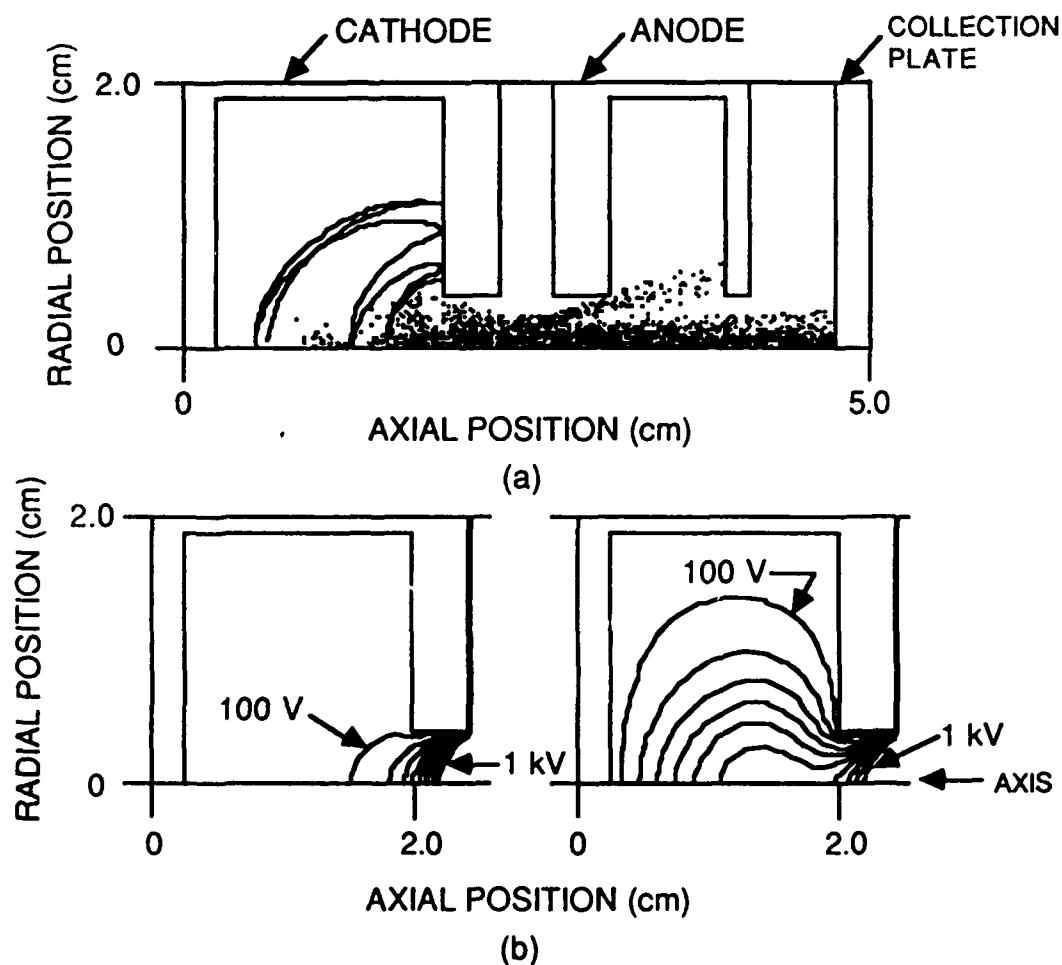

(a)

(b)

Figure 2. Plasma parameters for a BLT (0.4 Torr H_2, 10 kV): a) Primary beamlet trajectory (solid line) and secondary beam current density 60 ns after trigger.) Electric potentials at triggering (left) and at switching (right).
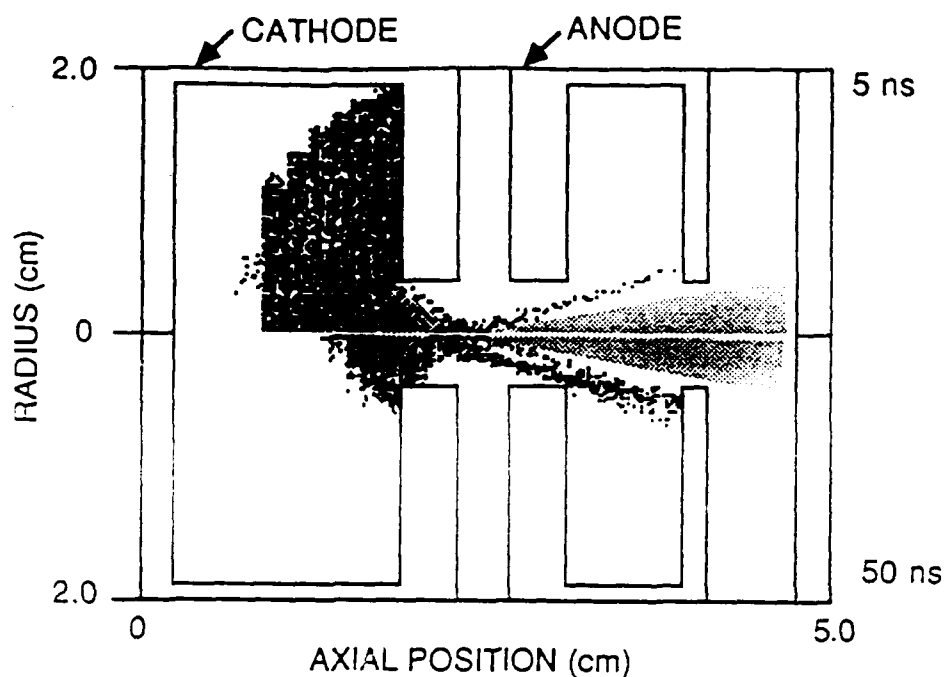
Figure 3. Primary beam current densities 5 ns (top) and 50 ns (bottom) after triggering (3 A/cm^2 maximum). The shaded portion represents weak beams.
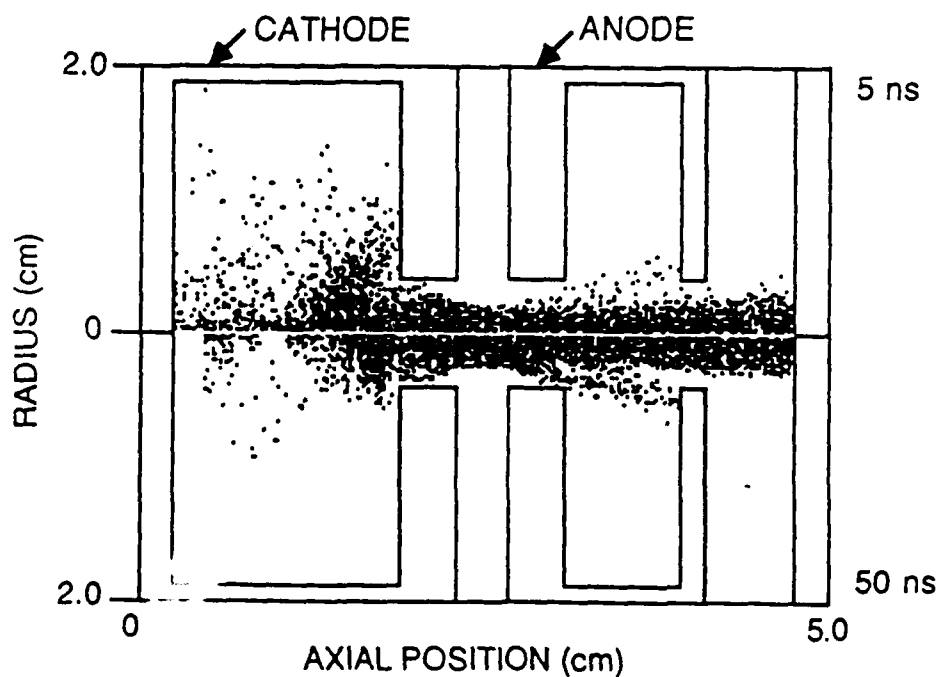
Figure 4. Secondary beam current densities 5 ns (top) and 50 ns (bottom) after triggering (7 A/cm^2 maximum).
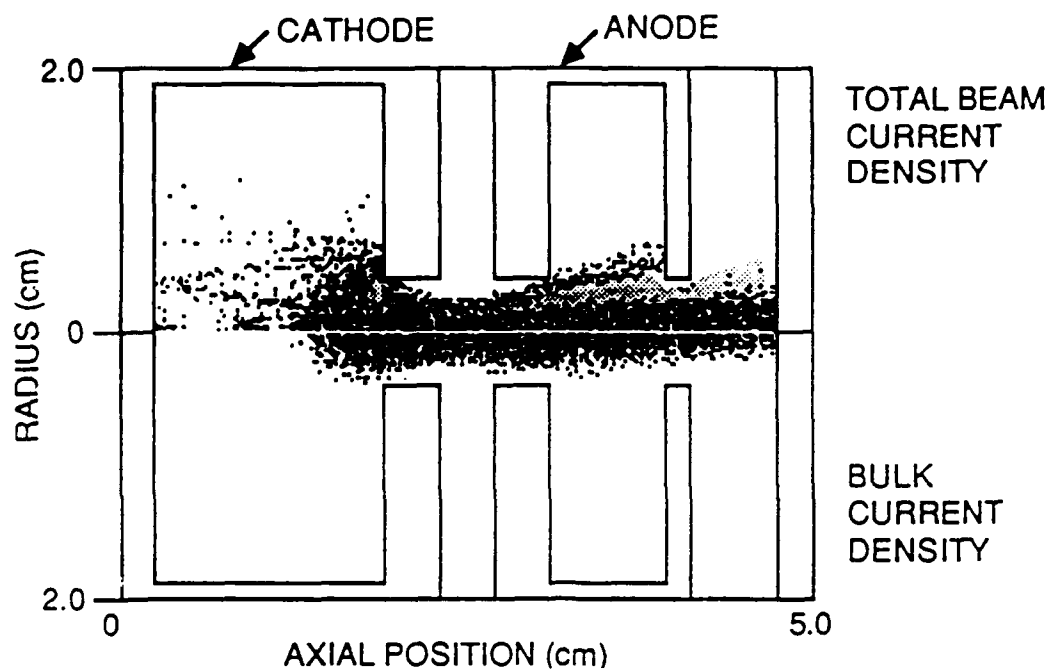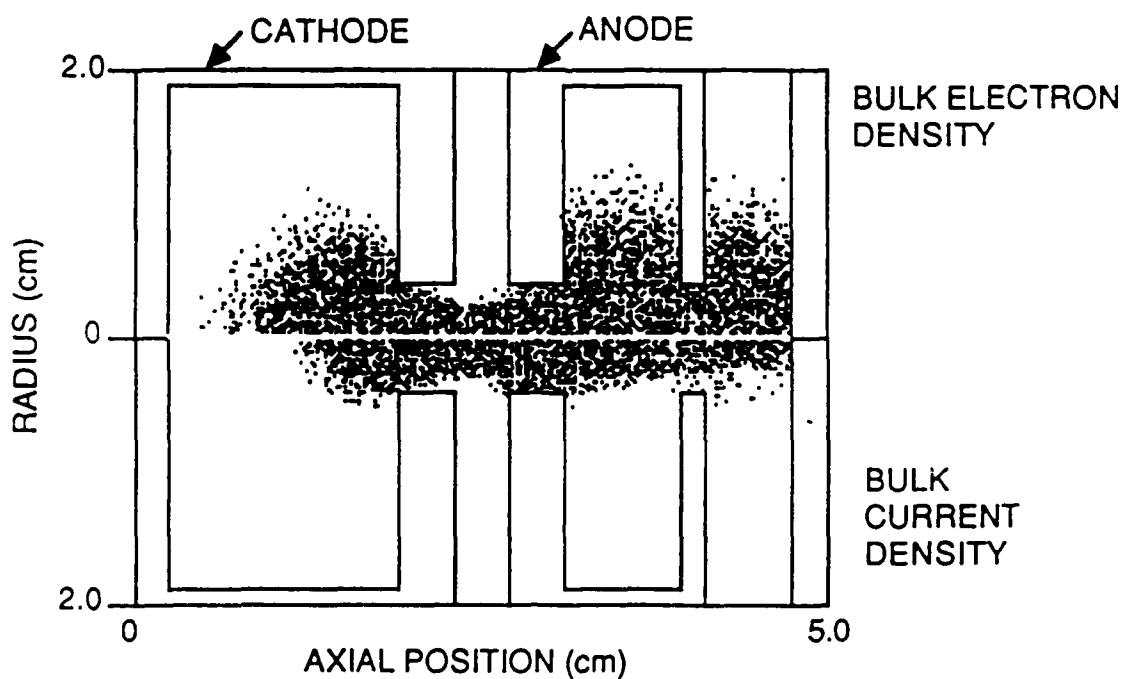
Figure 5. Plasma parameters comparing beam and bulk fluxes: a) Total beam current density (primary and secondary, 4 A/cm^2 maximum) and total bulk current density (790 A/cm^2 maximum) 40 ns after triggering; b) Bulk electron density (1.6 x 10^{13} cm^{-3} maximum) and bulk current (5 kA/cm^2 maximum) 55 ns after trigger.
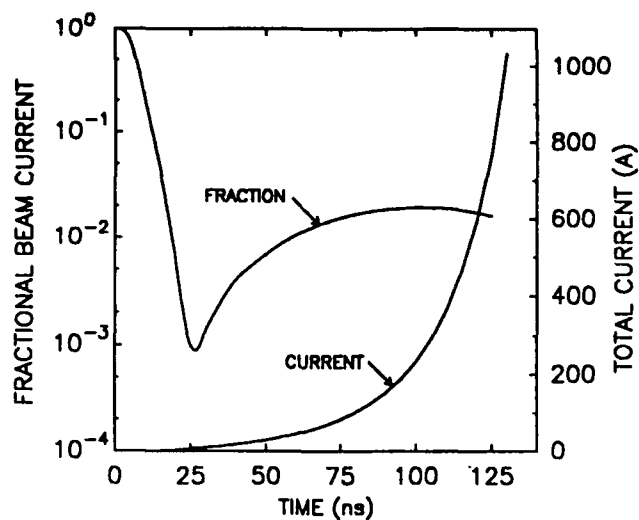
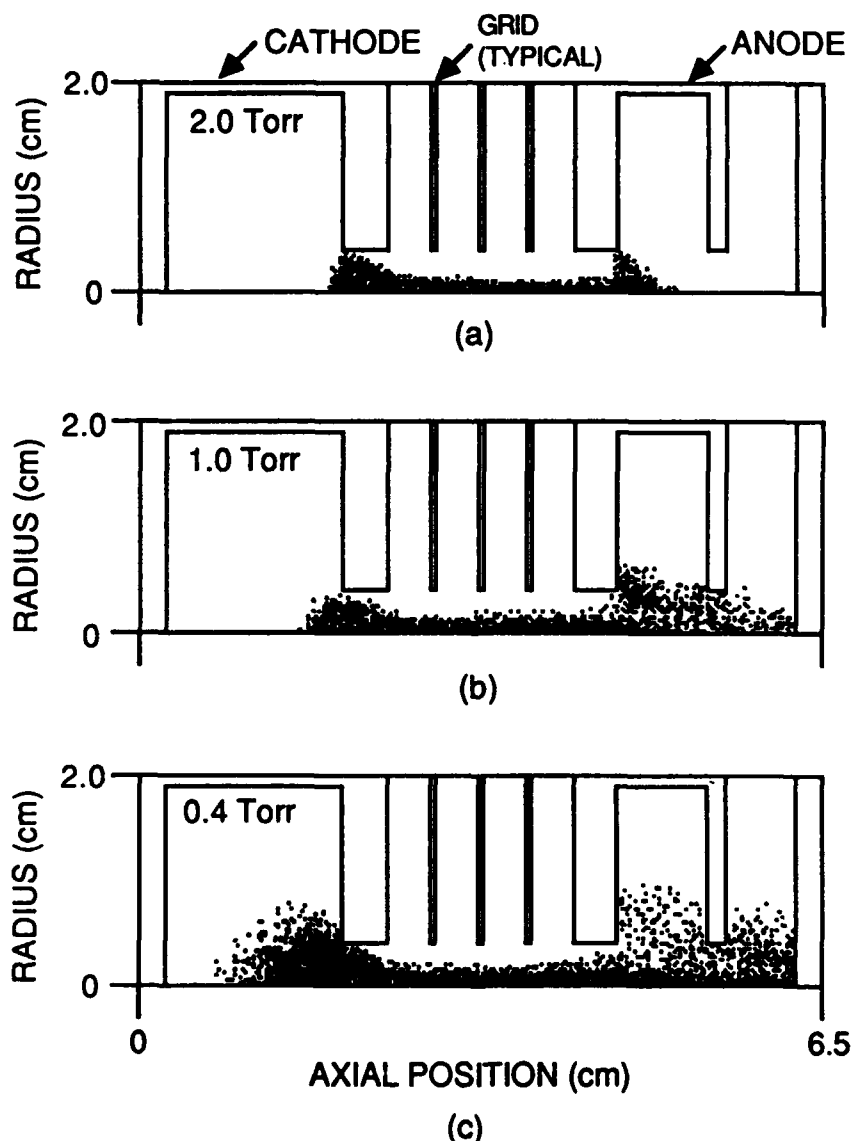Figure 6. Total current and fraction of current in the high emittance beam at the anode.

Figure 7. Total electron density in a multigrid BLT (40 kV) just prior to closure: a) 2.0 Torr; b) 1.0 Torr; and c) 0.4 Torr. Maximum densities are $\approx 10^{13}$ cm^{-3}.
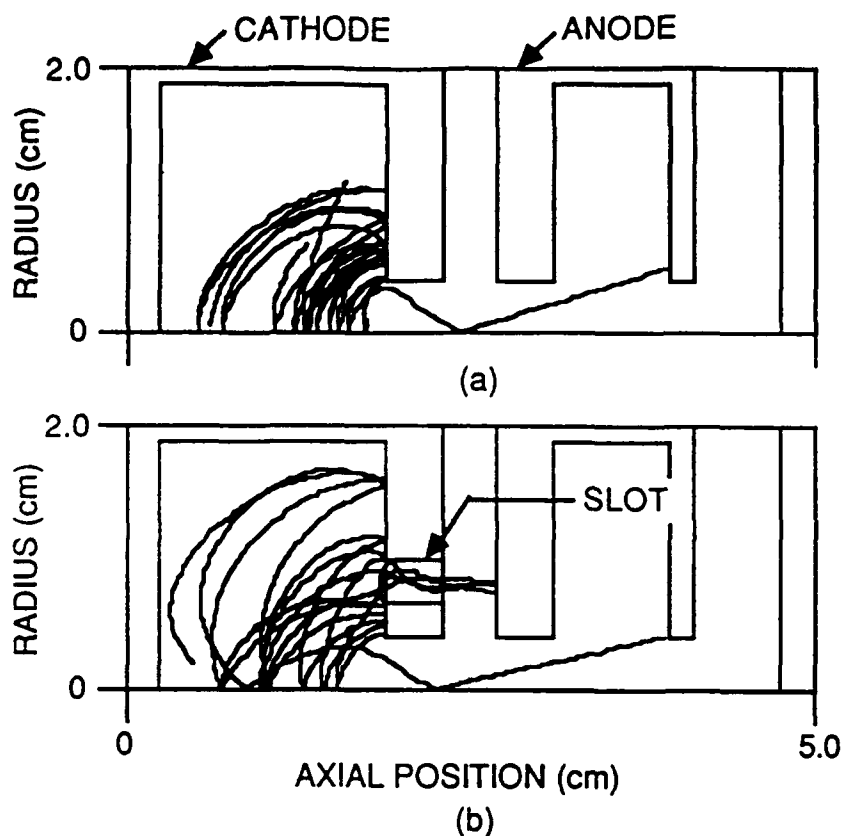
Figure 8. Selected primary beam trajectories: a) without a cathode slot;
b) with a cathode slot. The slot intercepts some trajectories, reducing
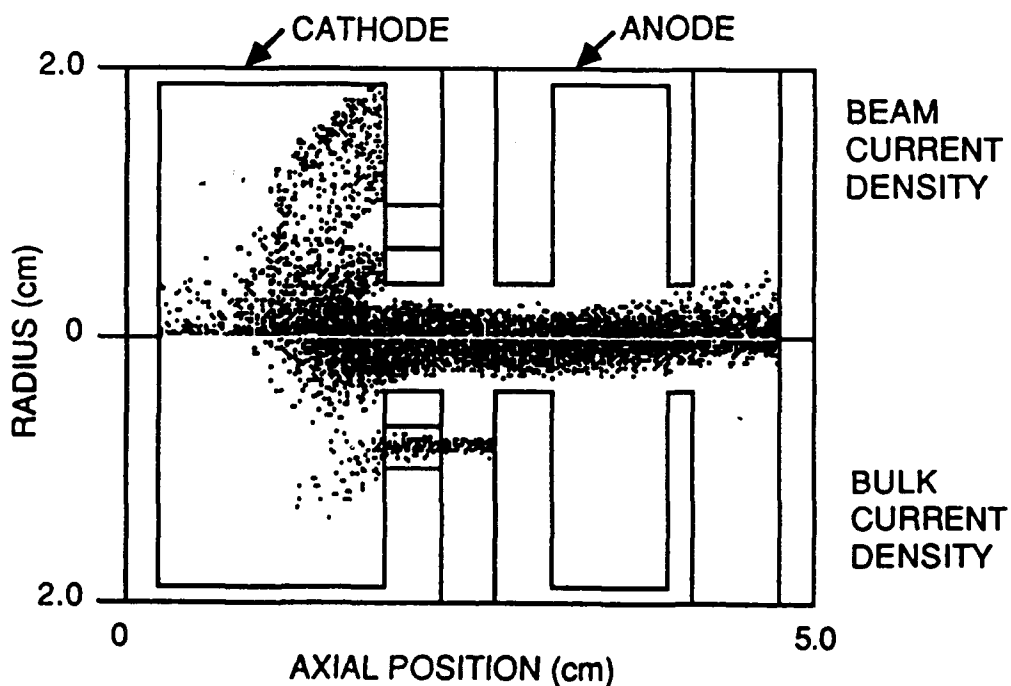the hollow cathode effects.

Figure 9. Total beam current density (6 A/cm^2 maximum) and bulk current
density (0.6 A/cm^2) 5 ns after triggering. A small amount of current
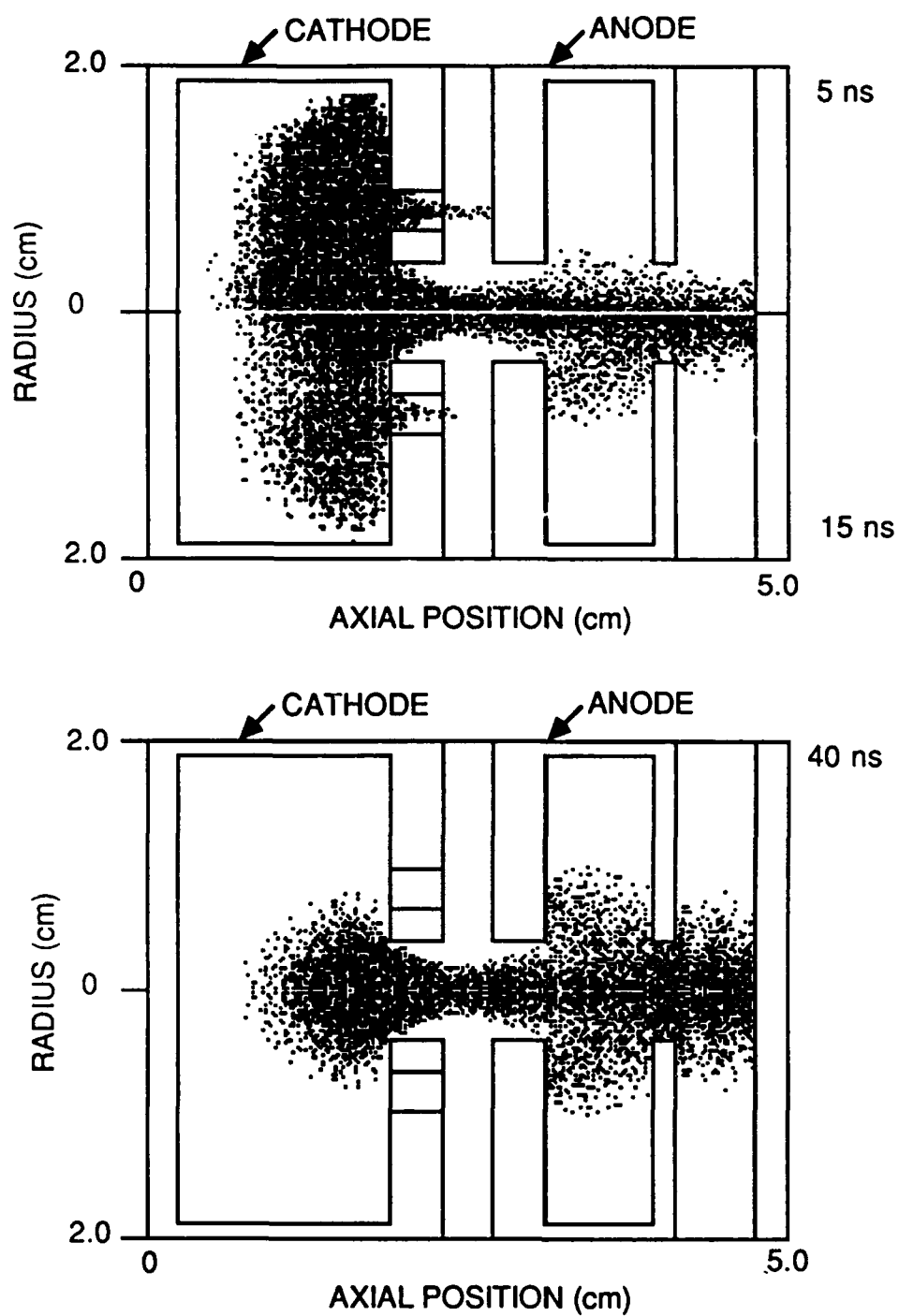is drawn through the slot.

Figure 10. Total electron density 5 ns (2.9×10^9 cm^{-3} maximum), 15 ns (9.6×10^{10} cm^{-3} maximum) and 40 ns (2.7×10^{12} cm^{-3} maximum) after triggering.
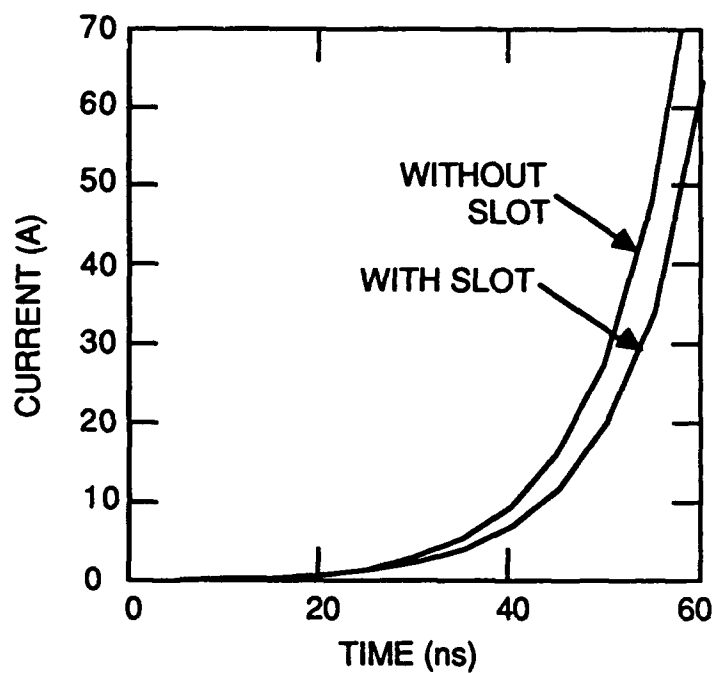
Figure 11. Total current with and without a cathode slot. The slot
    delays the closure slightly but otherwise has little effect on the
    operation of the switch.

MAGNETIC CONTROL OF HOLLOW CATHODE DISCHARGES

Glenn Gerdin
Dept of Electrical & Computer Engineering
Old Dominion University
Norfolk, Virginia 23529

MAGNETIC CONTROL OF LOW-PRESSURE DISCHARGES

Glenn A. Gerdin and Karl H. Schoenbach
Department of Electrical and Computer Engineering
Old Dominion University
Norfolk, VA 23529

ABSTRACT

Since hollow cathode discharges (HCD) can be operated in excess of 100 kA, successful interruption of such discharges could have a major impact on pulsed power technology. We have been modeling such discharges with a Monte-Carlo scheme to follow the non-equilibrium dynamics of the electrons moving in these configurations; in this manner we are able to simulate our previous observations of the magnetic suppression of the low-impedance HCD mode. The simulation scheme has been modified from the previous Cartesian grid to polar coordinates, so that the motion of the electrons in one plane of the cylindrical hole in the cathode can now be modeled. A non-iterative electric-field calculation has been used to estimate the electron multiplication factor as a function of gas pressure for an HCD configuration of similar dimensions to those of our experiment; the results show features similar to the transitions from the high-impedance mode to the low-impedance mode. A similar set of calculations involving an axial magnetic field has shown features qualitatively similar to the suppression of the low-impedance mode which we previously reported. These results suggest that the application of a sufficiently strong axial magnetic field should be able to interrupt the radial component of the HCD current through the effect similar to that of magnetic insulation. The significant progress in HCD modeling has permitted the design of an improved discharge configuration.

1

1.   RESEARCH GOALS

While the ultimate engineering goal for this research is the development of a magnetically-controlled plasma-discharge opening switch, the scientific goals are to build the scientific data base so one could understand how such a switch would operate and how one could optimize the performance of such a switch. Since hollow cathode discharges (HCD) have been shown to carry over 100 kA, and since we have shown experimentally that an applied axial magnetic field can be used to suppress the initiation of the low-impedance HCD mode, even when all other conditions were favorable, our research has been concentrated on understanding HCD phenomena both though experiment and theoretical computer simulation. The goals of the experimental program are 1) to perform experiments to test the predictions of the computer simulations and to strengthen the scientific data base, 2) to explore the use of magnetic fields to alter the impedance of the HCD, and 3) to design an optimal experiment to test this concept as a high-power opening switch. The goals of the theoretical computer-simulation effort are 1) to model the behavior of both the high and low impedance HCD modes, with and without axial magnetic fields, to facilitate the understanding of the experimental data to strengthen the HCD data base, 2) to attempt to identify the underlying mechanisms which could be exploited in the design of an opening switch, and 3) use these computer simulations in the design of an "optimal" experimental configuration, that will truly test the concept.

2.   APPROACH

To better test the results of the theoretical models and the computer simulation, the hollow cathode device needed to be redesigned to provide for better visual access to the interior of the cathode hole, and to provide for the penetration of a fast risetime magnetic field. Also, previous attempts to observe the effect of an axial magnetic field, with millisecond risetime, on a long-pulse high-current HCD, revealed problems with electrode heating, so the pulse-forming network was also redesigned to deliver a longer pulse (to 100 μsec from 10 μsec) at higher impedance (to 500 Ω from 50 Ω). The magnetic field circuit was also modified, so that it could deliver axial fields of up to 0.3 Tesla with a risetime of less than 100 μsec. Using this new apparatus, it is hoped that a more detailed comparison can be made between experiment and simulation, and some tests of the interruption mechanism can be performed.

Our Monte-Carlo computer-simulation code, necessary to study the effects of the non-equilibrium pendel electrons which have a dominant influence in the HCD, was *modified from the previous Cartesian grid to polar coordinates so the planar (r,ϕ) motion* of the electrons in one plane of the cylindrical cathode hole could be simulated. This code is now being expanded to a hybrid approach, to obtain a self-consistent electric field profile in this plane of the cathode hole. The code also permits the simulation of the effect of axial magnetic fields for the first time; since we are proposing to use such fields to control the HCD, this ability is essential to our computer-simulation effort. The overall scheme is to start with an initial guess of the electric field profile, and to use the Monte-Carlo code to follow the electron dynamics and use the results (e.g., the electron drift velocity and the ionization rate coefficients) in a fluid model, to determine charge density and current distributions in the (r,ϕ) plane. These results would then be inserted into Poisson's equation and Ampere's Law to obtain new field profiles, which would form the basis for the next

2

iteration beginning with another Monte-Carlo simulation of the electron dynamics. After the convergence of the field profiles, the result would be truly self-consistent, putting the comparison between experiment and simulation on a firmer basis. Because the actual orbits of the electrons are followed, it should be possible to identify mechanisms involving them, especially in the presence of an axial magnetic field, which could be exploited in the design of an opening switch.

3.   STATUS

The new apparatus has been designed and constructed and is in the initial stages of being tested. The Monte-Carlo code is now fully operational. We are using it in its present form, to simulate our previous experimental conditions to see if it can predict phenomena similar to those observed, even if the electric-field profile is not self-consistent but only an "educated" guess. The results of these simulations qualitatively reveal the same trends observed experimentally, such as the transition from the high-impedance to the low-impedance HCD mode with increasing gas pressure, and the suppression of the radial HCD by applying sufficiently strong axial magnetic fields. These simulations suggest that the underlying mechanism is a magnetic insulation effect. A report discussing these simulations appears on the following pages.

3

MODE TRANSITIONS IN HOLLOW-CATHODE DISCHARGES

G.A. Gerdin, K.H. Schoenbach, L.L. Vahala, and T. Tessnow

Department of Electrical and Computer Engineering
Old Dominion University
Norfolk, VA 23529

INTRODUCTION

Hollow-Cathode Discharges (HCD) have been studied for many years.[1] A major cause for the interest in these discharges is the relatively high current densities that can be conducted through the HCD; currents of over 100 kA with rates of rise of $2 * 10^{12}$ A/s have been observed.[2] This ability to carry high currents, plus the observation of sharp impedance changes with pressure,[3-7] seem to make the HCD a candidate for a high-power switch. Furthermore, the observation that an axial magnetic field of sufficient strength B_z, can be used to suppress the transition from the high-impedance mode to its low-impedance mode,[7] could indicate a means of switch control. To put these possibilities on a firmer footing, it is desirable to simulate the HCD computationally, to see if these HCD phenomena can indeed be explained on the basis of first principles. Once this is achieved, it is much easier to understand the underlying physical mechanism causing these mode transitions. The nature of this mechanism could then suggest confirming experimental tests, and suggest a means of control of these impedance transitions, and hence lead the way toward the development of a high-power switch. In this paper, substantial improvements in our ability to simulate the HCD are reported, and the results of some preliminary calculations are compared with experimental results.

Previous Theoretical Work

Since the pressure and gap length at which these HCD mode transitions occur is on the left-hand side of the Paschen curve,[3-7] the mean-free path for electron elastic collisions λ_{ec}, is not small with respect with respect to the dimensions of the system, so models using the local field approximation (LFA),[8,9] where the electron drift speed is directly proportional to the local electric field times a mobility, can not describe the entire electron population. Some high-speed electrons can oscillate back and forth between the surface of the cathode hole and the axis of the hole several times before escaping, and cause increased ionization over that predicted by an LFA model; these electrons are called "pendel" electrons. In the LFA models, the effect of these pendel electrons can be included in terms of a modified ionization coefficient,[8] but one expects these models to only give qualitative results in general, although certain features of the electrical breakdown in the HCD can be modeled reasonably well.[9]

To account for the pendel and other non-equilibrium electrons (i.e., those electrons not treated by the LFA models), methods involving Monte-Carlo calculations, solutions to the Boltzmann equation, and the convective scheme[10] could be employed. These

techniques have been applied to glow discharges, and the results of the first two methods have been reviewed in the literature.[11,12]

PRESENT APPROACH

To model the HCD plasma and mode transitions, a one-dimensional Monte-Carlo computational technique has been implemented. The single dimension represents the radial dimension of the cathode-hole plasma, which is assumed to have both axial and azimuthal symmetry to a first approximation. The motion of the electrons is in the (r,ϕ) plane, which is represented in Figure 1 by a dashed line labeled S. This is justified in treating the HCD mode transitions, because it is experimentally observed,[3-8] that the pressure at which these transitions occur, is independent of the distance between the cathode and the anode, and is dependent only on the applied voltage[7] and the diameter of the hole.[3]

The overall scheme to be employed in the present simulations is a hybrid approach,[13] where the electron kinetics is modeled by means of a Monte-Carlo technique, and the results (e.g., electron drift velocity and the ionization rate coefficients) are used in a fluid model, to determine the charge density and current distributions of the ions and electrons between the inner wall of the cathode hole and its axis. This is an iterative method,[13] which starts with an initial guess of the electric field distribution between the cathode wall and the device axis, with the subsequent results of the Monte-Carlo and fluid calculations (i.e., the spacial distribution of the electron and ion charge densities) inserted into Poisson's equation which yields a new electric field distribution.

The results reported here represent the initial stage of the iteration scheme. Here the initial field distribution is imposed, and the electron distributions, in space, and in velocity are computed from our Monte-Carlo code for various neutral gas pressures. The subsequent fluid and iterative calculations are beyond the scope of this work. Thus, the results of these calculations will be selected to illustrate the ability of this approach to treat non-equilibrium electrons and their predicted motion under experimental conditions. Even these initial calculations could be helpful in revealing other phenomena associated with these electrons, which may have been previously overlooked. In addition, a substantial improvement has been made in the Monte-Carlo code, which now treats the fully circular nature of the cathode hole (see Figure 1), instead of the two-parallel-plate cathode configuration previously considered.[14]

Physical Model of the Mode Transition.

As an example of the utility of such a model, calculations were performed to simulate the transitions from the high-impedance mode (HIM) to the low-impedance mode (LIM), using experimental parameters. To model this transition, a model for the HIM is needed which is compatible with the experimental observations. It is assumed that the HIM consists of three regions (see Figure 1a): the positive column-negative glow region (PCNGR), the cathode-fall region (CFR), and a cathode-hole plasma (CHP). In this model, the plasma densities of the CHP and the PCNGR are comparable in the HIM so that each represents a source of ions which bombard the

5

inner surface of the hole, giving rise to secondary electrons which carry the current through the PCNGR and CFR. Since the magnitude of the component of ion flux from each region is proportional to the plasma density in that region, the device current is determined by roughly equal ion fluxes from each. In the LIM, the density of the CHP becomes several orders of magnitude higher than that in the PCNGR, so that the CHP dominates as a source for ions which ultimately generate the device current. Thus, if increasing the pressure by a small percentage caused a sharp increase in CHP density in the model, this would be viewed as a transition from the HIM to the LIM.

Intuitively, one might expect that for a given applied voltage V_0, an azimuthally symmetric potential difference should exist between the wall of the cathode hole and its axis, with the ionization mean-free path λ_i being greater than the hole radius R_0 for the discharge to be in the HIM. Increasing the gas pressure should shorten λ_i and hence cause a transition to the LIM near the point where $\lambda_i \approx R_0$. Since λ_i is inversely proportional to the gas pressure for such discharges with low percentage ionization, then the transition pressure should only be a function of V_0 and R_0 as is consistent with experiment.[3-8] Thus, to a first approximation, the effect of the anode is only to establish a boundary condition for the electrical potential on the device axis, and that the dominant mechanism in determining the mode transition, is the radial (and azimuthal) motion, production, and loss of the charges in the CHP. In the one-dimensional model, axial motion, will be approximated by a loss time τ.

This three region model for the HIM is consistent with experimental observations involving the length of the anode-cathode gap, the energy and spatial distribution of the electron beam generated in this mode, and the appearance of the HIM. First, the position of the anode should not be important as long as the length of the anode-cathode gap is greater than the thickness of the CFR.[3-8] Second, the PCNGR and the CFR constitute the basic configuration of the high-voltage glow discharges between parallel plates,[15-17] which also produced electron beams collimated along the device axis.[15] For the high-voltage parallel-plate discharges, all but about 10 V of V_0 appear across the CFR, and the energy spread of electron beams produced were within 10% of eV_0.[15] For high-voltage hollow-cathode configurations, Rocca et al.,[18] observed a dark space in the region corresponding to the CFR at the mouth of the gun and determined from the energy distribution of the electron beam generated, that over 90% of V_0 appeared across this region; it was estimated that less than 10% of the remainder was responsible for the generation of the hole plasma.[18] Third, the electron beam produced by the HCD in the HIM, was found to be strongly collimated along the device axis;[18] presumably the filamentary appearance of the discharge in this mode[7] is due to the excitation and ionization of the gas caused by the passage of the electron beam (see Figure 1a).

To complete the model, one needs to predict how τ will scale with pressure and to "guess" the radial potential profile for the CHP. Since $\lambda_{ec} \geq R_0$ near the transition pressure, $\tau \propto h/v_m$, where h is the depth of the hole and v_m is the mean speed of the electrons in the CHP. Thus to a first approximation, τ should be independent of gas pressure. For the radial potential distribution of the CHP, $\Phi_v(r)$, the vacuum potential distribution at the open end of the hole[19] is used as the initial "guess"; here $\Phi_v(r)$ is

6

parabolic, where the potential difference between the central potential and the cathode potential $\Delta\Phi = 0.2 * V_0$. This is a region which is believed to have the strongest influence on the transition.[20] However, since the three region model for the HIM appears to represent a considerable distortion of the potential distribution from the vacuum case, results will also be presented with $\Delta\Phi = 0.1 * V_0$, which may be more compatible with experimental conditions.[18] The answer as to whether either of these "guesses" is close to being correct, awaits the results of the iterative scheme discussed above, which is beyond the scope of the results reported here.

The Monte-Carlo Model

In this model, the planar motion (r, ϕ) is calculated for primary electrons originally released from the cathode at a random initial energy W_{eo} (where $0 < W_{eo} < 10$ eV), and random initial planar direction. This motion is in the plane represented by the dashed line labeled S in Figure 1. Each primary particle is followed in the model for a constant length of time τ, which represents a mean loss time due axial motion. The secondary electrons are produced by the ionization events, and the energy of the to outgoing electrons is assumed to be shared equally. The planar motion of the secondary electrons is also followed in either of two possible models: 1) that the lifetime of the secondary electron is a full τ and that of the primary is that what is left of its original τ, say $\tau - t$, or 2) that since both electrons have the same energy after ionization event, they are indistinguishable, and hence both have a lifetime of $\tau - t$. Both models have been used and they give qualitatively similar results. However, calculations using the first model take considerably longer to perform, since each of the secondaries have a higher probability to create additional secondaries, because every particle created has the same lifetime τ. Results of the second model will be presented here for the purposes of illustration.

Scattering, excitation, and ionization events encountered by all these electrons, are treated through the use of the total cross sections for these processes in helium gas.[21] The scattering process is assumed to be isotropic; the total number of primary electrons is held fixed at one hundred particles.

RESULTS

In the present results M, the primary electron multiplication factor (i.e. the number of secondary electrons produced for each primary electron released from the cathode) will be calculated as a function of gas pressure p_0 for $B_z = 0$, to model the mode transitions.[7] If the potential distribution were fixed, and p_0 is varied, one might expect M to increase rapidly in the vicinity of p_0 where a radial breakdown occurs. This behavior could explain the mechanism for the HCD impedance transitions, if these transitions are related to radial breakdown. As can be imagined, M is roughly inversely proportional to the length of time (or lifetime) τ, that the electrons are followed in the program; τ is taken to be independent of the pressure at fixed V_0 as consistent with the model. τ was previously taken to be 80 ns, to simulate the net electron drift velocity in the axial direction,[14] in this study, τ was varied about 80 ns until an increase in M appears at about the same pressure as the mode transition occurred in the experiment. In the model, this occurs when $\tau \approx 40$ ns, as can be seen in Figure 2. In that figure, the

7

In the model, this occurs when $\tau \approx 40$ ns, as can be seen in Figure 2. In that figure, the variation of M with p_0 is presented for $\tau = 40$ ns, $V_0 = 15$ kV, $R_0 = 0.5$ cm, and $\Delta\Phi = 0.2*V_0$. As can be seen there is a significant increase in M for 100 mTorr $\le p_0 \le 200$ mTorr, whereas for similar V_0 and R_0, the experimental transition pressure $p_{0t} = 165$ mTorr.[7] This value for τ (40 ns) was then be used in the subsequent calculations so that those results may be more consistent with experiment. Thus the results of the model show at least the qualitative trend of a mode transition, even though τ itself can only be treated as a parameter at present. However, the existance of this trend in M with p_0 is very encouraging.

To consider the effect of an axial magnetic field, the radial distributions of electron number density $n_e(r)$, the ionization rate coefficient $k_i(r)$, and the electron energy distribution $f_e(E,r)$ were calculated for various B_z between 0 and 750 mT at $p_0 = 50$ and 200 mTorr. Here the B_z required to suppress the transition into the LIM would be evidenced by a "hole" appearing in the $n_e(r)$ and $k_i(r)$ distributions indicating the discharge can no longer be sustained. This a more quantitative version of the magnetron model discussed earlier[7], where the inability of the primary electrons to reach the center was taken as the criterion for the discharge to stay in the HIM. In this latter model $\Delta\Phi = V_0$ which would represent the case where the PCNGR extends down the axis of the CHP; this seems to be somewhat extreme for the initial guess for $\Delta\Phi$.

The results for $n_e(r)$ for various B_z are shown in Figure 3; here $\Delta\Phi = 3$ kV (corresponding to $V_0 = 15$ kV for $\Phi_v(r)$), $p_0 = 200$ mTorr, and $R_0 = 0.5$ cm (fixed throughout this work). As can be seen in the Figure, a depression appears in the center of the hole for $B_z = 250$ mT, whereas a peak in $n_e(r)$ occurs at the center for $B_z = 0$. This result could be interpreted as the B_z necessary to prevent the transition into the LIM.[7] This is also reflected in the corresponding $k_i(r)$, which is peaked on the axis for small B_z, but also is hollow for $B_z = 250$ mT. While the experimental value for the minimum B_z for LIM suppression B_{zm} was 150 mT, this may be due to the uncertainty in $\Delta\Phi$.

It should be noted that the absolute drop in the electron density to zero inside a certain radius illustrates one of the limitations of the model. That is, the diffusion processes that would at least partially fill the interior regions, take longer than the fixed lifetime τ, and so steep density gradients are predicted. Thus these results exaggerate the underlying trends predicted by the model and seen in experiment. However the model does indicate that through a lack of energetic particles in this interior region, the reaction rate coefficient is considerably reduced, and hence that the discharge cannot be sustained in this region. This process appears to be a magnetic insulation effect (see Figure 1b), which can be utilized as an opening effect for gas discharge switches.

REFERENCES

1. F. Paschen, Ann. Physik 50:901 (1916).
2. K. Frank, E. Boggasch, J. Christiansen, A. Goertler, W. Hartmann, C. Kozlik, C.G. Braun, V. Dominic, M.A. Gundersen, H. Riege, and G. Mechtersheimer, High power pseudospark and BLT switches, IEEE Trans. Plasma Sci. 16:317 (1988).
3. Z. Yu, J. Rocca, J. Meyer, and G. Collins, Transverse elcctron guns for plasma

8

excitation, J. Appl. Phys. 53:4704 (1982).

4. K. Frank and J. Christiansen, The fundamentals of the pseudospark and its applications, IEEE Trans. Plasma Sci. 17:748 (1989).

5. P. Choi, H. Chuaqui, J. Lunney, R. Reichle, A.J. Davies, and K. Mittag, Plasma formation in a pseudospark discharge, IEEE Trans. Plasma Sci. 17:770 (1989).

6. G. Kirkman-Amemiya, H. Bauer, and M.A. Gundersen, Analysis of the high current glow discharge occurring in the BLT and pseudospark switch, Bult. Amer. Phys. Soc. 31:2131 (1989).

7. M.T. Ngo, K.H. Schoenbach, G.A. Gerdin, and J.H. Lee, The temporal development of hollow cathode discharges, Trans. Plasma Sci. 18:669 (1990).

8. H. Helm, F. Howorka, and M. Pahl, Z. Naturforsch. 27a:1417 (1972).

9. H. Pak and M.J. Kushner, J. Appl. Phys. 66:2325 (1989).

10. T.J. Sommerer, W.N.G. Hitchon, and J.E. Lawler, Phys. Rev. A 39:6365 (1989).

11. A.J. Davies, IEE Proc. 133:217 (1986).

12. P. Segur, M. Yousfi, J.P. Boeuf, E. Marode, A.J. Davies, and J.G. Evans, in: "Electrical Breakdown and Discharges in Gases," E.E. Kunhardt and L.H. Luessen, ed., Vol. 89a of NATO ASI Series B, Plenum, New York (1983).

13. K.H. Schoenbach, H. Chen, and G. Schaefer, "A model of dc glow discharges with abnormal cathode fall," J. Appl. Phys. 67:154 (1990).

14. K.H. Schoenbach, L.L. Vahala, G.A. Gerdin, N. Homayoun, F. Loke, and G. Schaefer, "The effect of pendel electrons on breakdown and sustainment of a hollow cathode discharge, in: "Proceedings of the NATO Workshop on the Physics and Applications of Hollow Cathode Switches," Lillehammar, Norway, 17-21 July 1989," M.A. Gundersen, ed., Plenum, New York (1990).

15. G.W. McClure, "High-voltage glow discharges in D_2 gas. I. Diagnostic measurements," Phys. Rev. 124:969 (1961).

16. B.B. O'Brien, Jr., "Characteristics of a cold cathode plasma electron gun," Appl. Phys. Lett. 22:503 (1973).

17. G.G. Isaacs, D.L. Jordan, and P.J. Dooley, "A cold-cathode glow discharge electron gun for high-pressure CO_2 laser ionization," J. Phys. E: Sci. Instrum. 12:115 (1979).

18. J.J. Rocca, J. Meyer, and G.J. Collins, "Hollow cathode electron gun for the excitation of cw lasers," Phys. Lett. 87A:237 (1982).

19. T. Tessnow, private communication.

20. W. Hartmann and M.A. Gundersen, "Origin of anomalous emission in superdense glow discharge," Phys. Rev. Lett. 60:2371 (1988).

21. M. Hayashi, "Recommended values of transport cross sections for elastic collisions and total cross sections for electrons in atomic and molecular gases," Inst. Plasma Phys., Nagoya University, Report IPPJ-AM-19 (Nov. 1981).
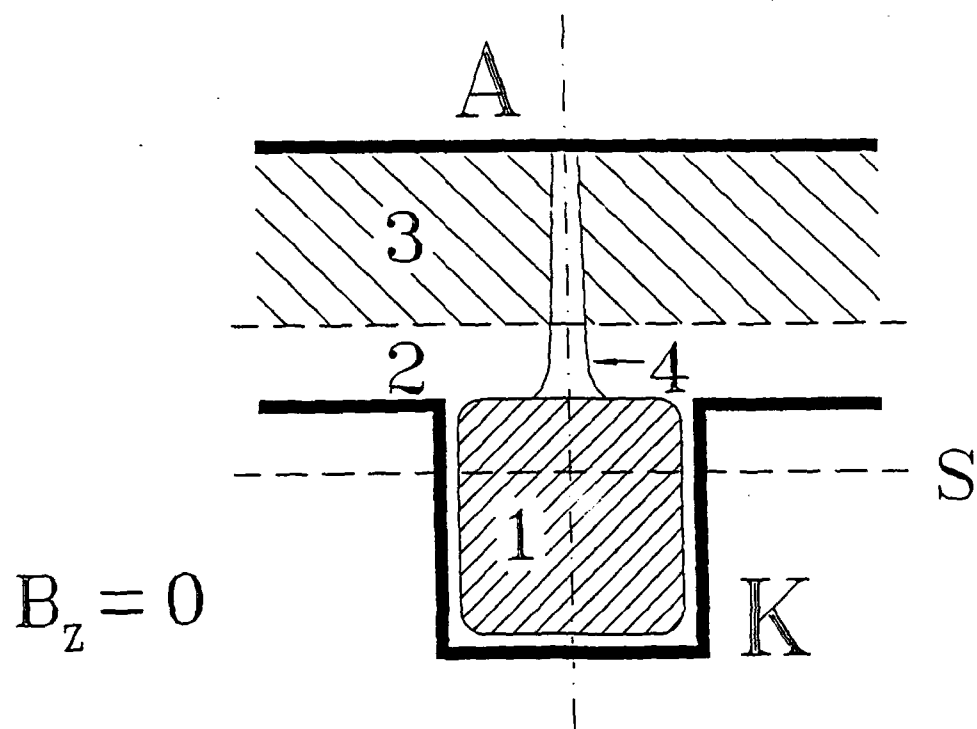
FIGURE CAPTIONS:

Figure 1. a) A schematic of the model for the high-impedance HCD mode (HIM) with zero or weak axial magnetic fields. Area 1) is the cathode-hole plasma (CHP); area 2) is the cathode-fall region (CFR); area 3) is the positive-column negative-glow region (PCNGR); and area 4) is the region through which the collimated electron beam passes. b) A schematic of the magnetic-insulation effect showing the constriction of the CHP (again area 1)) if the axial magnetic field B_z is greater than some threshold value B_{zm}. In both a) and b) A, K, and S label the anode, cathode, and (r,ϕ) plane where the electron motion is followed, respectively.

Figure 2. The variation in the primary electron multiplication factor M with gas pressure p_0 in mTorr for a primary lifetime of $\tau = 40$ ns, a cathode-hole radius $R_0 = 0.5$ cm, an applied potential of $V_0 = 15$ kV, and $\Delta\Phi = 0.2*V_0$. The corresponding transition gas pressure for this R_0 and V_0 was $p_{ot} = 165$ mTorr.

Figure 3. The radial electron density profiles in the plane labeled S in Figure 1, for an applied $\Delta\Phi = 3$ kV, a gas pressure $p_0 = 200$ mTorr, and a cathode hole radius $R_0 = 0.5$ cm. The vertical center line is the center axis of the hole, and horizontal distances are in mm. In the top figure, the axial magnetic field $B_z = 0$, and the vertical scale is linear in units of $10^{10}/cm^3$. In the bottom figure, the axial magnetic field $B_z = 250$ mT, and the vertical scale is linear in units of $10^8/cm^3$.
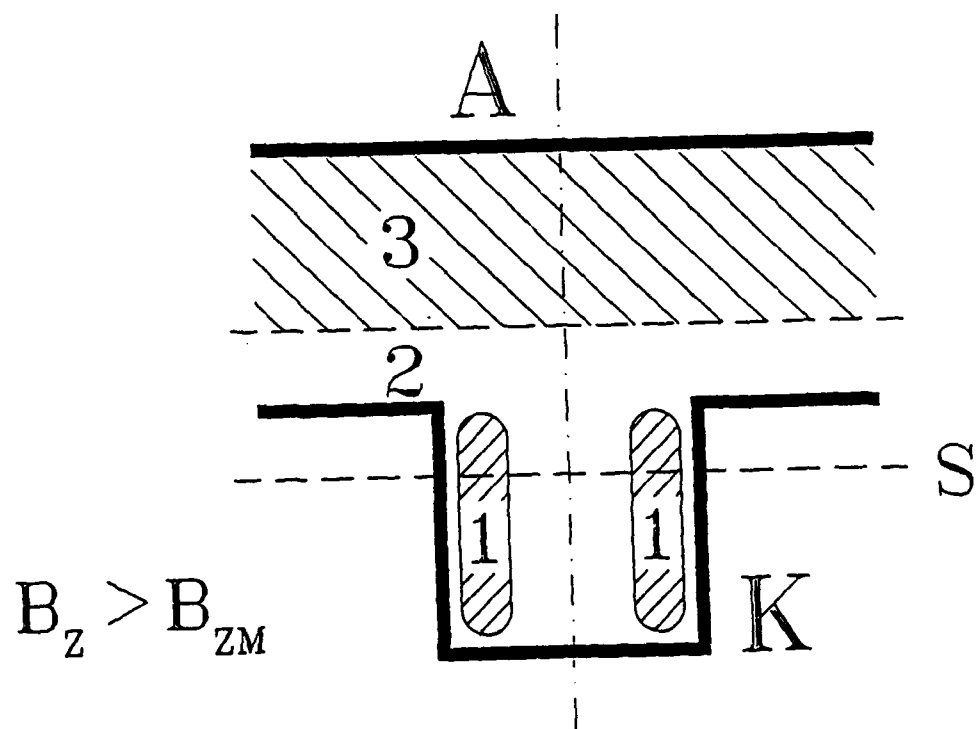
10

a)

$B_z = 0$

A

3

2   —4

1

S

K

b)

$B_z > B_{ZM}$

A

3

2

1   1

S

K

Figure 1

11

Figure 2

12

electron density V=-15000V p=200mTorr B=0mT

1.5

1.0

0.5

0.0

-4.0   -2.0   0.0   2.0   4.0   x

electron density V=-15000V p=200mTorr B=250mT
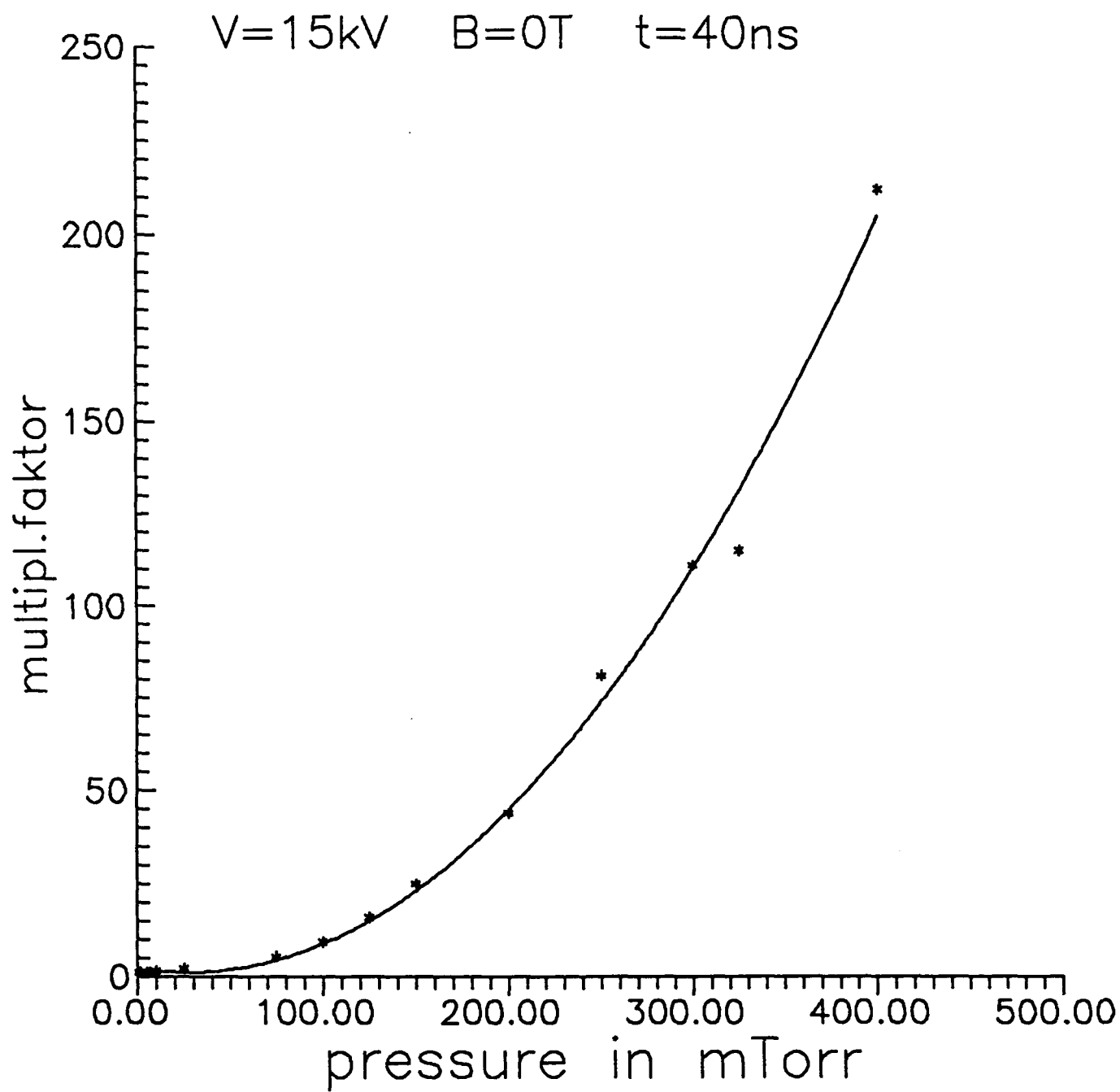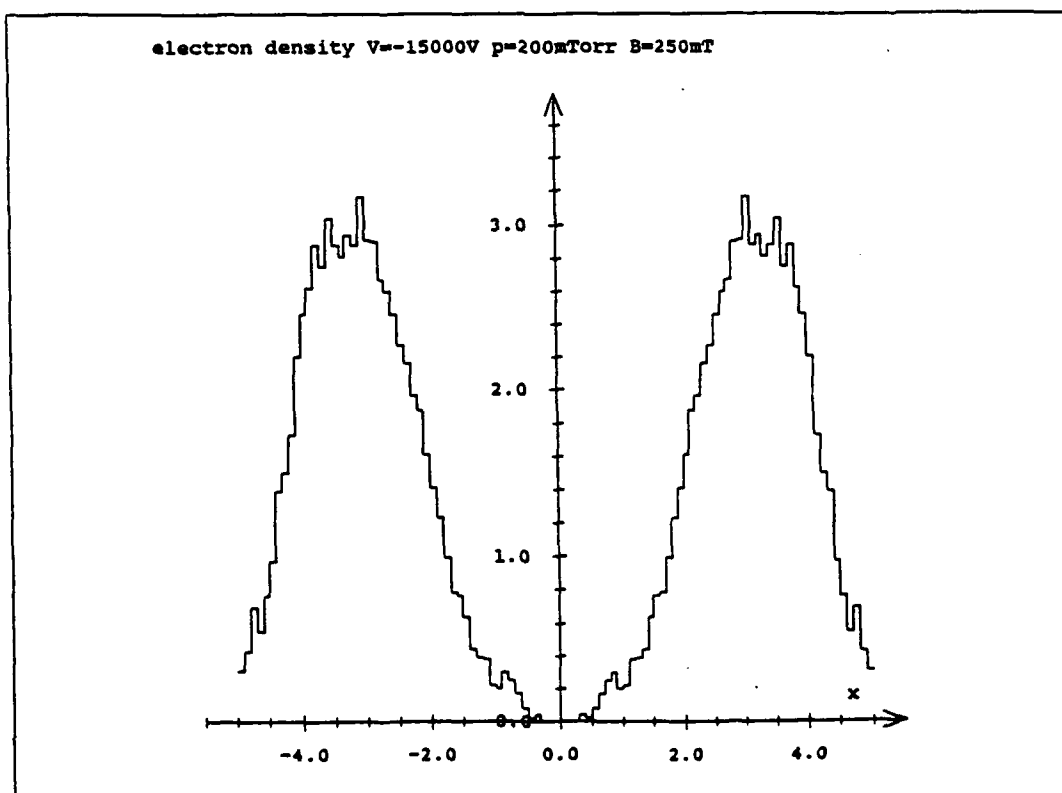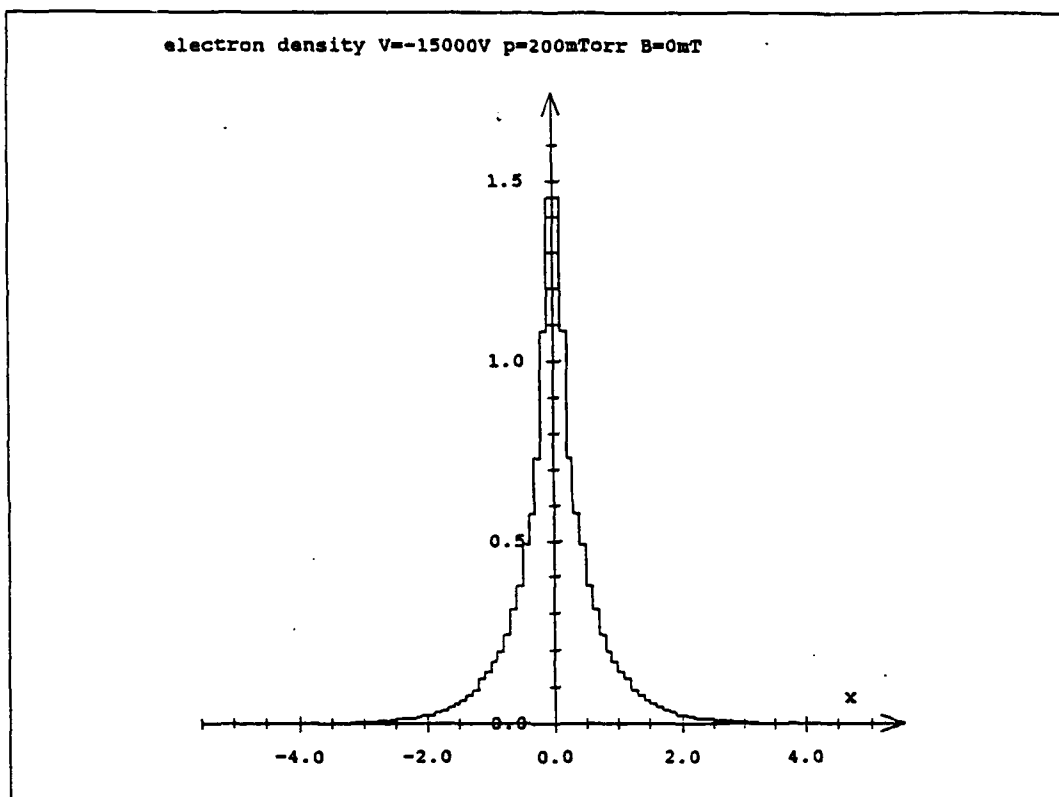
3.0

2.0

1.0

0.0

-4.0   -2.0   0.0   2.0   4.0   x

Figure 3

13

INSULATOR DAMAGE DUE TO 0.3 MA SURFACE DISCHARGES

Magne Kristiansen
Dept of Electrical & Computer Engineering
Texas Tech University
Lubbock, TX 79409-2019

INVESTIGATIONS IN MODELING OF NON-LINEAR SEMICONDUCTOR SWITCHES

Mark Browder
Center for Energy Conversion Research
The University of Texas at Arlington
Arlington, Texas 79409

Investigations in the Modeling of
Non-Linear Semiconductor Switches*

M. K. Browder and W. C. Nunnally
THE UNIVERSITY OF TEXAS AT ARLINGTON
Applied Physical Electronics Research Center
P.O. Box 19380
Arlington, Texas 76019

Abstract

A computer model, under development, that addresses the spatial dependencies of non-linear photoconductive switches is discussed. The mechanism, a double injection/trap filling process appears to explain numerous aspects of the switching phenomena associated with non-linear photoconductive switches. The approach and formulation are shown.

Introduction

Linear photoconductive switches (see Fig.1) have been employed for pulse power systems for a number of years. Characteristics such as voltages greater than 150 kV, switching times of tens of picoseconds and jitters of picoseconds has been demonstrated for impulse radar, electronic warfare and many other high peak power applications. Routine applications of linear, photoconductive switches have been limited to systems where the switch closure performance and relative jitter could not be obtained in any o er fashion.

Recent work by several investigators[1,2] has demonstrated an "avalanche like" closure phenomena that requires much less of the optical energy requirements of linear switches (typically 0.1% to 1.0%). Conduction is maintained through the switch until a critical voltage is reached at which the device "locks on" until the electrical energy is dissipated or removed.

The "avalanche like" closure phenomena and the "lock on" phenomena that maintains switch conduction are
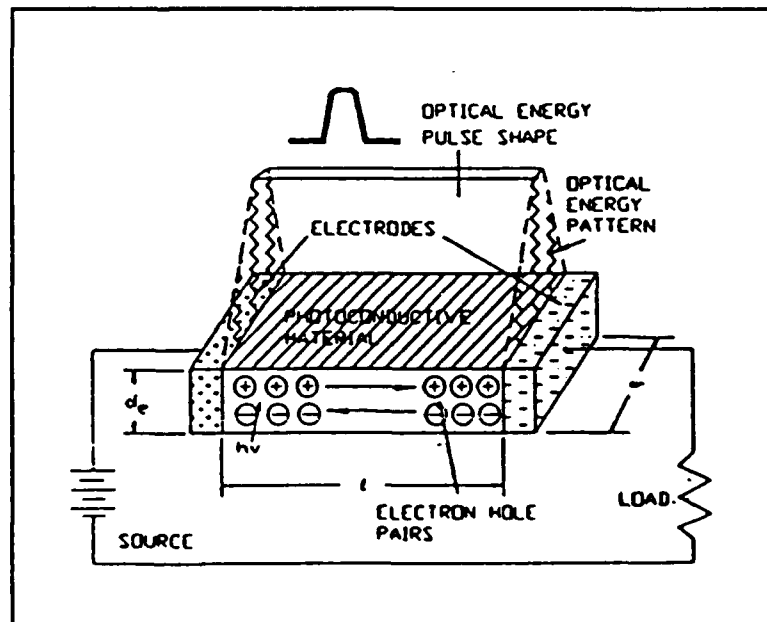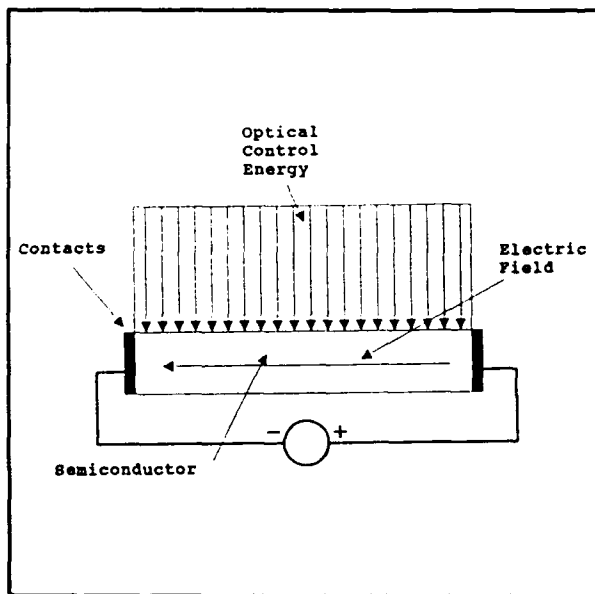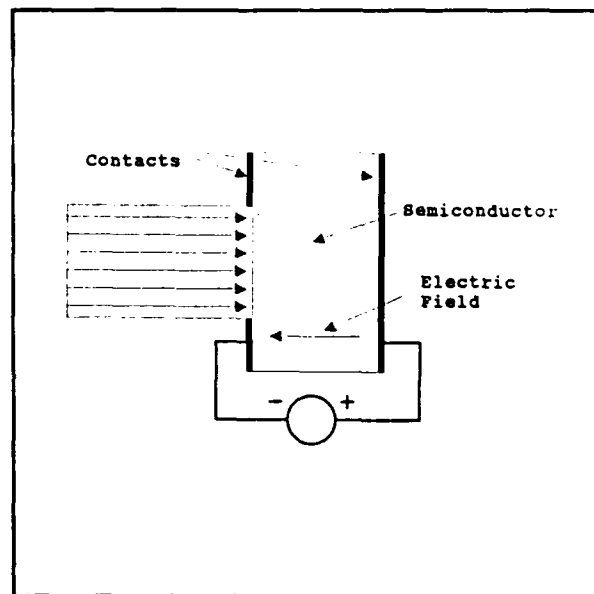

Figure 1 Linear Photoconductive Switch

1

presently not completely understood. Several closure performance limitations have been observed including: 1) closure time limited to several hundreds of picoseconds, apparently by drift times through the switch, 2) the conduction electric field in the switch is independent of the initial voltage and results in large power dissipation densities, and 3) the lifetime of "avalanche like" switches is a function of the switch current density which is indicative of current filamentation due to local thermal effects.

There are several objectives of the model. These are to 1) correlate experimental results, 2) explain "lock on", 3) explain closure of the switch with the optical energy both perpendicular and parallel to the electric field (see Fig 2), 4) determine if closure of the switch can be scaled, and 5) incorporate the model into a system model with source and load.

Figure 2a   Optical   Energy
Perpendicular to Electric Field

Figure 2b   Optical   Energy
Parallel to Electric Field

Background

Linear photoconductive switching is a process, in which, a single photon with an energy greater than or equal to the semiconductor band gap energy, produces a single electron pair. A large number of photons are used to generate a large electron-hole carrier density and thus rapidly reduce the resistance of the intrinsic semiconductor switch. The optically generated carriers maintain conduction of the switch until they recombine into the material at the characteristic recombination time. The temporal closure time is directly related to the integral of the optical power absorbed in the switch or the total optical energy. Thus, the operation of the linear switch is nearly independent of the applied voltage indicating that the temporal closure should be similar in the range of 1 - 100 percent of the maximum voltage.

Work by Schoenbach, Lakdawala, Mazzola, Brinkmann[3] et. al at

Old Dominion University in Norfolk, VA, has developed an optically controlled "on-off" switching process that relies on the optical control of interband trap population levels to maintain switch conductivity for periods of time much longer than the characteristic recombination time of GaAs. In this work the semiconductor switches are brought into conduction by optically generating an excess carrier density that saturates the interband traps. The interband trap specie and density normally controls the characteristic recombination time of the material. However, once the traps are saturated using optically generated carriers, the effective carrier recombination time is approximately equal to the trap thermal emission time which is much longer than the characteristic material value. After the initial turn on phase in which the switch acts as a linear photoconductive switch, the excess carrier density in the switch is maintained through double injection at both contacts (Brinkmann, Schoenbach, et. al).

In a double injection device with an applied electric field and large contact carrier densities, the free carrier densities of electrons and holes injected from each contact diffuse into the bulk material a characteristic length determined by the mobility, initial carrier density, contacts and the characteristic material recombination time. If conduction due to the "avalanche-like" closure phenomena is sustained through a double injection process, the switch closure should be limited by carrier transit time in the following manner. The carrier injection process and the recombination process reach a steady state equilibrium to produce the carrier density distributions illustrated in Fig. 3.

Figure 3 Carrier Density With and Without Traps Saturated

Nunnally, et. al at Los Alamos in 1984, determined that the minimum length of silicon switches must exceed the sum of the characteristic diffusion lengths for electrons and holes by an order of magnitude to obtain linear switch I-V characteristics (sponsored by NSWC-Dahlgren, 1984).

Given the steady state distribution of the carrier densities near each contact, there are two ways in which the optical energy can be delivered to the switch these were discussed earlier and are optical energy applied perpendicular to the electric field (Fig. 2a), and optical energy applied parallel to the electric field (Fig. 2b).

If the optical energy is applied perpendicular to the applied electric field as in a linear photoconductive switch, the optical energy will be absorbed uniformly between the electrical contacts
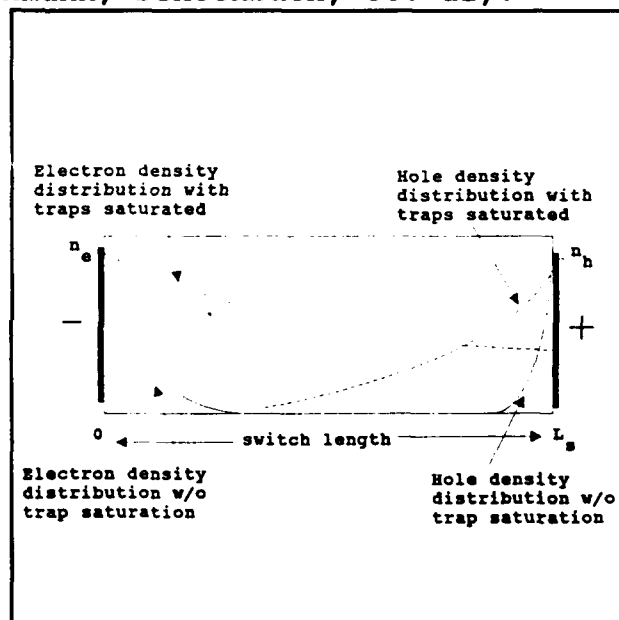
to create an increase in the local carrier density. If sufficient optical energy is delivered to the switch surface, the resulting, optically generated carriers will saturate the interband traps and change the effective recombination time by several orders of magnitude. At the point where the interband traps are saturated, without an excess of carriers, the switch is still not conducting. The steady state carrier diffusion distributions, initially determined by the characteristic material recombination time, must now reach equilibrium with the new, much larger, recombination time (see Fig. 4a). The distribution shift time is also related to the drift velocity of the carriers and thus the closure time will be related to the length of the switch. Note that in this case, perpendicular illumination, additional optical energy will reduce the closure time as in a linear photoconductive switch.
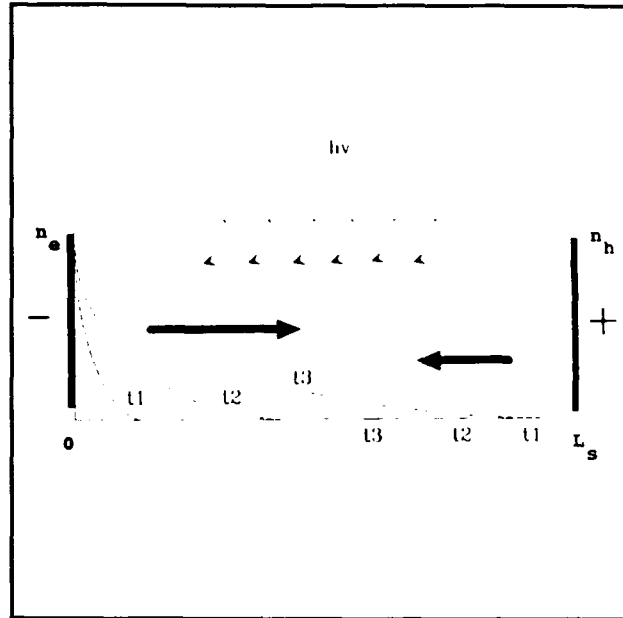
Figure 4a   Trap Saturation with Optical Energy Perpendicular to the Electric Field
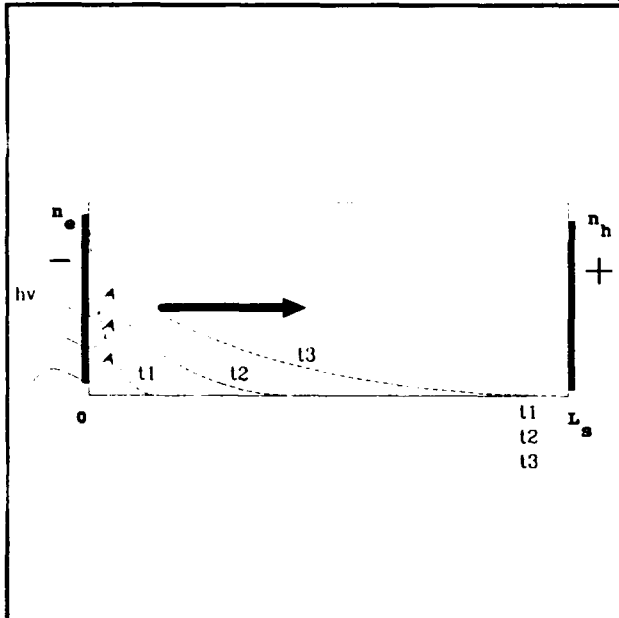
Figure 4b   Trap Saturation with Optical Energy Parallel to the Electric Field

Thus, a switch in which the optical illumination of the semiconductor is perpendicular to the applied electric field can function as a normal photoconductive switch or a pseudo-avalanche switch, depending upon the magnitude and pattern of the optical energy applied to the surface. I f , however, the optical energy is applied parallel to the electric field, the local carrier density is increased where the optical energy is absorbed. The optically generated, electron and hole carrier density perturbations then propagate from the area of optical absorption toward the opposite polarity contact. If the carrier density is sufficient to saturate the traps, the switch volume behind the carrier density perturbation remains conducting and traverses the switch contact separation (see Fig. 4b). In this manner, the closure time is definitely transit time limited and should scale with switch

length or distance between the contacts.

Analysis

Modeling the double injection and trap filling process requires a formulation dependent upon space and time. The basic equations for semiconductor device operations are somewhat difficult to derive, however, they are found directly from Sze[4]. These equations describe the static and dynamic operations of the excess carriers and are shown below. It is assumed in this first order model that all spatially dependent parameters vary only with respect to one coordinate. For the most part the derivation will follow Browder and Nunnally[5]. The continuity equations as a function of space and time are given by,
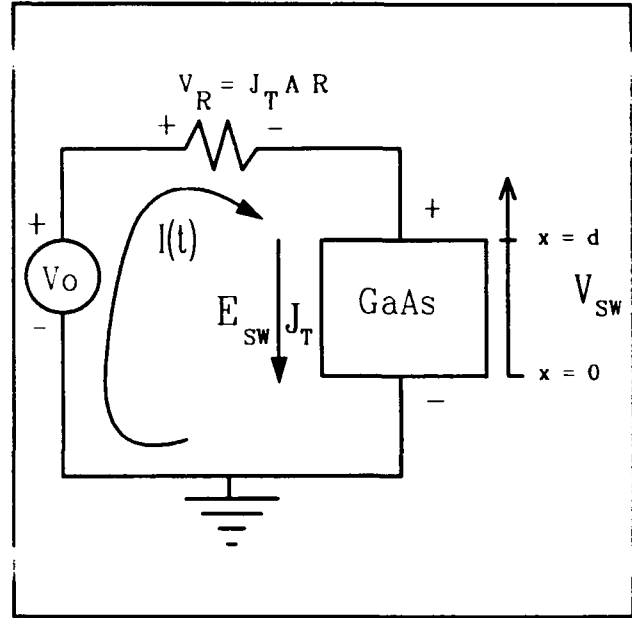

Figure 5 Switch Circuit Model

$$\frac{\partial p(x, t)}{\partial t} = G_p(x, t) - R_p(x, t) - \frac{1}{q}\nabla \cdot J_p \qquad (1)$$

$$\frac{\partial n(x, t)}{\partial t} = G_n(x, t) - R_n(x, t) + \frac{1}{q}\nabla \cdot J_n \qquad (2)$$

where n(x,t) and p(x,t) are the electron and hole densities respectively. $G_{n,p}(x,t)$ and $R_{n,p}(x,t)$ are the generation and recombination rates of the corresponding carriers, and q is electron charge.

$$G_n(x, t) = \alpha_I \Phi(x, t) + e_{nEL2}n_{EL2}(x, t)$$

$$+ c_{nEL2}n(x, t)n_{EL2}(x, t) \qquad (3)$$

$$R_n(x, t) = \kappa_d n(x, t)p(x, t) + \kappa_a n(x, t)^2 p(x, t)$$

$$+ c_{nEL2}n(x, t)n_{EL2}(x, t) \qquad (4)$$

5

$$G_p(x, t) = \alpha_I \Phi(x, t) + e_{pEL2} N_{TEL2} \tag{5}$$

$$R_p(x, t) = \kappa_d n(x, t) p(x, t) + \kappa_a n(x, t)^2 p(x, t)$$

$$+ C_{pEL2} p(x, t) + e_{pEL2} n_{EL2}(x, t) \tag{6}$$

In this particular model, only the EL2[6] trap is included. The model can easily be expanded to incorporate more traps.

$$J_n(x, t) = q(\mu_n E(x, t) n(x, t) + D_n \nabla n(x, t)) \tag{7}$$

$$J_p(x, t) = q(\mu_p E(x, t) p(x, t) - D_p \nabla p(x, t)) \tag{8}$$

are the electron current density and the hole current density. Also necessary are the trap density rate equations,

$$\frac{\partial n_{EL2}(x, t)}{\partial t} = (C_{nEL2} n(x, t) + e_p) N_{TEL2}$$

$$- n_{EL2}(x, t)(C_{nEL2} n(x, t) + C_{pEL2} p(x, t) + e_n + e_p) \tag{9}$$

and Poisson's equation,

$$-\nabla \cdot E(x, t) = -\frac{q}{\varepsilon}(p(x, t) - n(x, t) - n_{EL2}(x, t)) \tag{10}$$

where,

κ_d = direct recombination coefficient,

κ_a = auger recombination coefficient,

$n_{EL2}(x, t)$ = density of filled EL2 traps,

α_I = intrinsic absorption coefficient,

e_n, e_p = electron, hole emission rates,

e_{nEL2}, e_{pEL2} = EL2 electron, hole emission rates,

c_{nEL2}, c_{pEL2} = EL2 electron, hole capture rates,

N_{TEL2} = total EL2 trap density,

$\Phi(x, t)$ = Flux intensity(spatial, time).

These equations are then related to the outside circuit (see Fig. 5) through the boundary conditions and the total current density. Following Iverson and Smith's[7] derivation of the electric potential $V_{sw}(d,t)$; $V_{sw}(0,t)$ at the boundaries and the total current density $J_T(t)$ through the switch yields,

$$\frac{\partial}{\partial x} \left(J_n(x, t) + J_p(x, t) + e \frac{\partial E(x, t)}{\partial t} \right) = 0 \tag{11}$$

$$J_T(t) = J_n(x, t) + J_p(x, t) + J_D(x, t) \tag{12}$$

$$\nabla \cdot J_T = 0 \tag{13}$$

where,

$$J_D = e \frac{\partial E(x, t)}{\partial t} \tag{14}$$

which is the electromagnetic displacement current density.

The circuit current i(t) is related to $J_T(t)$ simply by,

$$i(t) = J_T(t) A \tag{15}$$

where A is the cross-sectional area of the effective current channel. Thus the electric potential at x = d is

7

$$\psi(d,t) = V_o - J_T(t) AR = V_{sw}(d,t) \tag{16}$$

where R is the load resistor. Since $J_T(t)$ is spatially invariant, by definition (Iverson[8]),

$$\frac{1}{d} \int_0^d J_T(t)\, dx = J_T(t) \tag{17}$$

plugging the above into the equations yields $V_{sw}(d,t)$ as a function of time, thus

$$\frac{\partial V_{sw}(d,t)}{\partial t} + \frac{d}{eAR} [V_{sw}(d,t) - V_o] =$$

$$\frac{q}{e} \left(\int_0^d E(x,t) (\mu_n n(x,t) + \mu_p p(x,t))\, dx + D_n n(x,t) \Big|_0^d - D_p p(x,t) \Big|_0^d \right) \tag{18}$$

Which completes the system of nonlinearly coupled, parabolic/elliptic partial differential equations. There are, however, several GaAs parameters that are dependent upon the electric field. All the parameters dependent upon the electric field can be related to the carrier velocities. The carrier velocities are in turn dependent upon the electric field. This is a somewhat simple model but should suffice for a first order model. The carrier velocity equations were obtained from White, Dease, Pocha, Khanaka[9].

$$V_n = \frac{\mu_{nmax} E + V_{nsat} \left(\frac{E}{E_{n0}}\right)^4}{1 + \left(\frac{E}{E_{n0}}\right)^4} \tag{19}$$

$$V_p = \mu_{pmax} \frac{E}{1 + \left(\mu_{pmax} \frac{E}{V_{nsat}}\right)} \tag{20}$$

where μ_{nmax} and μ_{pmax} are the maximum electron and hole mobilities, V_{nsat} is the saturation velocity of the electron, and E_{n0} is the electric field at which the electron velocity reaches a maximum. The electron and hole mobilities are then assumed (for all E) to be

8

$$\mu_n = \frac{v_n}{E} + u_{nsat} \qquad\qquad (21)$$

$$\mu_p = \frac{v_p}{E} \qquad\qquad (22)$$

where μ_{nsat} is the electron saturation mobility This makes the electron and hole diffusivities dependent upon the electric field. Correspondingly the capture rates of the traps are also dependent upon the electric field.

An explicit finite difference method was initially employed to solve the equations. The distinct advantage being the straightforward implementation of the equations. The method, however, proved to be somewhat unstable. The instabilities that were introduced tainted the solution. The problem is currently being rectified. A solution method similar to Iverson[10] is currently being pursued along with an upgrade in machines.

Although the initial computer runs proved fallible a qualitative view of the solution could be assessed. The carriers diffused into the material and propagation of the electrons began across the switch when the traps were filled with the light. The initial results displayed a dependence upon switch length.

Conclusion

The U.T. Arlington model takes into account the recombination dependence of diffusion associated with double injection and the related trap filling process. In addition, the model includes field dependent trapping parameters. These semiconductor parameters' dependencies upon the electric field in conjunction with the nonuniform space charge distribution (due to contact injection), appear to be of some importance in non-linear photoconductive switching.

Improved computer codes and computer facilities are currently being pursued to obtain more reliable solutions.

References

[1] G. M. Loubriel, M. W. O'Malley, F. J. Zutavern, "High Current Photoconductive Semiconductor Switches," Proceedings of the 6th IEEE Pulsed Power Conference, 1987, Arlington, VA.

[2] M. D. Pocha, R. L. Druce, M. J. Wilson, W. W. Hofer, "Avalanche Photoconductive Switching," Proceedings of the 7th IEEE Pulsed Power Conference, 1989, Monterey, CA.

[3] K. H. Schoenbach, V. K. Lakdawala, M. S. Mazzola, S. T. Ko, "A Novel Optoelectronic Closing and Opening Switch for Pulsed Power," Proceedings of the 24th Intersociety Energy Conversion Engineering Conference, pp. 1079-1083. 1989.

[4]   S. M. Sze, <u>Physics of Semiconductor Devices</u>, (John Wiley & Sons, 1981), p. 850.

[5]   M. K. Browder and W. C. Nunnally, "Analytical Studies of Non-Linear Photoconductive Switching in Bulk GaAs Semiconductor Switches," preprint from the <u>1990 Nineteenth Power Modulator Symposium</u>, 1990, San Diego, CA.

[6]   J. S. Blakemore (ed.), <u>Gallium Arsenide</u>, (American Institute of Physics, 1987), pp. 368-373.

[7]   A. E. Iverson, D. L. Smith, "Mathematical Modeling of Photoconductor Transient Response," <u>IEEE Transactions on Electron Devices</u>, Vol. ED-34, No. 10, Oct. 1987.

[8]   A. E. Iverson, "The Mathematical Modeling of Photoconductive Power Switches," <u>Transactions of The Society for Computer Simulation</u>, Vol. 5, No. 3, pp. 175-191, 1988.

[9]   W. T. White, C. G. Dease, M. D. Pocha, G. H. Khanaka, "Modeling GaAs High-Voltage Subnanosecond Photoconductive Switches in One Spatial Dimension," LLNL UCRL-102855 Preprint, Feb. 1990.

[10]   A. E. Iverson, <u>The Mathematical Modeling of Time-Dependent Photoconductive Phenomena in Semiconductors</u>, Los Alamos National Laboratory, Publication LA-11044-T (Thesis), July 1987.

EXTENDED DURATION BENCHTOP HYBRID COMBUSTOR

Martin Brouillette
STD Research Corporation
Post Office Box "C"
Arcadia, CA 91066

Benchtop Hybrid Combustor for
MHD Pulsed Power Supplies

C. D. Maxwell, S. T. Demetriades
and M. Brouillette

STD Research Corporation
Arcadia, California

ABSTRACT

Current military and civilian needs for pulsed power technology are discussed and various prospective high performance pulsed power systems are reviewed. It is found that the hybrid combustor-driven, self-excited high-interaction magnetohydrodynamic (MIID) generator concept pioneered by STD Research Corporation compares favorably with other proposed systems. Progress in the development of the portable multi-megawatt STD/MHD power generators is reported. The combination of improved combustor performance, expansion ratios, and loading more than doubled the efficiency of the STD/MHD generator over earlier results, both on the basis of gross and net electrical energy produced per kilogram of propellant. In fact, new records for enthalpy extraction were set during the last series of tests. Furthermore, demonstration of a method for generating a regular train of multi-megawatt power pulses without electronic power conditioning opened interesting possibilities for power conversion equipment mass reduction or elimination. Tests to date have uncovered no obstacles to the realization of lightweight, long-pulse MHD generators. The Phase I accomplishments of the Extended Duration Benchtop Hybrid Combustor (ED/BHC) are also reviewed and the Phase II work performed to date is reported. This experimental device will provide the basis for realistic testing and characterization of new and more potent hybrid fuel combinations, advanced combustor components, improved cooling techniques, new MHD combustor and generator materials, and demonstrate start-stop capabilities, all of which will lead to MHD pulsed power sources of even higher performance.

INTRODUCTION

The Nation's urgent need for devices able to generate high electrical power levels for short time durations has been acknowledged in many forums. In fact, pulsed power technology was recently recognized by the Pentagon (Ref. 1) as one of the technologies designated by the Secretary of Defense as "most critical to insuring the long-term qualitative superiority of United States weapon systems." The same report also pointed out that the Soviets hold a significant lead in this multi-use, generic technology. In addition to its importance to the national security of the United States, the development of pulsed power technologies will find important applications in many civilian fields.

©1990 STD Research Corporation

This paper discusses the need for pulsed power systems and describes various technological alternatives currently proposed and/or developed. The hybrid combustor-driven, self-excited high-interaction MHD generator pioneered by STD Research Corporation is presented as an advantageous system for pulsed electrical power at the multimegawatt level for long time durations (500 seconds). The latest record-breaking experiments performed with this device are reported. The progress of the Extended Duration Benchtop Hybrid Combustor (ED/BHC) is also presented. This research program, sponsored by SDIO/ONR as the Phase II of a Small Business Innovative Research (SBIR) award, will lead to the timely and affordable resolution of issues associated with long-duration hybrid combustion at elevated pressures. More specifically, this device will provide the basis for realistic testing and characterization of new and more potent hybrid fuel combinations, advanced combustor components, improved cooling techniques, new MHD combustor and generator materials, and demonstrate start-stop capabilities.

THE NEED FOR PULSED POWER

Pulsed power can be loosely defined as the technology able to generate, quickly and on demand, bursts of electricity from tens to hundreds of megawatts (and beyond) for time durations ranging from fractions of a second up to a few thousand seconds. In the present context, we define pulse power as the technology devoted to produce very powerful electrical pulses (gigawatts, terawatts and beyond) for extremely short time durations (fractions of a second). On the other hand, pulsed power can be defined as the technology concerned with the production of prime electrical power (a few kilowatts to hundreds of megawatts) on demand for sustained time durations ranging from seconds to minutes. Prime power from pulsed sources therefore has numerous military and civilian applications, which include pulse power devices.

The need for pulsed power supplies as prime power sources for other devices can be found in all branches of the military, for use on the ground, at sea or in space, in space exploration and in the exploration and exploitation of mineral resources.

Military applications require pulsed power for directed energy weapon, kinetic energy weapon, surveillance, countermeasure and aircraft/spacecraft launching/propulsion systems. Weapon systems currently being developed with the requirements for pulsed power include:

- kinetic energy weapons such as the electrical energy gun (EEG),
- free electron lasers (FEL),
- excimer lasers,
- chemical lasers,
- neutral-particle beam (NPB) systems,
- charged particle beam (CPB) systems.
- impulse radars.

©1990 STD Research Corporation

The power requirements of each system may differ dramatically. For example it is estimated that current proposed versions of ground-based free electron lasers would need power supplies able to deliver gigawatts of average electrical power; the same requirements apply to excimer lasers. Power requirements for the proposed space-based FELs and excimer lasers are expected to be somewhat lower. Other space-based weapon systems such as charged-particle beams and neutral particle beams will require about 50 to 500 MWe per platform. Power requirements for chemical lasers appear to be much lower (10-100 kWe) (Ref. 2). Finally, the operation of electrical energy guns typically will require a total of about ten 5-30 MWe electrical bursts, each lasting approximately 10 seconds (Ref. 3).

Pulsed power is also required for linear accelerators used to launch large masses. For example, electromagnetic mass aircraft launchers (EMAL) are projected to require 70 MWe bursts that last about 3 seconds. The EMAL principles can conceivably be applied to a catapult for mining the surface of the moon or other asteroid (Ref. 4). Direct earth-to-orbit electromagnetic mass launchers require multi-gigawatt or terawatt power levels.

Finally, important civilian applications include earth or planet sounding tomography for detailed underground exploration and mapping, earthquake fault and ore detection. For these applications, power levels in excess of 5 MWe are required for 2 or 3 pulses lasting about 5 seconds each (Ref. 5).

While the most demanding pulsed power requirements are those of SDI, some projected civil or NASA applications under discussion could certainly capitalize on the SDI investment.

PULSED POWER SYSTEMS

Many methods have been proposed to satisfy the power needs of the devices listed in the previous section. For example, pulsed power objectives must often be achieved within acceptable weight and volume limitations dictated by constraints in the performance of the application platform. Therefore, the suitability of a pulsed power source has to be carefully evaluated by taking into account the performance of the application platform as a whole. In many cases the feasibility of a pulsed power application is solely determined by the availability of the required power source.

At present, research in pulsed power plants is directed toward increasing efficiency, reducing volume and mass, and improving predictability and reliability. Some of these advances also involve the development of more environmentally acceptable systems and materials.

Finally, in addition to the improvement of the methods to produce and/or store the electrical energy, most of the proposed pulsed power scheme require the development of new ways to switch both power and loads to achieve the required instant-on operation. This requirement falls into the area of pulse power physics research.

For example, pulsed power requirements are extremely critical to the design of any orbiting platform; severe mass and cost penalties can be incurred by excessive conservatism in the estimation of power level and duration performance of a pulsed power system. Pulsed power subsystems, for illustration, are estimated to make-up some 20-50 percent of the total mass of the space platform for SDI applications.

©1990 STD Research Corporation

Pulsed power systems can be split into two general categories: open-cycle and closed-cycle systems. In open-cycle systems the working fluid is rejected to the surroundings. In closed-cycle systems the working fluid is recirculated and reused. Below is a brief list of some of the proposed pulsed power systems relevant to the applications outlined in the previous section:

Open-cycle systems:

- Open $H_2 - O_2$ fuel cell.
- $H_2 - O_2$ combustor turboalternator.
- $Li - HCl$ battery.
- $H_2 - O_2$ combustor MHD.
- Hybrid combustor MHD.
- Nuclear reactor turboalternator.
- Nuclear reactor MHD.

Closed-cycle systems:

- Ice-cooled $H_2 - O_2$ fuel cell.
- Ice-cooled fuel cell with radiator.
- Closed-combustor turboalternator.
- $Li - MetalS$ battery.

In addition, various combinations of prime power generation and storage are possible, with various performance characteristics. Such methods include: fuel cells, batteries, electrolysis, thermal media, flywheels (*e.g.*, homopolar generators), superconducting magnetic storage or a combination of these techniques.

Chemical MHD pulsed power systems are a variety of open-cycle power systems. An MHD generator is in essence an electromagnetic turbine in which the kinetic energy of an expanding rocket exhaust is converted directly to DC electrical energy through the interaction of free charges in the exhaust with an imposed magnetic field. MHD generators have already been configured as stand-alone pulsed power sources that can produce tens to hundreds of megawatts for tens to hundreds of seconds. Unlike a conventional turbine, an MHD pulsed power system has almost no inertia, and therefore can start and stop within tens of milliseconds. Because the rotating machinery of a conventional turboalternator is eliminated, MHD generators have some prospect for reducing the mass of power systems, especially for burst applications requiring peak powers measured in multi-megawatts.

In practice, the introduction of MHD technology was hampered by extreme high temperature materials requirements, nonuniformity in the electrical conductivity and fluid flow patterns, and the management of the exhaust effluents. Mitigation of the problem of obtaining satisfactory behavior of the fluid flow in the MHD channel during the conversion process requires attaining a highly ionized, high velocity gas stream having adequate uniformity. The gas flowing through the MHD channel consists of a mixture of the hot combustion products of an

©1990 STD Research Corporation

exothermic reaction seeded with an alkali metal to improve electrical conductivity when ionized. Small nonuniformities of gas density and/or ionization concentration (conductivity) can cause major flow instabilities, and the excess heating in these regions causes electrical disturbances and flow disruptions.

However, breakthroughs achieved by STD Research Corporation in the areas of high temperature materials, hybrid combustor technology, exhaust containment techniques and theoretical analysis and computer modeling of MHD flows have allowed the development of a unique hybrid combustor-driven, self-excited high-interaction MHD generator as a prime power source for many applications including pulse power devices. This generator has an extremely low fixed mass, no vulnerable moving parts and converts fuel mass to electrical energy efficiently.

Fig. 1 summarizes the performance of various prime pulsed power sources in a plot of energy density *vs.* specific power density. It is seen that the MHD generator proposed and developed by STD Research Corporation is projected to have a performance superior or at least equal to that of any other system from the point of view of specific power density. It should be noted that the data for the STD/MHD generator are based on actual experiments and computations making use of technologies available today. The data for the other power sources, however, are based on studies performed by various government contractors each employing a different set of assumptions to forecast the performance of these devices and most of these estimates are based on an optimistic far term view of technologies still embryonic.

STD/MHD PULSED POWER

Features of the STD/MHD Pulsed Power System

MHD systems compare favorably *vis-à-vis* gas turbines and other prime power candidates. Although MHD systems may have poorer fuel-mass-to-electricity conversion efficiencies than other candidates, their low dry weight is a clear advantage when fuel mass does not dominate system mass.

STD Research Corporation has been engaged in the research and development of MHD power generating systems for over 25 years and has demonstrated that these systems are capable of producing megawatts of power. A recent development has produced a hybrid propellant composition that is capable of delivering hundreds or thousands of megawatts for hundreds of seconds. The system has shown great promise of providing the high power bursts required for many military and civilian applications. Building on its breakthroughs in hybrid combustor technology, MHD analysis and other technologies, STD Research Corporation has developed the first transportable, multi-megawatt MHD power generator outside the Soviet Union. Unlike comparable Soviet device, however, the STD/ MHD generator is a multi-burst device that can stop and restart.

Even with present or near-term technology, specific powers an order of magnitude higher than any other prime power candidates are possible owing to the low dry weight of the MHD system and the relatively short run times and high burst powers required.

STD/MHD generators have many of the same characteristics as batteries:

- D. C. current source
- No inertia — quick on, quick off
- Rugged — no moving parts
- Noncryogenic

However, as is seen in Fig. 1 and discussed in the previous section, STD/MHD generators have comparable or higher specific energy and much higher specific power than batteries.

Like gas turbines and other open-cycle systems, MHD systems must minimize thrust and effluent effects. STD Research is developing total MHD exhaust containment and thrust cancellation systems that weigh no more than 10% of the propellant weight for space systems. Similar concepts appear to be adaptable to ground-based systems as well.

Some of the possible advantages of STD/MHD power systems are:

- *Affordability.* They are reloadable and sufficiently inexpensive to be expendable if required. In fact, the system cost per kilowatt of electricity produced by the STD/MHD generator is estimated to be almost three orders of magnitude less than that of turbomachinery-based concepts and ten times cheaper than batteries.

- *Safety.* The fuel is inert until exposed to very high temperatures in the presence of oxidizer. The fuel and oxidizer are both shock-resistant. The fuel and oxidizer are stored separately, which removes the possibility of accidental ignition. Because the solid fuel cannot ignite in ambient air or detonate, it does not require treatment as a combustible or a high-explosive. Furthermore, the liquid oxidizer feed system inhibits overpressures by reducing oxidizer flow: the hybrid combustor is instability-proof in the sense that any rise in combustor pressure limits oxidant flow automatically, which dampens the rate of combustion and avoids unwanted pressure excursions.

- *Storability.* The system employs no liquid helium or other cryogenic components or materials. (Although some reduction in fixed weight might be achieved with cryogenics, the additional components and complications generally do not warrant this approach when it is not necessary.) The oxidizer and fuel have essentially infinite shelf life. The system can be stored at any ambient temperature on the ground. The system requires no power in storage.

- *Quick Start/Restart Capability.* Start-up times from completely dormant to full power are less than one second. Restart times are less than 0.5 second. Electrical rise-times are on the order of 100's of milliseconds or less, once the combustor has ignited.

- *Reliability.* The system has no vulnerable moving parts. The moving parts are mainly the oxidizer and igniter control valves and, for cooled systems, the coolant pumps, and, if the oxidizer is pumped rather than pressure-fed,

©1990 STD Research Corporation

a turbopump and motor. The system is simple and has very few parts, significantly fewer than competing generating systems.

- *Ruggedness.* Because it is designed to accommodate relatively high combustion and magnetic pressures, and because it uses no delicate machinery, the system is capable of withstanding strong vibration and overpressures which would damage large rotating machinery.

- *Compactness and Light Weight.* The system inherently has low specific volume (m^3/MJ), high specific power (kW/kg), and high specific energy (MJ/kg).

- *Multiplicity of Uses.* MHD prime power sources are very versatile and can be used for a wide variety of missions requiring pulsed power.

Progress of the STD/MHD Pulsed Power System

In 1984, STD Research Corporation demonstrated a simple, rugged, portable MHD power system driven by a very energetic hybrid combustor. This system was capable of 4-second pulses with peak powers up to 4.8 MW at a full flow rate of about 20 kg/s. Specific energy (power divided by mass flow) was about 0.25 MJ/kg based on gross power (total power from the generator terminals) and about 0.11–0.16 MJ/kg based on net power (generator power less magnet dissipation, or total power to the load) (Ref. 6). In the course of subsequent geophysical tests at STD Research in 1986 (Ref. 5) the power output was improved to 6.1 MW, and bursts of higher efficiency were observed during some combustor transients. Neither in these tests nor in the earlier, pioneering MHD-powered electromagnetic sounding studies in the Soviet Union (Ref. 7), was fuel efficiency an overriding concern, because the duration of the tests was less than 10 seconds. However, pulsed systems with firing durations longer than a few hundred seconds quickly become dominated by fuel mass.

In 1984–87 interest again developed in multi-megawatt MHD power systems for space applications, and fuel efficiency assumed a central importance. Competitive space systems would have open-cycle MHD generators with specific energies of about 2 MJ/kg in space, which corresponds to about 1 MJ/kg on earth (Ref. 8). Furthermore, to power some high-impedance loads, the mass of the voltage conversion equipment might rival the propellant mass (Ref. 8).

Quasi-three-dimensional numerical computations performed at STD Research indicate that efficiency is increased when operating closer to the optimum Mach number M for maximum σU^2, where σ and U are respectively the electrical conductivity and the velocity of the plasma. For the energetic STD hybrid propellant, the optimum Mach number is about $M = 3.5$ to 4.0. System calculations indicate that a 100 bar combustor would optimize the weight of a space system. In 1989 a series of tests, summarized in Table I, was carried out to develop additional combustion data for the final design of a high pressure hybrid combustor. Peak power increased to 7.9 MW during Test 89-002.

©1990 STD Research Corporation

Following completion of a new, high-pressure combustor, tests began in February 1990 to verify the combustor operating parameters over a range up to 104 bar. The results of these experiments are summarized below.

Latest Experimental Results

The last series of tests, which concluded in May 1990, verified the new high-pressure combustor design and showed a substantial increase in MHD generator efficiency. A summary of 1990 test parameters is given in Table II. In these tests it was decided to scale down rather than up in order to take advantage of the better economics, harsher environments and more exacting requirements of smaller flow rates.

Figures 2, 3 and 4 show the arrangement of the components of the MHD system tested in the 1990 test series. The hybrid combustor and MHD generator are mounted on a steel frame that can be elevated at one end, usually to 5° or 10°, to avoid contact between the plume and the ground. Fig. 5 shows a simplified electrical schematic of the self-excited MHD generator circuit.

The high pressure combustor is prominent in Fig. 2. The pressure vessel is rated at 2000 psig. The combustor design is based on a nominal flowrate of 20 kg/s, but it has flexibility to accommodate flow rates ranging from 4 to 50 kg/s. Pressurized oxidizer is stored in the spherical run tank pictured in Fig. 2. Computer-controlled pneumatic valves admit streams of igniter propellant and oxidizer to the chamber according to a preset computer control program.

Tables I and II compare the matrix of tests of the 1989 and 1990 series. While operating conditions vary somewhat from test to test in each series, the 1990 test series generally aimed at higher pressure and lower mass flow rates. For example, the mean operating pressure (over all tests) in the 1989 series was 48 ± 12 bar at a mean mass flow rate of 18.3 ± 3.2 kg/s, while the mean operating pressure during 1990 was 77 ± 23 bar at a mean mass flow rate of 9.2 ± 2.8 kg/s. The higher efficiencies achieved in the 1990 series are evident from the fact that, despite the use of half the mass flow rate on average in 1990, the mean of the measured peak gross power was about 8% higher in 1990 than in 1989. The net power was about 34% higher in 1990 on average.

The mean value of the pressure pulse width (defined as the pulse width at 1/3 of maximum pressure) is 3.24 ± 0.85 sec in 1989, while the corresponding time is 5.2 ± 1.7 sec in 1990.

It is emphasized that these variations are taken over all runs to indicate concisely the approximate range of operation.

The electrical conductivity is estimated from the instantaneous internal impedance found at the time of opening of the load shorting switch S2 (*cf.* Fig. 5). At that moment, the generator voltage-current characteristic is used to determine the instantaneous internal impedance and therefore to estimate the average conductivity (*cf.* Ref. 6). It was possible to follow this procedure in only about half of the tests in each series. While this is not a large statistical sample, it is worth noting that the mean of the conductivities measured over all tests in

©1990 STD Research Corporation

1989 (130 ± 30 S/m) is higher than the 1990 values (103 ± 30 S/m) because of the higher values of load resistance selected in 1990.

The operation of the generator with the high pressure combustor is illustrated in Fig. 6. The dip in pressure at 13.2 seconds occurs when the main oxidizer valve closes and the purge gas drives the oxidizer remaining in the lines into the combustor. The combustor pressure also declines somewhat before the main valve is closed. This is due to erosion of the uncooled nozzle, which had already been fired once before this test and allowed to oxidize. Second and subsequent firings of these uncooled nozzles always produced higher erosion; however, it appears that several solutions to this problem exist, including nozzle cooling and the use of more resistant materials for long duration operation at high pressure. This geometrical effect becomes insignificant as the size of the device is increased.

Fuel grain regression measurements of the port diameter were made after each test. Fig. 7 shows that the fuel erosion is quite uniform after the first 10 inches of the port length. The excess erosion in the injector head end is due to a nonoptimized spray pattern from the oxidizer injectors. This problem becomes insignificant as the length of the grain increases for the contemplated applications. The uniform erosion pattern in the ports indicates that simple grain geometries will be adequate for long duration operation.

The models used to predict combustor and generator performance were validated in the 1990 test series. Fig. 8 indicates good agreement between the pre-test predictions and the measured values of combustor pressure, fuel erosion rates, total mass flow, and MHD power output.

A means of forming a power pulse train in the self-excited circuit is illustrated in Fig. 9. By modulating the oxidizer flow rate, it is possible, with relatively small and easily produced fluctuations in the combustor pressure, to alter the electrical conductivity of the working fluid just enough to produce sharp power pulses, with rise and fall times of about 30 milliseconds in the case of Test 90-012. If this effect is properly exploited, it may be possible to substitute the MHD generator for relatively heavy switching and power conditioning equipment. If tailored properly, the loss in efficiency of the generator might be small enough to warrant its use in place of power conversion equipment.

The present series of tests is aimed at the eventual extension of this generic, multiple-use technology to lightweight generator applications requiring longer pulses (>100 sec) and high-impedance loads (> 100 Ω) (Ref. 8). Because of the dominance of the propellant mass and voltage conversion equipment in such applications, the crucial parameters of such systems are net specific energy (net electrical energy output per unit propellant mass) and power conversion equipment specific power (converted power per unit mass of converter). In Test 90-010 of the present series, a peak net specific energy extraction of 0.47 MJ/kg was achieved, a new world record for net enthalpy extraction for MHD generators. This achievement surpassed the value of 0.45 MJ/kg achieved in Test 56 of the Avco Mark V generator (Ref. 9).

The significant improvement demonstrated by the STD/ MHD devices underscores the need for a sustained effort to reach the full potential of this

technology.

THE STD EXTENDED DURATION
BENCHTOP HYBRID COMBUSTOR

The optimization of the large STD hybrid combustor (solid fuel, liquid oxidizer) requires additional critical data that can only be obtained by testing as well as additional detailed analytical computations. While the fuel used in the STD Research Corporation hybrid combustor has a very slow burning rate, the size of the combustor still is appreciable. For example, at 1500 psia, the burning rate is only about 1 mm/sec. However, even for this low rate, a 1000 second firing duration will require a full web thickness of one meter. This combustor would be at least 2 meters in diameter, would consume over 50 kg/s of propellant and would cost several million dollars to build and operate.

Since the cost of constructing and operating these giant devices is high, it is desirable to employ a small scale model to obtain the desired experimental data and to demonstrate the suitability of new materials or designs.

The extended-duration benchtop hybrid combustor (ED/BHC) is being developed to produce a test device for affordable, small-scale, realistic experiments with high-pressure (1500 psia) and long duration (30 seconds). The ED/BHC achieves sustained long-duration hybrid combustion in a small and economical package by keeping the geometry of the device constant over time. This is accomplished by feeding the grain into the combustor at the same rate as it is eroding due to combustion. This methods allows the size of the combustion chamber to be kept small and the costs to be kept low.

When completely developed during Phase II, this apparatus will bring about an order-of-magnitude reduction in the cost and will speed up the schedule for the development of multi-megawatt pulsed power systems. The device will provide the basis for realistic testing and characterization of new and more potent hybrid fuel combinations, advanced combustor components, improved cooling techniques, new MHD combustor and generator materials, and demonstrate start-stop capabilities.

Examples of some of the data that are required to demonstrate a design or predict performance using the STD Research Corporation analytical and numerical models include: (1) the effects of combustor gas temperature and pressure on the burning rate of the solid fuel; (2) the effects of fuel/oxidizer ratio and combustion products on heat transfer, electrical conductivity and other thermodynamic properties; (3) the effects of long burning durations on the properties of the solid fuel; (4) the performance of a total exhaust effluent containment device. This information together with the performance-predicting capabilities already in place at STD Research Corporation will provide the knowledge required to optimize large hybrid combustors.

Phase 1 Test Results

During the Phase I effort, three basic combustor designs were tested using both N_2O_4 and gaseous oxygen as the oxidizer materials. N_2O_4 was used with both

©1990 STD Research Corporation

cooled and uncooled nozzles. Gaseous oxygen was used with a graphite heat sink nozzle. Both configurations using N_2O_4 utilized a concave fuel grain surface similar to that shown in Fig. 10. The configuration used with gaseous oxygen used a convex face on the fuel grain to maintain a constant 0.20 inch separation between the fuel grain and nozzle face (Fig. 11). Oxygen injection was still from the nozzle side, i.e., initially counterflow or countercurrent.

N_2O_4 Tests

Two combustor configurations were tested with N_2O_4. Initially the ignition pulse was too short to ignite the fuel grain. The pyrotechnic igniter was then augmented with a sustaining composition to extend the pulse length. Fuel grain ignition was attained after that.

Ten tests were conducted with the stainless steel heat sink nozzle shown in Fig. 12 and Fig. 13. N_2O_4 was injected through the two 0.015 inch diameter ports which were machined by electron discharge (EDM) through the stainless steel nozzle. Ignition occurred normally but could not be sustained. The examination of the fuel surface after the tests indicated that the combustion was confined to the area near the injector holes (Fig. 14). This observation indicated that a more complex injector is required in order to distribute the N_2O_4 across the face of the fuel. The combustion stopped after approximately three seconds for this experiment. This effect indicated that either the two hole injector supplied enough cool N_2O_4 to quench the flame or that not enough heat was supplied to the fuel by the low pressure combustion gases to liquefy and vaporize the aluminum in order to sustain combustion. The solution to the first observation was to use a more complex twelve slot injector to spread the N_2O_4 more finely and uniformly across the fuel. The solution to the second effect was be to raise the operating pressure to 400 psia where test data had shown that insufficient heat was transferred to the fuel to continue to melt and vaporize the aluminum at the low combustion pressures.

Ten firings were conducted with a twelve-slot oxidizer injector and the water cooled nozzle shown in Fig. 15. Ignition was normal but, again, combustion could not be sustained during the first few tests. Parametric variations were made in N_2O_4 pressure and valve timing to investigate the problem. On the ninth test, an attempt was made to increase the oxidizer jet momentum by increasing injection pressure, but this resulted in a flooding of the combustion chamber with excess liquid N_2O_4. On the tenth test, after experimenting with the valve and flow settings of the various tests, an optimum flow configuration resulted in fuel ignition and several seconds of sustained combustion. After a few seconds, however, the copper nozzle assembly collapsed under the force applied on it by the fuel grain being pushed forward by the pressurized piston fuel feed. It should be noted that when the solid fuel grain became saturated with N_2O_4 it became soft and could be forced into the chamber. When the fuel grain was examined after the tests, it was found to have its outer sides converge inwards so that they plugged up the oxidizer injector holes due to excessive piston pressure. Fig. 16 shows the cooled nozzle after the first test of this series.

©1990 STD Research Corporation

Fig. 17a shows the flame produced by the ignition pulse (N_2O_4 injection off) and Fig. 17b shows that produced when fuel combustion occurs (N_2O_4 injection on). As can be seen the ignition flame is much smaller than the combustion flame. Fig. 18 shows a typical pressure trace with high initial pressure with a tail off as the combustion is extinguished.

Gaseous Oxygen Test

One test with multiple restarts was made using gaseous oxygen and the combustor shown in Fig. 19. The oxygen injection pressure was limited to 200 psi in order to keep the chamber pressure under 100 psi. Although this pressure was low, full ignition was attained and combustion was sustained. It is likely that graphite, part of the converging portion of the nozzle, reached ignition temperature and, in the oxidizer rich environment, produced sufficient heat to maintain the combustion. After ten seconds the combustion became slightly erratic but the fuel continued to burn. Several restarts were made by simply reintroducing oxygen into the chamber onto the hot components. The graphite nozzle and injection face, designed to be inexpensive and expendable, finally became overheated and burned through in the proximity of the injector holes where excess oxygen was present. Fig. 20 shows the disassembled chamber. Fig. 21 shows the combustor during operation.

This test demonstrated that a convex fuel surface along with a high velocity oxidizer stream can deliver sufficient oxidizer to the fuel to sustain combustion even with a crude four-hole injector.

Summary of Phase I Accomplishments

Three different small scale combustors were designed, fabricated and tested during the Phase I program. Questions concerning the minimum size of the device, ignition technique, the configuration of the injector and fuel surface as well as cooling methods have been answered during that phase of the program. The Phase I activity accomplished the following:

1. The end-burning hybrid combustor concept was proved feasible.

2. The size of the device was determined by the ability to fabricate the smallest size oxidizer injection holes in a practical manner. This consideration determined the minimum fuel rod diameter to be 6.17 cm.

3. A pyrotechnic igniter was developed and provided reliable ignition. An electric match (squib) was ignited from a 12 V DC source which in turn ignited a paste composed of 60% KNO_3, 20% Boron and 20% acetate. This paste was augmented with a material composed of 60% ammonium perchlorate, 20% magnesium and 20% epoxy resin binder to provide a one second igniter burning duration.

4. It was found that the oxidizer injection jet has to flow in a direction concurrent with the flow of combustion products.

©1990 STD Research Corporation

5. It was established that the operating pressure and gas velocity should be high enough to provide sufficient heat transfer from the combustion gases to liquefy and vaporize the quantity of aluminum fuel required to sustain stable combustion.

6. The most effective method to cool the nozzle of the experimental combustor is by using flowing-water cooling coils. Calculations showed that the nozzle can be cooled with water for a combustion pressure up to 1500 psia.

Phase II Progress

At the start of the Phase II contract on December 1989, STD Research Corporation prepared a detailed program plan that is compatible with the appreciable reduction in schedule and funding from the original proposal. The new plan, with milestone events shown in the Fig. 22, will result in a demonstration test of the extended-duration benchtop hybrid combustor (ED/BHC) within fifteen (15) months. Although the shorter duration and lower level of funding will require a limitation in the number of design improvements that can be performed, it is the opinion of STD Research Corporation that the program will be successful in developing this very valuable device.

Trade-off studies of the fuel geometry indicated that a two-element rectangular fuel grain allows the most flexibility in changing the combustion gas flow area while still maintaining a uniform regression rate across the face of the fuel. Fig. 23 illustrates the fuel geometry that was chosen. By using rectangular fuel elements instead of circular ones, the port area of the combustor remains constant along the mean flow axis. The rectangular elements are enclosed in a pressure vessel having a size slightly larger than twice the length of each fuel element. In the present design, there can be either two or four such fuel elements (Fig. 24). It can be seen that the gas flow area can be changed easily by merely changing the spacing between the two fuel elements. A decrease in flow area, accomplished by reducing the distance between the fuel elements, increases the combustion gas pressure as well as the combustion gas flow velocity. This results in an increase of the burning rate of the fuel. Conversely, moving the fuel elements farther apart increases the flow area and decreases the fuel burning rate. This arrangement allows the fuel-to-oxidizer mixture ratio to be varied at will to perform experiments over a wide range of parameters. After preliminary tests with the two element configuration establish the fuel burning rates, the combustor can easily be modified to a four element configuration (Fig. 24). The four-element design has the advantage of eliminating the two walls that must be cooled or insulated in the two-element configuration. However, complexity is increased, with respect to the fuel feed system, for example.

A cross-section of the combustor is presented in Fig. 25. It is seen that the combustion port is nominally 1 inch by 1 inch and that the 1-inch thick steel walls of the combustion chamber are protected from the high temperature gases by a 0.5-inch thick layer of graphite backed-up by a thin layer of insulating material. To further prevent undesirable heating of the steel, strategically located ceramic bars and water cooling passages are positioned all along the length of the combustor.

©1990 STD Research Corporation

The strength of this combustor case was analyzed by modeling the various surfaces as flat plates and the angles as beams. The boundary conditions were chosen to produce the most conservative results. It was found that the design will be safe for operation at a combustion pressure of 1500 psi. The combustion case was built at STD Research Corporation and successfully hydrotested to a pressure of 2000 psi.

Fuel feed of the rectangular fuel elements is accomplished by a system comprising a computer-controlled stepper motor mounted on the combustor with two alignment rods to guide each fuel push rod. Thermocouples will be cast in the fuel at various locations to provide heat transfer data and also locate the fuel burning surface during operation. We have chosen to use commercially available "electric cylinders;" each of these devices comprises a ball screw, mounting ball bearings, demultiplication spur gears and a DC stepper motor. The motor will be powered by a drive that translates TTL pulses into shaft rotation increments. The grain feed system will be computer-controlled, using an open- or closed-loop command algorithm.

The pyrotechnic ignition system successfully developed during Phase I had the shortcoming that it could not be used for multiple restarts without disassembling the combustor. However, it is planned to test the larger size Phase II combustor in a multiple restart mode. To achieve this goal, it is planned to use an hypergolic bipropellant ignition system using a liquid fuel and N_2O_4. After ignition of the hybrid occurs, the flow of ignition fuel is stopped and the flow of N_2O_4 continued for the normal hybrid operation. Such a system has successfully been used by STD Research in previous small and large scale combustors. The oxidizer injection and ignition systems use a single injection nozzle to disperse the oxidizer in a square-patterned spray into the combustion chamber. The liquid ignition fuel is injected directly into the combustion chamber where it reacts with the oxidizer. This avoids the need for having a separate combustion chamber for the ignition system. The entire assembly is protected from the hot combustion gases by a graphite liner which is backed by a layer of machinable ceramic to reduce the heat load. The injection/ignition assembly is also equipped with integral water flow passages for cooling.

The nozzle assembly is designed to be disassembled from the main combustor chamber for inspection and replacement of parts and observation of the fuel grain surfaces. The nozzle surfaces exposed to the hot combustion gas, as well as surfaces adjacent to the burning fuel surfaces, are protected with insulation and fabricated from graphite in addition to being water-cooled. The cooled nozzle is designed with passages through which the cooling fluid can flow at velocities up to 10 m/s. The parts that are exposed to the hot gas are machined from fine-grained graphite for increased strength, and the throat is made from pyrolithic graphite for better ablation resistance and heat transfer. We will attempt to reduce ablation at the throat by keeping it cool with strategically located water cooling passages. The nozzle housing is made from copper for good heat transmission. The combustor case will be shielded from the heat load by a ceramic thermal block.

A small trailer is being refurbished to house the hybrid combustor and

©1990 STD Research Corporation

ancillary equipment. Our self-sufficient and portable testing facility will include two electric generators to supply power for the computer and controls.

This is work in progress and Fig. 22 shows the program schedule. The program will be completed in March 1991.

CONCLUSIONS

This paper discussed the need for pulsed power systems and described various technological alternatives currently proposed and/or developed. The hybrid combustor-driven, self-excited high-interaction MHD generator pioneered by STD Research Corporation was presented as an advantageous system for pulsed electrical power at the multimegawatt level for long time durations (500 seconds). The latest record-breaking experiments performed with this device were reported. The progress of the Extended Duration Benchtop Hybrid Combustor (ED/BHC) is also presented. Experiments performed with this device will lead to the timely and affordable resolution of issues associated with long-duration hybrid combustion at elevated pressures. More specifically, this device will provide the basis for realistic testing and characterization of new and more potent hybrid fuel combinations, advanced combustor components, improved cooling techniques, new MHD combustor and generator materials, and demonstrate start-stop capabilities.

ACKNOWLEDGEMENTS

REFERENCES

1. "Critical Technologies Plan," Department of Defense Report AD-A219 300, Washington, 15 March 1990.
2. "Advanced Power Sources for Space Missions," National Research Council, National Academy Press, Washington, 1989.
3. R. Asoklis, Chairman, "Final Report of the Prime Power and Platforms Panel," Electrical Energy Gun System Study, Tactical Technology Office, Defense Advanced Research Projects Agency, Washington, November 1 1988.
4. G.L. Kulcinski and H.H. Schmitt, "The Moon: An Abundant Source of Clean and Safe Fusion Fuel for the 21st Century," Report UWFDM-730, Fusion Technology Institute, University of Wisconsin, Madison, August 1987.

5. H.F. Morrison, C.D. Maxwell, R. Zolinger, W.D. Jackson and S.T. Demetriades, "Application of an MHD Generator to Electromagnetic Sounding," *Proc., 25rd Symposium on Engineering Aspects of MHD,* Bethesda, MD, June 1987.

6. C.D. Maxwell and S.T. Demetriades, "Initial Tests of a Lightweight, Self-Excited MHD Power Generator," *Proc., 23rd Symposium on Engineering Aspects of MHD,* Somerset, PA, June 1985.

7. E.P. Velikhov, B.P. Zhukov, A. E. Sheindlin, *et al.,* "Status and Prospects for the Development of Geophysical MHD Power," *Proc., 8th International Conference on MHD Electric Power Generation,* V. 5, pp. 59–64, Moscow, USSR, September 1983.

8. C.D. Maxwell and S.T. Demetriades, "Feasibility Assessment for Space-Based Multi-Megawatt MHD Power Systems: Preliminary Conceptual Design," STD Research Corporation Report STDR-87-9(J) prepared under Contract DE-AC22-87PC79664, February 1988.

9. A. C. J. Mattsson, *et al.,* "Performance of a Self-Excited MHD Generator," Avco Everett Research Laboratory Research Report 238, prepared under Contract AF 33(615)-1862, October 1965.

Table I. 1989 Test Data Summary

Test Number		89-002	89-003	89-004	89-005	89-006	89-008	89-009	89-010	89-011
Date	(1989)	3-Mar	8-Mar	10-Mar	16-Mar	20-Mar	23-Mar	27-Mar	29-Mar	14-Apr
Pressure Pulse Width, Δt_P	(s)	2.46	2.26	2.66	3.09	4.47	4.42	2.69	3.61	3.70
MHD Channel Number		2	2	2	2	2	2	2	2	2
Average Mass Flow Rate	(kg/s)	19.5	17.1	17.0	14.0	17.3	19.0	19.7	15.7	25.3
Peak Combustor Pressure	(bar)	61	50	36	44	39	55	45	33	67
Avg. Combustor Pressure	(bar)	37	32	28	29	34	40	35	24	60
Load Resistance	(mΩ)	42	33	34	35	32	32	33	32	45
Gross Power (peak)	(MW)	7.93	5.03	4.40	0.03	2.34	5.74	4.76	1.22	0.62
Net Power (peak)	(MW)	5.48	3.11	2.90	0.00	1.96	3.70	3.37	0.96	0.37
Peak Voltage	(kV)	0.720	0.710	0.540	0.508	0.400	0.680	0.655	0.380	0.200
Peak Current	(kA)	11.20	7.90	9.60	0.80	6.10	11.40	10.60	3.30	3.10
σ at S2 Opening	(S/m)	158	—	102	—	—	107	155	—	—

Table II. 1990 Test Data Summary

Test Number		90-003	90-004	90-005	90-006	90-007	90-009	90-010	90-012*
Date	(1990)	27-Feb	8-Mar	15-Mar	23-Mar	12-Apr	25-Apr	27-Apr	3-May
MHD Channel Number		1	1	1	1	3	3	3	3
Pressure Pulse Width, Δt_P	(s)	4.83	3.75	4.38	8.92	5.02	4.50	4.85	12.91
Average Mass Flow Rate	(kg/s)	7.5	8.7	11.8	7.5	10.6	13.9	9.0	4.4
Peak Combustor Pressure	(bar)	80	85	104	48	91	102	56	47
Avg. Combustor Pressure	(bar)	54	72	90	40	78	86	45	37
Load Resistance	(mΩ)	37	—	61	86	86	86	86	75
Gross Power (peak)	(MW)	3.66	3.55	3.93	2.86	5.51	5.09	3.91	2.21
Net Power (peak)	(MW)	1.32	—	3.29	2.86	5.51	5.09	3.71	1.04
Peak Voltage	(kV)	0.725	0.570	0.644	0.591	1.093	0.723	0.726	0.586
Peak Current	(kA)	6.80	7.35	10.44	7.93	11.22	11.46	7.68	4.95
σ at S2 Opening	(S/m)	—	—	142	106	68	120	79	—

* Tests 90-011 and 90-012 combined.
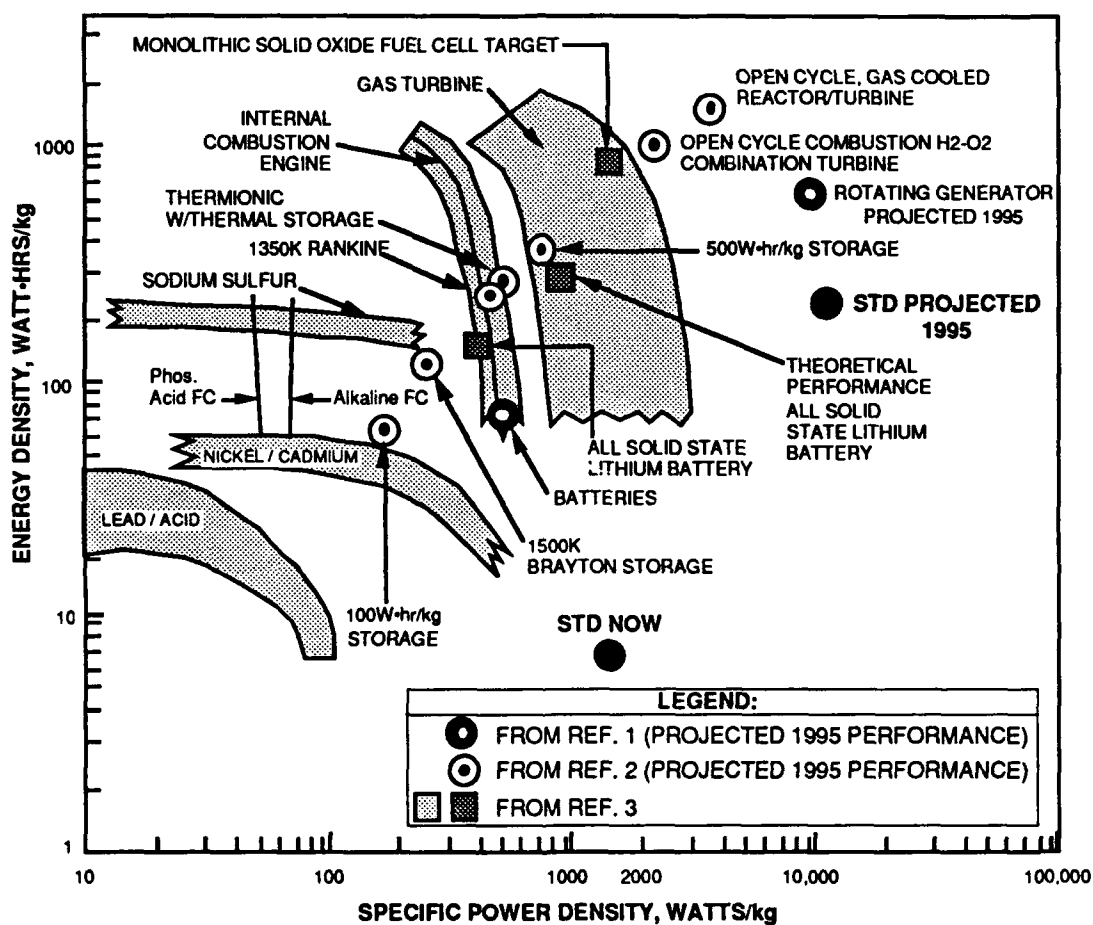
Fig. 1. Prime pulsed power source performance comparisons.

9543
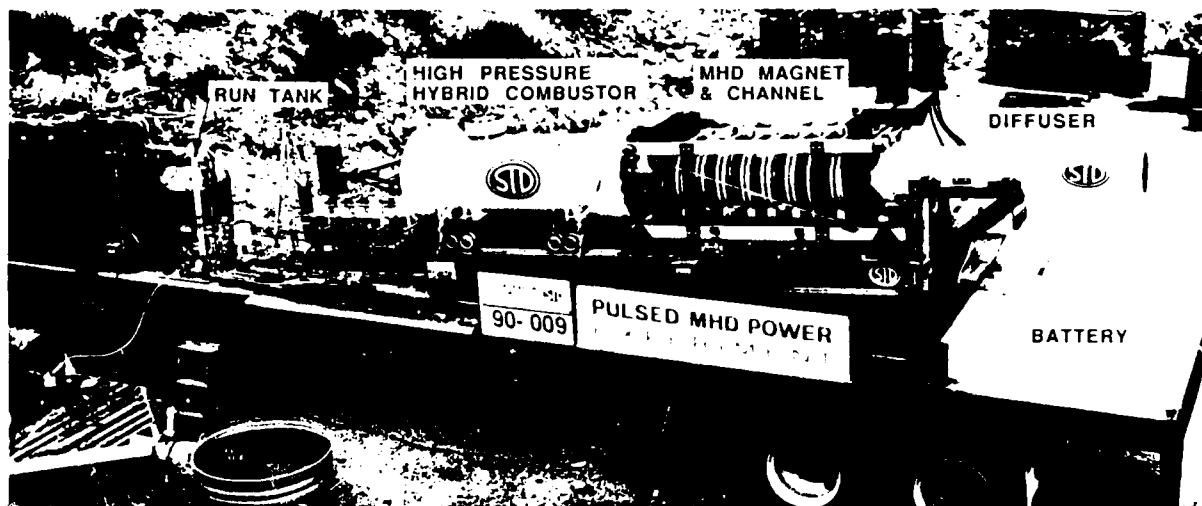
Fig. 2. Principal components of the self-excited STD/MHD generator.

Fig. 3. Mid-test plume during Test 90-005.

Fig. 4. Aerial photo of the test site during Test 90-011 showing instrumentation trailer and MHD trailer.
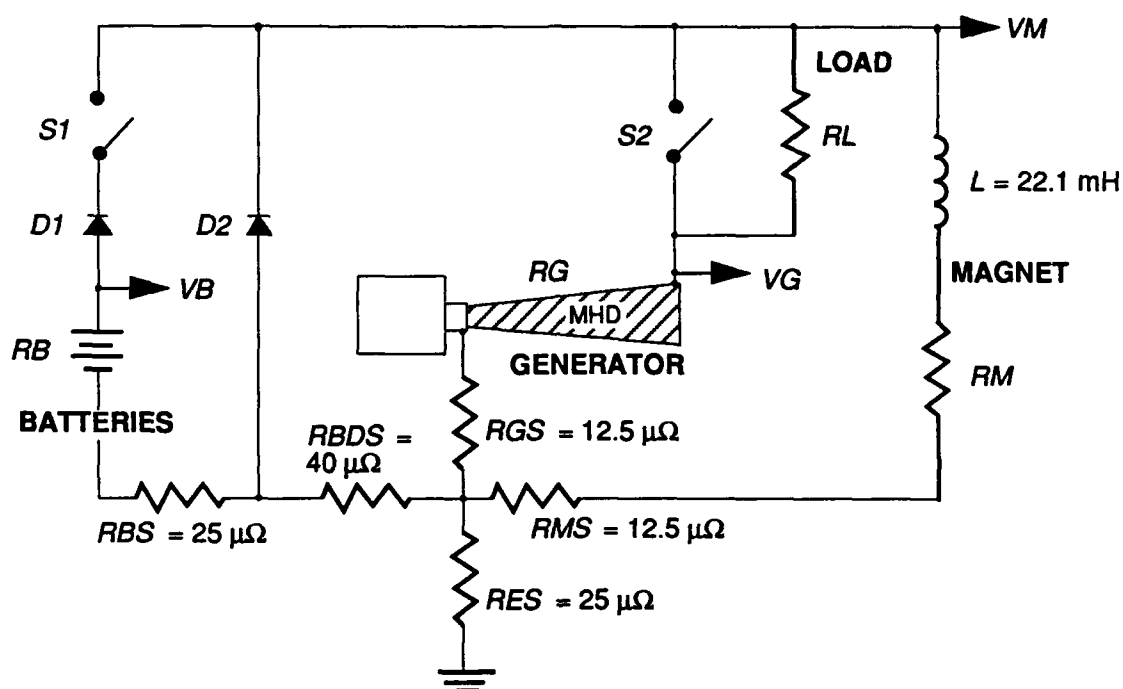
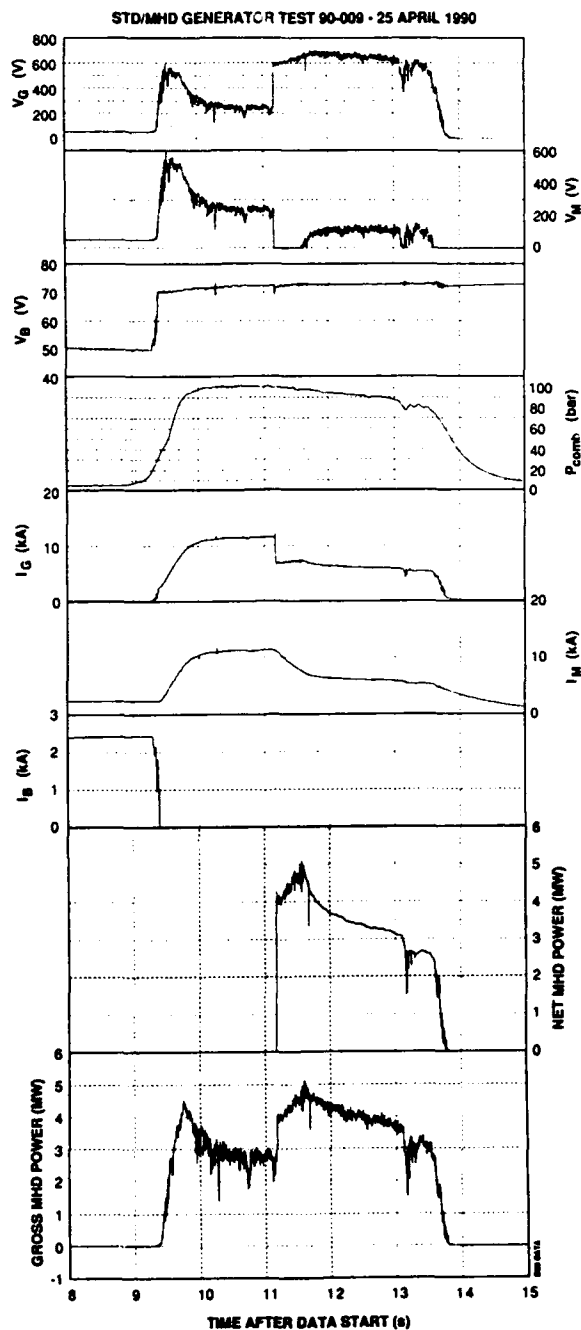**Fig. 5.** Simplified electrical schematic of the self-excited MHD generator.

Fig. 6. Measured variation of voltages, currents, pressure and power during high pressure Test 90-009 of STD/MHD generator. Gross and net powers are derived from the measured currents and voltages. The net power is computed from the voltage drop across the load and the measured load resistance.

©1990 STD Research Corporation
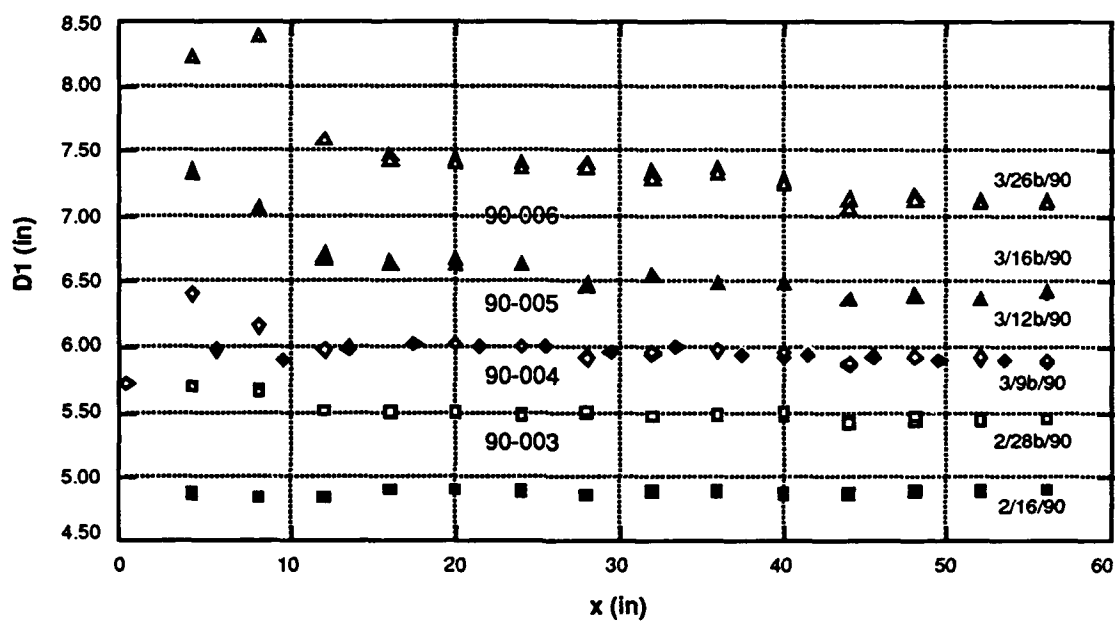
Fig. 7. Axial variation of the diameter of a fuel grain port of STD/MHD generator before and after tests 90-003 through 90-006. $x=0$ corresponds to the oxidizer injection head and $x=60$ to the end of the port near the exhaust nozzle.

9360

©1990 STD Research Corporation

COMBUSTOR PRESSURE (bar)

GROSS POWER (MW)

TOTAL MASS FLOW RATE (kg/s)

FUEL REGRESSION RATE (mm/s)
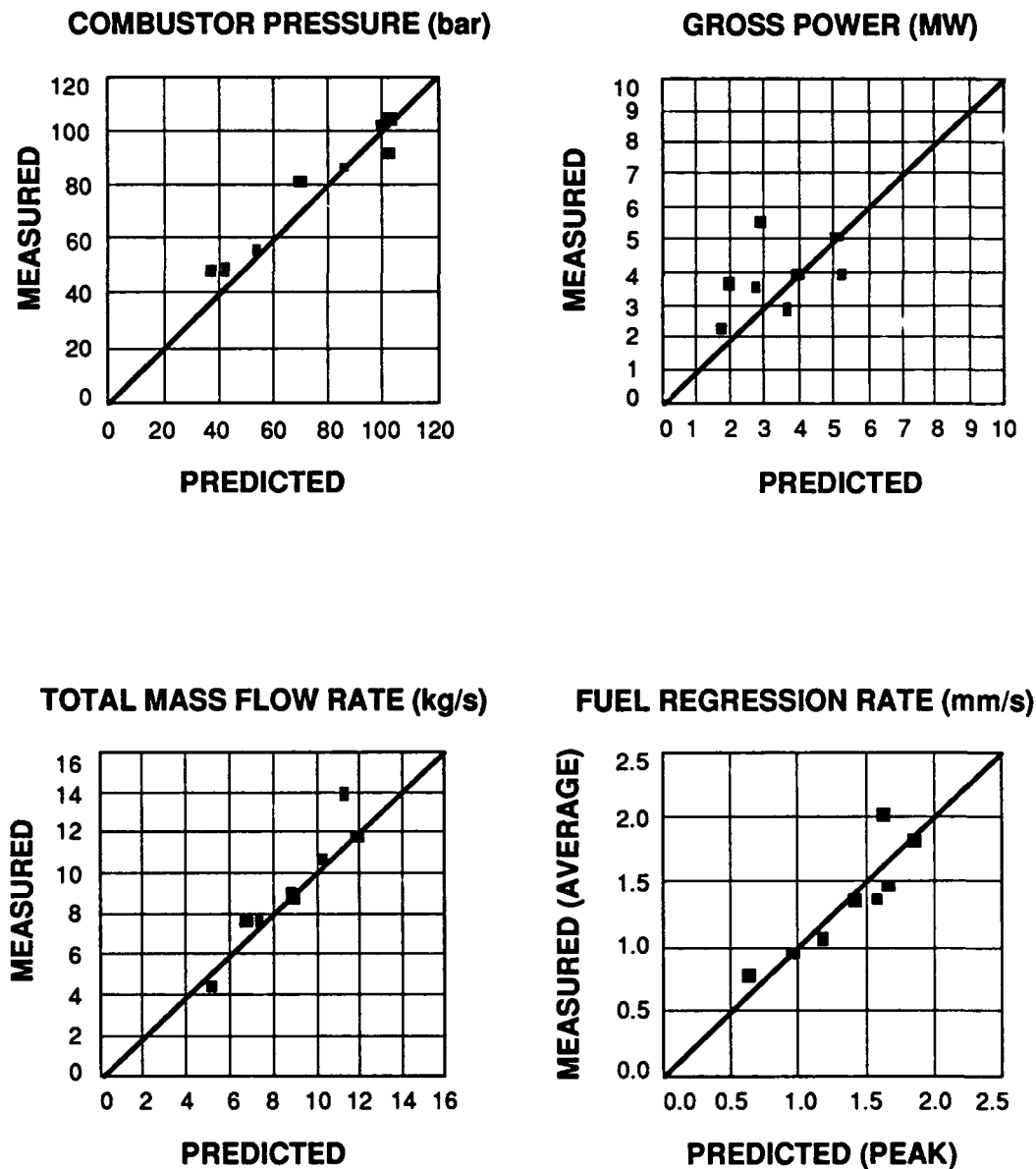
Fig. 8. Comparison of measured and predicted values of mass flow rate, pressure, fuel regression rate, and peak power output during the 1990 test series of the STD/MHD generator.

9514

- 23 -   ©1990 STD Research Corporation
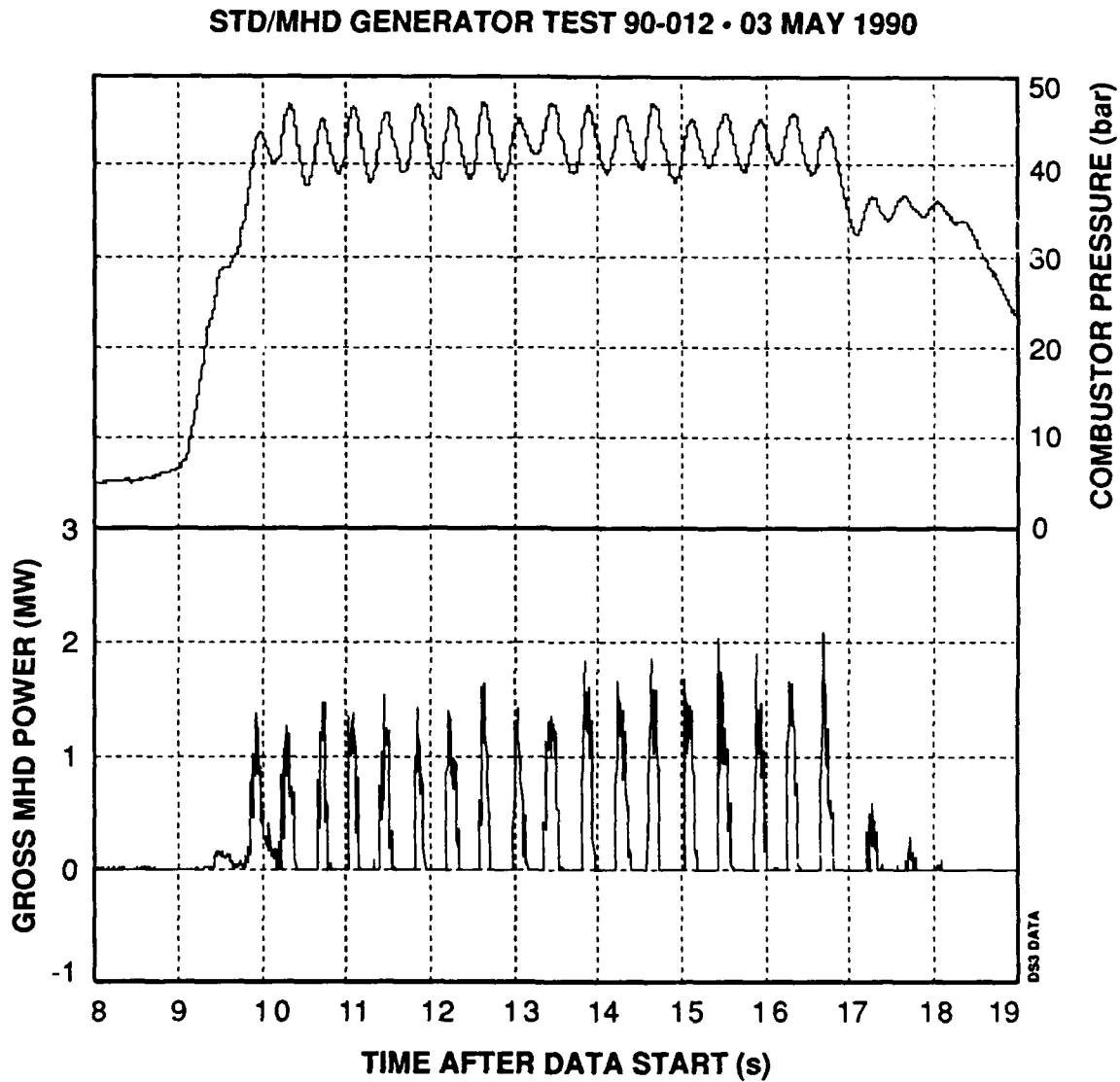
Fig. 9. Variation of combustor pressure and power during test 90-012 of the STD/MHD generator. Small variations in pressure chop the power into regular, discrete pulses.

©1990 STD Research Corporation
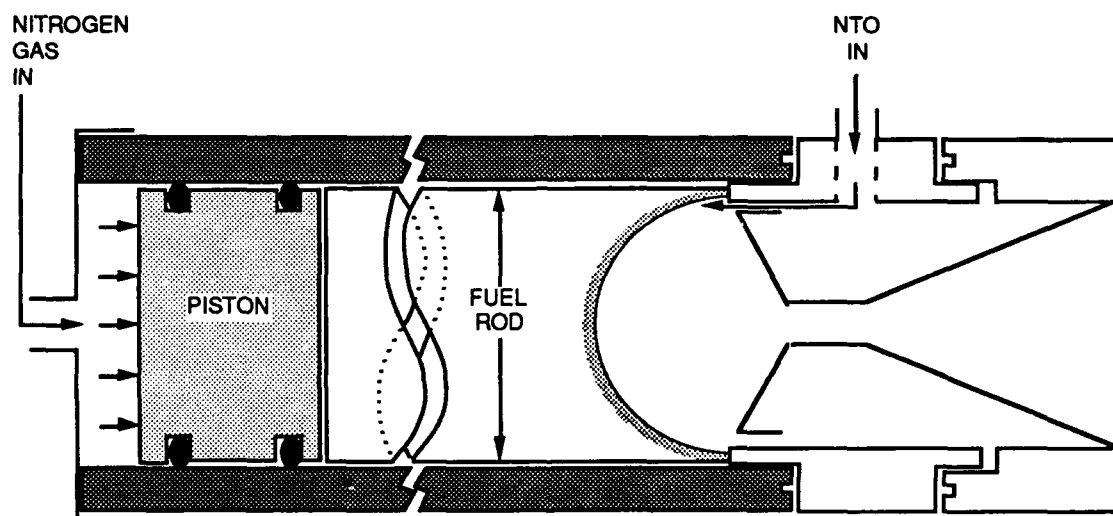
Fig. 10. Schematic of the STD ED/BHC Phase I combustor with concave fuel surface.

9076

©1990 STD Research Corporation
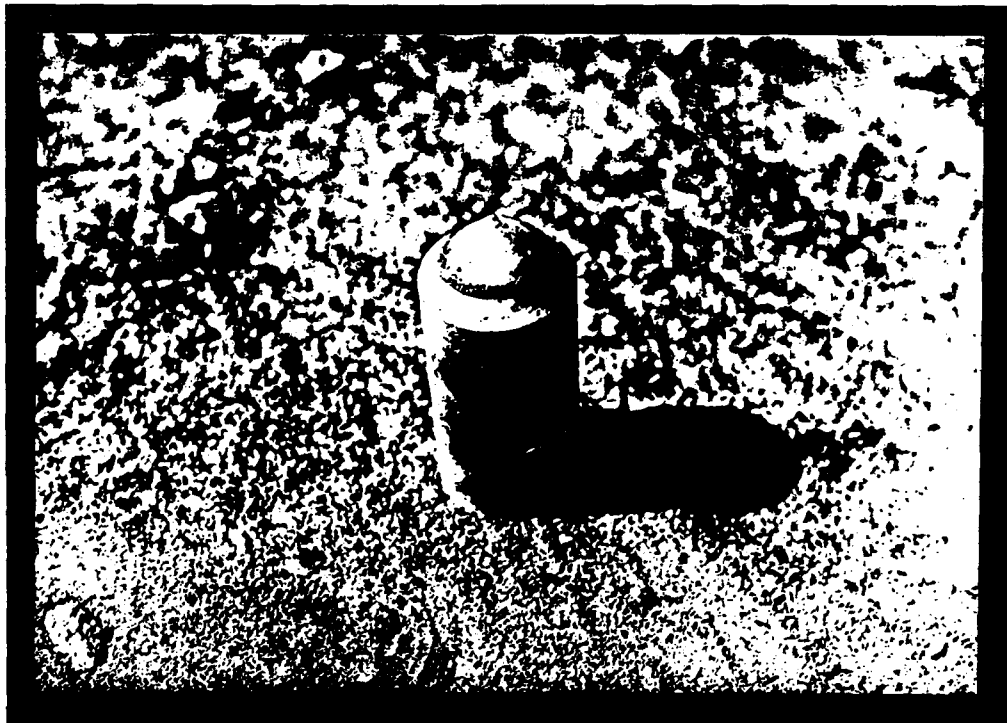
Fig. 11. Convex fuel surface of the STD ED/BHC Phase I combustor.

9088

©1990 STD Research Corporation
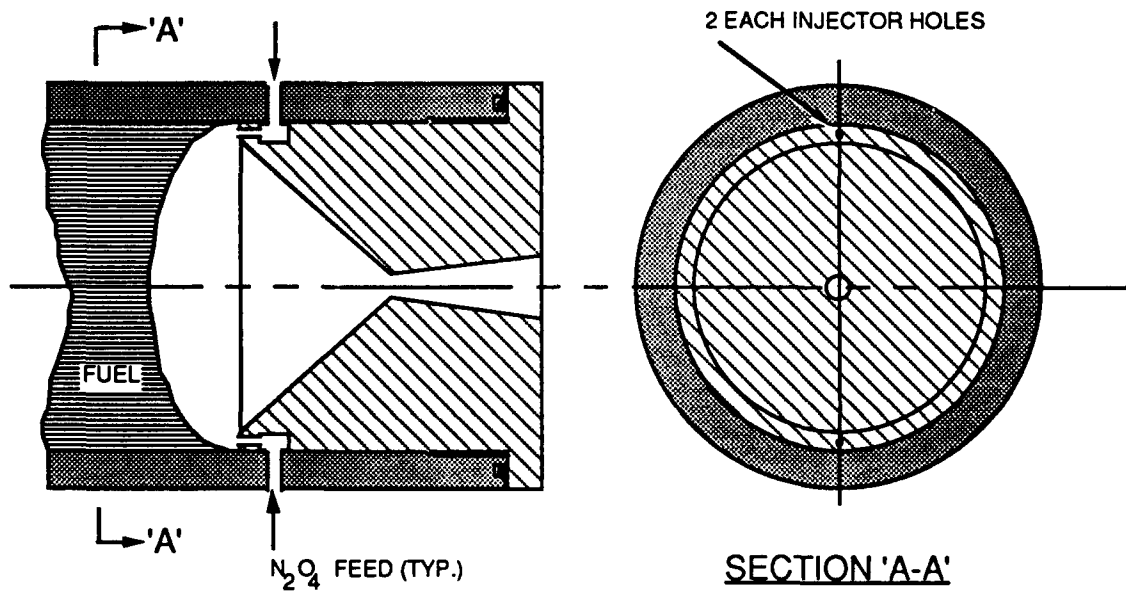
Fig. 12. Two-hole injector with stainless steel heat sink nozzle of STD ED/BHC Phase I combustor.
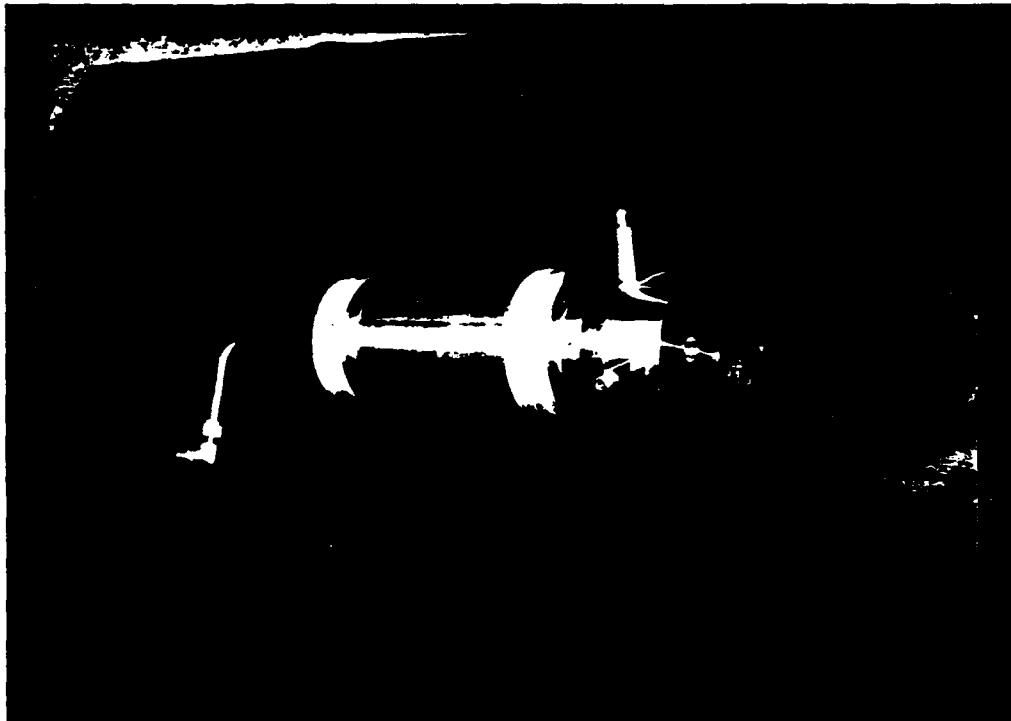
Fig. 13. Photograph of two hole injector and stainless steel heat sink nozzle of STD ED/BHC Phase I combustor.

9091

©1990 STD Research Corporation
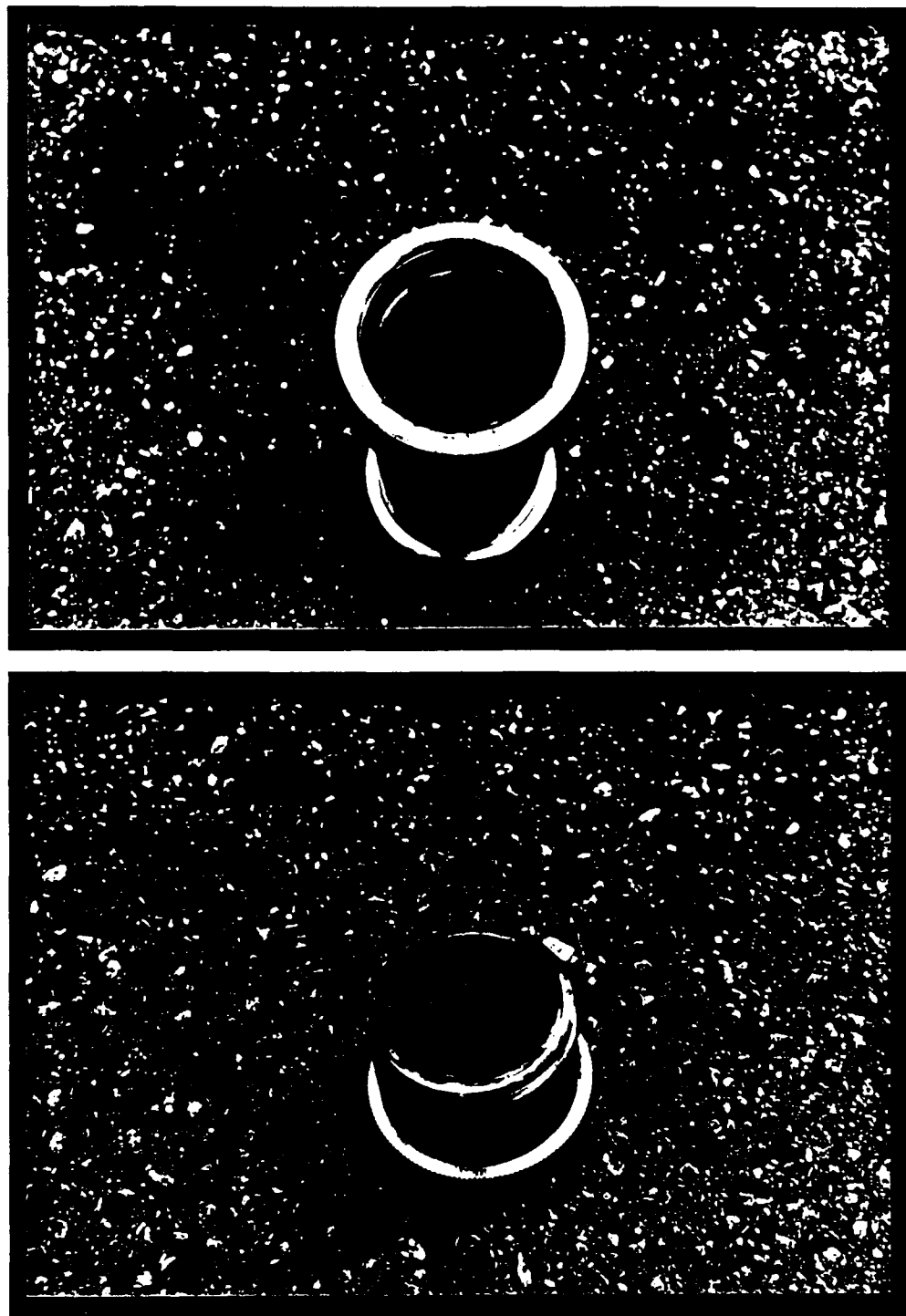
Fig. 14. Photograph of two-hole injector and stainless steel heat sink nozzle of the STD ED/BHC Phase I combustor after many tests.

9092
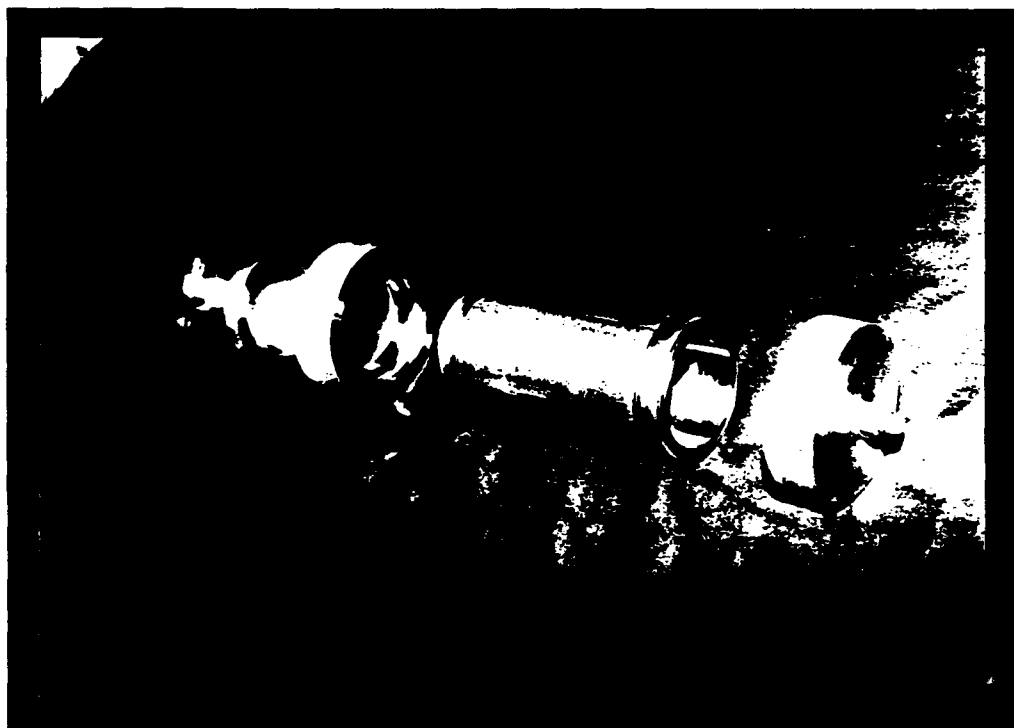
Fig. 15. Photograph of 12-slot injector and water cooled nozzle of STD ED/BHC Phase I combustor.

9093

©1990 STD Research Corporation
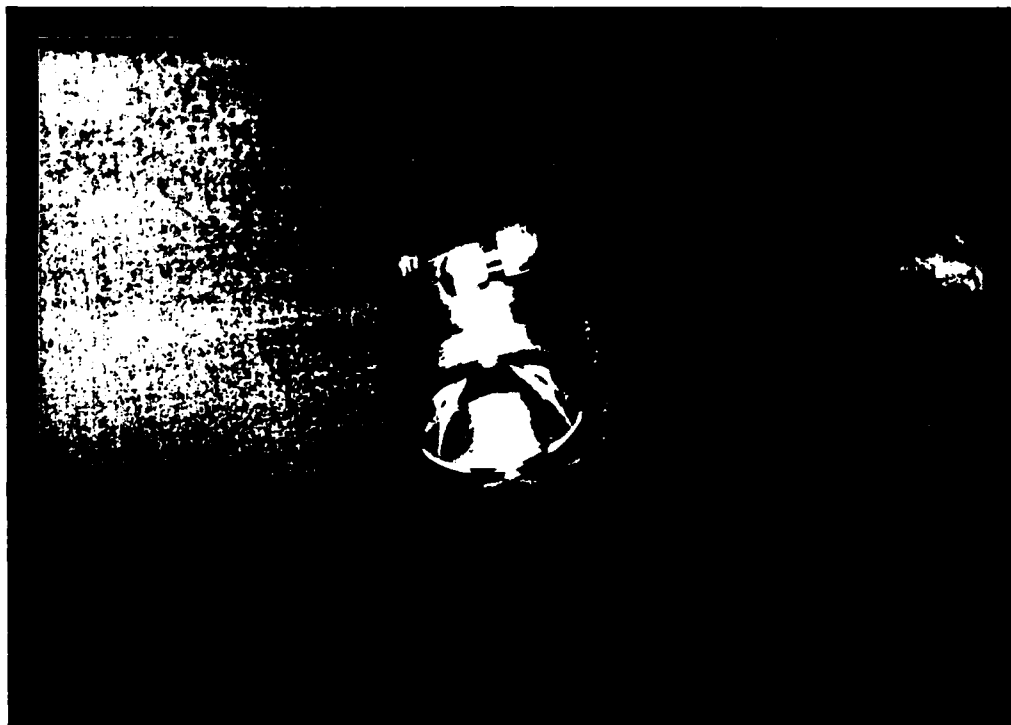
Fig. 16. Photograph of 12-slot injector and water cooled nozzle of STD ED/BHC Phase I combustor after first test.

9094
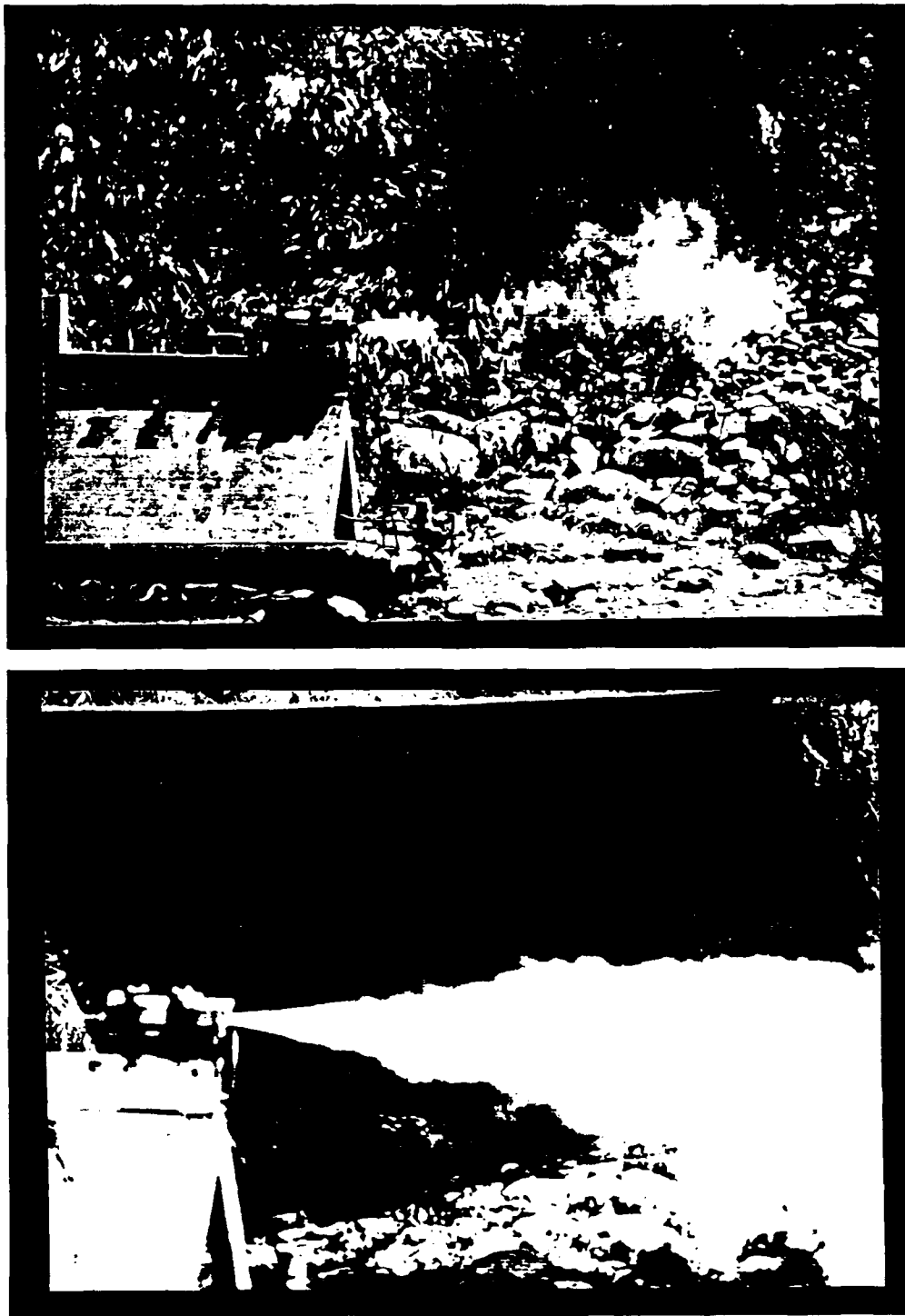
Fig. 17. Photographs of: (a) flame from igniter, (b) flame from fuel/NTO combustion of STD ED/BHC Phase I combustor.
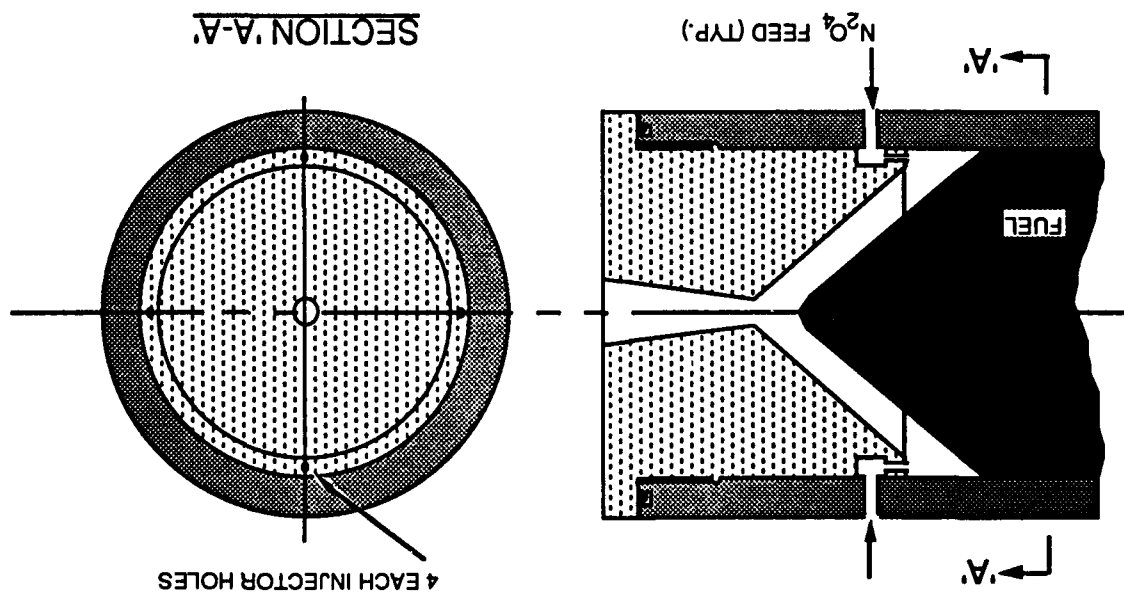
9095

©1990 STD Research Corporation
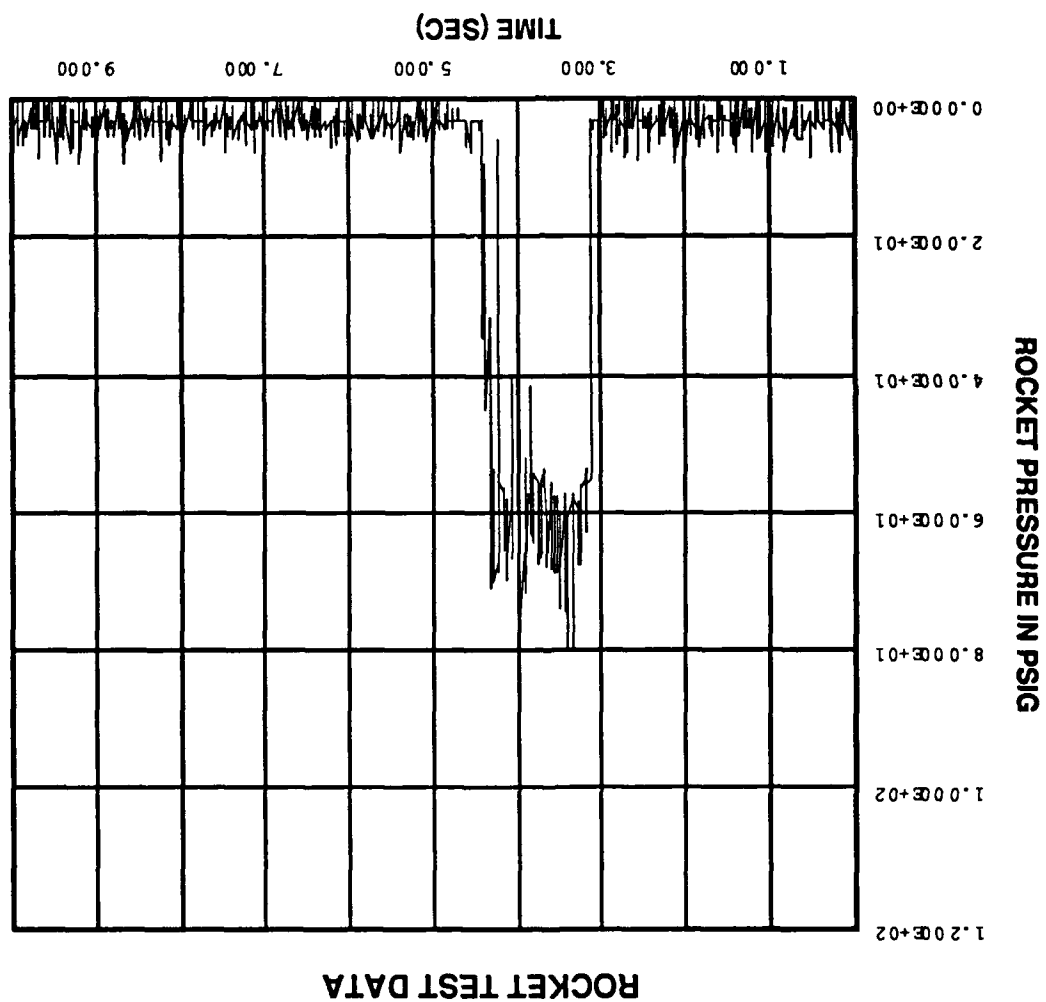
Fig. 18. Typical pressure versus time trace for the firing of the STD ED/BHC Phase I combustor.
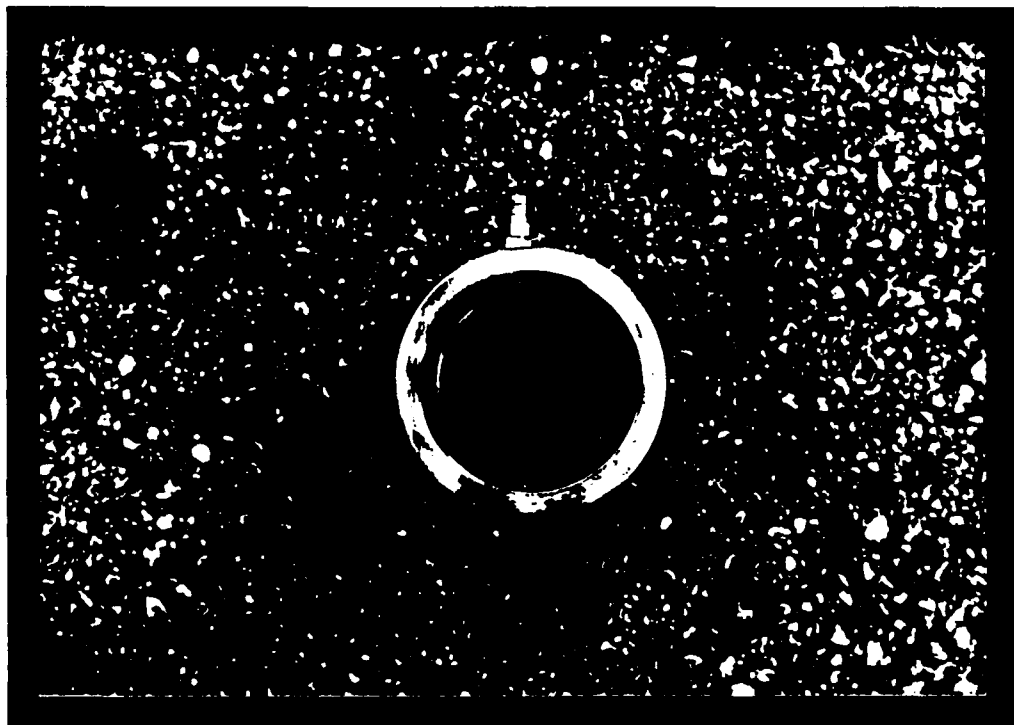
Fig. 20. Photograph of 4 hole injector and graphite nozzle combustor after firing of STD ED/BHC Phase I combustor.
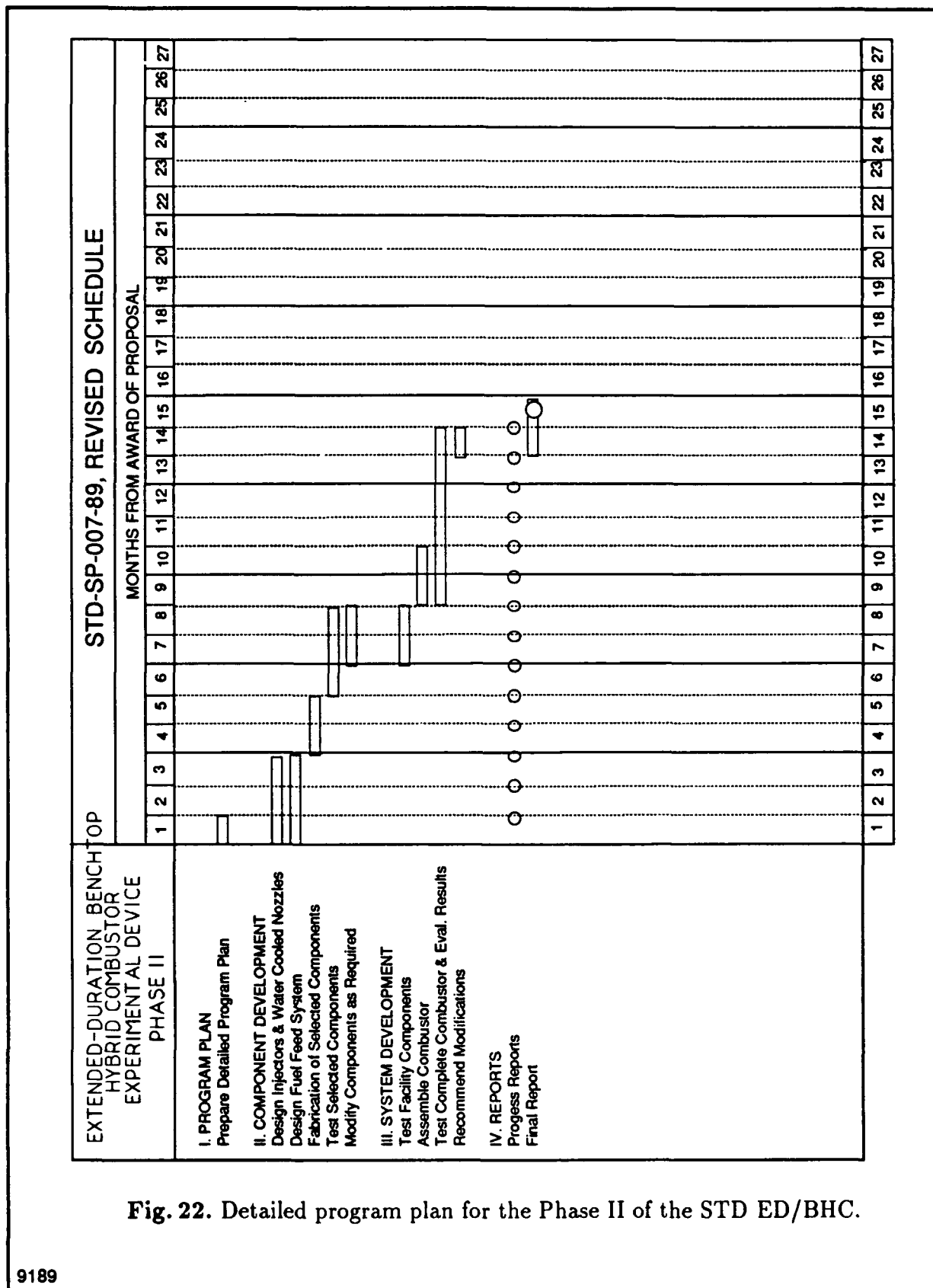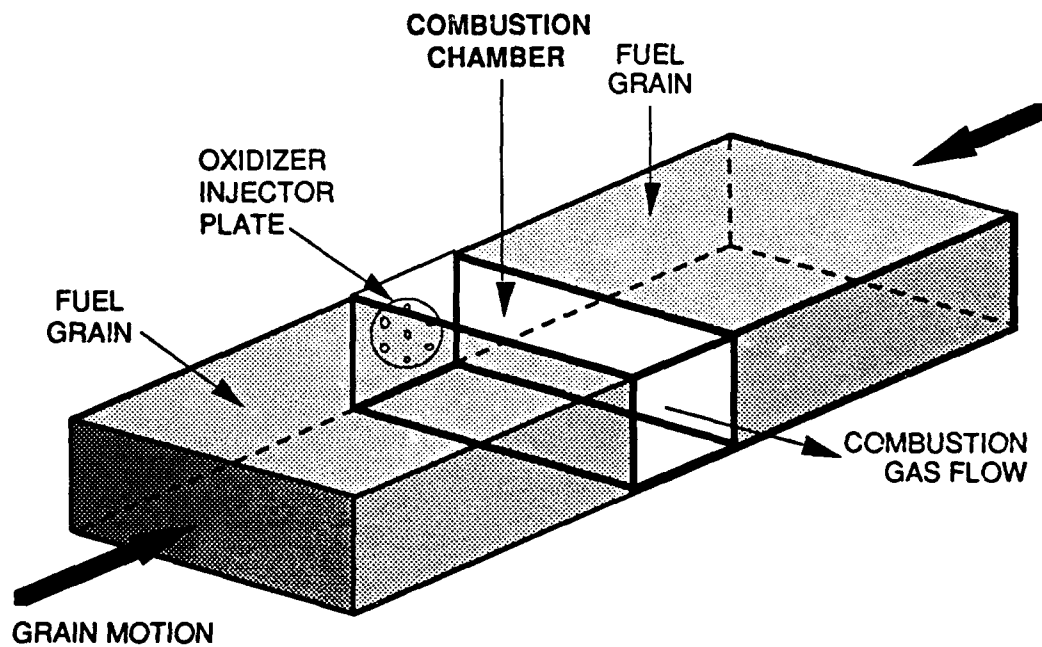
9099

©1990 STD Research Corporation
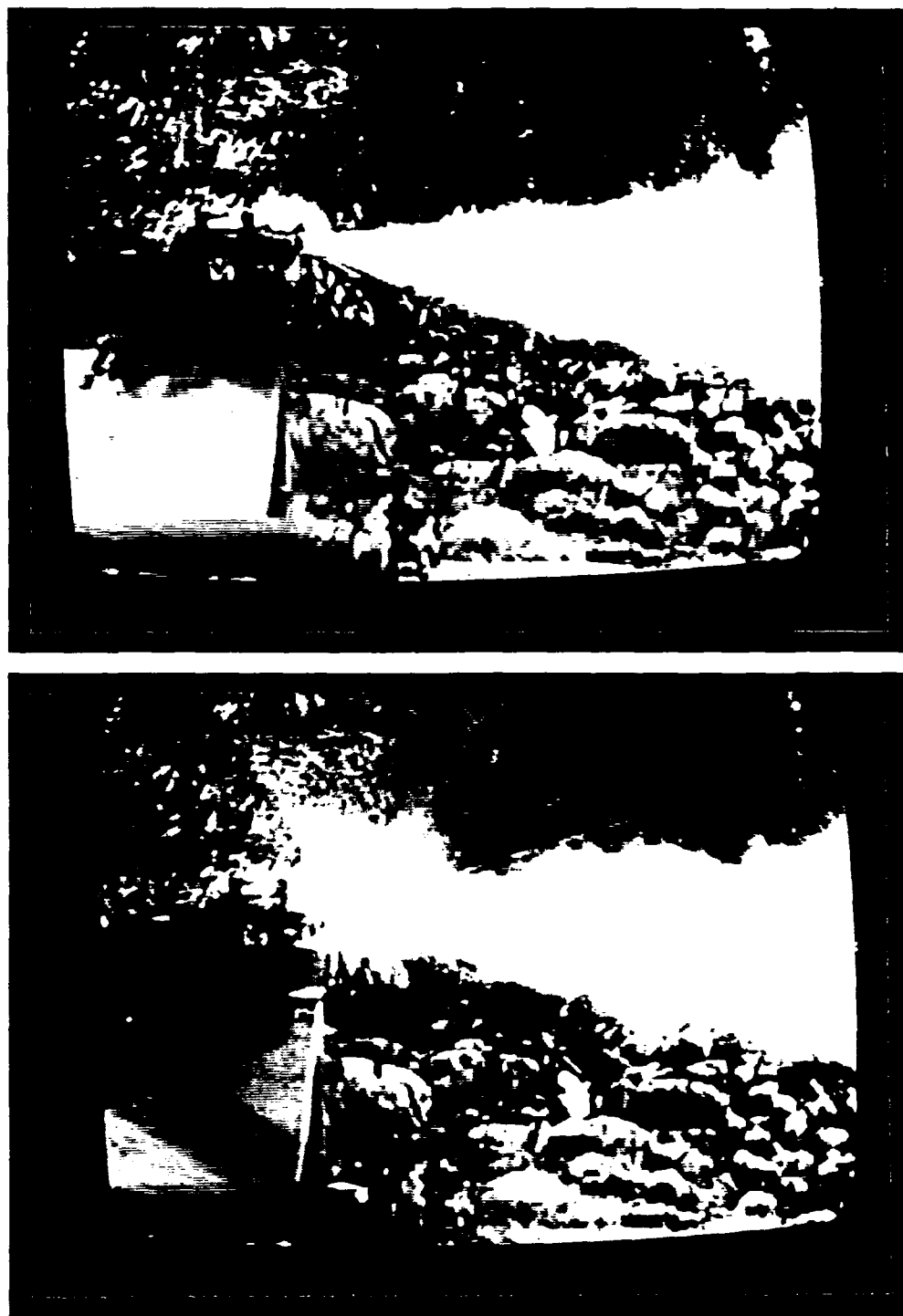
Fig. 21. Photograph of 4 hole injector and graphite nozzle during test of the STD ED/BHC Phase I combustor.
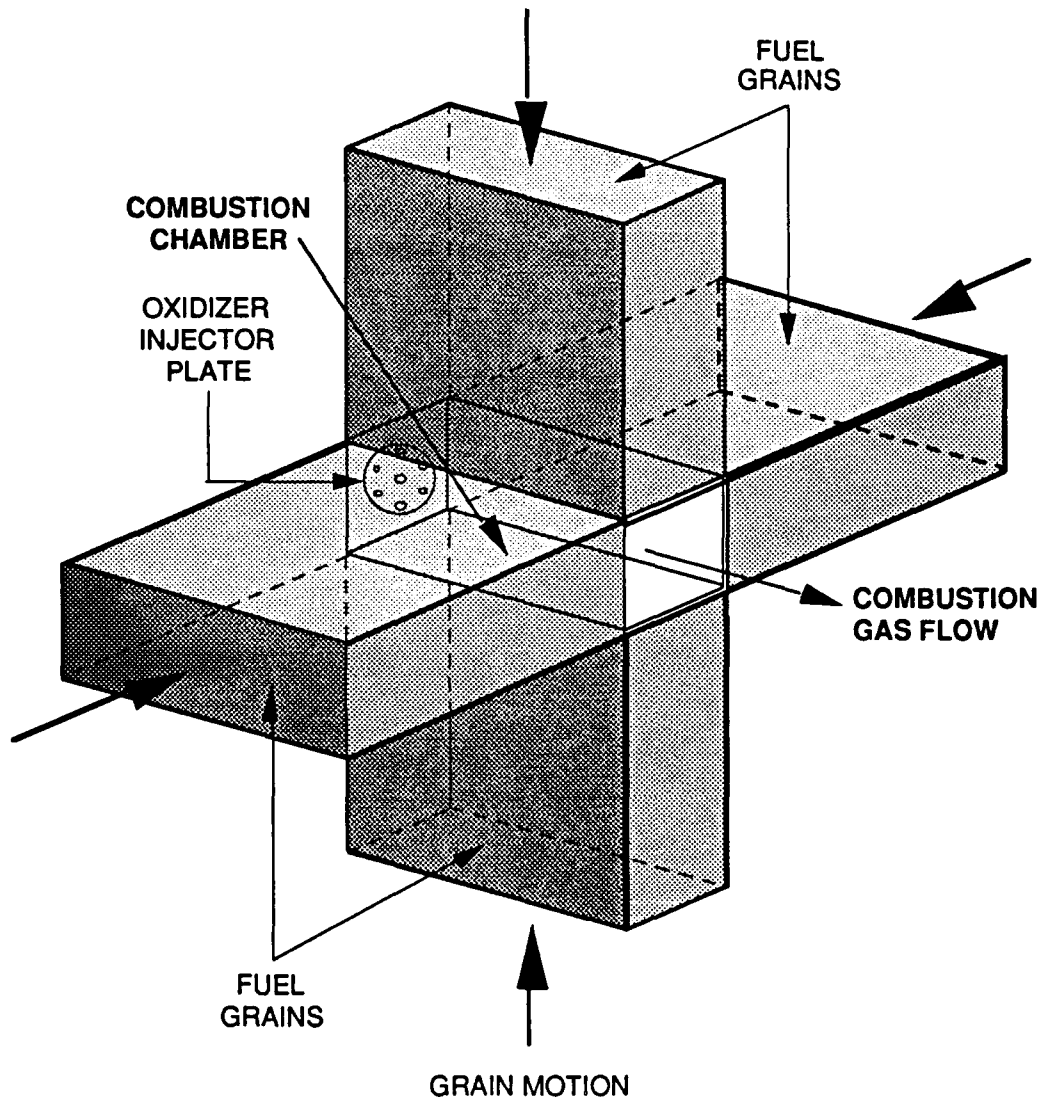
1000

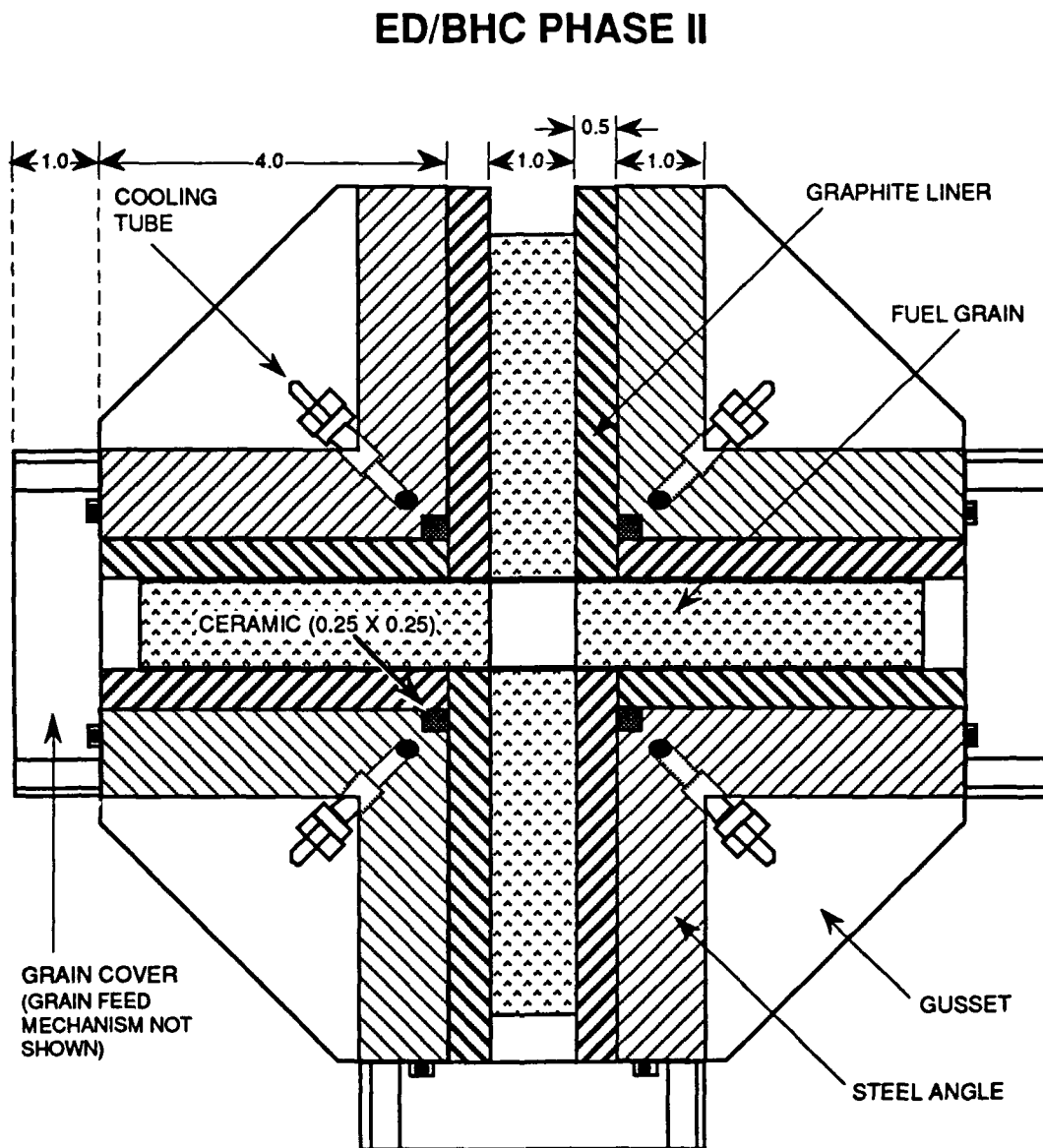**Fig. 22.** Detailed program plan for the Phase II of the STD ED/BHC.

9189

Fig. 23. Schematic of the two-element fuel configuration for the STD
ED/BHC Phase II combustor.

©1990 STD Research Corporation

Fig. 24. Schematic of the four-element fuel configuration for the STD ED/BHC Phase II combustor.

©1990 STD Research Corporation

Fig. 25. Cross section of the STD Phase II extended duration/benchtop hybrid combustor (STD ED/BHC). Four-grain configuration is shown. All dimensions in inches.

9419

©1990 STD Research Corporation

HIGH POWER HIGH REP RATE MODULATORS

George Kirkman
Integrated Applied Physics
50 Thayer Road
Waltham, MA 02154

High Power Modulator Development Based on the Back Lighted Thyratron Switch

G. Kirkman-Amemiya, M. S. Choi, M. A. Gundersen, S. S. Merz,
and N. Reinhardt

Integrated Applied Physics Inc.
140 East Santa Clara Street #19
Arcadia, California 91006

ABSTRACT

A project to develop improved high power high repetition rate modulators for accelerator and pulsed laser applications is described. The modulator development is based on the back lighted thyratron or BLT switch which has demonstrated improved performance in voltage holdoff >100kV, peak current >80kA, rate of current rise >6×10^{11}A/sec and ability to handle high reverse currents >40kA. The BLT is optically triggered allowing for implementation of modulators requiring multiple switches.

I. INTRODUCTION

Many particle beam accelerator and pulsed laser systems are limited by the performance of the pulsed power modulator which in many cases is limited by the performance of the switch. In this project we are developing improved modulators based on a new development in high power switch technology. The new switch is the back lighted thyratron or BLT switch and is a thyratron switch that has shown improved performance in the areas of peak current , voltage holdoff, rate of current rise, triggering and construction.

A. The back lighted thyratron switch

The Back of the cathode Light activated Thyratron or BLT switch[1] is an optically triggered version of the Pseudospark switch[2]. The BLT operates with peak currents and current rates of rise comparable to high pressure spark gaps but with the repetition rates and low electrode erosion characteristic of hydrogen thyratrons. Unlike the hydrogen thyratron the switch requires no cathode heater power and has a much simpler gridless structure, also the symmetric structure of the BLT allows it to conduct reverse currents without electrode damage. Unlike the Pseudospark switch the BLT is optically triggered allowing for complete electrical isolation of the triggering circuit.

The switch structure is cylindrically symmetric consisting of two cup shaped electrodes with flat bottoms that face each other and are separated by about 3-5mm, each electrode has an aperture on the cylinder central axis of 3-5mm diameter. The electrodes are positioned within a cylindrical ceramic or glass insulator and the structure is filled with a low pressure gas usually hydrogen at about 25-40 Pa. For this pressure and electrode separation the switch has a high breakdown voltage by operating on the left side of Paschen minimum[3]. In this region the mean free path between ionizing collisions for electrons released from the cathode is comparable to or larger than the electrode separation making and ionization avalanche and electrical breakdown highly unlikely. A higher breakdown voltage is obtained by decreasing the gas pressure or decreasing the electrode separation. The central apertures perturb the field giving a longer effective path for breakdown with a lower breakdown voltage. When electrons are added to the region of the cathode aperture an ionization avalanche can occur producing a homogeneous discharge plasma confined to this central region of the electrodes. A hollow cathode type discharge is formed that gives a rapid rise in ionization and current through the switch. The ions produced during these transient phases bombard the cathode producing secondary electron emission and heating the cathode surface to a temperature where thermionic emission is possible[4]. The discharge continues in a high current dense glow discharge phase using the thermionic cathode produced at the front surface of the cathode electrode. The switch conducts at a current density of several kA/cm2 that continues for a time determined by the external circuit. The operating voltage is similar to that of hydrogen thyratrons up to about 35kV for typical single gap devices however the peak currents and rate of current rise are significantly higher than thyratrons. The switch has operated at peak currents over 80kA in 500nsec pulses and at several kA with pulse lengths from 50nsec to several μsec. The rate of current rise is usually limited by the external circuit and has been observed[5] to be $>6 \times 10^{11}$A/sec at 22kV and 9kA when operating in a fast test circuit. The high peak currents and rise rates are important to several pulsed power applications such as lasers, modulators for accelerators and fast pulsed magnet systems that typically require magnetic pulse sharpening and compression to obtain the required pulse shape, in some applications replacing the thyratron by a BLT switch may eliminate the need for magnetic circuitry[6]. Also circuits that have poorly matched loads, such as the excimer laser discharge can produce reverse currents that are damaging to thyratrons due to arcing that can occur on reverse conduction, the symmetric structure of the BLT allows it to handle nearly 100% reverse currents without damage.

Triggering of the BLT switch is accomplished by unfocussed UV light incident on the back side of the BLT cathode. Only

a small number ($\sim 10^9$) electrons are required to initiate this discharge. These electrons can be provided through photoemission using an unfocused UV light source such as a laser or flashlamp. Measurements of delay and jitter[7] of the discharge formation have shown that with 1.5×10^9 starting electrons produced by photo emission the discharge is initiated with a delay of about 80nsec and jitter <1nsec for a 3mm electrode spacing at 26Pa H_2 and 10kV initial voltage. The values of delay and jitter increase when the number of starting electrons, gas pressure or applied voltage is decreased. We have investigated several optical triggering methods including laser, flashlamp and light guided by an optical fiber. In each case a small amount of unfocused light is incident on the back surface of the cathode near the central aperture.

II. PRELIMINARY EXPERIMENTS

Preliminary proof of principle experiments have been used to establish the feasibility of using the BLT switch in high power modulators. These experiments were directed at demonstrating the use of BLT switches in modulator configurations requiring simultaneous triggering of many switches and the scaling of the BLT switch to higher voltage, >100kV operation. For these experiments demountable switches with O-ring seals were used, therefore high average power and life testing was not possible.

A. Fiber optic triggering

An important advantage of the BLT switch is the optical triggering of the switch which allows many switches to be triggered simultaneously from a single light source. In multiple switch modulator development this advantage is exploited by using a fiber optic delivery system to distribute light from one source to trigger many switches.

Optical triggering using a fiber-optic to deliver a UV light pulse to the back surface of the cathode near the cathode aperture has been evaluated in the demountable switch shown in figure 1. In this method a UV transmitting plastic coated silica or all silica fiber is used to bring light into the cathode back space and direct it to the cathode surface near the hollow cathode aperture. Using the fiber-optic with a XeCl-laser resulted in a small delay and jitter with a small amount of light incident. The best jitter and delay times were 0.4 nsec and 78 nsec respectively operating at a pressure of 26Pa H_2 and 10 KV anode voltage using 4.4 mJ of XeCl laser light at 308 nm incident on the molybdenum cathode surface.
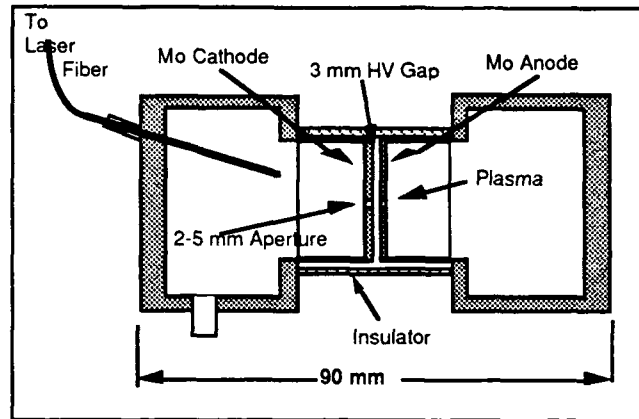
3

Figure 1. Structure of a BLT switch with optical triggering through an optical fiber. The switch is filled with low pressure gas and is triggered by unfocused UV light incident on the back of the cathode surface.
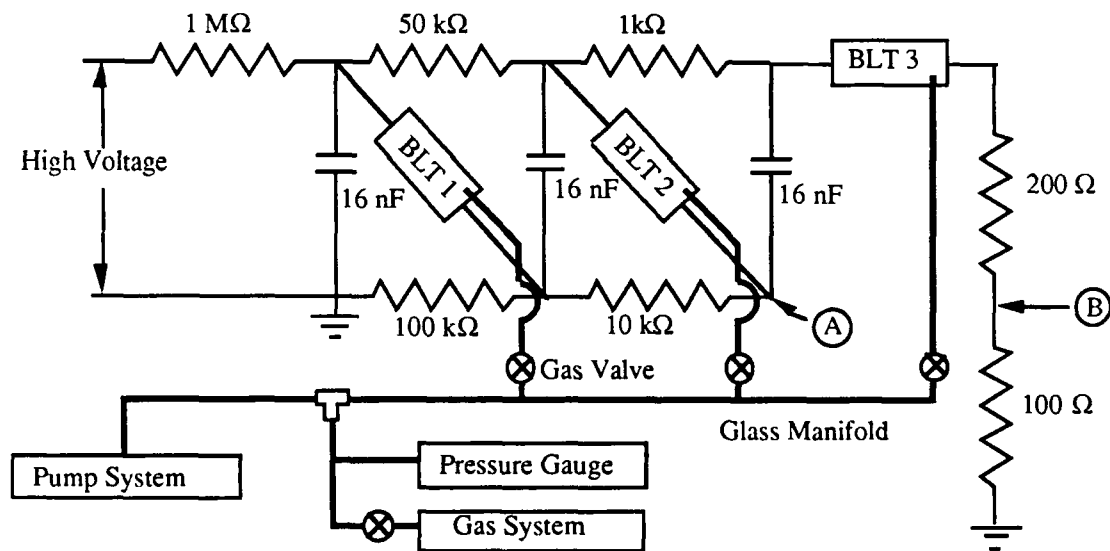

Figure 2. BLT Marx bank with electrical and gas handling connections shown.

B. BLT Marx bank

A Marx bank is typically switched by spark gaps operating at or very near self-breakdown. Many stage Marx banks can fail to fire because although the first gap closes, the overvoltage erected by each stage may not be sufficiently large to trigger the following spark gaps. It is therefore common practice in Marx bank technology to trigger more than one gap. However, as a result of the high voltages involved the triggering circuit is affected by feedback from the stage voltage when the individual gaps close. Isolation of individual switches can be very difficult with electrically triggered switches. Optical triggering provides a method to isolate circuits from each other, eliminating the feedback problem.

Figure 2 shows the electrical and vacuum arrangements for a three stage BLT Marx bank. Each BLT is connected from the cathode side to the vacuum and gas handling system through glass valves which provide electrical isolation among the BLTs. The valves also allowed independent variation of the pressure in each switch. The gas used in these experiments was Hydrogen. The BLTs were triggered simultaneously by an excimer laser pulse through an optical fiber. The laser wavelength and pulse duration were 308nm and 10nsec respectively. The light energy incident at the cathode of each switch was about 3mJ.

For this work, 16nF capacitors were charged to 35kV and were discharged by optically triggering the BLT1 and BLT2 simultaneously. BLT3 was operated in a self-breakdown fashion as the output switch of the Marx bank giving a maximum peak voltage of 105kV. The output pulseshape depended on the load resistor used and was measured at point B. Using a total load resistance of 300Ω an output pulsewidth of $1.6\mu sec$ with a risetime of 50nsec was obtained. The Marx bank was operated a a repetition rate of 4Hz.

This experiment demonstrated a BLT based Marx bank designed to obtain medium high voltages, when optically triggered in low repetition rate operation. These results have demonstrated the feasibility of developing modulators that require simultaneous optical triggering of several BLT switches.

C. Multiple gap BLT switches

The optically triggered structure of the BLT switch allows for simple scaling to higher voltages by stacking multiple BLT electrode structures to form a multiple gap switch.

5

Optical triggering gives electrical isolation of all stages and allows for the simultaneous triggering of all switch gaps. The absence of a continuously heated cathode simplifies construction and improves operation by allowing a more open structure to obtain a high holdoff voltage. We have completed proof of principle demonstrations of multiple gap BLT switches.

Two, three and four gap BLT switches that could be triggered by a flashlamp or through a fiber optic were tested and are shown in figure 3. These tests demonstrated scaling of voltage with increasing gap number and triggering of the multiple gap discharge. The switches had glass insulators such that the discharge character could be observed to verify that a diffuse pseudospark discharge was initiated in all gaps. The best voltage and peak current obtained in single shot operation was 100kV, 76kA, 3×10^{11}A/sec dI/dt, 630J/pulse, 12.6mC/pulse total charge, 400nsec pulse length and 25kA reverse current .

III. BLT SWITCH DEVELOPMENT

For reliable operation at high powers with long lifetimes hermetically sealed switches of ceramic-metal construction are required. Most of the work on this project to date has been the development of a sealed ceramic BLT switch.

The switch design chosen was a 64mm diameter single gap ceramic-metal BLT switch. This switch is IAP part number BLT-250 and can be produced in both optically and electrically triggered versions. The switch is designed to operate at 40-50kV and peak currents >20kA.

A considerable amount of effort has gone into perfecting the fabrication and processing techniques required to produce reliable switches. Our switches are of brazed ceramic and metal construction, leak checked to $<10^{-10}$ atm-cc/sec, then processed by baking under 10-7 torr vacuum at 350C for >12hrs. The switch operates at 25-50 Pa H_2 with the gas pressure maintained by a hydrogen reservoir. New reservoir technology allows us to use a small reservoir consuming only a few watts of electrical power to maintain the gas pressure and getter impurities to ensure stable long life operation of the BLT-250 switch.

Both optical an electrical triggering methods were designed to give the fast current rise and low jitter required. Optical triggering results in the simplest and most reliable switch structure but requires a pulsed laser or flashlamp system for triggering. Electrically triggered switches were designed to give a switch that could be a direct replacement for a standard thyratron switch.
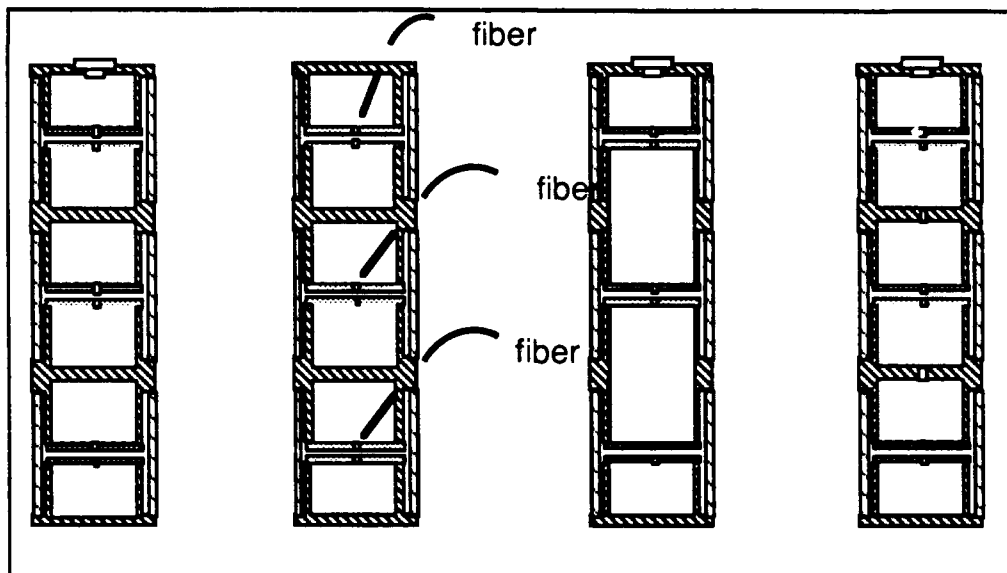
6

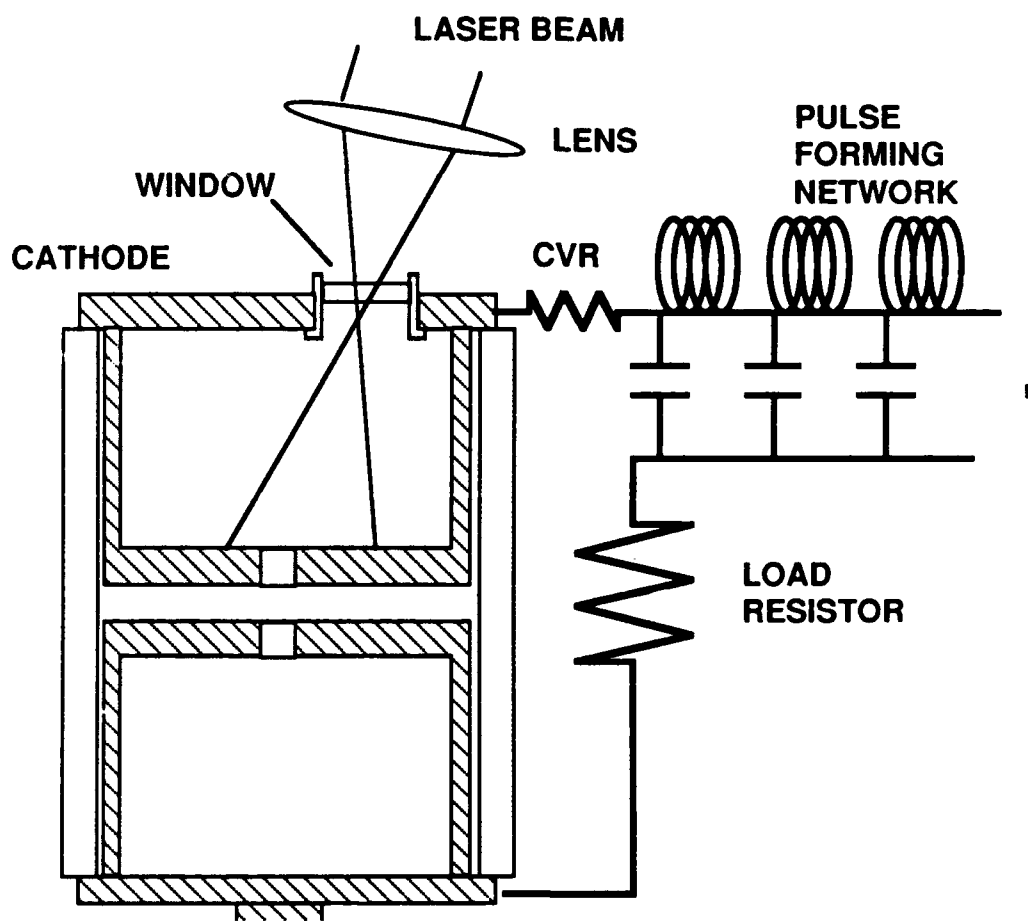Figure 3. Several versions of the multiple gap BLT switch.

Figure 4 The BLT-250-W switch and test set up for optical triggering.

IV. EXPERIMENT

The BLT switch has been operated in several types of test circuits subjecting it to various pulse conditions. The simplest circuits use a standard RLC discharge circuit to produce high peak currents and also high reverse currents, the switch has also been tested in excimer laser discharge circuits to demonstrate it's performance in a real device application and in fast risetime square pulse forming line type networks producing conditions typical of accelerator applications.

A. Capacitor discharge circuits

Several different capacitor discharge circuits have been used to test the switch under varying pulse conditions. For high repetition rate testing typical circuits consist of a capacitance of 20 to 100nF discharged through a one to ten ohm load resistor. The capacitor discharge circuit for very high peak current testing consisted of two $0.4\mu F$ capacitors switched in parallel. Carbon block load resistors were used which could be changed to produce various levels of peak current and reverse current. A 1Ω load resistor would produce an overdamped discharge, 0.25Ω produces near critical damping and for the highest peak and reverse currents the load resistors are replaced by a short circuit to give a ringing discharge. The repetition rate in this circuit was limited by the power supply and resistive charging to about 5Hz.

B. Excimer laser test circuits

Testing in an excimer laser consisted of direct socket replacement of a 3 inch diameter ceramic thyratron switch with an electrically triggered BLT-250 switch. The laser used for these tests was manufactured by Questek Inc. The laser was run with a gas fill of helium to simulate the excimer laser discharge load.

C. Square pulse forming line circuits

The pulse forming line to give a square current pulse consisted of two pulse forming lines symmetrically feeding the switch in parallel. Each line is a ten section Type E equal capacitance network with each section consisting of 4nF capacitance provided by two doorknob type ceramic ($SrTiO_3$) capacitors and 16nH inductance provided by parallel copper plate conductors. Each line has an impedance of 2Ω and gives a pulse length of about 150nsec. The lines are switched by the BLT switch into a resistive load of 1Ω provided by carbon block load resistors. The repetition rate in this circuit was limited by the power supply to about 25Hz. A second pulse forming line with 1.25ohm impedance and 100nsec pulse length was designed and fabricated for

switch testing at IAP. The line consists of two 2.5 ohm lines in parallel each having ten sections each with 12.5nH inductance provided by parallel conducting plates and 2nF capacitance provided by two 1nF, 50kV capacitors. The pulse forming lines are switched to a 1.25 ohm load made up of 4 parallel 5ohm carbon resistors. Using this type of load did not allow for an exact match to the pulse forming line and therefore some positive reflected current was observed indicating a positive load mismatch. The current through the switch was measured using a 5mohm current viewing resistor (CVR), and observed on a digitizing oscilloscope with a 3.5nsec risetime and vertical resolution 0.4% of full scale.

V. RESULTS

A. Capacitor discharge

The BLT switch has been tested in several capacitor discharge circuits producing various peak currents and pulse lengths. Included in these tests was the operation of a BLT-250 switch for > 20 million pulses at 25kV, 3kA, 100Hz with no degradation of performance. All of these tests have been limited in repetition rate, average power and duration by the available equipment and not the BLT switch.

Two sealed ceramic-metal BLT switches of preliminary design were tested. The switches were designated BLT-C-01 and -02. BLT-C-01 was tested at 15kV anode voltage, 5.5kA peak forward current, 1kA reverse current $6.5X10^{10}$ A/sec dI/dt, 185nsec pulse length, 30Hz, 5.6J/pulse for a total of $4X10^5$ pulses which is a total charge transfer of 300C with no degradation of performance. BLT-C-02 was tested at 10kV anode voltage, 3.5kA peak forward current, 1kA reverse current $4.3X10^{10}$ A/sec dI/dt, 180nsec pulse length, 100Hz, 2.5J/pulse for a total of>$2X10^7$ pulses which is a total charge transfer of 10,000C with no degradation of performance (this test was stopped due to a failure in the power supply used for testing). Analysis of each switch after these tests showed very little wear to the electrode surfaces and no measurable macroscopic erosion of electrode material.

An electrically triggered BLT-250 switch has been tested in a capacitor discharge circuit consisting of a 20nF capacitor discharge through an 11Ω resistive load. This switch was run at 25kV anode voltage, 2.8kA peak forward current, 200nsec pulse length, 100Hz, 6.25J/pulse for a total of 10 million pulses, 5000C total charge with no degradation of performance. The switch was dismantled after these tests and the electrode erosion measured. It was found that only about 0.06g of electrode material had been eroded. The charge transfer per gram of electrode eroded was ≈83,000 C/g which is considerably better than spark gap performance which is typically about 20,000 C/g.

9

An optically triggered BLT-250 switch was tested in two capacitor discharge circuits one to give a 200nsec pulse length and 2.8kA at 12.5kV and another to give a 400nsec pulse length and 9.5kA at 12.5kV, both circuits were slightly overdamped. The switch was tested at repetition rates up to about 10Hz. The switch was triggered using a KrF excimer laser or a +5kV pulse applied to the trigger electrode and a combined method applying both the electrical an optical pulse.

Jitter values of 1.5nsec were obtained using the optical trigger and 3.7nsec using the electrical trigger. Both measurement are one sigma values using a statistical sampling of the delay time of 1000 shots. Good optical triggering was possible with laser energy as low as 600μJ per pulse. Triggering jitter is strongly dependent on the gas pressure in the switch which is determined by the reservoir current. Low jitter is obtained by operating at high reservoir current however at high reservoir current the hold off voltage capability of the switch is decreased. It is important to carefully adjust the reservoir current to the highest value possible for the hold off voltage desired. In these tests the circuit was RC charged by a DC power supply. Higher voltage operation at the same reservoir current and jitter values should be obtained by using a command or pulse charged circuit. Typical charging parameters for such a circuit could be: a charging time on the order of 10μsec, a dwell time of the same order or less and then a dead time on the order of 100μsec before recharging.

It was possible to trigger the switch with very low laser energy by combining the electrical and optical triggering. In this method a voltage pulse of 2-5kV is applied to the trigger pin followed by the laser pulse a few hundred nsec later the switch closure then takes place with timing synchronized to the light pulse. Using this method it may be possible to trigger many switches synchronized by a single light source since the laser energy required by each switch is very low.

B. Excimer laser tests

An electrically triggered BLT-250 switch was tested in an excimer laser with a gas discharge load and 72nF storage capacitor. Maximum conditions achieved were 135Hz at 30kV 4.4kW. The switch was run continuously at 25kV, 100Hz at an average power of 2.25kW for 2 million pulses with no degradation of performance. The current in these tests was ≈10kA with current reversal and high dI/dt, conditions which are damaging to conventional thyratron switches. During these tests the maximum temperature of the switch were 75 C at the cathode flange and 102 C on the ceramic body.
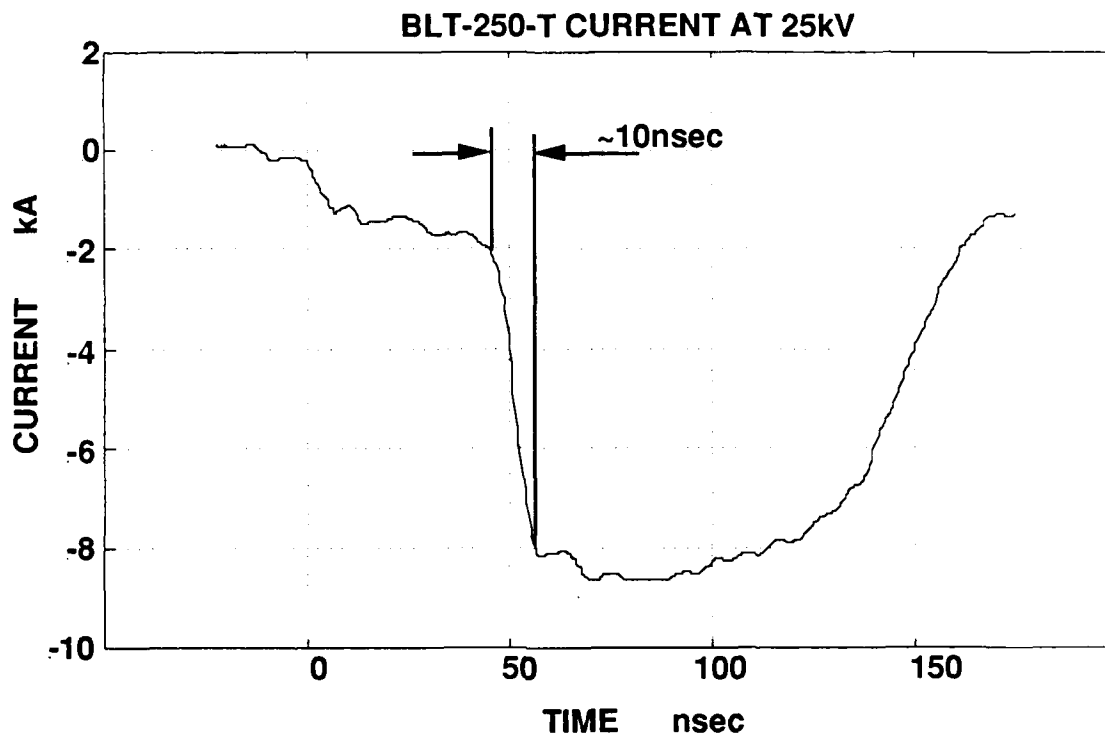
Figure 5. Current waveform obtained with the BLT switch operating at 25kV showing the extremely fast current rise characteristic of the superemissive self heated cathode. The current rises from 2kA to 8kA in about 10nsec a rate of current rise that is normally impossible with standard thyratron switches.

C. Pulse forming line tests

An optically triggered switch designated the BLT-250-W was tested in the 1.25ohm pulse generator. The switch is the basic BLT-250 electrode structure with a sapphire window to allow UV light into the cathode back space. Figure 4 shows the experimental arrangement for testing the optically triggered switches. A KrCl excimer laser operating at 222nm wavelength was used as the triggering source. The laser energy incident near the cathode aperture was <10mJ in a 10nsec pulse. These tests were limited to 25kV and 10Hz by the charging power supply.

Figure 5 shows the current pulse obtained at 25kV showing a slow initial rise during cathode heating then an extremely fast rise from 25% to 100% peak current. At 25kV the discharge current rises more than 6kA in 10nsec which is about 6 times faster than is possible with the fastest thyratron switches. The best pulse shapes were obtained at 22.5kV. At 22.5kV the peak current was ~8kA with a 10-90% rise time of 40nsec and a 55nsec flat top with about +/-2% ripple. Improvements in optical triggering and circuit methods should be able to reduce the 0-25% risetime to give a 0-100% risetime <25nsec.

Testing with the 1Ω square pulse forming line resulted in 150nsec pulses up to 10.5kA at 20kV with a 10-90% rise time of 45nsec and pulse top variation <2%, figure 6a. At lower voltages the risetime was observed to be longer resulting in a lower peak current to voltage ratio. At 5kV the rise time was 73nsec and the peak current only 2.4kA. The longer risetime is due to a slower heating of the self heated cathode. Under low voltage and current conditions this effect is observed as a slow rising high impedance phase of the discharge before initiation of the high current phase of the discharge. At 2.5kV the peak current is 1kA, the current has a slow rising phase from 0 to 500A lasting 120nsec then increases to 1kA in the next 30nsec, figure 6b. This behavior has also been observed in streak photography as a fast increase in discharge radius after a slow development of a confined discharge channel.

D. High current tests

Using the capacitor discharge circuit the switch was tested at peak currents from 3.5kA to >80kA with pulse lengths of about 500nsec. The rise time was observed to be constant and the peak current and rate of current rise increase linearly with voltage in the range of 5 to 25kV. In all cases no current interruption was observed and circuit limited pulse shapes were observed. Under short circuit conditions the switch was operated at 17.5kV, 122.5J/pulse and 5Hz giving a peak current of 60kA followed by 40kA reverse current. The
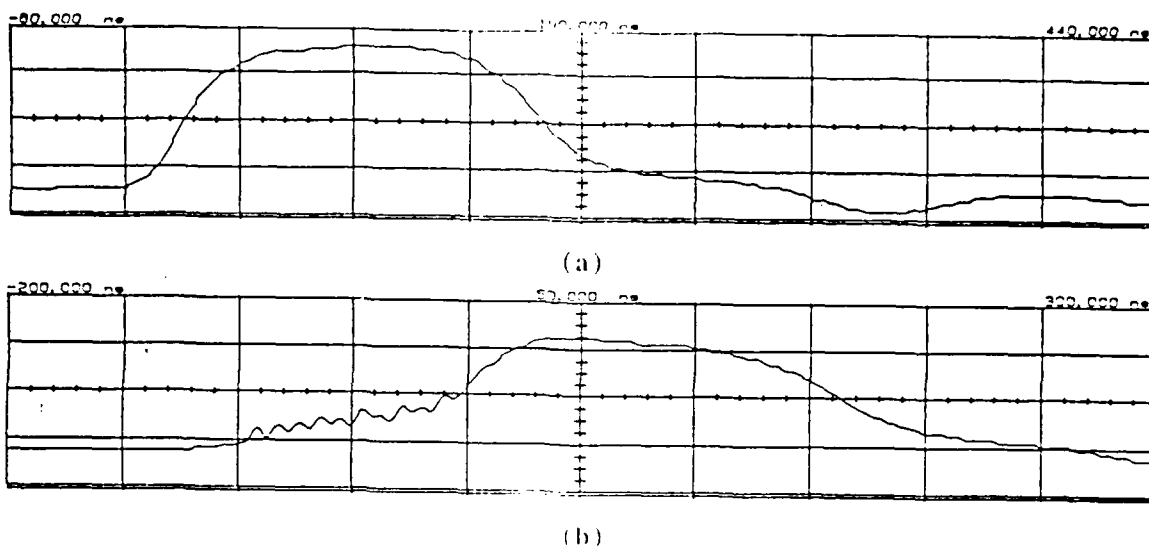
(a)

(b)

Figure 6. Current pulse shapes obtained with the 1 ohm pulse forming line.
(a) 20kV, 3.4kA/div, 10.5kA peak current with a 45nsec risetime. (b)
2.5kV, 400A/div, 1kA peak current with a 115nsec risetime. Horizontal
scale is 50nsec/div for both (a) and (b). Both are flashlamp triggered at 5Hz
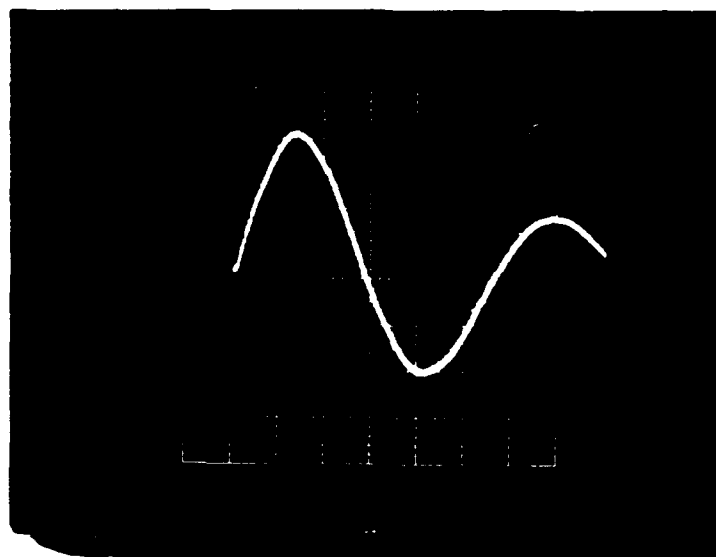at a gas filling of 39Pa H_2.

Figure 7. Current pulse obtained with the 0.8μF capacitor discharge circuit
with no load resistance. 17.5kV, 20kA/div, 60kA peak current followed by
40kA reverse current, horizontal scale is 200nsec/div. The switch was
flashlamp triggered at 5Hz at a gas filling of 36Pa H_2.

13

rise time was 140nsec, a dI/dt of 3.4×10^{11}A/sec. The ringing current waveform is shown in figure 7. A circuit inductance of 40nH and resistance of 60mΩ were calculated from the current waveform. Under these conditions the switch was run continuously for $>10^4$ pulses with no degradation of performance observed.

VI. FUTURE WORK

In continuing work we are fabricating and testing a series of BLT-250 switches. It is important to verify the switches performance and reliability by fabricating and testing several switches of the same design. Also included in future work will be the fabrication and testing of sealed ceramic-metal multiple gap switches for high voltage operation.

A. Life testing

Life testing of the BLT switches requires continuous operation of a test facility operating at high repetition rate and high average powers. In previous testing we have been limited by available equipment to 8 or 10 hours per day operation at average power levels of 1 to 2 kW. We are presently beginning tests using a 20kW computer controlled system which will allow continuous operation at high repetition rates. We plan to use this system to test the BLT-250 switches for $>10^9$ pulses.

B. High voltage testing

High voltage testing of single and multiple gap BLT switches at high repetition rates is planned. For this work we will extend the capabilities of our 20kW test system by adding a pulse charging section consisting of a thyratron or BLT switch and a pulse transformer to give output voltages >150kV.

C. Modulator development

The first year to eighteen months of this project will concentrate on the development of the BLT switch for advanced modulator development. The first modulator testing planned will be a BLT Marx bank using sealed ceramic-metal BLT switches. These tests will demonstrate BLT Marx bank operation at high repetition rates and high average power. Based on the performance obtained with the BLT switches various additional modulator designs may be tested.

VII. CONCLUSION

This work has demonstrated in proof of principle experiments that the BLT switch is capable of improving the performance of modulators requiring multiple switches. The scaling of the BLT switch to voltages >100kV has been demonstrated

using multiple gap switches. Design, fabrication and preliminary testing of sealed ceramic-metal BLT switches has been completed.

A design for the single gap sealed ceramic-metal BLT switch to be developed has been determined. Much of the work on the sealed switches has been in establishing the design and fabrication techniques for these switches. It is expected that life testing of several BLT-250 switches at high repetition rates and high average powers will be proceeding in the immediate future.

ACKNOWLEDGMENTS

REFERENCES
1. G. F. Kirkman and M. A. Gundersen, "Low pressure, light initiated glow discharge switch for high power applications," *Appl. Phys. Lett.*, vol. 49, p. 494, 1986.
2. K. Frank, E. Boggasch, J. Christiansen, A. Goertler, W. Hartmann, C. Kozlik, G. Kirkman, C. Braun, V. Dominic, M. A. Gundersen, H. Riege and G. Mechtersheimer, "High power pseudospark and BLT switches," *IEEE Trans. Plasma Sci.*, vol. 16, no. 2, p.317, 1988.
3. M. J. Schonhuber, "Breakdown of gases below paschen minimum: basic design data of high voltage equipment," *IEEE Trans. Power Appar. Syst.*, vol. 88, p. 100, 1969.
4. W. Hartmann, V. Dominic, G. Kirkman, and M. A. Gundersen, "An analysis of the anomalous high current cathode emission in pseudospark and BLT switches," *J. Appl. Phys.*, vol.65 no. 11, p. 4388, 1989.
5 G. Kirkman-Amemiya, DOE Final Report contract No. DEAC0389ER80794, to be published.
6. G. Kirkman, W. Hartmann, and M. A. Gundersen, "A flashlamp triggered high power thyratron type switch," *Appl. Phys. Lett.*, vol. 52, p. 613, 1988.
7. C. G. Braun, W. Hartmann, V. Dominic, G. Kirkman, M. Gundersen and G. McDuff, "Fiber optic triggered high power low pressure glow discharge switches," *IEEE Trans. Electron Devices*, vol. 35, no. 4, p. 559, 1988.

LIST OF PARTICIPANTS

3RD SDIO/ONR PULSE POWER PHYSICS MEETING

OMNI INTERNATIONAL HOTEL

Norfolk, Virginia 23529

August 2 -3, 1990

List of participants

Charles Beason
WL/AWA Kirkland AFB
Albuquerque, NM 87117
(505) 846-7369
Fax # (505) 846-0148

Martin Brouillette
STD Research Corporation
P.O. Box C
Arcadia, CA 91066
(818) 357-2311

Mark Browder
Center for Energy Conversion Research
The University of Texas at Arlington
Arlington, Texas 79409
(817) 794-5100

Voitek Byszewski
GTE Labs Inc.
40 Sylvan Road
Waltham, MA 02254
(617) 466-2470
Fax # (617) 890-9320

Brian Ditchek
GTE Labs Inc.
40 Sylvan Road
Waltham, MA 02254
(617) 466-2526

William Donaldson
Laboratory for Laser Energetics
250 East River Road
Rochester, NY 14623-1299
(716)275-5347

Dennis Fessenden
Code 3241
Naval Surface Systems Center
New London, CT 06320
(203) 440-4513

Gerry J. Fitzpatrick
Polymer Division
N.I.S.T.
Bldg. 220 - B344
Gaithersburg, MD 20899
(301) 975-2737

Alan Garscadden
AF Wright Aeronautical Laboratory
Wright Patterson AFB
Ohio 45433-6563
(513) 255-2923

Glenn A. Gerdin
Dept of Electrical & Computer Engineering
Old Dominion University
Norfolk, VA 23529
(804) 683-3744

Arthur H. Guenther
R & D Institute
Pinon Building
1220 St. Francis Drive
Santa Fe, New Mexico 87503
(505) 667-1331

Martin Gundersen
Dept. Elec. Eng-Electrophysics
SSC-420, MC 0484
Los Angeles, CA 90089
(213) 743-6195

Anthony Hyder
Office of the Vice President for Research
202 Sanford Hall
Auburn University
Auburn, Alabama 36849-5112
(205) 844-4784

David Jacobs
DNA/RAEV
6801 Telegraph Road
Alexandria, VA 22310-3398
(703) 325-7087

George Kirkman
Integrated Applied Physics
50 Thayer Road
Waltham, MA 02154

Magne Kristiansen
Dept of Electrical &
Computer Engineering
Texas Tech University
Lubbock, TX 79409-2019
(806) 742-2224

Mark Kushner
Gaseous Electronics Laboratory
Dept of Electrical & Computer Engineering
University of Illinois
Champaign, IL 61820
(217) 244-5137

Vishnu K. Lakdawala
Dept of Electrical & Computer Engineering
Old Dominion University
Norfolk, Virginia 23529
(804) 683-4665

Chi H. Lee
Dept. Electrical Engineering
University of Maryland
College Park, MD 20742
(301) 454-6852

David Lojewski
HQ Defense Nuclear Agency
6801 Telegraph Road
Alexandria, VA 22310
(703) 325-6733

Larry H. Luessen
Naval Surface Weapons Center
Code F-12
Dahlgren, VA 22448-5000
(703) 663-8026

Michael S. Mazzola
Naval Surface Warfare Center
Code F-12
Dahlgren, VA 22448-5000
(703) 663-8026

Gerard Mourou
Ultrafast Science Laboratory
University of Michigan
Ann Arbor, MI 48109-2099
(313) 763-4875

Mark Newton
Lawrence Livermore National Laboratory
P.O. Box 808, Mail Stop L-627
Livermore, CA 94550
(415) 422-1861

Jorge J. Rocca
Dept of Electrical Engineering
Colorado State University
Fort Collins, CO 80523
(303) 491-6796

Gabriel D. Roy
Office of Naval Research
Code 1132P
800 N. Quincy Street
Arlington, VA. 22217-5000
(202) 696-4403

Pete Rustan
SDIO/T/IS
Pentagon
Washington, DC 20301-7100
(202) 693-1527

Karl H. Schoenbach
Dept of Electrical & Computer Engineering
Old Dominion University
Norfolk, VA 23529
(804) 683-4625

Santosh K. Srivastava
Jet Propulsion Laboratory
California Institute of Technology
Pasadena, CA 91109
(818) 354-3246

David Stoudt
Naval Surface Warfare Center
Code F-12
Dahlgren, VA. 22448-5000
(703) 663-8057

Tangali S. Sudarshan
Dept. Electrical & Computer Eng.
University of South Carolina
Columbia, SC 29208
(803) 777-7302

Richard van Brunt
Bldg. 220, Room B344
National Institute of Science & Technology
Gaithersburg, MD 20899
(301) 975-2425

Frazer Williams
University of Nebraska
Department of Electrical Engineering
Lincoln, NE 68588
(402) 472-1970

William Moeny
Tetra Corporation
4905 Hawkins St., NE
Albuquerque, NM 87109
(505) 345-8623